

Characterization and Erosion Behaviour Study of Carbide Based Thermal Spray Coatings on Steel

Ph.D. THESIS

by

Anurag Hamilton
(ID: 2014RMT9060)



**DEPARTMENT OF METALLURGICAL AND MATERIALS ENGINEERING
MALAVIYA NATIONAL INSTITUTE OF TECHNOLOGY JAIPUR,
JAIPUR-302017, RAJASTHAN (INDIA)**

DECEMBER2017

Characterization and Erosion Behaviour Study of Carbide Based Thermal Spray Coatings on Steel

A THESIS

Submitted in partial fulfillment of the requirements for the award of the degree

of

DOCTOR OF PHILOSOPHY

in

METALLURGICAL AND MATERIALS ENGINEERING

by

Anurag Hamilton
(ID: 2014RMT9060)



DEPARTMENT OF METALLURGICAL AND MATERIALS ENGINEERING
MALAVIYA NATIONAL INSTITUTE OF TECHNOLOGY JAIPUR, JAIPUR-
302017, RAJASTHAN (INDIA)

DECEMBER 2017

**© MALAVIYA NATIONAL INSTITUTE OF TECHNOLOGY, JAIPUR-2017
ALL RIGHTS RESERVED.**

Dedicated to Lord Almighty, for enabling me to pursue my doctorate. It is not my credit but his profound compassion and grace that enabled me to complete this work.

To Rev. Raju Soni & Rev. Ashok Massey for their missionary zeal, perseverance, and dedication. I owe them a sincere gratitude for their prayers and guidance.

To my wife, Glorina Walter for her unfaltering faith and patience. I am grateful to her for supporting me during my difficult times. Without her support this thesis would have been tough to complete, I owe much of this work to her.

To, Mr. & Mrs. Hamilton for encouraging me to pursue my doctorate.

To, Mr. & Mrs. Walter and Mr. Mohit Walter for their love and support. I am grateful to them for putting their trust on me even when things looked grim and almost slipped out of hands.



DEPARTMENT OF METALLURGICAL AND MATERIALS

ENGINEERING

**MALAVIYA NATIONAL INSTITUTE OF TECHNOLOGY JAIPUR,
RAJASTHAN (INDIA)**

CERTIFICATE

This is to certify that the thesis entitled “**Characterization and Erosion Behaviour Study of Carbide Based Thermal Spray Coatings on Steel**” being submitted by me to the Malaviya National Institute of Technology Jaipur for the award of the degree of **Doctor of Philosophy** is a bonafide record of original research work carried out by me. The content of the thesis has been checked using software “Turnitin” for Plagiarism.

I have incorporated all the suggestions/queries/changes raised by the Examiner in the Thesis Evaluation Reports.

(Anurag Hamilton)

This is to certify that above statement made by the candidate is true to our knowledge.

Prof. Dr. Ashok Sharma
(Supervisor)

Prof. Dr. Upender Pandel
(Co-Supervisor)

Ph.D. viva-voce examination of Mr. Anurag Hamilton, Research Scholar, was held on 18-12-2017 in Department of Metallurgical & Materials Engineering, MNIT Jaipur. The candidate defended the viva-voce successfully to the satisfaction of Oral Defense Committee. The Committee recommends for the award of Ph.D. Degree.

Signature of Supervisors

Signature of External Examiner

ACKNOWLEDGEMENT

I would like to express my sincere gratitude and indebtedness to my supervisors, Prof. Dr. Ashok Sharma and Prof. Dr. Upender Pandel, Department of Metallurgical and Materials Engineering, MNIT Jaipur, for their guidance, unceasing enthusiasm, untiring efforts, and their constructive suggestions throughout the course of study. Their experience, availability to discuss new ideas and willingness to give their knowledge was instrumental in the completion of this thesis. I owe them much gratitude.

I wish to express my sincere gratitude to Prof. A. K. Bhargava, Head of Department of Metallurgical and Materials Engineering, Prof. Upender Pandel (Ex-HOD), Prof. S. K. Gupta and Dr. R. K. Duchaniya, Convener, Departmental Post Graduate Committee, for providing their valuable support and guidance whenever needed during my research work. I am thankful to all the faculty members of the Department of Metallurgical and Materials Engineering, MNIT Jaipur for their support and encouragement.

I would like to extend my gratitude to Dr. S. K. Goel, Executive Director and Mr. S. S. Kasana, Star Wire (India) Ltd, Ballabgarh Haryana, for extending the technical facilities. I am also grateful to the entire team of Quality and Material Testing laboratory especially Mr. Mahipal for metallographic polishing of my samples.

I am grateful to Mr. Harish Sharma, DGM, Mr. Sandeep Kumar, Manager and Mr. Vinod Kumar, Engineer- Hard coating facility, Nathpa Jhakri Hydro Power Station, Satluj Jal Vidyut Nigam Limited, Jhakri for allowing me to visit the hydropower plant and hard coating facility. I am also grateful to them for allowing me to inspect the eroded hydroturbine components. Their fruitful interaction helped me in understanding the erosion problem faced by hydropower plants.

I thank my senior colleague Dr. Avnish Kumar, Department of Valve steel (QA/R&D) , Star Wire (India) Ltd., Ballabgarh, Haryana for his selfless support and guidance. I am grateful to him for his out of the way assistance throughout my course of study.

I thank my senior Mr. Guru Prakash, IIT Roorkee for his support and guidance.

I would like to thank Prof. Per Nylén and Er. Stefan Björklund, M/s PTC Innovation, Sweden for HVOF Thermal Spraying.

I would also like to thank Mr. Hari Prasad Karwa, Managing Director, Metallizing Export Company, Jodhpur for HVOF Thermal Spraying.

I would also like to thank Mr. B. D. Rohhila, M/s Krishna Tools, Faridabad, Haryana for fabrication of the samples. I am grateful to him for giving priority to my research samples in spite of his prior commitments.

I would also like to thank Mr. Sachin Kumar Rathi, Ms. Vatsala Chaturvedi, Mr. Arun Kumar and Mr. Robin Gupta and all the Research Scholars of the Department for their help in my work.

I would like to acknowledge our technical and administrative staff of the department Mr. Lalchand Kumawat, Mr. Rishikesh Babu, Mr. Vidhyasagar, Mr. R.M. Vairagi, Mr. Nathu Singh, Mr. Mahesh, Mr. Lalaram, Mr. Jagdeesh, Ms. Sunita and Mr. Kishan for their help at various stages of the work.

I am also grateful to Rev. J. K. Sharma and Rev. Sunil Paul for their prayers and guidance that they provided during my course of study.

ABSTRACT

Hydropower plants located in the Himalayan region face the typical problem of heavy silt erosion of underwater components, especially during monsoon season. This results in a reduction in efficiency of hydropower plants. Silt erosion mainly occurs due to impingement of hard silt particles (700-1000 HV) entrained in the water on the underwater parts of the hydroturbine (300-400 HV).

The research work reported in this thesis primarily concentrates on addressing silt erosion problem in the hydroturbine components. A surface engineering route was taken to counter the problem. Thermal spray coatings were applied on hydroturbine steel, and their erosion behavior was studied. Mechanism of material removal in the case of uncoated and coated steel was also investigated.

In the first part of the study, erosion behavior of uncoated steel at different impingement angles and velocities was studied. Currently used CA6NM hydroturbine steel was taken as a base material. Solid particle erosion resistance of CA6NM steel was evaluated by air jet erosion tester as per ASTM G76-13 at three different impingement angles (30°, 60° and 90°) and two impingement velocities (35 m/s and 70 m/s) respectively. Higher cumulative volume loss was observed at 70 m/s impingement velocity in comparison to 35 m/s impingement velocity. This was attributed to the higher kinetic energy of erodent in the case of 70 m/s impingement velocity. CA6NM steel showed ductile behavior during erosion as highest cumulative volume loss was observed at 30° impingement angle, followed by 60° and 90°. Eroded surfaces of steel were studied using field-emission scanning electron microscopy (FESEM) to understand the mechanism of erosion and its morphology.

In the second part of the study, WC-10Co-4Cr powder was thermally sprayed using currently used high-velocity oxy fuel (HVOF) and the rapidly emerging high-velocity air fuel (HVAF) process on as-cast CA6NM steel. X-ray diffraction (XRD) analysis of coated surfaces revealed a higher degree of WC decarburization in HVOF coating in comparison to HVAF coating. Higher particle velocity and lower particle temperature during spraying were the main factors, which resulted in a lower degree of decarburization in HVAF coating. Higher hardness, fracture toughness, tensile adhesion and lower porosity were also observed in HVAF coating compared to HVOF coating. Cross-sectional micrographs of HVOF coating revealed interlaminar oxidation. However, same features were not observed in HVAF coated steel. HVAF sprayed WC-10Co-4Cr coating on CA6NM steel exhibited significant improvement in the erosion resistance compared to HVOF sprayed WC-10Co-4Cr coating at

both impingement velocities. Both coatings exhibited mixed mode of erosion as the highest cumulative volume loss was observed at 60° impingement angle, followed by 90° and 30° impingement angles. The better erosion performance of HVAF sprayed coating was attributed to the combination of homogeneous and well-bonded structure with low porosity along with high hardness, fracture toughness and tensile adhesion than HVOF sprayed coatings.

CONTENTS

Certificate	
Acknowledgement	i
Abstract	iii
List of Figures	ix
List of Tables	xv
Nomenclatures	xvi
1. Introduction	1-6
1.1. Background	1
1.2. Objectives of the Study	3
1.3. Outline of the Thesis	3
2. Literature Review	7-34
2.1. Hydropower Plant and its Functioning.....	7
2.1.1. Types of hydro turbine	7
2.1.2. Silt erosion problems in hydroturbine components	10
2.2. Types of Erosive Wear	11
2.2.1. Solid particle erosion	12
2.2.2. Slurry erosion	12
2.2.3. Cavitation erosion	13
2.2.4. Liquid impingement erosion	14
2.3. Mechanisms of Erosion in Hydroturbine.....	14
2.4. Factors Influencing Erosion.....	17
2.4.1. Impingement variables.....	17
2.4.2. Particle variables.....	19
2.4.3. Base material variables.....	20
2.5. Evolution of Hydroturbine Material.....	21
2.6. Martensitic Stainless Steel.....	22
2.6.1. Effect of alloying elements	23
2.7. Thermal Spray Process.....	24
2.7.1. Various types of thermal spray process.....	25
2.7.2. WC-Co based coating for erosion resistance application.....	30
2.7.3. Decarburization in carbide based cermets.....	30

2.7.4.	Thermal spray coating properties for erosion resistant applications.....	31
2.7.5.	Erosion performance of HVOF and HVAF sprayed WC-Co coatings	33
2.8	Identification of Research Gap.....	33
3.	Materials and Methods	35-48
3.1.	Selection of Base Material.....	35
3.2.	CA6NM Martensitic Stainless Steel Characterization.....	36
3.2.1.	XRD analysis.....	36
3.2.2.	Microhardness and roughness testing.....	36
3.2.3.	Tensile and Charpy impact testing.....	36
3.2.4.	Density measurement.....	37
3.2.5.	Optical and FESEM analysis.....	37
3.3.	Thermal Spray Coating	38
3.3.1.	Selection of feedstock powders.....	38
3.3.2.	HVOF thermal spraying	38
3.3.3.	HVAF thermal spraying.....	41
3.4.	Feedstock Powder Characterization.....	42
3.5.	Coating Characterization.....	42
3.5.1	Coating roughness.....	42
3.5.2	XRD analysis.....	43
3.5.3	FESEM and EDS analysis.....	43
3.5.4	Coating density and porosity.....	43
3.5.5	Microhardness.....	43
3.5.6	Fracture toughness.....	43
3.5.7	Tensile adhesion.....	44
3.6	Solid Particle Erosion Testing.....	45
4.	Results and Discussions	49-90
4.1.	Characterization of CA6NM Steel.....	49
4.1.1.	Microstructure and XRD study.....	49
4.1.2.	Mechanical properties and density.....	51
4.1.3.	Fractography of tensile and Charpy specimen.....	51
4.2.	Erosion Performance of CA6NM Steel.....	52

4.2.1	Effect of impingement angle on formation of erosion scar.....	52
4.2.2	Effect of impingement angles and velocities on cumulative volume loss.....	54
4.2.3	Erosion mechanism and FESEM Analysis of eroded surfaces.....	56
4.3.	Characterization and Erosive Wear Study of HVOF Sprayed WC-10Co-4Cr Coating on CA6NM Steel.....	63
4.3.1.	Feedstock powder characterization.....	63
4.3.2.	XRD study of feedstock powder and HVOF sprayed coating.....	63
4.3.3	Cross-sectional microstructure of HVOF sprayed coating.....	64
4.3.4	Cross-sectional micro hardness, indentation fracture toughness and tensile adhesion of HVOF sprayed coating.....	65
4.3.5	Effect of HVOF sprayed WC-10Co-4Cr coating on erosion resistance of CA6NM steel substrate.....	66
4.3.6.	Analysis of eroded HVOF sprayed coating surface.....	70
4.4.	Characterization and Erosive Wear Study of HVAF Sprayed WC-10Co-4Cr Coating on CA6NM Steel.....	77
4.4.1.	Feedstock powder characterization.....	77
4.4.2	XRD study of feedstock powder and HVAF sprayed coating.....	77
4.4.3	Cross-sectional microstructure of HVAF sprayed coating.....	78
4.4.4.	Cross-sectional micro hardness, fracture toughness and tensile adhesion of HVAF sprayed coating.....	80
4.4.5	Effect of HVAF sprayed WC-10Co-4Cr coating on solid particle erosion resistance of CA6NM steel.....	81
4.4.6.	Analysis of eroded HVAF sprayed coating surface.....	84
5.	Conclusions and Suggestions for Future Work	91-93
References	94
Appendices	113-118
I	113
II	115
III	117

LIST OF FIGURES

Fig. No.	Figure Captions	Page No.
1.1.	Eroded Hydroturbine components of Nathpa Jhakri Hydro Power station, SJVN Limited, Jhakri, India	2
2.1.	Layout of hydropower plant	8
2.2.	Schematic layout of impulse turbine	9
2.3.	Schematic layout of Francis turbine	10
2.4.	Schematic layout of Kaplan turbine	10
2.5.	Classification of erosion	12
2.6.	Schematic layout of solid particle erosion mechanism	13
2.7.	Schematic diagram showing mechanisms of silt erosion	14
2.8.	Schematic diagram showing formation of lips	15
2.9.	Schematic diagram showing formation of craters	16
2.10.	Mechanism of cavitation in hydroturbine	16
2.11.	The relationship between the impingement angle and the erosion rate for ductile and brittle material	18
2.12.	Schematic diagram showing erosion versus time for 1020 type steel at 30 m/s and 70 m/s impingement velocity	19
2.13.	Modified Schaeffler diagram	24
2.14.	Schematic diagram showing process of thermal spray coating	25
2.15.	Schematic diagram showing the process of coating deposition	25
2.16.	Classification of thermal spray process according to process temperature and velocity	26
2.17.	Schematic diagram of plasma spray process	27
2.18.	Schematic diagram of detonation gun (D-Gun) spraying process	28
2.19.	Schematic diagram showing high-velocity oxy-fuel (HVOF) spray process	29
2.20.	Schematic diagram showing high-velocity air-fuel spray (HVOF) process	30
2.21	Cross-sectional microstructure of WC-10Co-4Cr coating processed by (a) HVOF spraying and (b) HVOF spraying	32

3.1.	Tensile test specimen as per ASTM E8/E8M-15a specification (all dimensions in mm)	37
3.2.	Charpy V-notch impingement test specimen as per ASTM E23-12c specification (all dimensions in mm)	37
3.3.	HVOF thermal spray coating unit at Metalizing export company, India	40
3.4.	(a) Round rotating carousel used for sample mounting, (b) HVAF thermal spray system (HVAF M3, Uniquecoat) at PTC Innovation, Sweden	41
3.5.	Schematic depiction of the Vickers indentation and crack geometry	44
3.6.	Schematic diagram showing tensile adhesion test	45
3.7.	Schematic view of air jet erosion tester used for solid particle erosion testing	46
3.8.	Morphology of alumina particles	44
3.9.	Schematic diagram of the double disk apparatus	48
4.1.	(a) Optical and (b) FESEM micrograph of as-cast CA6NM steel	50
4.2.	XRD pattern of cast CA6NM steel	50
4.3.	FESEM fractographs of tensile specimen of as-cast CA6NM steel (a) lower magnification (150 X) and (b) higher magnification (5000 X).	51
4.4.	FESEM fractographs of Charpy impact specimen of Cast CA6NM steel (a) lower magnification (100 X) and (b) higher magnification (5000 X).	52
4.5.	Schematic diagram showing interaction of erodent with surface of sample at (a) 30°, (b) 60° and (c) 90° impingement angle	53
4.6.	Photographs of the erosion scar formed on eroded samples at 30°, 60° and 90° impingement angles and their respective sample holder.	53
4.7.	Cumulative volume loss of as-cast CA6NM steel as a function of erosion time at 30° impingement angle for 35 m/s and 70 m/s impingement velocities	54
4.8.	Cumulative volume loss of as-cast CA6NM steel as a function of erosion time at 60° impingement angle for 35 m/s and 70 m/s impingement velocities	55
4.9.	Cumulative volume loss of as-cast CA6NM steel as a function of erosion time at 90° impingement angle for 35 m/s and 70 m/s impingement velocities	55
4.10.	Comparison of cumulative volume loss of as-cast CA6NM steel at 30°,	56

	60° and 90° impingement angles for 35 m/s and 70 m/s impingement velocities	
4.11.	FESEM micrograph of as-cast CA6NM steel before erosion	57
4.12.	FESEM micrographs of eroded surfaces of as-cast CA6NM steel at 30° impingement angle on different locations for 35 m/s impingement velocity	57
4.13.	FESEM micrographs of eroded surfaces of as-cast CA6NM steel at 30° impingement angle on different locations for 70 m/s impingement velocity	58
4.14.	FESEM micrographs of eroded surfaces of as-cast CA6NM steel at 60° impingement angle on different locations for 35 m/s impingement velocity	59
4.15.	FESEM micrographs of eroded surfaces of as-cast CA6NM steel at 60° impingement angle on different locations for 70 m/s impingement velocity	60
4.16.	FESEM micrographs of eroded surfaces of as-cast CA6NM steel at 90° impingement angle on different locations for 35 m/s impingement velocity	61
4.17.	FESEM micrographs of eroded surfaces of as-cast CA6NM steel at 90° impingement angle on different locations for 70 m/s impingement velocity	62
4.18.	FESEM micrograph of WC-10Co-4Cr feedstock powder used for HVOF spraying (a) Lower magnification (2000 X) and (b) Higher magnification (5000 X)	63
4.19.	XRD pattern of WC-10Co-4Cr feedstock powder and HVOF sprayed WC-10Co-4Cr coating on CA6NM steel	64
4.20.	Cross-sectional FESEM micrographs of HVOF sprayed WC-10Co-4Cr coating (a) At lower magnification and (b) At higher magnification	65
4.21.	Indentation and crack micrograph on the HVOF sprayed WC-10Co-4Cr coating cross section of CA6NM steel	66
4.22.	Cumulative volume loss of as-cast CA6NM steel and HVOF coated steel as a function of erosion time at 30° impingement angle for 35 m/s and 70 m/s impingement velocities	68

4.23.	Cumulative volume loss of as-cast CA6NM steel and HVOF coated steel as a function of erosion time at 60° impingement angle for 35 m/s and 70 m/s impingement velocities	68
4.24.	Cumulative volume loss of as-cast CA6NM steel and HVOF coated steel as a function of erosion time at 90° impingement angle for 35 m/s and 70 m/s impingement velocities	69
4.25.	Comparison of cumulative volume loss of as-cast CA6NM steel and HVOF coated steel at 30°, 60° and 90° impingement angles for 35 m/s and 70 m/s impingement velocities	69
4.26.	FESEM micrograph of HVAF coated CA6NM steel before erosion	71
4.27.	FESEM micrograph of eroded surface of HVOF coating at 30° impingement angle on different locations for 35 m/s impingement velocity	71
4.28.	FESEM micrographs of eroded surface of HVOF coating at 30° impingement angle on different locations for 70 m/s impingement velocity	72
4.29.	FESEM micrographs of eroded surface of HVOF coating at 60° impingement angle on different locations for 35 m/s impingement velocity	73
4.30.	FESEM micrographs of eroded surface of HVOF coating at 60° impingement angle on different locations for 70 m/s impingement velocity	74
4.31.	FESEM micrographs of eroded surface of HVOF coating at 90° impingement angle on different locations for 35 m/s impingement velocity	75
4.32.	FESEM micrographs of eroded surface of HVOF coating at 90° impingement angle on different locations for 70 m/s impingement velocity	76
4.33.	Morphology of WC-10Co-4Cr feedstock powder used in HVAF spraying (a) Lower magnification (2000 X) and (b) Higher magnification (5000 X)	77
4.34.	XRD pattern of feedstock powder and HVAF sprayed WC-10Co-4Cr coating on CA6NM steel	78
4.35.	Cross-sectional FESEM micrographs of HVAF coated CA6NM steel (a)	79

	At lower magnification(200 X) and (b) At higher magnification(10000 X).	
4.36.	Indentation and crack micrograph on the HVAF sprayed WC-10Co-4Cr coating cross section of CA6NM steel	80
4.37.	Cumulative volume loss of as-cast CA6NM steel and HVAF coated steel as a function of erosion time at 30° impingement angle for 35 m/s and 70 m/s impingement velocities	82
4.38.	Cumulative volume loss of as-cast CA6NM steel and HVAF coated steel as a function of erosion time at 60° impingement angle for 35 m/s and 70 m/s impingement velocities	83
4.39.	Cumulative volume loss of as-cast CA6NM steel and HVAF coated steel as a function of erosion time at 90° impingement angle for 35 m/s and 70 m/s impingement velocities	83
4.40.	Comparison of cumulative volume loss of as-cast CA6NM steel and HVAF coated steel at 30°, 60° and 90° impingement angles for 35 m/s and 70 m/s impingement velocities	84
4.41.	FESEM micrograph of HVAF coated CA6NM steel before erosion.	85
4.42.	FESEM micrograph of eroded surface of HVAF coating at 30° impingement angle on different locations for 35 m/s impingement velocity	85
4.43.	FESEM micrograph of eroded surface of HVAF coating at 30° impingement angle on different locations for 70 m/s impingement velocity	86
4.44.	FESEM micrograph of eroded surface of HVAF coating at 60° impingement angle on different locations for 35 m/s impingement velocity	87
4.45.	FESEM micrograph of eroded surface of HVAF coating at 60° impingement angle on different locations for 70 m/s impingement velocity	88
4.46.	FESEM micrograph of eroded surface of HVAF coating at 90° impingement angle on different locations for 35 m/s impingement velocity	89

4.47.	FESEM micrograph of eroded surface of HVAF coating at 90° impingement angle on different locations for 70 m/s impingement velocity	90
-------	--	----

LIST OF TABLES

Table No.	Title of Table	Page No.
1.1.	Eroded Hydroturbine components of Nathpa Jhakri Hydro Power Station, SJVN Limited, Jhakri, India	2
2.1.	List of the major hydropower plants in India	8
2.2.	Classification of river sediment	11
2.3.	Requirements and criteria for the selection process of turbine material	22
2.4.	Comparison of thermal spray process and coating characteristics	26
3.1.	Chemical composition of cast CA6NM steel (wt %).	35
3.2.	HVOF process parameters	39
3.3.	HVAF process parameters	42
3.4.	Parameters used in solid particle erosion testing	47
4.1.	Mechanical properties and density of as-cast CA6NM steel	51
4.2.	Thickness, as sprayed coating surface roughness, porosity and density of HVOF sprayed WC-10Co-4Cr coating on CA6NM steel	65
4.3.	Indentation fracture toughness, Microhardness and tensile adhesion of HVOF sprayed WC-10Co-4Cr coating on CA6NM steel.	66
4.4.	Improvement in erosion resistance of cast CA6NM steel at 30°, 60° and 90° impingement angles after application of HVOF coating.	67
4.5.	Thickness, as sprayed coating surface roughness, porosity and density of HVAF sprayed WC-10Co-4Cr coating on CA6NM steel	79
4.6.	Indentation fracture toughness, Microhardness and tensile adhesion of HVAF sprayed WC-10Co-4Cr coating on CA6NM steel	81
4.7.	Improvement in erosion resistance of cast CA6NM steel at 30°, 60° and 90° impingement angles after application of HVAF coating	82

NOMENCLATURES

AISI	American iron and steel institute
APS	Atmospheric plasma spraying
ASTM	American society for testing and materials
D-Gun	Detonation gun spraying
EDS	Energy dispersive X-ray spectrometer
FESEM	Field emission scanning electron microscopy
HVAF	High velocity air fuel
HVOF	High velocity oxy–fuel
MSS	Martensitic stainless steel
OFP	Oxy fuel process
ppm	Parts per million
UTS	Ultimate tensile strength
XRD	X-ray diffraction

thesis

by Anurag Hamilton

FILE	ANURAG_COMBINED_THESIS_07_JUNE.PDF (20.1M)		
TIME SUBMITTED	27-JUN-2017 04:13AM	WORD COUNT	19403
SUBMISSION ID	827734194	CHARACTER COUNT	100138

CHAPTER 1

Introduction

1.1. Background

Hydropower plants play a vital role in fulfilling India's domestic energy requirements. **It is the most substantial and economic source compared to other sources of energy.** The Himalayan rivers provide a great potential for hydropower generation due to its steep gradient and topography. However, due to geographically young mountains of the region amount of silt in river increases to alarmingly high level during the monsoon season. In Himalayan region during monsoon season, silt contents exceed 50 kg of silt per cubic meter of water, which is way above the permissible limit (1 kg of silt per cubic meter of water). The Silt particles (700–1000 HV) present in the water **interacts** with the surface of the hydro turbine and results in silt erosion, which in turn, **causes severe damage to hydro turbine components. The damaged hydro turbine components due to silt erosion are shown in Fig. 1.1.** In particular, blades, guide vanes, bearing bodies and nozzles, etc. bears high risks of being damaged by silt particles. The gradual removal of material from underwater parts changes the profile of turbine, which reduces the lifespan of the hydro turbine and its overall efficiency. The silt erosion intensity depends on the (i) Particle variable: particle **size, shape, and hardness.** (ii) Impingement variable: velocity of silt and fluid, **impact angle, flux rate or concentration, the medium of flow.** (iii) Base material **variables: microstructure and mechanical properties.** Among these, base material properties **play an important role, as it is the only variable that can be easily controlled to reduce erosion.**

The silt erosion menace can be tackled by three approaches: (i) Effective de-silting arrangement (ii) Developing silt resistance equipment design **(iii)** by surface engineering route. However, during monsoon season it becomes very difficult to stop the interaction of silt with turbine even after application of de-silting arrangement and incorporating silt resistance equipment design. Hence, the most viable alternative is by application of surface engineering. Different researchers have suggested various **surface engineering routes to enhance the properties of turbine steel. However, it has been found that the erosion resistance of the turbine steel can be improved by the deposition**

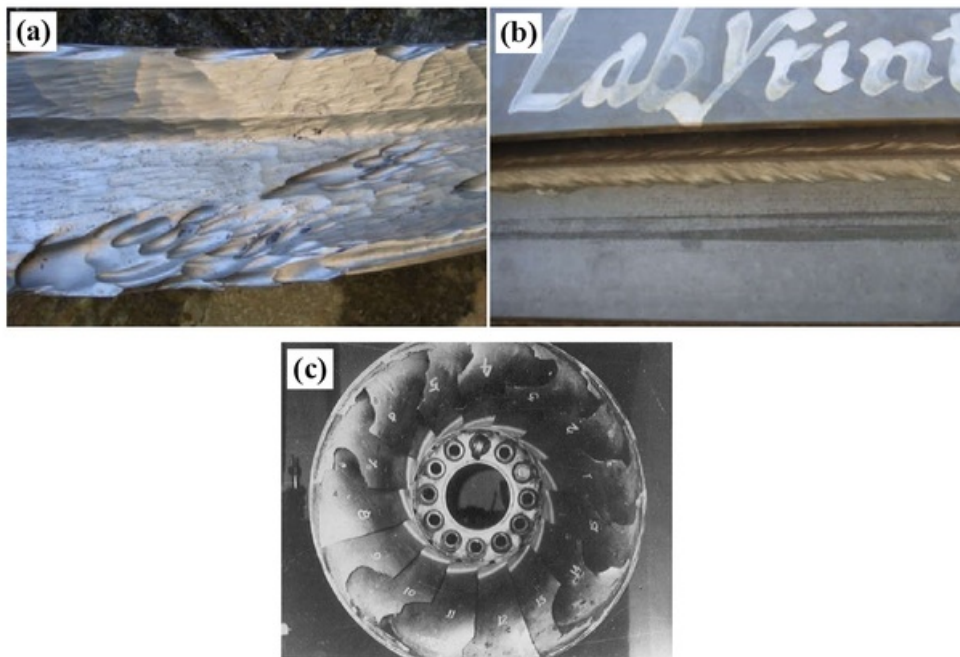


Fig. 1.1. Eroded Hydro turbine components of Nathpa Jhakri Hydro Power station, SJVN Limited, Jhakri, India.

of thermal spray coatings. Thermal spray techniques are versatile means of developing coating with low porosity, good adhesive strength, low oxide contents, and high inter-splat strength. Several different types of coating powders have been attempted by various researchers to improve erosion resistance of turbine blades. It has been observed that WC-Co-Cr based coating give excellent erosion performance in comparison to other type of powders, which is due to the presence of hard WC particle in a tough and ductile Co-Cr matrix. Also, chromium provides an improvement in the corrosion resistance of the metallic binder phase. At present, high velocity oxy-fuel (HVOF) process (Flame temp.-2800°C, Particle velocity- 200-1000 m/s) is widely used for developing erosion resistant coating on hydro turbine steel. However, this process leads to decarburization of WC to W_2C , which deteriorates the erosion resistance of the coating. Recently, high-velocity air fuel (HVOF) system is gaining attention among researchers. This process operates at a much lower combustion temperature (Flame temp.- 1950°C) using compressed air (not oxygen) for combustion. Which significantly increases the decarburization of WC and produces a homogenous and dense coating. HVOF technique also reduces the production cost of coatings by using compressed air

instead of pure oxygen. Therefore, there is a scope to explore the possibility of application of HVOF coating for erosion resistance application of hydro turbine. In literature, application of HVOF coating on CA6NM hydro turbine steel as a solution to silt erosion problem has not been addressed.

Hence, in this present work, HVOF and HVOF sprayed WC-10Co-4Cr coating was deposited on a CA6NM steel substrate. A detailed microstructural and phase compositional study was carried out on the coatings. Mechanical properties of the coatings were also evaluated. Consequently, their erosion resistance was assessed using solid particle erosion test at various impingement angles and impact velocities. The percentage improvement in erosion resistance of CA6NM steel after application of HVOF and HVOF coating was also discussed.

1.2. Objectives of the Study

The main objective of this study is to prevent silt erosion of hydro turbine material by developing suitable carbide based thermal spray coatings. In order to achieve the main objective the following specific objectives was carried out:

1. Study of erosion behavior of cast CA6NM steel at different impingement angles and impact velocities.
2. Study of WC-10Co-4Cr coating characteristics sprayed by HVOF process on cast CA6NM substrate.
3. Analyze and compare the erosion resistance of HVOF sprayed WC-10Co-4Cr coating on cast CA6NM steel with the uncoated counterpart.
4. Study of WC-10Co-4Cr coating characteristics sprayed by HVOF process on cast CA6NM substrate.
5. Analyze and compare the erosion resistance of HVOF sprayed WC-10Co-4Cr coating on cast CA6NM steel with the uncoated counterpart.

1.3. Outline of the Thesis

The thesis has been organized into five chapters as follows:

Chapter 1 provides an introduction to the basic background of the research including objectives of the research as well as the structure of the thesis.

Chapter 2 presents a comprehensive review of available literature. The chapter begins with a brief introduction about hydropower plant and types of turbine. It discusses silt erosion problem faced by hydro turbine components. Types of erosive wear (Solid

particle, Slurry, Cavitation and Liquid impingement erosion) is also described in brief. The mechanism of erosion is a complex phenomenon and governed by various factors. The various contributing factors for erosion such as Cutting by silt particles, Cavitation, Subsurface damages, Plastic deformation, Fatigue and Synergy are discussed. Erosion dependent variables have been categorized into three categories: Particle variable, Impingement variable, Base material variables. Each variable is discussed in detail to gain insight into their effect on erosion of material.

The principle of thermal spraying and different types of thermal spraying process used for erosion resistance application of hydro turbine are discussed in the last section of the chapter. Various properties and microstructure features of thermal spray coatings are also discussed. The main focus was paid to HVOF and HVOF spraying techniques due to their versatile advantages in term of coating deposition. WC-Co based cermet coatings are presented as a coating for protecting hydro turbine surfaces. Hard WC particles in the coating provide high hardness and wear resistance while the metal binder (Co) offers the sufficient coating toughness, which in turn, results in higher erosion resistance. This chapter also reviews the literature on erosion performance of various WC-Co/WC-Co-Cr coatings deposited by HVOF and HVOF thermal spraying. After a comprehensive review of the available literature, research gap has been described at the end of the chapter.

Chapter 3 describes the materials, equipment, and methodology employed to complete the present study. The chapter is divided into three sections.

The first part discusses the selection of base material, evaluation of mechanical properties of steel and its characterization. The second part of the study focuses on thermal spray coatings. Ten different WC-10Co-4Cr powder was deposited on CA6NM steel using two different thermal spray process (HVOF & HVOF). The sprayed coatings were characterized in terms of coating roughness, phases present, Index of carbide retention, cross-sectional microstructure, microhardness, coating porosity, density and fracture toughness. The last section of the chapter provides a detailed description about erosion tester used to evaluate the erosion behavior of uncoated and coated steel.

Chapter 4 presents the results of the experimental work performed in this study and their discussion. This chapter is divided into four sections.

The first section discusses the characterization of CA6NM steel. The CA6NM steel was characterized in terms of microstructure, phases and mechanical properties.

The second section deals with erosion performance of CA6NM steel at different

impingement angles and impact velocities.

The **third section** discusses the characterization of HVOF sprayed WC-10Co-4Cr coated CA6NM steel and its erosion performance at different impingement angles and impact velocities.

The **last section** focuses on HVAF sprayed WC-10Co-4Cr coating on CA6NM steel and its characterization. It also discusses erosion performance at different impingement angles and impact velocities.

Chapter 5 presents the conclusions of the experimental work performed in this study and suggestions for future work.

References

Appendix I presents the solid particle erosion experimental data of uncoated CA6NM steel substrate.

Appendix II presents the solid particle erosion experimental data of HVOF coated CA6NM steel substrate.

Appendix III presents the solid particle erosion experimental data of HVAF coated CA6NM steel substrate.

Publications arising from this work and reprint of published paper are attached at the end of this thesis.

CHAPTER 2

Literature Review

This chapter contains a comprehensive review of the literature related to hydropower plant, types of turbine, types of erosion, erosion dependent variables and erosion mechanism. Thermal spray technique and their role in combating erosion is also discussed. The studies related to erosion behaviour of thermal spray coating processed through high velocity oxy-fuel (HVOF) and high velocity air fuel (HVOF) process are also added. After a comprehensive review of the available literature, research gap has been described at the end of chapter.

2.1. Introduction to Hydropower Plant

Hydropower plants play a vital role in fulfilling growing energy requirements worldwide. Hydropower plants utilize the potential energy of the stored water to generate electricity. In India, Himalayan rivers provide a great potential for hydropower generation due to its steep gradient and topography. India ranks fifth in terms of utilizable hydro-potential on the global scenario. Presently the total installed capacity in India including all resources is 302.833 MW, in which the contribution of hydro energy is 15%. Table 2.1 shows the list of the major hydropower plants situated in India. A schematic layout of a hydropower plant is shown in Fig. 2.1. Hydro turbine is the heart of the hydropower plants. The hydraulic energy of the water is converted into mechanical energy through turbine blades, and this energy is transmitted to generator shaft through coupling in this way a hydropower plant generates electricity. Generated electricity is transferred to electrical grid based on requirement.

2.1.1. Types of turbine

Turbines can be classified into two types as impulse and reaction turbines.

(a) Impulse turbine

The impulse turbine uses the velocity of the water to move the runner. An impulse turbine is suitable for high head and low flow applications. The water stream strikes

Table 2.1 List of the major hydropower plants in India

Sr. No.	Name of hydropower plant	State	Installed capacity
1	Tehri Dam	Uttarakhand	2400 MW
2	Koyna Dam	Maharashtra	1960 MW
3	Srisaïlam Dam	Andhra Pradesh	1670 MW
4	Nathpa Jhakri	Himachal Pradesh	1500 MW
5	Sardar Sarovar	Gujarat	1450 MW
6	Bhakra Dam	Punjab	1325 MW
7	Indira Sagar Dam	Madhya Pradesh	1000 MW
8	Kalinadi	Karnataka	1240 MW
9	Nagarjunasagar Dam	Andhra Pradesh	965 MW
10	Idukki Dam	Kerala	780 MW

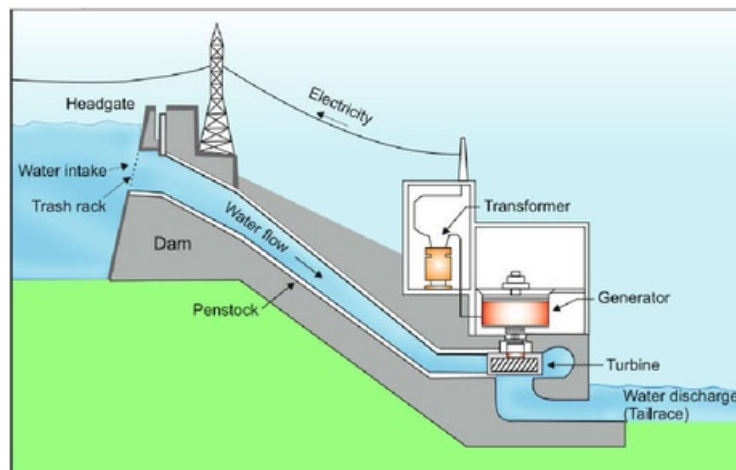


Fig. 2.1. Schematic layout of hydropower plant

each bucket on the runner. Fig. 2.2 shows the mechanism of Impulse turbine used in hydropower plant. The Pelton wheel is the well known example of impulse turbine. In the Pelton wheel, the entire head (pressure head, velocity head, and elevation head) of the water is converted into large velocity head at the exit of supply nozzle. This impulse of individual jets of fluid striking the buckets generates the torque which rotates the

turbine.

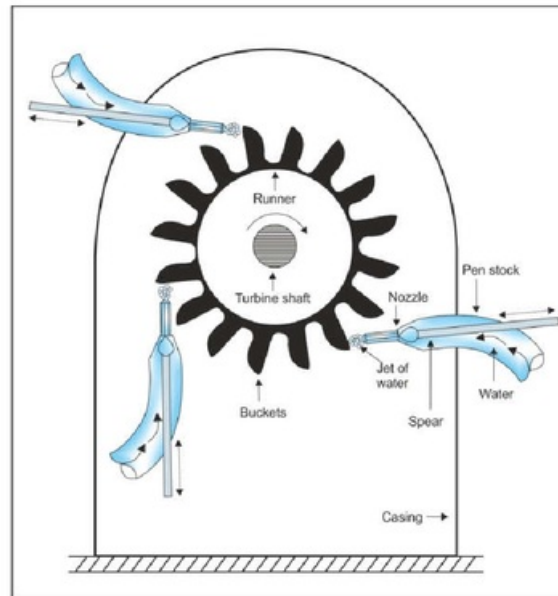


Fig. 2.2. Mechanism of impulse turbine

(b) Reaction turbine

A reaction turbine develops power from the combined action of pressure and moving water. The runner is placed in the water stream flowing over the turbine blades. In a reaction turbine, unlike an impulse turbine, the working fluid completely fills the passageways through which it flows. The inlet guide vanes direct the water into the rotor with a tangential component of velocity. Reaction turbines are preferred for sites with lower head and higher flows. Francis and Kaplan turbines are the two primary types of reaction turbine. Francis turbine is enclosed in a casing, and the blades have special curved features designed to gain optimal performance from the turbine, as shown in Fig. 2.3. Kaplan turbine is also known as the **propeller turbine** because its runner resembles the propeller of a ship as shown in Fig. 2.4. It has adjustable blade to obtain the optimal efficiency in different pressure conditions. Therefore, Kaplan turbine can gain maximum efficiencies and operate under a low head condition which is not possible in Francis turbines.

2.1.2. Silt erosion problem in hydro turbine

Although hydropower is the most important and cheapest renewable source of energy, hydropower plants encounter problems like silt erosion, which reduces its operational capabilities. In general purpose, turbines are designed for clear water. However, during monsoon season it becomes nearly impossible to avoid interaction of silt and turbine components. This leads to severe problem of silt erosion. Hydro turbine consists of static and moving parts. Both of them are exposed to erosion. Spiral casing, draft tube

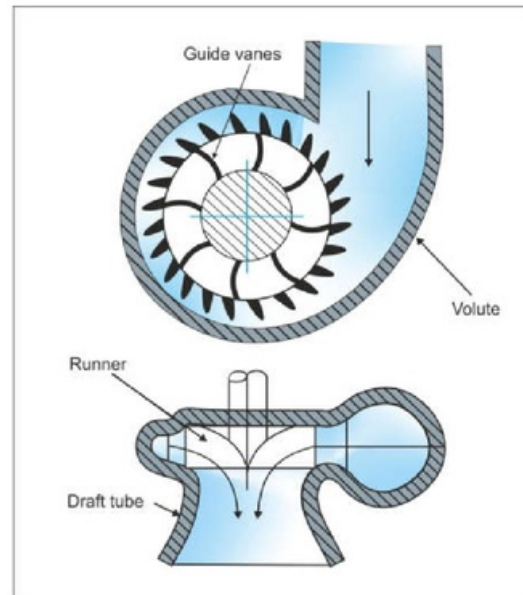


Fig. 2.3. Mechanism of Francis turbine

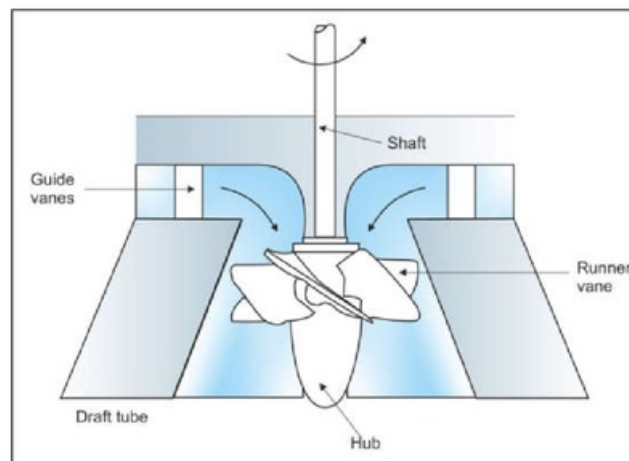


Fig. 2.4. Mechanism of Kaplan turbine

etc. are classified as static parts. Runner, guide vanes, shafts etc comes under moving parts. The high velocity fluid (10 to 150 m/s) coming from reservoir contains clay, silt and sand particles. Table 2.2 shows the classification of river sediment. In order to stop them from entering the hydro turbine, desilting arrangements are put in place. However during monsoon season it becomes impossible to stop the interaction of silt particles with Hydro turbine components. These silt particles contains quartz (70-80%) which

Table 2.2 Classification of river sediment

Particle	Clay	Silt	Sand	Gravel	Cobbles	Bounders
Size (mm)	<0.002	0.002-0.06	0.06- 2	2-60	60-250	>250

measures 7 on Moh's scale and result in erosion. Hydro turbine are found to undergo significant erosion when they are exposed to rivers that exceed 1 kg of silt per cubic meter of water. The problem is particularly severe in Himalayan Rivers where the silt content during the rainy season exceeds 50 kg of silt per cubic meter of water. Silt erosion not only reduces efficiency and life of hydropower turbines but also causes a problem in operation and maintenance. The erosion rate of 3.4 mm/year has been reported for the needle and the buckets of Pelton turbine, which resulted in a reduction of around 1.21% in the efficiency of hydro turbine.

2.2. Types of Erosive Wear

ASTM G40 standard defines erosion as progressive loss of material from a solid surface due to mechanical interaction between that surface and a fluid, a multi component fluid or impinging liquid or solid particles. There are mainly four types of erosive wear depending upon interaction of target material and impinging particle as shown in Fig. 2.5

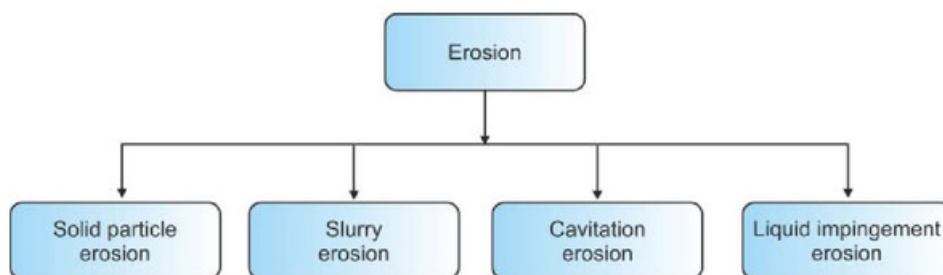


Fig. 2.5 Classification of erosion

2.2.1. Solid particle erosion

The loss of material resulting from the repeated impact of small, solid particles travelling at substantial velocities is frequently termed as solid particle erosion. The response of a material to solid particle erosion by solid particles is influenced by the properties of the material such as the hardness and microstructure. Solid particle erosion in service conditions usually include thinning of components, a macroscopic scooping appearance following the gas/particle flow field, surface roughening, lack of directional grooving characteristic of abrasion and in some cases, the formation of ripple patterns on metals. Fig. 2.6 shows the solid particle erosion mechanism. Solid particle erosion is a result of the impact of a solid particle A, with the solid surface B, resulting in part of the surface B been removed. This type of erosion is commonly found in hydroturbine blades, soot blowers and cyclone separators.

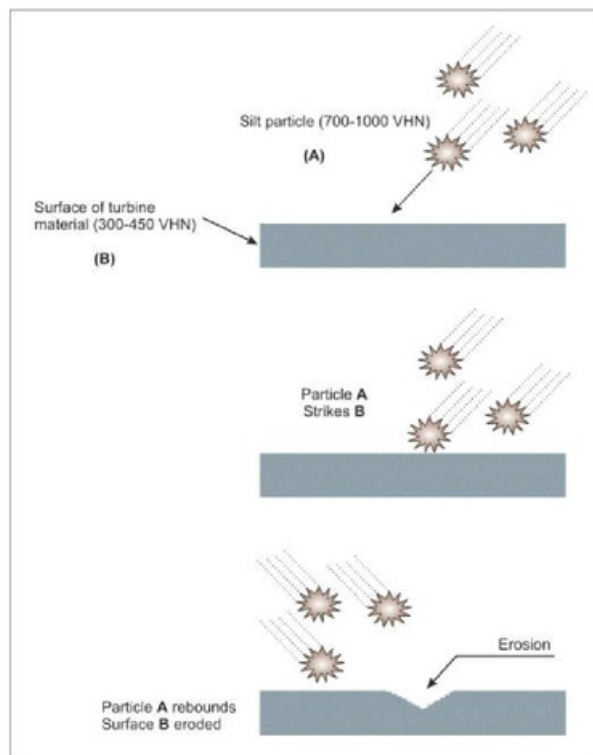


Fig. 2.6 Solid particle erosion mechanism

2.2.2. Slurry erosion

Slurry erosion can be defined as the type of wear, or loss of mass, that is experienced by a material exposed to a high-velocity stream of slurry. Slurry can be described as a

mixture of solid particles in a liquid, usually water, of such a consistency that it can be pumped. Slurry erosion is caused by the interaction of a liquid suspension of solid particles and a target which experiences loss of material by the repeated impact of suspension particles.

2.2.3. Cavitation erosion

It is a type of erosion in which damage to a solid surface occurs by the implosion of gas bubbles near a surface. The surrounding liquid rushes in to fill the void that is created due to collapsing of the bubble. A jet is formed, and it can develop stresses exceeding the yield strength of materials. Cavitation erosion can occur on the surfaces of metals and nonmetals. It may produce undesirable noise levels and reduce the useful life of very valuable property. The material is removed due to pits formation by microscopic fracture. Cavitation occurs in fluid propulsion devices like hydroturbines, pumps, ship propellers and dam spillways.

2.2.4. Liquid impingement erosion

Liquid impingement erosion is defined as progressive loss of original material from a solid surface due to continued exposure to impacts by liquid drops or jets. This type of erosion is often encountered in piping, especially in pipes made from materials that rely on a passive oxide film for corrosion resistance. The mechanical action of the liquid removes the protective oxide. This repeated action can perforate pipe elbows when velocity is high.

2.3. Mechanisms of Erosion

The mechanism of erosion is a complex phenomenon and governed by various factors. Fig. 2.7 gives a schematic view of the various damaging forces responsible for the erosion damages. Silt erosion generally occurs by following mechanisms:

(a) Cutting by silt particles, Cavitation and Subsurface damages

Erosion by silt particles depends on the angle at which the silt particles impinge on the target surface. At low impact angles, erosion occurs due to the formation of surface ploughs and lips. It is because of the impacting silt particles strike the target surface with tangential force, which results in the formation of ploughs and lips in the direction of the particle flow. The extruded target material form lips on the edges of the ploughs which are under highly work hardened state. The amount of work hardening

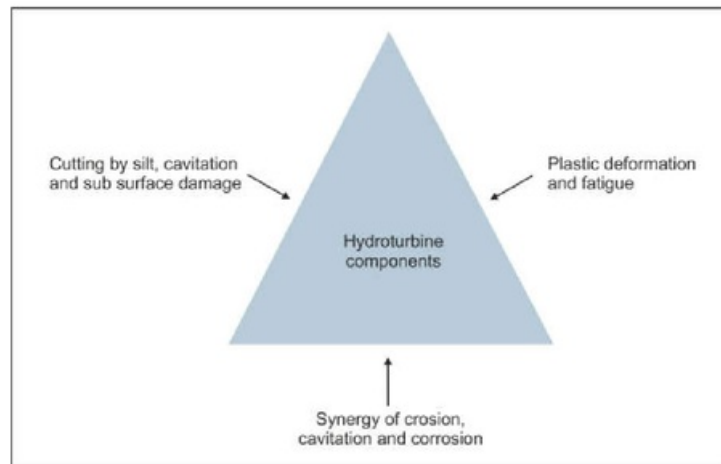


Fig. 2.7 Schematic diagram showing mechanisms of silt erosion

continuously increases and causes embrittlement and subsequent removal of debris. At high impact angle, the role of plastic shear is very limited. Hence the removal of chunks of material from the target surface happens by the mechanism of brittle fracture. It results in the formation of craters. The schematic diagram showing the formation of lips and craters is shown in Fig. 2.8 and 2.9.

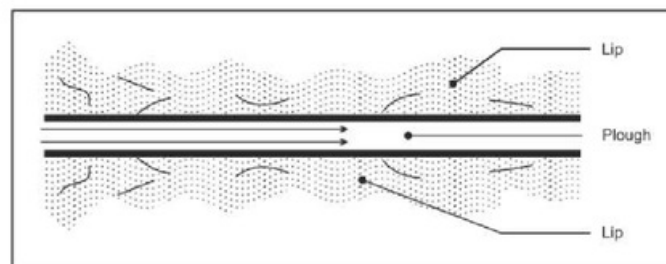


Fig. 2.8 Schematic diagram showing formation of Lips

Formation of ploughs and craters on the surface of hydro turbine due to silt erosion, alters the surface profile of hydro turbine surface. Which results into excessive generation of bubbles. The bursting of air bubbles may generate high-intensity shock waves (70 MPa). These waves try to penetrate into the body of the material and cause severe damages at the surface as well as in the interior of the underwater parts as presented in Fig. 2.10 Impacting high energy silt particle and implosion of bubbles transfer their energy into the material. As a result, cracks are nucleated at sensitive locations like inclusions and coarse precipitate particles. These cracks traverse through

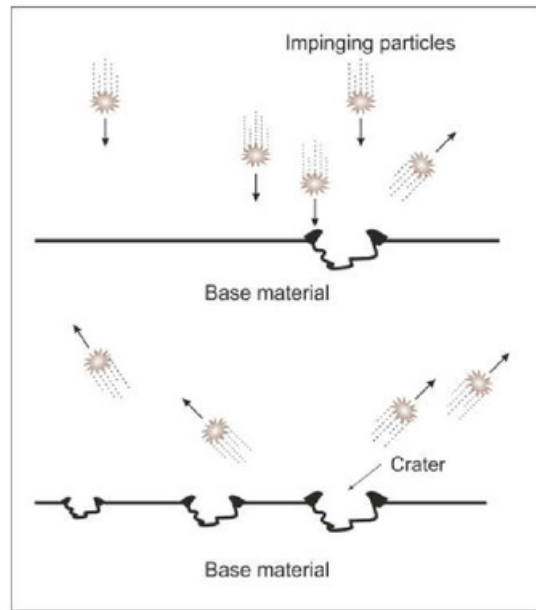


Fig. 2.9 Schematic diagram showing formation of craters

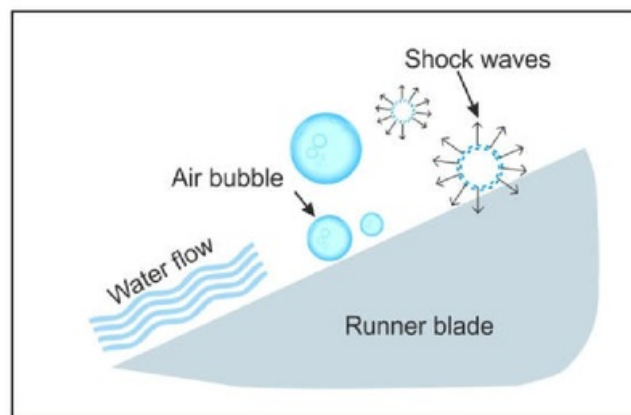


Fig. 2.10 Mechanism of cavitation in hydroturbine

the top and bottom parts of the component leading to rapid failure and the total problem of metal failure by erosion is compounded.

(b) Plastic deformation & Fatigue

Plastic deformation and fatigue also contribute to the erosion of hydroturbine. The excessive pressure caused by water streams may cause distortion in the profile leading to turbulence and rapid damage. When a material possessing coarse grain size and low

thickness is given substantial deformation, the grains develop a tendency to alienate from each other. This results in the formation of a so-called 'honeycomb structure', in which one can observe various grain segments having a tendency to separate from each other. Plastic deformation plays a significant role in the whole mechanism of failure of underwater parts in hydroelectric projects. It is thus important that the blade should be made from a material possessing high strength and fine grain sizes. Repeated impact of silt and water develops cyclic stress leading to fatigue damage, which in turn, results in failure of material due to erosion.

(c) Synergy of erosion, cavitation, and corrosion

In actual service condition, all the above mentioned parameters acts together. This results in much higher erosion rate than the sum of erosion due to silt and liquid separately. It is often referred to as the synergetic erosion. Medium silt content causes four times higher erosion than the cavitation in clean water (without silt), and the combined effect of cavitation and erosion is 16 times greater than cavitation alone. The particle entrainment in the cavitating medium increases the concentration of bubble nuclei and consequently promotes the occurrence of cavitation. The repeated bubble formation and collapsing may cause the rupture of the electrochemically formed protective passive film which results in decreased corrosion resistance of the metal.

2.4. Factors Influencing Erosion

There are various factors or variables that influence the erosion of material. There classification is as follows

- (i) Impingement variables: impingement angle, velocity of silt and fluid, flux rate or concentration, the medium of flow.
- (ii) Particle variables: particle size, shape and hardness.
- (iii) Base material variables: microstructure, mechanical properties such as hardness, ductility, work hardening behaviour and physical properties like specific heat, melting point and density.

2.4.1. Impingement variables

The features of impingement variables include impingement angle, velocity of water carrying silt, temperature, media of the flow, and turbulence

(a) Impingement angle

The impingement angle is defined as the geometrical angle between a specimen surface and a nozzle axis. Erosion behavior of material strongly depends upon its nature. Ductile, brittle and composite material have different erosion behaviour at different impingement angles. Finnie et al. reported that ductile material suffers maximum erosion at an impact angle of about 20° and offer good erosion resistance at normal incidence angle, On the other hand, brittle materials suffer severe erosion under normal

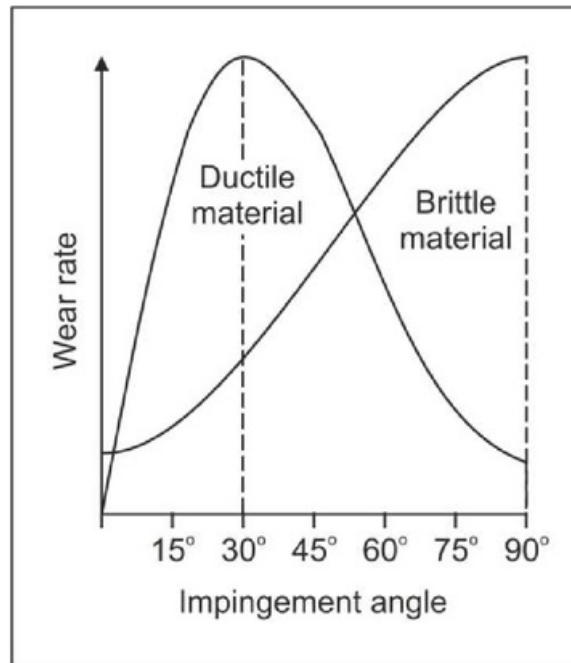


Fig. 2.11. The relationship between the impact angle and the erosion rate for ductile and brittle material

impact (90°) but offer excellent erosion resistance at low angle as demonstrate in Fig. 2.11

(b) Velocity of water and silt

The intensity of erosion is proportional to the cube of the velocity of water, carrying silt particles in suspended condition. Material damage due to plastic deformation and cutting occurs at the same time, and the ratio of these damage mechanisms depends on the velocity of the particle and the impact angle together with other parameters. Up to certain velocity, also referred as critical velocity or threshold velocity, the particle cannot skid on the surface because friction and cutting action does not take place. As the velocity increases higher than critical velocity, cutting component increases, which

amplify the erosion rate drastically. Fig. 2.12 shows the erosion verses time for type 1020 steel at 30 m/s and 70 m/s impact velocity. The relation between erosion and velocity of the particle is

$$\text{Erosion} \propto \text{Velocity}^n$$

Where, the values of exponent 'n' depend on the material and other operating conditions. Considering the impact of particles due to kinetic energy, as the cause of material removal. Theoretically, the value of n is 3.

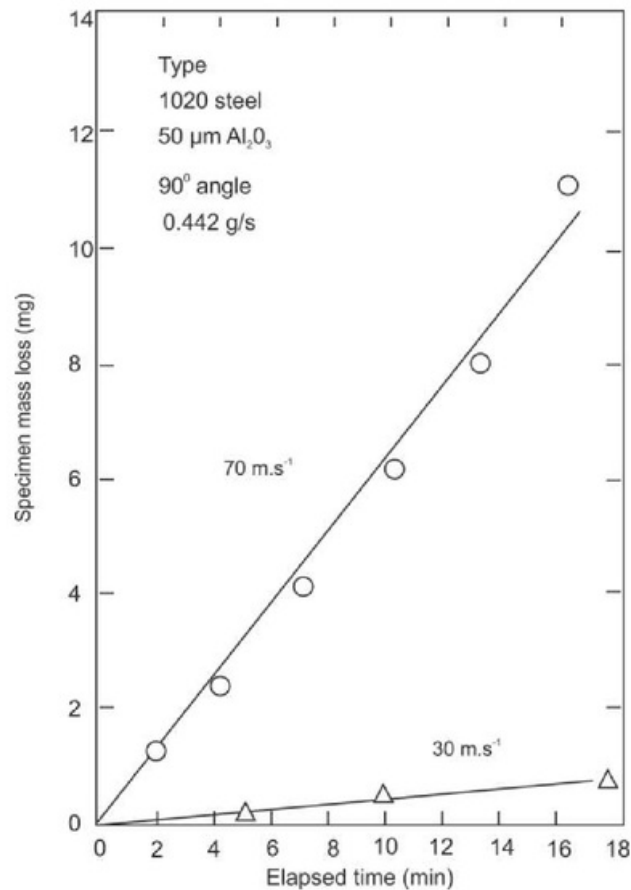


Fig. 2.12 Schematic diagram showing erosion verses time for type 1020 steel at 30 m/s and 70 m/s impact velocity

2.4.2. Particle variables

(a) Size and shape of the particle

The intensity of erosion is directly proportional to the size of the particles. Particle sizes above 0.2 to 0.25 mm are extremely harmful. It has been found that large size silt particles (above 0.25 mm) even with hardness lesser than five on Moh's scale cause wear. Similarly, fine silt even with size less than 0.05 to 0.1 mm, containing quartz wears out the underwater parts. The fine silt can also be dangerous if the turbine is operating under the high head. Sharp and angular particles cause more erosion in comparison to rounded ones. Experiments by Bahadur and Badruddin et. al. have also shown variation in the erosion due to particle shape. Feng and Ball et. al. have reported that the shape and kinetic energy of solid particles are the dominant parameters in case of erosion of ductile materials.

(b) Hardness of particle

The intensity of the erosion is also directly proportional to the hardness of particles. Those particles have a hardness value above five on Moh's scale are considered harmful. Incidentally, most of the Himalayan silt contains more than 70 % Quartz particles on average with hardness value 7 in Moh's scale (700-1000VHN). Hence, the hardness of the particle is a highly influencing factor in the erosion rate. Tsai et al. observed that the erosion of steels has increased by 40-100 times by SiC particles compared to that of coal. Levy and Chik et al. have found that soft particles like calcite and apatite cause less wear due to breaking-up of particles during impact.

(c) Concentration

The silt concentration is one of the dominating factor influencing erosive wear rates. Concentration is the total mass (or volume) of impacting particles present in the unit mass (or volume) of the fluid. Turenne et. al. reported that wear increases with sand concentration because of the higher amount of erodent particles impinge on the surface of the sample. Padhy et. al. concluded that the erosive wear rate increases with an increase in the silt concentration irrespective of the silt size. Sometimes, concentration is also called particle flux rate, or the mass of the impacting material per unit area and time. It can also be represented in terms of percentage of particles in a given fluid mass (or volume). Especially for river sedimentation, concentration is usually expressed in grams per litre (g/l). However, often parts per million (ppm) by weight is used, which is equivalent to mg/l, with the approximation of 1,000 ppm equal to 1 kg/m³ of water being normal usage.

2.4.3. Base material variables

The selection of material for the turbine components is strongly dependent on material variables. The hardness of the material, its chemical composition, microstructure and its work hardening property influence the intensity of erosion. The choice of the material for a particular component is to be made considering its ability to meet the functional requirements like impact strength and ability to withstand cyclic loading in addition to its wear resistance.

(a) Microstructure

Microstructure plays a major role in determining the erosion resistance of material. Adherence to the composition alone is not sufficient to impart proper erosion resistance. Salik and Buckley et. al performed erosion studies on AISI 1045 steel in the annealed, normalized, spheroidized, austempered, water quenched and tempered conditions. It was observed that the metallurgical changes affected the erosion resistance more significantly than the change in hardness. Green et. al. investigated the erosion of plain carbon steels. They found that erosion rate decreased with increasing cementite volume in pearlitic steels of constant lamellar spacing. Clark and Llewellyn et. al. reported that ferritic structures in low carbon steels displayed lower erosion resistance. However, at comparable low hardness levels, the 0.35–0.45% carbon steels displayed much superior erosion resistance than the lower carbon materials. The erosion resistance was found to increase with growing share of pearlite in the structure. Suchanek et. al. found that the erosion resistance of quenched carbon and low alloy steels increased with the increase in C content. It was attributed to the presence of M_7C_3 and $M_{23}C_6$ complex carbides in the microstructure.

(b) Mechanical Properties

Erosion wear strongly depends on material mechanical properties. Since the erosion mechanism involves the formation of wide and deep ploughs containing lips at their edges, the various mechanical properties of the target material become an important parameter in affecting erosion. Various studies have shown that hardness is perhaps the most important property as it provides resistance to indentation and scratching by hard particles. Thus for high erosion resistance, a material of high hardness with some definite amount of ductility is perhaps the best choice. Ductility and hardness have a roughly inverse relationship, increasing one invariably reduce the other. Naim et al. found in 18% maraging steel that erosion increases with the increasing hardness at constant ductility, which was in conflict with the results of Finnie et al., who showed

that erosion decreases with increasing hardness. Naim et al. also noted an increase in erosion rate as the ductility is reduced by cold working primarily at constant strength. In actual service, the erodent particles impact on the target surface and hence the impact energy should also play a major role.

2.5. Evolution of Hydro turbine Material

Till now various grades of steels have been developed for hydro turbine application. The selection of materials for hydraulic turbine are based on the criteria and requirements as listed in Table 2.3

Table 2.3 Requirements and criteria for the selection process of turbine material

Requirements to be fulfilled	Criteria for the choice of material
. Operational Condition	Static load, Dynamic load, Temperature And Corrosion/Abrasion/Erosion/Cavitation
Operational Requirement	Reliability, Maintainability and Life time
Production feasibility	Weldability, Availability in market and Machinability
Price and delivery time	Material cost, labor cost and Delivery time

Initially turbine components were made of cast iron, which was later replaced by cast steel and riveted plates due to higher requirement of strength and toughness. In 1950's the Cast steel was replaced by fabricated steel. After this 18Cr8Ni Austenitic steel was developed which offered good resistance to corrosion and cavitation, however, their fatigue and creep resistance are poor. They still find application in small hydropower plants. Martensitic steel 13Cr1Ni was developed as replacement for 18Cr8Ni, but due to lower Ni content hardness and toughness of steel was on lower side which in turn results in reduced corrosion, cavitation and sand erosion resistance. In 1960 CA6NM (ASTM -A743) steel was developed. It is also known as 13Cr-4Ni MSS. It showed better erosion and corrosion resistance than all the steels developed before for hydro turbine application. The reason for its better properties is owed to strength-to-toughness ratio. Currently, it finds wide application in construction of hydro turbine components such as guide vanes, needle, nozzles and labyrinth. A higher chromium content 16Cr-

5Ni was also developed for salt water application. It has similar strength and erosion performance and higher corrosion resistance as of CA6NM steel

2.6. Martensitic Stainless Steel

The name 'martensite' comes from the German scientist 'Martens'. Martensitic grades of stainless steel were developed in order to provide a group of stainless steels which are corrosion resistant and hardenable by heat treatment. They are similar to the carbon steels or low alloy steels and they have a body centered tetragonal crystal lattice and they are classified as a hard ferro magnetic. Carbon percentage plays a important role in martensitic stainless steel. With a suitable heat treatment, the desired hardness and strength can be achieved in martensitic stainless steels since the strength of the steel obtained by the heat treatment depends on the carbon content. If the carbon content is high, there is an increase in strength and hardness but a decrease in both ductility and toughness.

The most widely used martensitic grades are CA6NM, CB7Cu1 and CB7Cu2. CA6NM cast steel was initially developed at the George Fischer steel foundry to have a high impact strength, good weldability and corrosion with a low carbon content. Temper embrittlement is reduced by adding molybdenum while increasing the nickel content achieves a microstructure free of δ -ferrite. However, in actual practice some δ -ferrite is retained in cast structure.

The most commonly used grades of CA6NM are:

- CA6NM Gr A487 Class A
- CA6NM Gr A487 Class B
- CA6NM Gr A743

CA6NM Grade A743 is widely used for construction of hydro turbine components. It also has a good corrosion resistance. A743 denotes the pressure code used by the oil industry.

2.6.1. Effect of alloying elements

The effect of alloying elements present in martensitic stainless steel can be expressed as chromium (Cr) equivalent if they stabilize ferrite and nickel (Ni) equivalent if they stabilize the austenite. The Schaeffler diagram is used to predict the structure of stainless steel based on the function of Ni and Cr equivalent as shown in Fig. 2.13. The general effects of the alloying elements in austenitic stainless steel are as follows:

Chromium is the most important alloying element in the stainless steel and acts as a ferrite stabilizer. Chromium also increases the resistance to oxidation at high temperatures and erosion resistance. It is mainly responsible for the excellent corrosion resistance.

Nickel is a strong austenite stabilizer and facilitates the formation of austenite at room temperature. It is a non-carbide forming element and improves impact toughness and fatigue resistance in combination with Cr and Mo. Nickel is the only alloying element that increases hardness, tensile strength and toughness of the steel without any loss of ductility.

Carbon is a strong austenitizing element and increases the strength by interstitial solid solution hardening. If present in a greater amount, forms chromium carbides thus depleting Cr in the matrix and hence reduce the corrosion resistance. It also reduces the ductility, impact toughness, and weldability of the steel.

Manganese is also austenite stabilizer and can replace Ni to some extent. It is weak carbide former and favourably affects the forgeability and weldability. However greater contents of Mn (>2%) results in an increased tendency towards cracking and distortion during quenching. Similar to Cr, it enhances segregation of the impurities to the grain boundary and induces temper embrittlement. The addition of Mn improves nitrogen solubility and suppresses the formation of delta-ferrite.

Molybdenum is pronounced carbide former and a ferrite stabilizer. It can induce secondary hardening during the tempering of quenched steel. The addition of Mo produces fine-grained steels, improves fatigue strength and can delay temper embrittlement. Molybdenum increases the resistance towards crevice corrosion in chloride atmosphere and pitting corrosion. It improves nitrogen solubility but also promotes sigma and chi phase formation.

Silicon is a non-carbide former in steel and eliminates stress corrosion in Cr-Ni austenitic steels. Silicon, beyond 0.40%, causes a marked decrease in ductility in plain carbon steels.

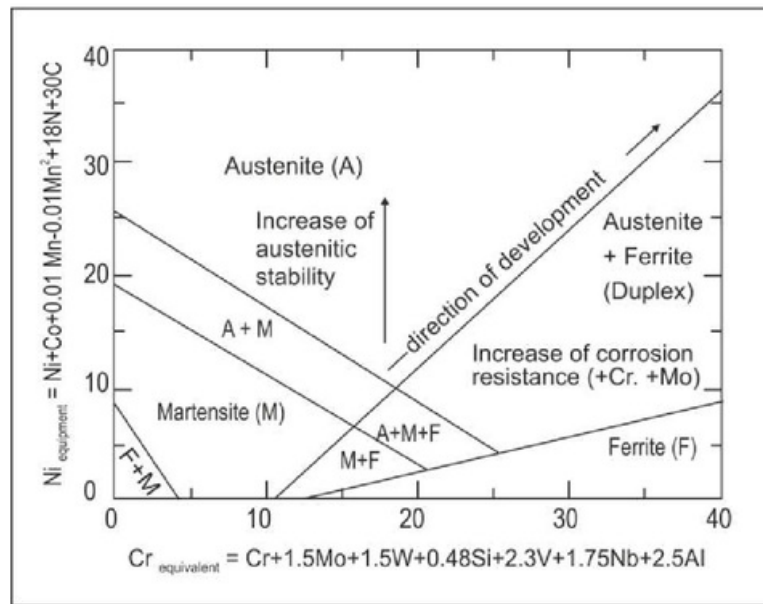


Fig. 2.13. Modified Schaeffler diagram.

2.7. Thermal spray process

Thermal spray process was invented by a young Swiss inventor named Dr. Max Schoop in 1911. Thermal spraying is a group of processes in which molten metal is deposited on a substrate by spraying. Thermal spray coating processes differ from other conventional coating processes as it is not an atomistic processes (individual ions or atoms attach to a surface). Instead, metallic, ceramic, cermet materials in the form of powder, wire, or rod are fed to a torch or gun with which they are heated to near or somewhat above their melting point. Schematic diagram showing process of thermal spray coating is shown in

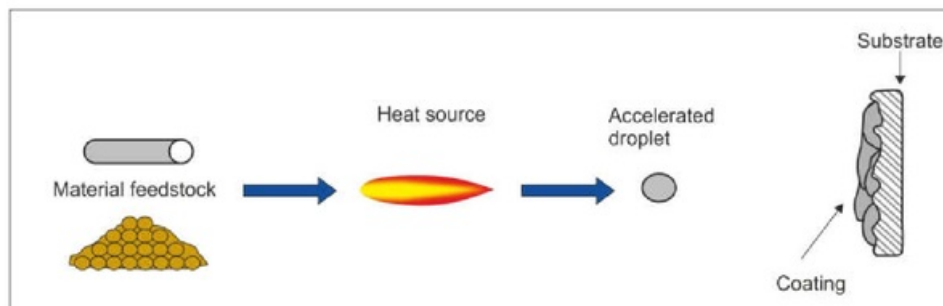


Fig. 2.14 Schematic diagram showing process of thermal spray coating

Fig. 2.14. The resulting molten or nearly molten droplets of material are accelerated in a gas stream and projected against the surface to be coated. On impact particles are

flattened and solidified to form a disk shape structure called “splat”. Overlapping “splats” on the substrate build up a coating of any desired thickness. Schematic diagram showing process of coating deposition is shown in Fig. 2.15.

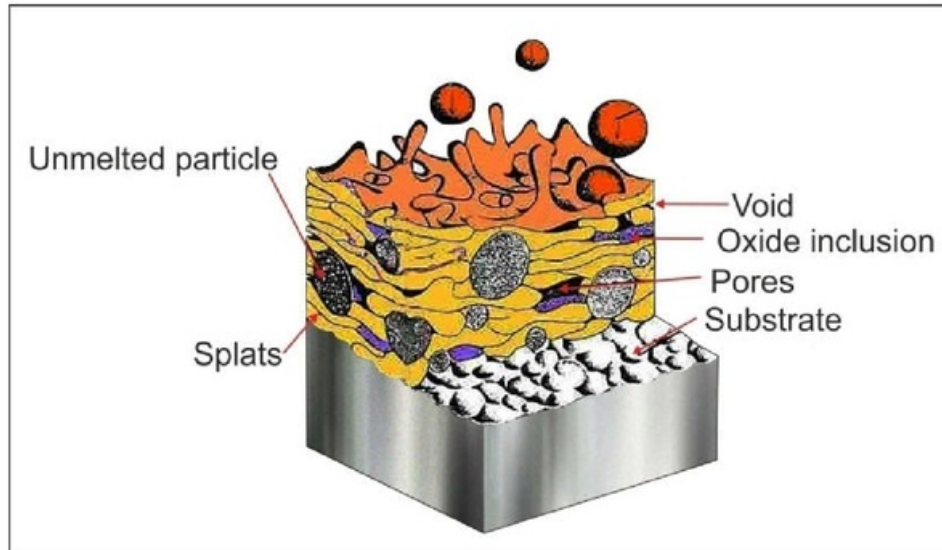


Fig. 2.15 Schematic diagram showing process of coating deposition.

The total coating thickness is usually generated in multiple passes of the coating device. The bonding between the substrate and coating is formed through mechanical interlocking

2.7.1. Various types of thermal spray process

There are different types of thermal spray techniques that are developed till date and put into practice. The most widely used thermal spraying processes for erosion resistance application are as follow:

- (a) Plasma spraying
- (b) Detonation gun spraying (D-gun)
- (c) High velocity oxy-fuel spraying (HVOF)
- (d) High velocity air-fuel spraying (HVOF)

Thermal spray process are also classified according to process temperature and velocity that they employ, as shown in Fig. 2.16.

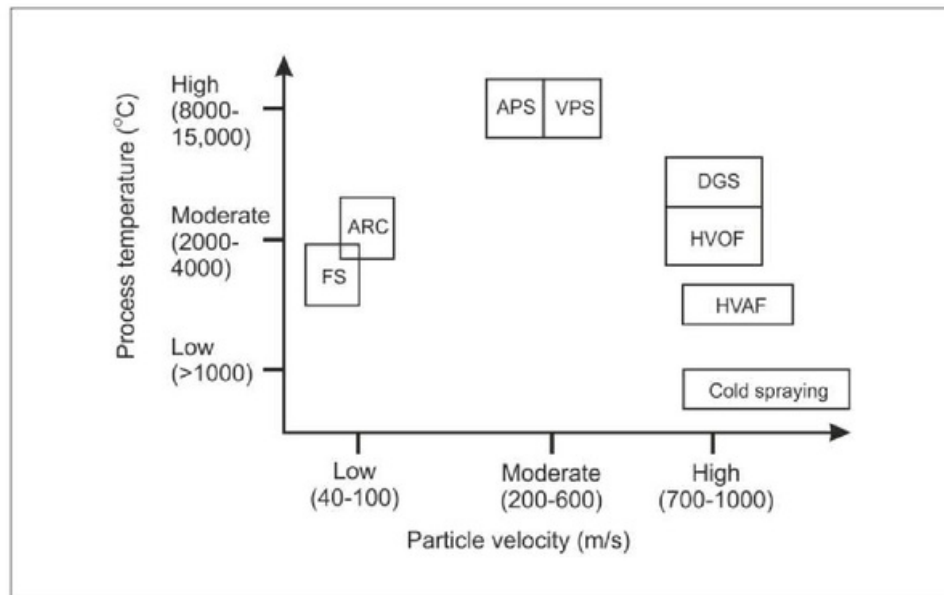


Fig. 2.16 Classification of thermal spray process according to process temperature and velocity.

HVOF and D-gun are industrially established thermal spray processes. However, they lead to inferior coating properties which deteriorates the erosion resistance. Recent investigations have shown that high velocity air fuel (HVAF) spraying is a rapidly emerging thermal spray technology for depositing surface coatings to combat wear, erosion and high-temperature corrosion and has challenged the D-Gun and HVOF process. The comparison of the thermal spray processes and their essential characteristics are given in Table 2.4.

(a) Plasma spraying

In the plasma spray process the electrical discharge between the cathode and anode heats up the working gas. This working gas expands in atmosphere and generates plasma jet stream. Thermal energy of the electric arc are used to melt the particles and they are sprayed upon the substrate. The working gas is usually a mixture of some gases like Ar+He+H₂ or Ar+He+N₂. The main advantage of the plasma spraying process is the high flame temperature that is generated depending on the gas used and the operating energy often reaches 720 MJ. The high temperature of the spray torch and the rapid cooling of deposits result in complex chemical transformations, which leads to the formation of metastable phases within the coatings, which are undesirable. The presence of oxygen is

Table 2.4 Comparison of thermal spray process and coating characteristics.

Attributes	Plasma	D-gun	HVOF	HVAF
Propellant/media	Inert gas	Detonation shock waves	Combustion jet	Combustion jet
Gas types	Ar, He, H ₂ , N ₂	O ₂ , C ₂ H ₂	C ₃ H ₆ , C ₃ H ₈ , C ₂ H ₂ , CH ₄ , C ₁₂ H ₂₆ , LPG, O ₂	C ₃ H ₆ , C ₃ H ₈ , air
Flame or exit plasma temperature, °C	8300	3900	3300	1900-1950
Particle velocity, m/s	200-800	910	200-1000	600-1250
Material feed rate, g/min	50-150	17	15-50	400 max
Density range, %	90 – 95	> 95	> 95	> 95
Bond strength, MPa	<68	82	68	>70
Oxides	Moderate to coarse	Small	Moderate to dispersed	Negligible

found to promote the nucleation of oxy carbides and extensive decarburization which are undesirable for erosion resistance point of view. The disadvantages of plasma spray process are the higher cost and complexity of the process. The plasma spray process is shown schematically in Fig. 2.17.

(b) Detonation gun (D-Gun) spraying

The detonation gun process is invented in 1955 by Praxair Surface Technologies, Inc. In D-Gun process mixture of fuel. Oxygen and feedstock powder is introduced in long tube/barrel and is ignited by spark plug. The resulting high-pressure shock waves (detonation wave) heats and accelerated the entrained powder particles in the barrel. These particles then come out of the barrel and impact the component held by the manipulator to form a coating. Depending upon the ratio of the combustion gases, the temperature of the hot gas stream can be as high as 3900°C. In D-gun spraying processes decomposition of the carbide based coating is minimized in comparison to plasma spraying due to lower heat enthalpy and shorter duration involved in the coating process. The detonation gun spray process is shown in Fig. 2.18.

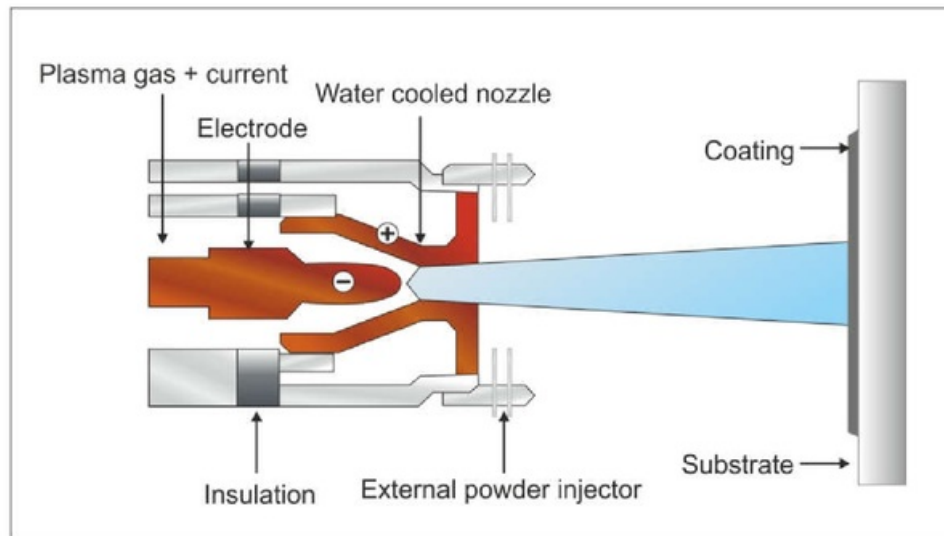


Fig. 2.17. Schematic diagram of plasma spray process, adapted from.

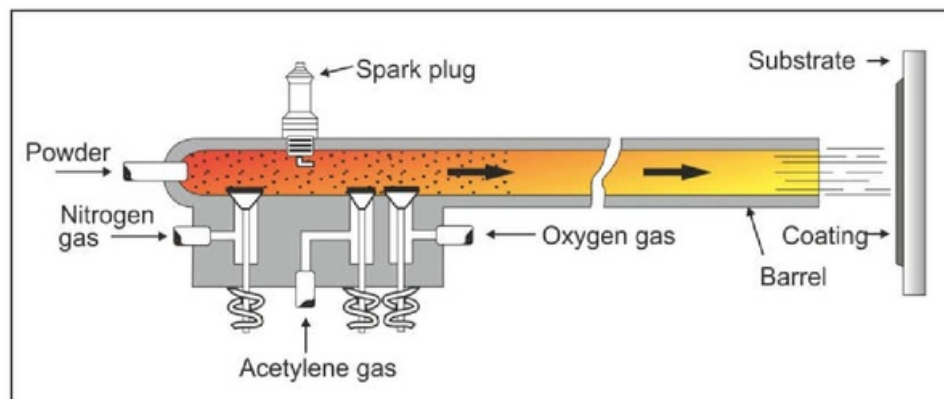


Fig. 2.18. Schematic diagram of Detonation gun (D-Gun) spraying process, adapted from.

(c) High velocity oxy-fuel (HVOF) spray process

The high velocity oxy fuel process is one of the most popular and industrially established thermal spray process and has been widely adopted by many industries since the mid 1980s. Currently, this process finds wide application in erosion resistance application of hydroturbine. The HVOF coating process uses significantly lower deposition temperatures relative to air plasma spraying and D-Gun spraying methods. Additionally, the higher particle velocity of HVOF spraying during deposition provides several advantages such as lower porosity, high mechanical interlocking, high adhesion

strength and high hardness. In the HVOF process the combustion fuel and oxygen are led to the combustion chamber together with the spray powder. the resulting flame expands supersonically through the nozzle. The speed of particle impact on the substrate is much greater, resulting in improved coating characteristics. The powder may be fed axially or radially into the combustion chamber or supplied through a side nozzle and is melted and accelerated by the flame. The main factors influencing the formation of HVOF thermal spray coatings are the fuel used and process parameters such as oxygen to fuel ratio, spray distance, and powder feed rate. The high velocity oxy-fuel spray process spray process is shown in Fig. 2.19.

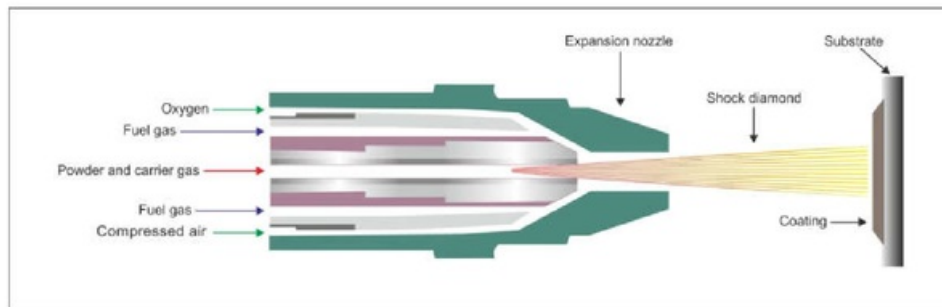


Fig. 2.19 Schematic diagram showing high velocity oxy-fuel spray process (HVOF)

(d) High velocity air-fuel (HVOF) spray process

HVOF process is a fast emerging process and its a modification of the HVOF process In this process coatings are sprayed with compressed air systems rather than oxygen, since the former lead to shorter contact time of spray particles with the flame and lower temperatures of materials, both of which lead to less fecarburization of WC. In the HVOF the spray particles are heated below material melting point, thus remaining in a solid state during coating deposition. In order to form a good-quality coating, they are accelerated to rather a high velocity (600-1250 m/s). Propane is the primary fuel gas in thermal spraying. However, propylene gas is used instead of propane to increase the gas temperature when spraying high-melting point materials. Compressed air provides cooling of the gun. When partially melted particles are impacting to the substrate, thermally softened particles undergoes intensive plastic deformation, forming a non-porous coating. Deformation of the substrate during particle impact results in a good coating bonding due to mechanical bonding at the substrate-particle interface. The high velocity oxy-fuel spray process spray process is shown in Fig. 2.20.

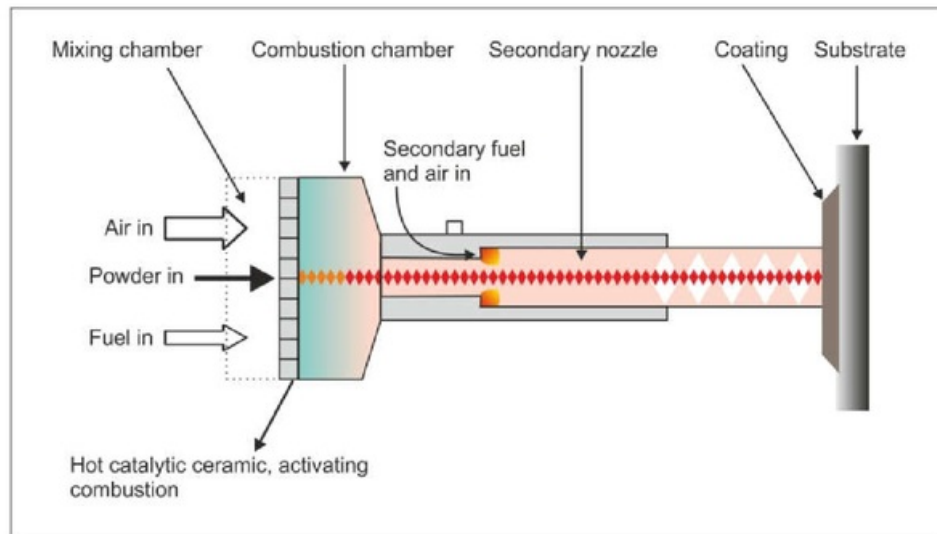


Fig. 2.20 Schematic diagram showing high velocity air-fuel spray (HVOF)

2.7.2. WC-Co based coating for erosion resistance application

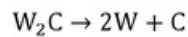
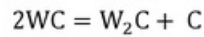
The selection of coating powder for erosion resistance application depends upon the severity and erosion environment. For hydroturbine application coating with high hardness and toughness is required, in order to resist the impact of hard silt particles. In past, several different types of coating powders have been attempted by various researchers to improve erosion resistance of turbine blades. However, it has been observed that WC-Co based cermet coating gives excellent erosion performance in comparison to other type of powders, which is due to the presence of hard WC particles in a tough and ductile Co-Cr Cermet materials (ceramic and metal) in the form of coatings find wide application in hydroturbine components due to their combination of abrasion, erosion and corrosion resistance.

The addition of chromium to the cobalt binder has shown significant improvement in the erosion and corrosion resistance of the coating. Several attempts have been made to reduce the erosion damage to hydroturbine underwater components by deposition of cermet coatings. Extensive works have been done on evaluation of different properties and performance of thermally sprayed cermet coatings. Most of these studies are around WC-Co coatings produced by various thermal spray techniques.

2.7.3. Decarburization in carbide based cermets

In order to obtain cermet coatings for erosion resistance application it is necessary that they must possess adequate microstructure and inter splat bonding. The interfacial

nature and quality of coatings are greatly affected by decarburization and formation of W_2C phase. Decarburization of WC leads into metastable phases which are brittle and undesirable, presence of these phases reduce the erosion resistance. The decomposition of WC is a two step mechanism, the first reaction involves the decomposition of WC to W_2C followed by the oxidation assisted decarburization of W_2C to metallic tungsten



The overall reaction is kinetically driven i.e. dependent on time and temperature ,making the degree of decarburization sensitive to the process flame temperature and flame velocity. In HVOF process higher decarburization of WC is observed in comparison to HVOF process, which is mainly attributed to higher temperature and in flight time. Higher process temperature leads to melting of WC particles which results into higher decarburization. In HVOF process higher velocity and lower flame temperature are used because of that particle in flight time is less and less decarburization of particles takes place.

2.7.4. Thermal spray coating properties for erosion resistant applications

there are several properties that are required for erosion resistance application and are as follow.

(a) Microstructural properties

The microstructure of coating be observed by optical or electron microscope, and is a good indicator of quality of coating. The microstructure of coating consist of laminar splats of WC particle in Co-Cr matrix. coating porosity is also a good indication of the quality of coating. In HVOF process lower porosity is generated which results in higher density, which in turn results in better erosion resistance. Medium coating porosity (1 - 5%) and high porosity coatings (in the range of 5 - 10%) of the same hardness deposited by different techniques (HVOF, D-gun and Plasma spraying). The cross sectional microstructure of WC-10Co-4Cr coating sprayed by HVOF and HVOF techniques are shown in Fig. 2.14, where the differences in porosity and interlamellar oxidation level in HVOF and HVOF coating can be clearly seen. Therefore, HVOF coated steel shows higher erosion resistance than HVOF coated steel.

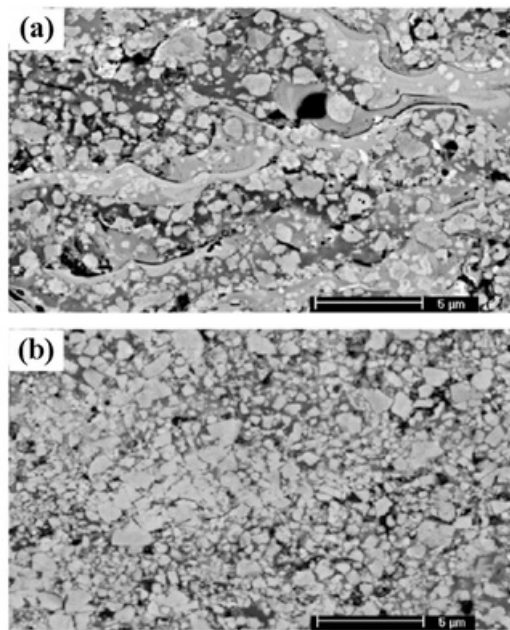


Fig. 2.14. Cross-sectional microstructure of WC-10Co-4Cr coating processed by (a) HVOF spraying, (b) HVAF spraying [60].

(b) Mechanical properties

The quality of thermal spray coatings and its erosion performance are strongly dependent upon its hardness. When coating hardness is higher than erodent hardness then erosion doesn't take place. However, when hardness of erodent is higher than coating micro cutting of the coating surface may take place. therefore high coating hardness is essential for getting better erosion resistance. Hardness improvement due to formation of brittle phase W_2C is undesirable and result in lowering of erosion resistance. The toughness of a coating material is also an important mechanical characteristic since fracture determines the erosion resistance against the impacted erodent particles at different impact angles. Lima et al. [232] reported that the fracture toughness is the most relevant property corresponding to the erosion resistance of WC-Co spray coatings in comparison to the hardness. Thakur et al. also observed that fracture toughness and hardness has a strong influence on the erosion behaviour of WC-CoCr nano-structured coating. At low impact angle of 15° and 30° , the micro cutting is more prominent, while at a normal impact angle of 90° , direct and fatigue fracture dominant. In conclusion, both high fracture toughness and hardness of the coating are necessary at all erosion conditions of impact angles. At low impact angle, high hardness

and fracture toughness are required. At high impact angle of 90° , high toughness and low hardness are required to improve the erosion resistance.

2.7.5. Erosion performance of HVOF and HVAF sprayed WC-Co coatings

Thakur et. al. investigated the slurry erosion behavior of HVOF sprayed WC-Co-Cr cermet coatings with two different WC grain sizes. Slurry erosion testing was performed using a pot-type slurry erosion tester to evaluate slurry erosion resistance of the coatings. It was observed that WC-Co-Cr cermet coating deposited with fine grain WC provides higher slurry erosion resistance as compared to conventional cermet coating. Goyal et al. have conducted a slurry erosion studies on HVOF deposited WC-10Co-4Cr and $\text{Al}_2\text{O}_3 + 13\text{TiO}_2$ coatings on CF8M turbine. The bare steel and $\text{Al}_2\text{O}_3 + 13\text{TiO}_2$ coating showed the ductile and brittle mechanisms respectively whereas WC-10Co-4Cr coating exhibited mixed behavior (mainly ductile). It was observed that WC-10Co-4Cr coating was found to be useful to increase the slurry erosion resistance of steel remarkably. Santana et. al. studied the solid particle erosion behaviour of high velocity oxygen fuel (HVOF) sprayed WC-12Co and WC-10Co-4Cr coatings. The erosion tests were conducted at 30° and 90° impact angles using SiC particles It has been found that the WC-10Co-4Cr coating exhibited a higher erosive wear resistance as compared to the WC-12Co coating. Wang et. al. studied the cavitation and slurry erosion resistances of high-velocity oxygen fuel (HVOF) and high-velocity air fuel (HVAF) sprayed WC-10Co-4Cr coatings. They observed that the HVAF-sprayed WC-10Co-4Cr coating has a lower degree of decarburization and better hardness, fracture toughness, porosity, cavitation and sand slurry erosion resistances than that of HVOF-sprayed WC-10Co-4Cr coatings respectively. Kumar et. al. studied the cavitation resistance of 86WC-10Co-4Cr coating sprayed by HVOF and HVAF thermal spraying. The HVAF coating has shown a low porosity, high hardness, and good cavitation resistance as compared to HVOF spraying. They suggested that that process parameter plays a vital role in achieving improved cavitation resistance. Li et. al. studied the erosion behavior of HVOF and HVAF processed WC-Co-Cr coatings using at four different impingement angles (15° , 45° , 75° and 90°) using alumina as erodent. The results indicate that the micro-cutting and coatings spallation was main erosion mechanisms for coatings which were lower in HVAF spraying.

2.8. Identification of Research Gap

Currently, HVOF process is widely used in hydropower plants for spraying WC-10Co

-4Cr coating on CA6NM steel. However, this process leads to considerable amount of decarburization of WC into W_2C . Which reduces the erosion performance of coating. HVOF process is fast emerging process and it has potential to replace the HVOF coating for hydroturbine application. Most of research done on HVOF coating is done to evaluate its wear performance. However, erosion studies of HVOF sprayed WC-10Co-4Cr coating on CA6NM steel for hydroturbine application is not addressed in literature. Hence, in the present investigation solid particle erosion performance of HVOF sprayed WC-10Co-4Cr coating on CA6NM steel at three different impingement angles and two different impact velocities was studied.

CHAPTER 3

Materials and Methods

This chapter describes the materials, equipment, and methodology employed to complete the present study. The chapter is divided into three sections. The first part discusses about the selection of base material, evaluation of mechanical properties of steel and its characterization by field-emission scanning electron microscopy (FESEM) and X-Ray diffraction (XRD) methods. The second part of the study focuses on thermal spray coatings. It discusses about feedstock powder selection, HVOF, HVOF coating deposition procedure and their respective process parameters. Feedstock powder characterization was carried out using FESEM and XRD. Both the coatings were characterized in terms of cross-sectional microstructure, porosity, volume fractions, phases, microhardness and fracture toughness. The last section of the chapter provides a detailed description of air jet erosion tester used to evaluate the erosion behavior of uncoated and coated steel.

3.1 Selection of Base Material

As - cast CA6NM martensitic stainless steel (ASTM A743 grade) is used as a substrate material for coating deposition and erosion behavior study. It finds wide application in the construction of hydro turbine components. Optimum combination of strength and ductility makes it a potential candidate for application in hydroturbine components [1]. The steel was received in as - cast condition from M/s Star Wire (India) Ltd., Ballabgarh (Haryana) in the form of 250 x 250 x 50 mm plate. As - cast steel test block was machined, and samples of 25 x 25 x 5 & 25 x 20 x 5 mm were prepared using wire-cut electric discharge machine (EDM) for erosion testing. Plates of 103 mm x 50 mm x 5 mm was also cut from the same test block for coating deposition. The chemical composition of the steel is given in Table 3.1.

Table 3.1 Chemical composition of cast CA6NM steel (wt %).

Element	C	Cr	Ni	Mn	Si	Mo	S	P	Fe
wt-%	0.06	11.88	3.65	0.61	0.45	0.61	0.002	0.028	Bal.

3.2 CA6NM Martensitic Stainless Steel Characterization

Mechanical properties and microstructure of steel have an enormous effect on its erosion performance. Therefore, It is necessary to characterize the martensitic steel before conducting the erosion testing and proceeding for coating deposition. It will help to study the correlation of structure properties and erosion performance of the martensitic steel. In the present investigation, following methods of the martensitic steel characterization and techniques were used:

- (i) X-Ray diffraction (XRD)
- (ii) Micro hardness and roughness testing
- (iii) Tensile and Charpy impact testing
- (iv) Density measurement
- (v) Optical and FESEM analysis

3.2.1. XRD analysis

To identify the phase composition, the XRD pattern of martensitic steel was recorded with X'Pert Powder PANalytical with Cu K α radiation. It was operated at an applied voltage of 45 kV with 40 mA current. The XRD was used with a step size 0.02° and a step time of 0.6 s in the angle range 20° to 120°.

3.2.2. Micro hardness and roughness testing

Vickers Microhardness of martensitic steel was measured using INNOVATEST (NEXUS 4000) hardness tester under a 300 g load with 10 s dwell time. Average of ten readings were reported. In order to provide similar erosion conditions samples were mirror polished and surface roughness was measured using a surface roughness tester (Surftest SJ 301, Mitutoyo).

3.2.3. Tensile and Charpy impact testing

Standard cylindrical tensile specimens were prepared with a gauge length of 20 mm and gauge diameter of 4 mm according to ASTM E8/E8M-15a [2] specifications as shown in Fig. 3.1. The tensile tests were performed on H25KTinius Olsen machine with a crosshead speed of 1 mm/min. Standard Charpy impact specimens of dimension 10 mm \times 10 mm \times 55 mm were prepared as per ASTM E23-12c [3] (V-notch) specification as shown in Fig. 3.2. Both the tests were conducted at room temperature, and an average of three samples are reported.

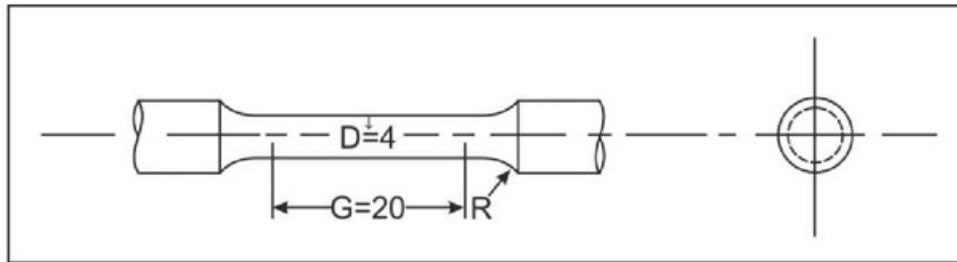


Fig. 3.1. Tensile test specimen as per ASTM E8/E8M-15a specification (all dimensions in mm)

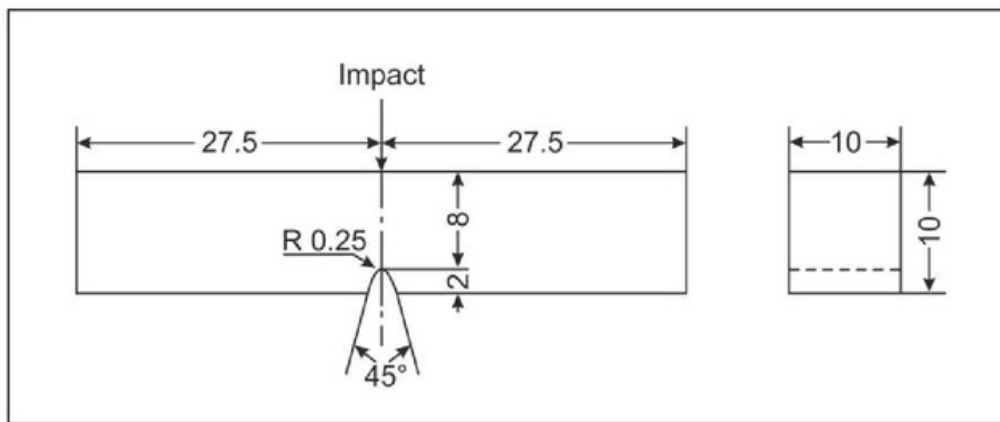


Fig. 3.2. Charpy V-notch impact test specimen as per ASTM E23-12c specification (all dimensions in mm)

3.2.4. Density measurement

The experimental density of martensitic steel was measured as per ASTM B962-15 [4] Standard using Archimedes principle.

3.2.5. Optical and FESEM analysis

The optical micrograph of martensitic steel was examined using an inverted metallurgical microscope (Model: SuXma- Met 1, Conation Technologies). Field emission scanning electron microscope micrograph was analyzed using NOVA Nano 450 FESEM operated at 20 kV. The samples were mirror polished and etched using picral (5 gm picric acid, 5 ml HCL and 95 ml ethanol) in both the cases.

3.3. Thermal Spray Coating

In order to overcome the problem of silt erosion in hydroturbine components, surface engineering route was selected. Thermal spray coating was deposited on CA6NM martensitic steel using HVOF and HVAF process. WC-10Co-4Cr powders were used for deposition as it results in significant improvement in hardness of the surface.

3.3.1. Selection of feedstock powders

Successful deposition of thermal spray coating is mainly dependent upon two factors i.e. thermal and kinetic energy [5]. Either has to be dominant in order to achieve uniform coating. In HVOF spraying higher flame temperature and lower particle velocity is used, which accounts for high thermal and low kinetic energy. On the other hand, HVAF process employs higher velocity and low flame temperature, which result in high kinetic and low thermal energy [6]. HVOF focuses more on thermal energy and HVAF on Kinetic energy. However, due to the application of higher thermal energy in HVOF process oxidation of WC takes place and it results in decarburization of the coating [7,8]. Finer the size of powder higher is the oxidation due to high surface to volume ratio which causes decarburization of WC into the molten binder at higher flame temperature [9]. Taking that into account a coarser powder is generally used for HVOF coating. In HVAF spraying finer powder is preferred as coarser powders need higher kinetic energy to deform and get deposited on the surface [5]. At the same time as there is no risk of decarburization, finer powders are preferred as finer powder leads to better properties[10].

Therefore, two different sizes of WC-10Co-4Cr powder were used for HVOF and HVAF thermal spraying to achieve the greater deposition efficiency. Coarse agglomerated and sintered powder with particle size of -45 to +15 μm was used for HVOF thermal spraying. Fine powder (AMPERIT[®] 556.059, agglomerated and sintered) with the nominal particle size of -30 to +5 μm was used for HVAF spraying.

3.3.2. HVOF thermal spraying

Grit blasting was performed on the substrate before coating to remove any contamination from the surface of the substrate and also create a rough surface to increase the mechanical interlocking of the sprayed coating to the substrate. WC-10Co-4Cr powder was sprayed on martensitic steel plates (103 mm x 50 mm x 5 mm) using HVOF thermal spray system at M/s Metalizing Export Company Jodhpur India using Hypojet-HP2100 HVOF gun. The HVOF thermal spray unit mainly consists the three parts: (i) gasses control panel, (ii) powder feeder,

and (iii) spray gun. The complete HVOF unit is shown in Fig. 3.3. Oxygen gas and liquid petroleum gas (LPG) were used for the combustion and producing chemical energy for maintaining the temperature of the throat of the gun, where WC-10Co-4Cr powder remains in



(a) HVOF spraying gun



(b) Oxygen cylinder



(c) Powder feeder

(d) Gas control panel

Fig. 3.3. HVOF thermal spray coating unit at Metalizing Export Company India

Table 3.2. HVOF process parameters

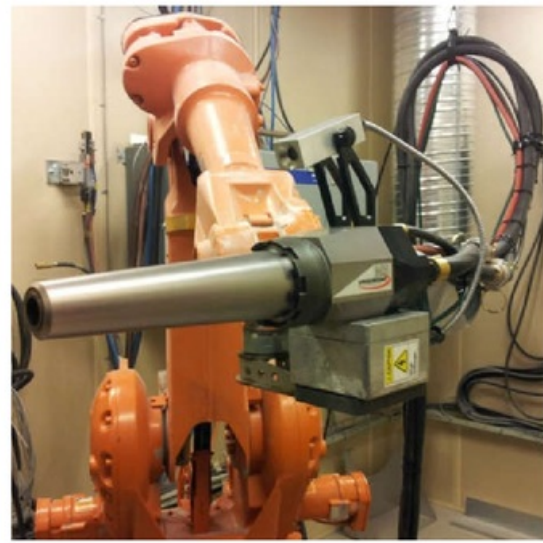
Parameters	Value
Fuel	LPG
Spray distance (mm)	160-180
Powder feed rate (g/min)	40
Oxygen flow rate (l/min) & Oxygen pressure (MPa)	300 - 320 & 0.98
Air flow rate (l/min) & Air pressure (MPa)	440 & 0.5
Fuel flow rate (l/min) & Fuel pressure (MPa)	80 - 85 & 0.44
Deposition rate ($\mu\text{m}/\text{pass}$)	25-30
Carrier gas flow rate (SCFH)	10-15
Step size (mm)	3.5
Number of passes	13

3.3.3. HVAF thermal spraying

Prior to spraying, substrate was grit blasted by M3 HVAF gun (Uniquecoat Technologies USA). WC-10Co-4Cr powder was sprayed onto martensitic steel plates (103 mm x 50 mm x 5 mm) at M/s PTC Innovation Sweden using the same gun that was used for grit blasting the substrate. HVAF thermal spray system is shown in Fig. 3.4. Samples were mounted on a 300 mm round rotating carousel during spraying. The HVAF gun was placed in front of the samples at a stand-off/spray distance of 300 mm to give a horizontal spray jet. Propane was used as the main combustion fuel gas (fuel 1) as well as secondary combustion gas (fuel 2). Nitrogen was used as the powder carrier gas and compressed air jets were used to cool the samples during spraying. The HVAF process parameters are specified in Table 3.3. The optimum process parameters were suggested by coating manufacturer and are used industrially.



(a)



(b)

Fig. 3.4. (a) Round rotating carousel used for sample mounting, (b) HVAF thermal spray system (HVAF M3, Uniquecoat) at PTC Innovation Sweden

Table 3.3 HVAF process parameters

Parameters	Value
Fuel 1 and Fuel 2	Propane
Spray distance (mm)	300
Gun traverse velocity (m/min)	100
Step size (mm)	5
Powder feed rate (g/min)	200
Nitrogen carrier gas flow (l/min)	60
Air pressure (MPa)	0.80
Fuel 1 pressure (MPa)	0.69
Fuel 2 pressure (MPa)	0.72
Deposition Rate ($\mu\text{m}/\text{pass}$)	20
Number of passes	17

3.4. Feedstock Powder Characterization

Characteristics of feedstock powder play an important role in the microstructure and performance of the coatings. Characterization of powder was conducted as follows:

- (i) FESEM for morphology analysis.
- (ii) XRD was used to determine constituent phases in the feedstock powders

PANalytical instrument was used to perform the XRD analysis in the angle range of 20° to 100° with a step size 0.02° and a step time of 0.6 s.

3.5. Coating Characterization

Erosion performance of HVOF and HVAF coating is strongly dependent on coating Micro structural features. Examination of micro structural features is important to analyze the quality of coatings. In the present study, following methods of coating characterization and techniques were used:

3.5.1. Coating roughness

Surface roughness of as sprayed thermal sprayed coating give important insight into the coating process and its quality. After deposition of WC-10Co-4Cr coating on CA6NM martensitic steel using HVOF and HVAF process, as sprayed surface roughness was measured using surface roughness tester (Model: SJ410, Mitutoyo). In order to achieve uniform starting condition before erosion all the samples were mirror polished and surface roughness was measured using same tester.

3.5.2. XRD analysis

XRD was utilized to analyze the phases present in HVOF and HVAF sprayed WC-10Co-4Cr coating over an angle range of 20° to 100°. The index of carbide retention (I) in coating was calculated by the integral intensities of (100) peak of WC (I_{WC}) at $2\theta = 35.6^\circ$ and the (101) peak of W_2C (I_{W_2C}) at $2\theta = 39.6^\circ$. It gives the value of WC retention against the formation of W_2C phase in coating. It is calculated using equation [11] as given below:

$$I = \frac{I_{WC}}{(I_{WC} + I_{W_2C})}$$

3.5.3. FESEM & EDS analysis

To characterize the microstructure of coating, samples were cut using the linear precision saw and hot mounted in resin powder (PhenoCure, BUEHLER) using the automatic mounting press (SimpliMet 3000, BUEHLER). Mounted samples were polishing to 1 μ m finish. The polished cross section of coating were observed using FESEM to analyze the microstructure

of coating EDS analysis is used to analyze the phases present in coating. The coating thickness of the was measured using FESEM images taken at low magnification (200X) on polished cross-sections.

3.5.4. Coating density and porosity

Image analysis was done on cross-sectional FESEM micrograph (10,000X) of the coating to evaluate volume fraction of the WC, binder (Co-Cr) and porosity. The density of the coating was calculated by volume fraction of the WC and binder (Co-Cr). The density of the WC ($\rho_{WC} = 15.7 \text{ g/cm}^3$) and binder ($\rho_{Co-Cr} = 8.6 \text{ g/cm}^3$) was taken to calculate the density of the coating [12,13].

3.5.5. Microhardness

Vickers micro Hardness measurements of HVOF and HVAF sprayed coating were performed on the polished transverse section of the coatings with INNOVATEST (NEXUS 4000) hardness tester at 300 g load with 10 s dwell time.

3.5.6. Fracture toughness

The fracture toughness of coating was determined by the indentation method. A Vickers indenter was used on metallographically prepared cross sections of coating with a 5 kg load with 10 s dwell time. The indenter was loaded such that the two indent diagonals were parallel and perpendicular to the substrate/coating interface respectively. The length of the cracks, both parallel and normal to the substrate-coating interface, produced by the indentation technique was measured using FESEM micrograph.

The fracture toughness (K_c) of the coatings was determined by the indentation method using the Evans and Wilshaw equation [14] as given below:

$$K_c = 0.079 \frac{P}{a^{3/2}} \log 4.5 \left(\frac{a}{c} \right)$$

Where 'P' applied indentation load (mN), and 'a' and 'c' correspond to the length of the indentation half-diagonal (μm) and crack length from the center of the indent (μm), respectively as shown in Fig.3.5.

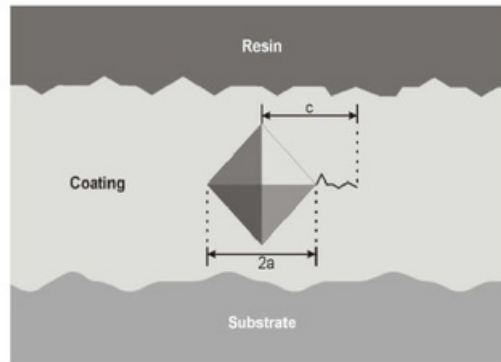


Fig. 3.5. Schematic depiction of the Vickers indentation and crack geometry.

3.6. Solid Particle Erosion Testing

The erosion behavior of cast and coated CA6NM steel were evaluated using air jet erosion tester (Model: TR , DUCOM Bangalore). Erosion test was performed as per ASTM G-76-13 [15] test standard. Schematic diagram of the air jet erosion tester [12] used for these experiments is shown in Fig. 3.6. The erosion test parameters utilized in the present study are provided in Table 3.4. In this erosion tester, the abrasive particles were accelerated from a nozzle by using a compressed air stream that caused them to impact on the surface of the material. Figure 3.7 shows the FESEM micrograph of alumina particle (50 μm) used for erosion testing; it was observed that particles are flaky and angular in shape. To provide an initial standard surface condition before erosion test, all specimen were abraded using 0/0, 1/0, 2/0, 3/0, and 4/0 grades of emery paper. Cloth wheel polishing was done to obtain a mirror finish using a diamond paste. Each sample was removed after every 2 min to determine the mass loss. The impingement

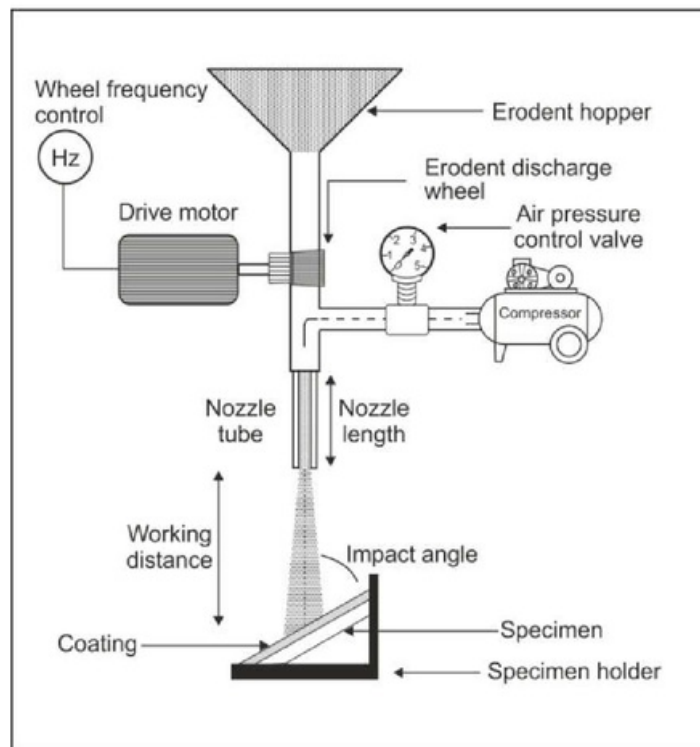


Fig. 3.6. Schematic view of air jet erosion tester used for solid particle erosion testing

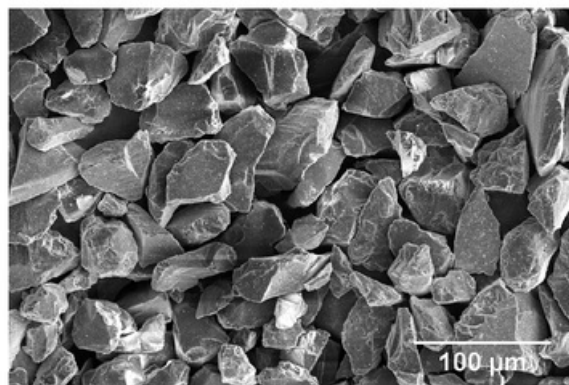


Fig. 3.7. Morphology of alumina particles.

angles used for the tests were 30° , 60° and 90° . These angles were selected to evaluate the behaviour of these materials at low, intermediate and high impingement angles. A particle velocity of 35 and 70 m/sec is used to replicate severe erosion condition, and an abrasive

flow rate of 2 g/min were used to conduct the tests. Particle velocity was measured with an accuracy of ± 2 m/s, using the double disc rotating method [16–18] as shown in Fig. 3.8.

Table 3.4 Parameters used in solid particle erosion testing.

Erodent particle	Alumina
Average erodent particle size	50 μ m
Impact velocity	35 & 70 m/s
Erodent discharge	2 gm/min
Test gas	compressed air
Standoff distance	10 mm
Nozzle diameter	1.5 mm
Impact Angle	30°, 60° and 90°
Test duration	Cycles of 2 min
Test temperature	Room temperature
Sample size	(25x25x5) and (25x20x5) mm

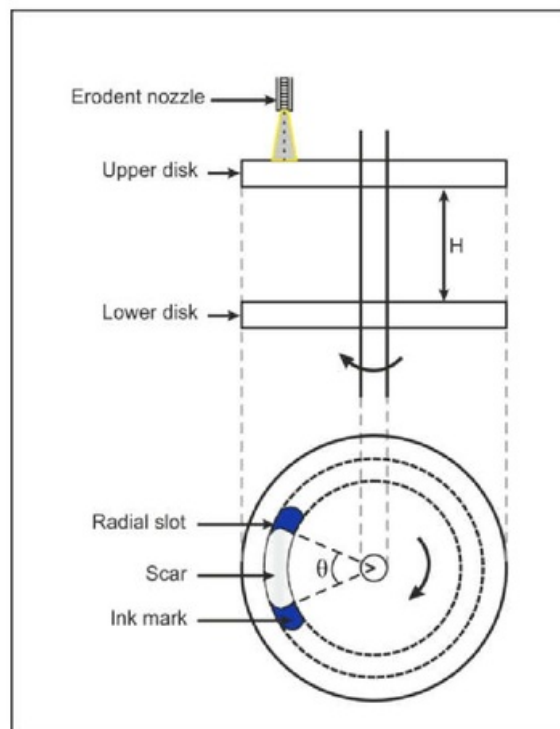


Fig. 3.8. Schematic diagram of the double disk apparatus.

In this apparatus, two disks are attached to a common rotating shaft. A radial slot is cut on top disk and the lower disk is coated with thin layer of paint. Stream of erodent is allowed to strike on top disk for 10 minutes and elliptical shape scar is formed on the bottom disk, which is measured using a protractor. Velocity is measured using formula as given below

$$V = [H \times N] \times [360/A]$$

Where, H = Distance between disks in m (0.03)

N = Revolution per second of double disk system(5000/60)

A = Angle of Incidence

The abrasive flow rate was measured by collecting the abrasive in a container during 1 min. Before and after the tests, each specimen was weighed using a digital balance with an accuracy of 0.0001 g to observe the difference in weight loss for each test. The weight loss was converted into volume loss to obtain the precise data because the WC-10Co-4Cr coating and substrate possess different densities. Micrographs of the eroded surfaces were obtained using an FESEM to analyze the specimens and to identify the possible erosion mechanisms.

CHAPTER 4

Results and Discussions

The results of the experimental work performed in this study and their discussion are presented in this chapter. This chapter is divided into four sections. The first section discusses about the characterization of CA6NM steel. The second section deals with erosion performance of CA6NM steel at different impingement angles and impact velocities. The third section discusses characterization of HVOF sprayed WC-10Co-4Cr coated CA6NM steel and its erosion performance at different impingement angles and impact velocities. The last section focuses on HVOF sprayed WC-10Co-4Cr coating on CA6NM steel and its characterization. It also discusses erosion performance at different impingement angles and impact velocities.

4.1. Characterization of CA6NM Steel

Erosion performance of steel mainly depends upon its microstructure and mechanical properties. Evaluation of microstructure and properties are necessary to gain insight into erosion behavior of steel. In this section microstructure, XRD study, mechanical properties of CA6NM steel are presented.

4.1.1. Microstructure and XRD study

The optical and FESEM microstructure of as - cast CA6NM steel is illustrated in Fig. 4.1 (a & b). The microstructure of as - cast CA6NM steel consists of lath martensitic needles. Apart from them, the structure also exhibits the presence of delta ferrite [19]. X-ray diffraction patterns of the as - cast CA6NM is shown in Figure 4.2. The diffraction pattern showed peaks of martensite.

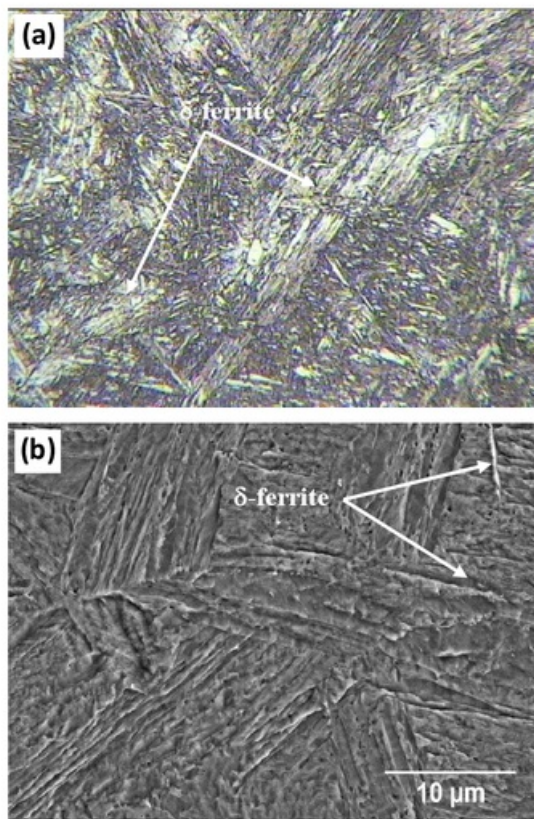


Fig. 4.1. (a) Optical and (b) FESEM micrograph of cast CA6NM steel.

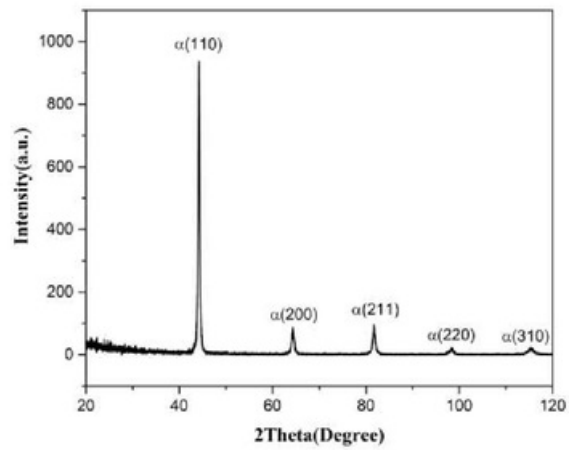


Fig. 4.2. XRD pattern of cast CA6NM steel

4.1.2. Mechanical properties and density

Analysis of mechanical properties of steel is important in understanding its erosion behavior. Table 4.1 shows the mechanical properties and density of cast CA6NM steel. It is observed that steel in cast condition contains an optimum combination of strength and ductility.

Table 4.1 Mechanical properties and density of cast CA6NM steel

Mechanical Properties	Cast CA6NM steel
Microhardness (HV _{0.3})	338 ± 29
YS (MPa)	652 ± 48
UTS (MPa)	892 ± 66
Ductility (% elongation)	13 ± 4
Impact energy (J)	42 ± 8
Density (g/cm ³)	7.70

4.1.3. Fractography of tensile and Charpy specimen

Tensile fractographs of cast CA6NM steel at lower and higher magnifications are shown in Fig 4.3. The fracture surface of the cast CA6NM steel is ductile, and dimples can be seen on the fractured surface, which point to fact that plastic deformation has taken place before fracture..

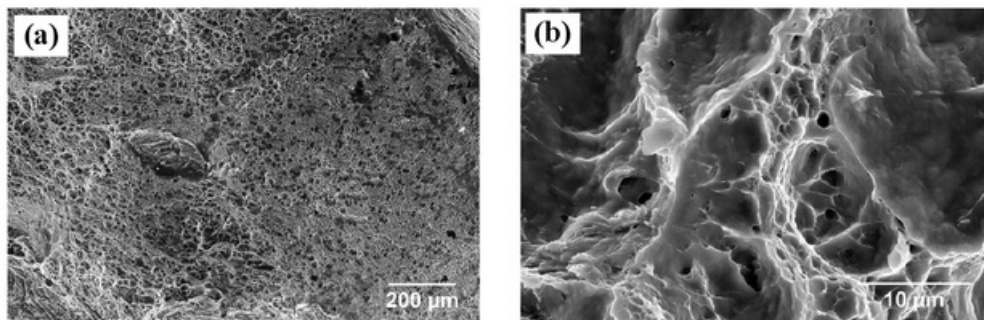


Fig. 4.3. FESEM fractographs of tensile specimen of cast CA6NM steel (a) lower magnification, (b) higher magnification.

The FESEM fractographs of Charpy V-notch fractured samples of cast CA6NM steel is given in Fig. 4.4 at lower and higher magnification respectively. Fracture surface shows ductile features. It is mainly composed of dimples, which points to relatively high toughness

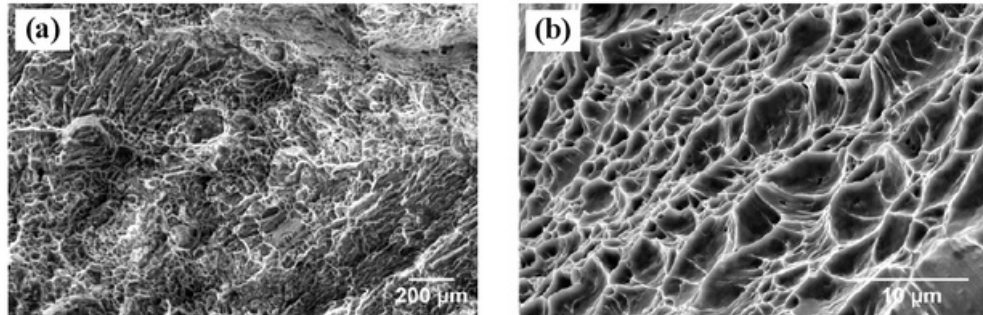


Fig. 4.4. FESEM fractographs of Charpy impact specimen of Cast CA6NM steel (a) lower magnification, (b) higher magnification.

4.2. Erosion Performance of CA6NM Steel

Erosion performance of CA6NM steel was evaluated at 35 and 70 m/s impact velocity and at three different impingement angles (30°, 60° and 90°) using alumina as erodent. Effect of impingement angle on cumulative volume loss and FESEM images of eroded surfaces are presented in this section.

4.2.1. Effect of impingement angle on formation of erosion scar

Erosion mechanism of material is dependent upon angle of impingement between erodent and surface of sample. Variation in angle of impingement results into change of erosion scar morphology. Schematic diagram showing interaction of erodent with surface at different impingement angles is shown in Fig. 4.5. It is observed that as the impingement angle rises from 30° to 90°, vertical component of the kinetic energy of impacting particle increases. This results in decrease of area of contact between erodent and surface, thus reducing the size of erosion scar that is formed on the surface of the samples. Photographs of the erosion scar formed on samples at 30°, 60° and 90° impingement angles and their respective sample holders are shown in Fig. 4.6. The sample size used for 30° impingement angle is 25x20x5 mm. While for 60° and 90° impingement angle the sample size is 25x25x5 mm. The smaller size of 30° impingement angle sample prevents the contact of sample and nozzle during

retrieving and placing of sample in holder. The center region of the eroded scar (Region "1") shows the region of erosion, and on its periphery, it is surrounded by a region of elastically loaded material (Region "2") [20]. At 30° impingement angle, the contact area of erodent with the substrate is high, and erosion scar of an ellipsoid shape covering the entire length of the sample is observed. At 60° impingement angle material is eroded forming a perfect ellipsoid shape depression, it is because the contact area is lower than 30° . While at 90° impingement angle the contact area of erodent with surface is lowest and it created a perfect circular shape depression.

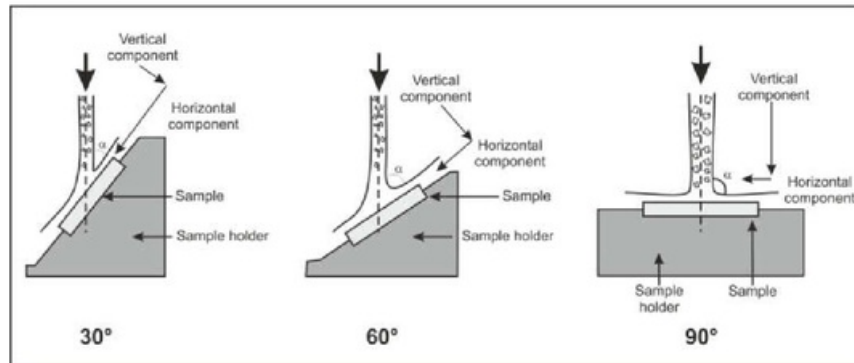


Fig. 4.5. Schematic diagram showing interaction of erodent with surface of sample at (a) 30° , (b) 60° and (c) 90° impingement angle

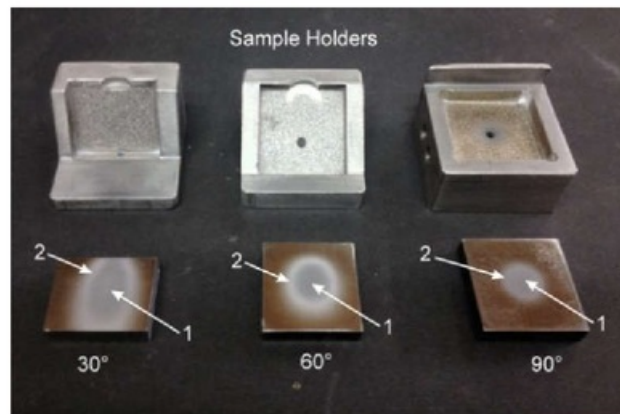


Fig. 4.6. Photographs of the erosion scar formed on eroded samples at 30° , 60° and 90° impingement angles and their respective sample holder.

4.2.2. Effect of impingement angles and impact velocities on cumulative volume loss

Cumulative volume loss of the cast CA6NM steel as a function of erosion time (upto 14 minutes with interval of 2 minutes) at 30°, 60° and 90° impingement angle for 35 and 70 m/s impact velocity are shown in Fig. 4.7 to Fig. 4.9. It is observed that cumulative volume loss increased linearly with increase in erosion time. It can be observed that cumulative volume loss at 30°, 60° and 90° impingement angles for 35 m/s impact velocity is lower than that observed at 70 m/s impact velocity. Which is mainly due to the higher kinetic energy of impacting particles at higher impact velocities. The relationship between cumulative volume loss and impingement angles for cast CA6NM steel is shown in Fig. 4.10. It is noticed that cumulative volume loss continuously decreases with increasing impingement angle and reaches a minimum at 90° angle. Maximum cumulative volume loss was observed at 30° impingement angle, which points to fact that material has eroded in ductile manner, the same behavior has been observed earlier by other researchers [21–24] for erosion of ductile materials.

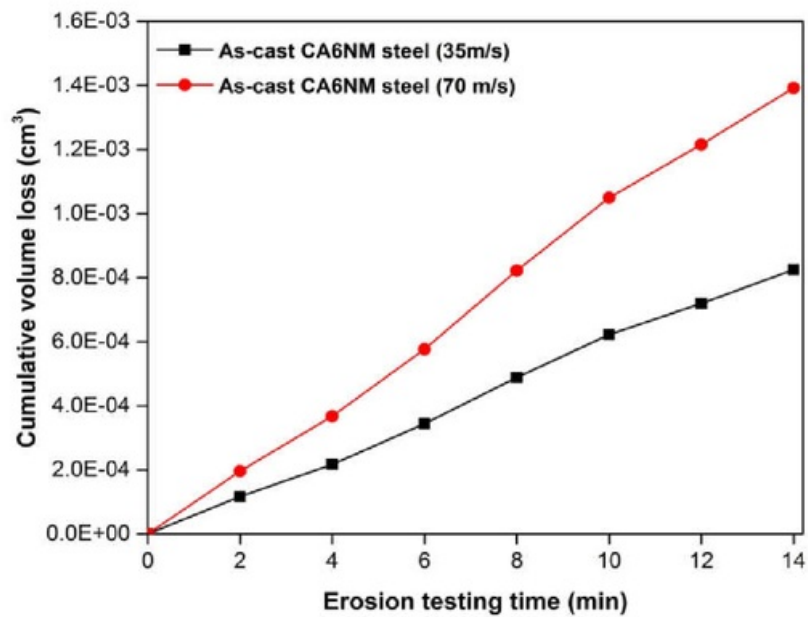


Fig. 4.7. Cumulative volume loss of as cast CA6NM steel as a function of erosion time (14 minutes) at 30° impingement angle for 35 and 70 m/s impact velocity.

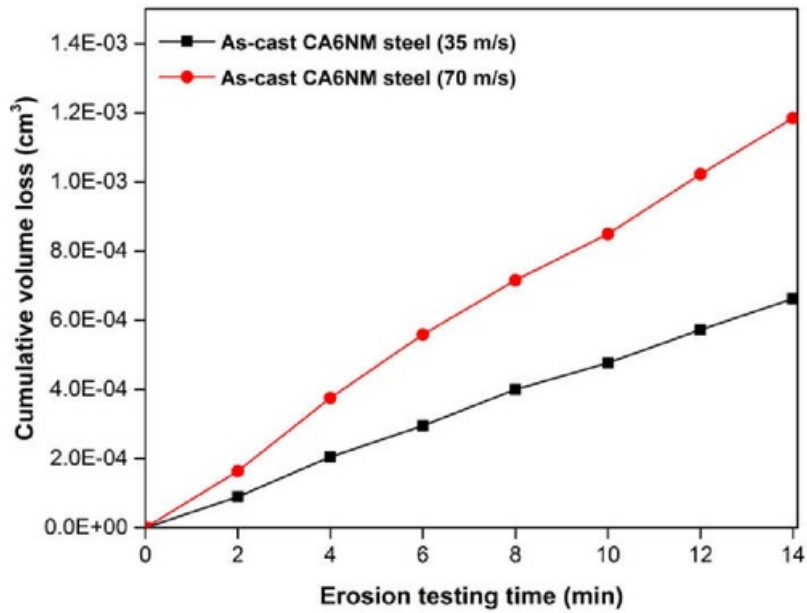


Fig. 4.8. Cumulative volume loss of as cast CA6NM steel as a function of erosion time (14 minutes) at 60° impingement angle for 35 and 70 m/s impact velocity.

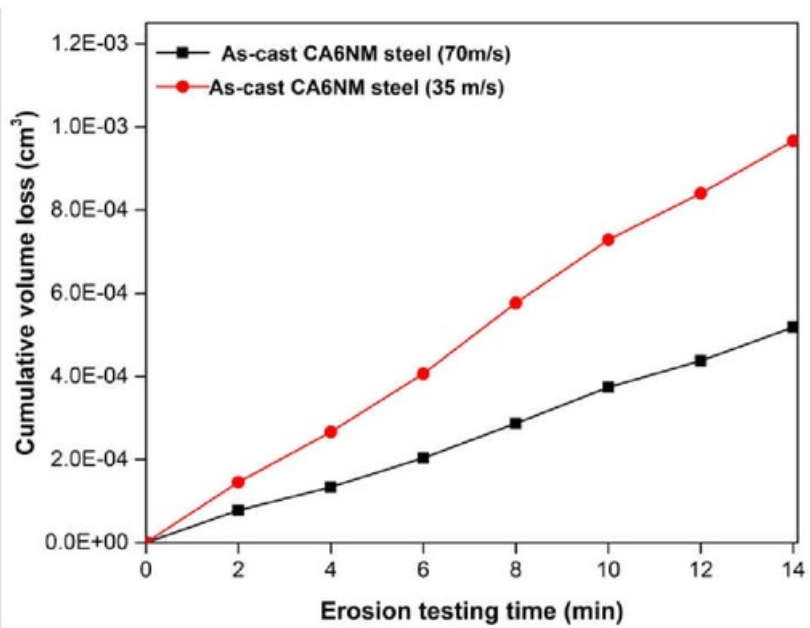


Fig. 4.9. Cumulative volume loss of as cast CA6NM steel as a function of erosion time (14 minutes) at 90° impingement angle for 35 and 70 m/s impact velocity.

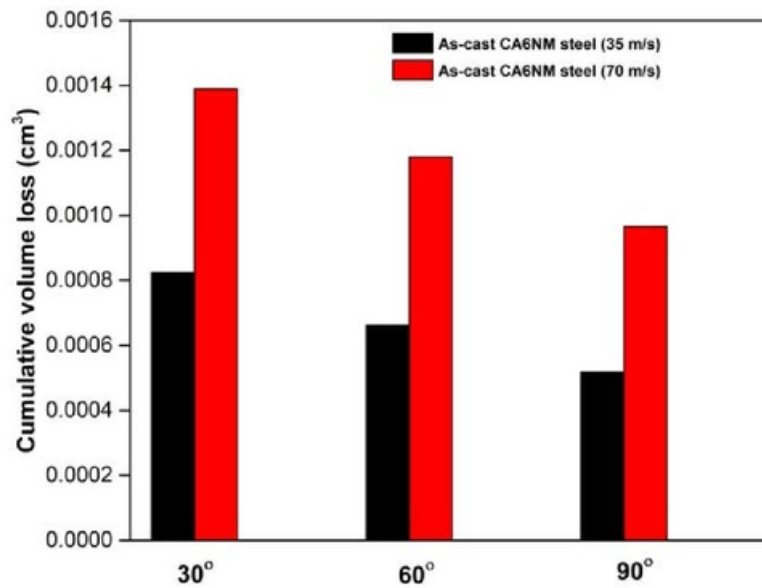


Fig. 4.10. Comparison of cumulative volume loss of as-cast CA6NM steel at 30°, 60° and 90° impingement angles for 35 and 70 m/s impact velocity.

4.2.3. Erosion mechanism and FESEM Analysis of eroded surfaces

Analysis of FESEM micrographs of eroded surface is important to understand the erosion features. FESEM micrograph of CA6NM steel before erosion is shown in Fig. 4.11. FESEM micrographs of eroded surfaces of as-cast CA6NM steel at 30° impingement angle on different location for 35 and 70 m/s impact velocity are shown in Fig. 4.12 and Fig. 4.13 respectively. In the case of 30° impingement angle, the horizontal component (shear force) of the kinetic energy of the impinging particles is higher than vertical component (normal force) [25], as shown in Fig. 4.5. Thus, the force to slide on the surface is higher than the force to penetrate the surface, and it results in the formation of lips on the surface of steel. Figure 4.12 shows the formation of lips on the surface of steel. Similar erosion features were also observed in samples eroded at 70 m/s impact velocity (Fig. 4.13). However, it was more prominent in comparison to the one observed in 35 m/s eroded samples.

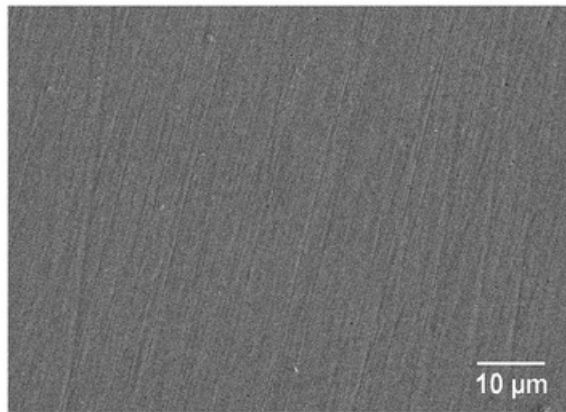


Fig. 4.11. FESEM micrograph of as-cast CA6NM steel before erosion.

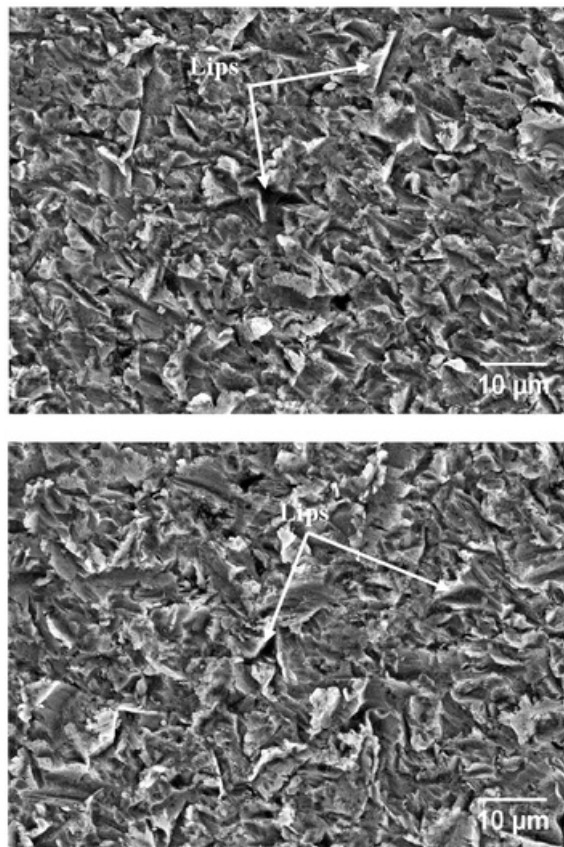


Fig. 4.12. FESEM micrographs of eroded surfaces of as-cast CA6NM steel at 30° impingement angle on different locations for 35 m/s impact velocity.

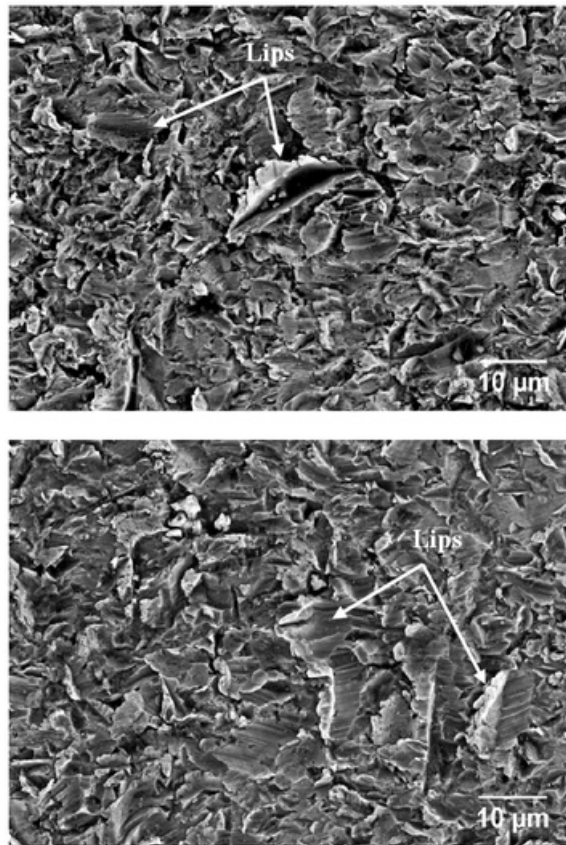


Fig. 4.13. FESEM micrographs of eroded surfaces of as-cast CA6NM steel at 30° impingement angle on different locations for 70 m/s impact velocity

Figure 4.14 and Fig. 4.15 shows the FESEM micrographs of eroded surfaces of as-cast CA6NM steel at 60° impingement angle on two different locations for 35 and 70 m/s impact velocity. For medium impingement angle (60°), the horizontal component (shear force) of the kinetic energy of the impinging particles and the vertical component (normal force) are close to equal, as shown in Fig. 4.5. The material removal mainly takes place due to combined action of cutting and extrusion, which results in the formation of lips and craters. The eroded surfaces show the formation of lips and craters. It indicates that material was removed by the combination of cutting and extrusion. However, the erosion features are less prominent in samples eroded at 35 m/s impact velocity in comparison to the sample eroded at 70 m/s impact velocity.

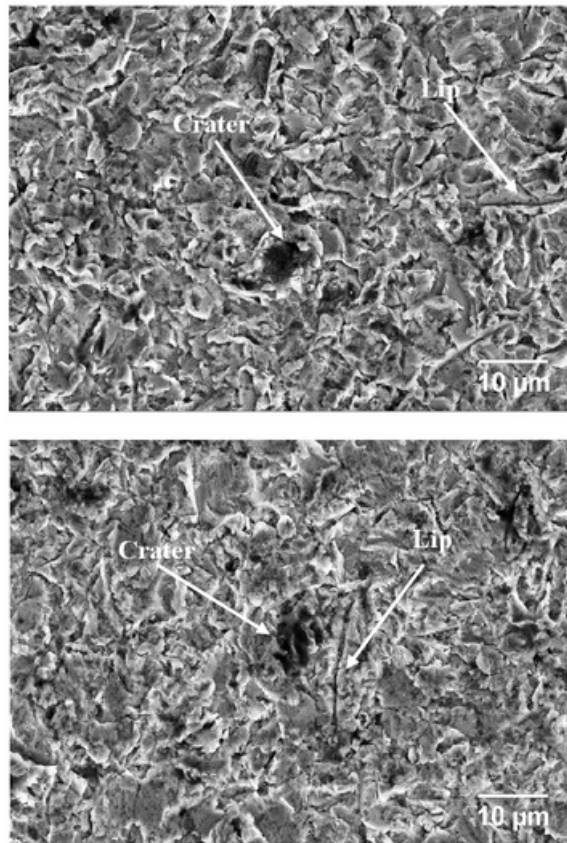


Fig. 4.14 FESEM micrographs of eroded surfaces of as-cast CA6NM steel at 60° impingement angle on different locations for 35 m/s impact velocity

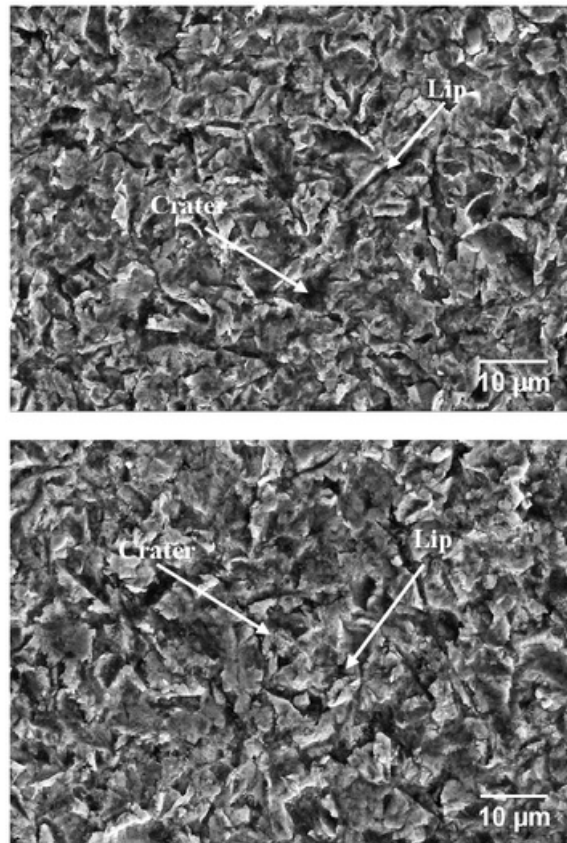


Fig. 4.15 FESEM micrographs of eroded surfaces of as-cast CA6NM steel at 60° impingement angle on different locations for 70 m/s impact velocity

FESEM micrographs of eroded surfaces of as-cast CA6NM steel at 90° impingement angle on two different locations for 35 and 70 m/s impact velocity are shown in Fig. 4.16 and Fig. 4.17 respectively. For the high impingement angle (90°), the vertical component (Normal force) of the kinetic energy is higher than horizontal component (shear force), as shown in Fig. 4.5. That provides bigger indented force and erodent penetrates into the surface resulting in the formation of craters. At 90° impingement angle, extrusion of sample takes place and formation of craters are observed in samples. However, craters are small in the case of samples eroded at 35 m/s impact velocity.

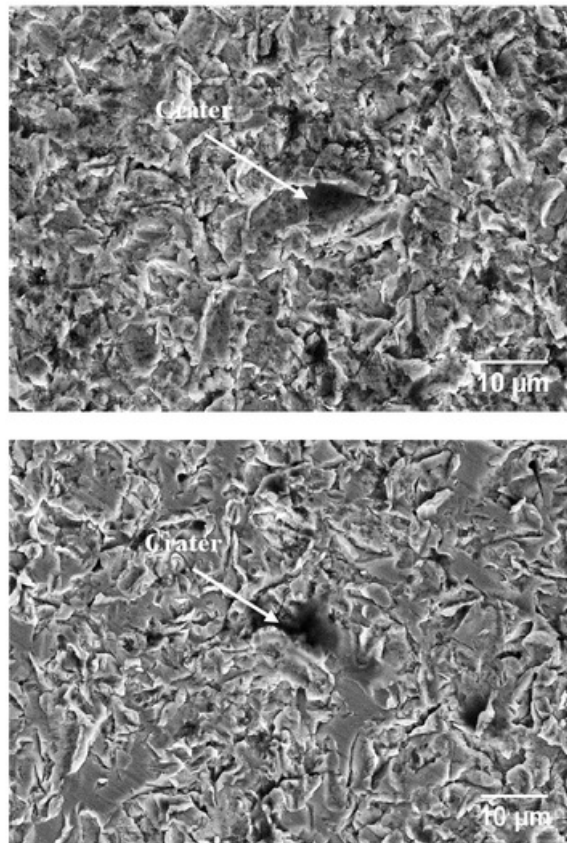


Fig. 4.16 FESEM micrographs of eroded surfaces of as-cast CA6NM steel at 90° impingement angle on different locations for 35 m/s impact velocity

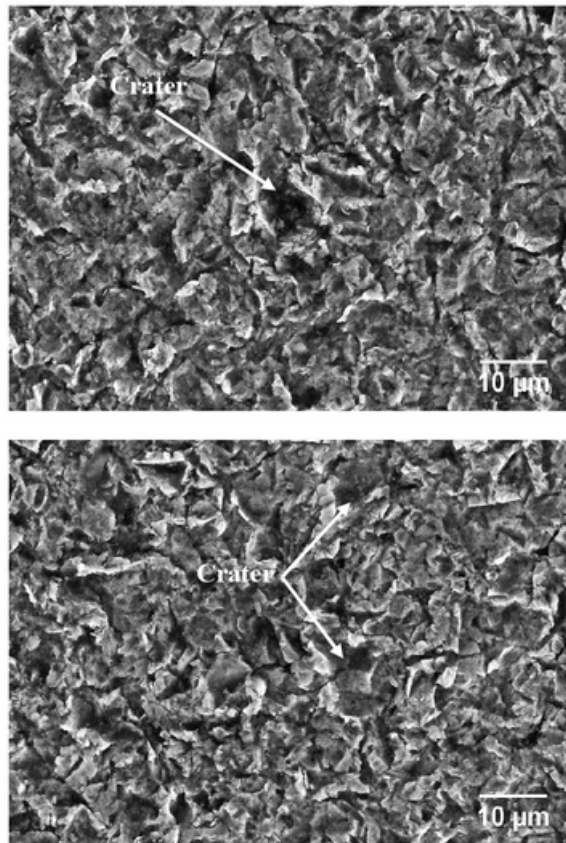


Fig. 4.17 FESEM micrographs of eroded surfaces of as-cast CA6NM steel at 90° impingement angle on different locations for 70 m/s impact velocity

FESEM micrographs taken under all the above condition shows that extensive plastic deformation has taken place on surface of steel. It is observed that in all the impingement angles erosion features are less prominent in samples eroded at 35 m/s impact velocity in comparison to that of 70 m/s. This phenomenon is mainly attributed to lower kinetic energy of erodent particles in the case of 35 m/s impact velocity

4.3. Characterization and Erosive Wear Study of HVOF Sprayed WC-10Co-4Cr Coating on CA6NM Steel

4.3.1. Feedstock powder characterization

Morphology of the WC-10Co-4Cr feedstock powder used in HVOF spraying of CA6NM steel is shown in Fig. 4.18. The morphology of feedstock powder was found to be spherical. The spherical morphology improves the feedability and sprayability of powder during spraying. The spherical morphology also reduces the moisture absorption and helps in uniform heating of powder. Feedstock powder also exhibit porous nature. The porous powders do not shatter during impact on surface, as the kinetic energy is converted into crushing the powder. This leads to homogenous and well bonded coating.

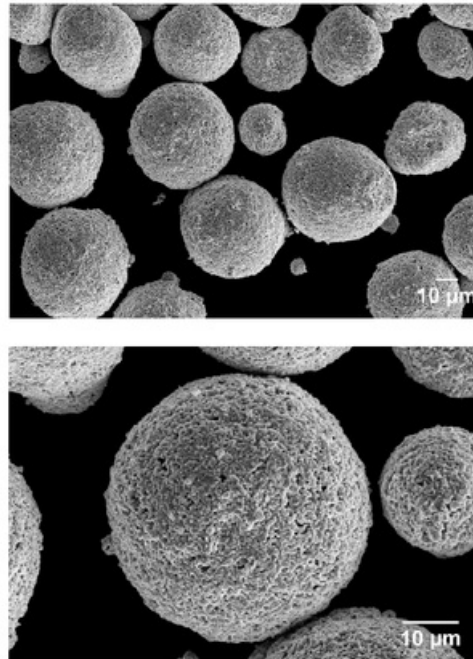


Fig. 4.18. FESEM micrograph of WC-10Co-4Cr feedstock powder used for HVOF spraying of CA6NM steel.

4.3.2. XRD Study of feedstock powder and HVOF sprayed coating

The X-ray diffraction patterns for the surface of the HVOF sprayed WC-10Co-4Cr coating and the feedstock powder is shown in Fig. 4.19. Diffraction peaks of feedstock powder

corresponds to mainly WC, with a minor peak of Co. WC was found to be primary phase, small amount of ternary carbides (Co, Cr)₃W₃C (M₆C type) are also noticed. After HVOF spraying some changes in XRD pattern has been observed. WC was found to be primary phase. A new phase W₂C is observed. This is formed due to decarburization of WC phase during spraying. Higher flame temperature and lower particle velocity during HVOF process increases the particle in-flight time, which in turn, results in decarburization of WC into W₂C [7,26]. The retention of WC retention was found to be 87.47 %.

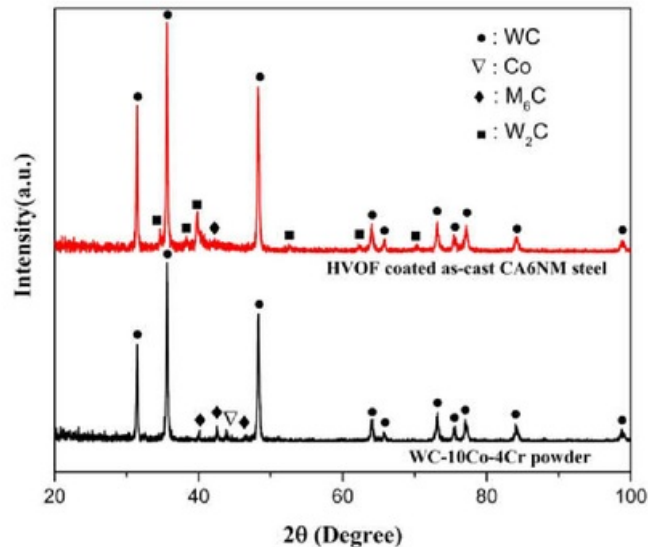


Fig. 4.19. XRD pattern of WC-10Co-4Cr feedstock powder and HVOF sprayed WC-10Co-4Cr coating on CA6NM steel.

4.3.3. Cross-sectional microstructure of HVOF sprayed coating

The cross-sectional FESEM micrograph of the HVOF sprayed WC-10Co-4Cr coating on the CA6NM steel has been shown in Fig. 4.20. At lower magnification (Fig. 4.20(a)) coating-substrate interface, coating, and the substrate can be seen clearly. It is observed that coating has a homogeneous lamellar structure which is well bonded to the substrate. The thickness, as-sprayed surface roughness and density of the coating are presented in Table 4.2 . At higher magnification (Fig. 4.20(b)) pores and interlaminar oxidation can be seen.

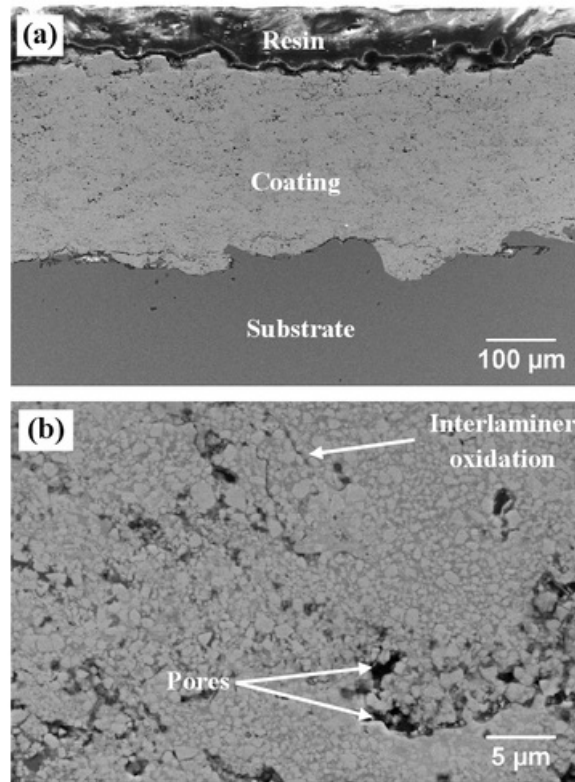


Fig. 4.20. Cross-sectional FESEM micrographs of HVOF sprayed WC-10Co-4Cr coating (a) At lower magnification, (b) At higher magnification.

Table 4.2 Thickness, as sprayed coating surface roughness, porosity and density of HVOF sprayed WC-10Co-4Cr coating on CA6NM steel

HVOF coating data	CA6NM steel
Coating Thickness (μm)	307 ± 7
As-sprayed surface roughness R_a (μm)	4.76 ± 0.40
Porosity (vol. %)	4.29 ± 0.8
Density (g/cm^3)	11.56

4.3.4. Cross-sectional micro Hardness and Indentation fracture toughness of HVOF sprayed coating

Cross-sectional microhardness and indentation fracture toughness values of HVOF sprayed

WC-10Co-4Cr coating on CA6NM steel is given in Table. 4.3. The microhardness of the coatings was measured along the depth from the coating to the substrate. The fracture toughness value was calculated at the polished cross section of the coating. It was observed that cracks are generated parallel to the coating–substrate interface, as shown in Fig. 4.21. Cracks were not observed in the perpendicular direction, which is attributed to the anisotropic behavior of coating.

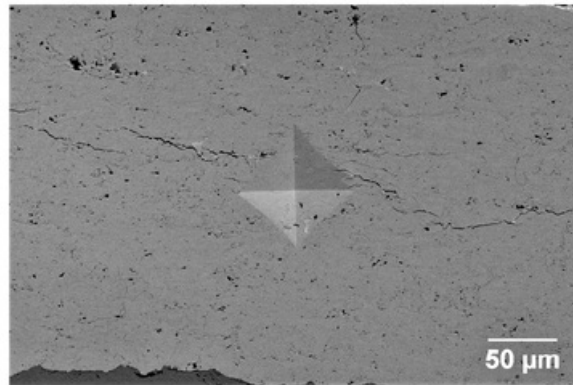


Fig. 4.21. Indentation and crack micrograph on the HVOF sprayed WC-10Co-4Cr coating cross section of CA6NM steel.

Table 4.3 Microhardness and fracture toughness of HVOF sprayed WC-10Co-4Cr coating on CA6NM steel.

	Indentation fracture toughness (MPa m ^{1/2})	Cross-sectional microhardness (HV _{0.3})
WC-10Co-4Cr coating	2.31 ± 0.19	1107 ± 41

4.3.5. Effect of HVOF sprayed WC-10Co-4Cr coating on erosion resistance of CA6NM steel substrate

Fig. 4.22 to Fig. 4.24 shows the variation in cumulative volume loss of uncoated and HVOF coated CA6NM steel as a function of erosion time (up to 14 minutes with interval of 2

minutes) at 30°, 60° and 90° impact angles respectively. It can be seen that in all the cases cumulative volume loss increases linearly with increasing the erosion time. It is also observed that HVOF sprayed WC-10Co-4Cr coating on CA6NM steel showed lower cumulative volume loss compared to uncoated steel under all the impingement angles. Comparison of cumulative volume loss of uncoated and HVOF coated CA6NM steel at 30°, 60° and 90° impingement angles for 35 and 70 m/s impact velocity is shown in Fig. 4.25. The uncoated steel showed ductile mode of erosion behaviour as highest cumulative volume loss is observed at 30° impingement angle. However, in the case of HVOF coating highest cumulative volume loss was observed at 60° impingement angle, followed by 90° and 30°. This mode is neither ductile (highest cumulative volume loss at 30°) nor brittle (highest cumulative volume loss at 90°). Hence, this behaviour was called mixed mode of erosion and it is in accordance with earlier findings. Mixed mode of erosion is mainly attributed to composite nature of coating. The hard WC particle provides brittleness and soft Co-Cr matrix gives ductile character to the coating. The percentage improvement in erosion resistance after application of HVOF coating on cast CA6NM steel is shown in Table 4.4. It is observed that there is around 44 to 72 % improvement in erosion resistance after application of HVOF coating.

Table 4.4 Improvement in erosion resistance of cast CA6NM steel at 30°, 60° and 90° impact angles after application of HVOF coating.

Sample	Process conditions	Erosion resistance improvement (%)					
		(30° angle)		(60° angle)		(90° angle)	
		35 m/s	70 m/s	35 m/s	70 m/s	35 m/s	70 m/s
Cast steel	-	-	-	-	-	-	-
HVOF	Cast steel + HVOF sprayed WC-10Co-4Cr coating	72%	70%	46%	44%	45%	44%

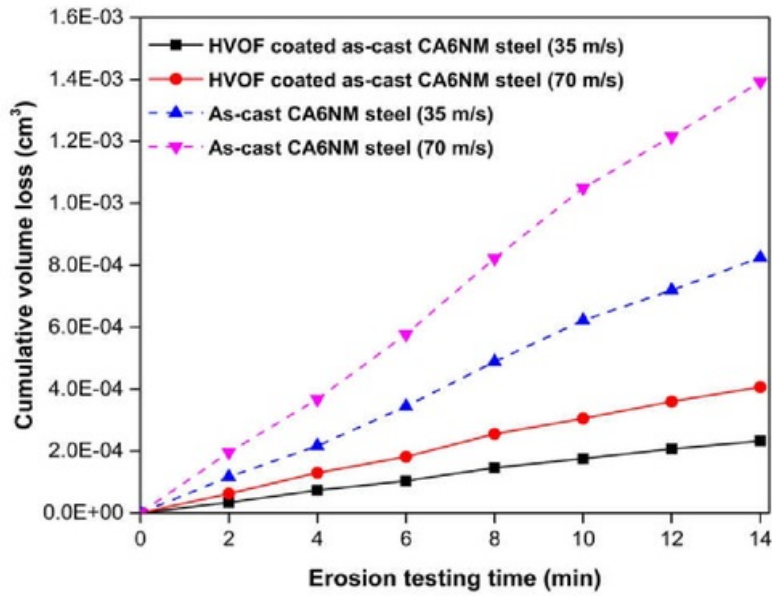


Fig. 4.22. Cumulative volume loss of as cast CA6NM steel and HVOF coated steel as a function of erosion time (14 minutes) at 30° impingement angle for 35 and 70 m/s impact velocity.

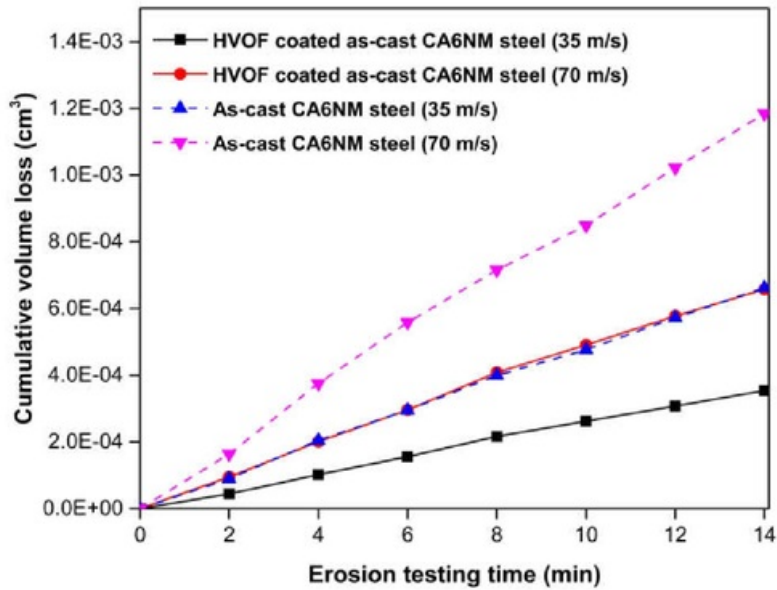


Fig. 4.23. Cumulative volume loss of as cast CA6NM steel and HVOF coated steel as a function of erosion time (14 minutes) at 60° impingement angle for 35 and 70 m/s impact velocity.

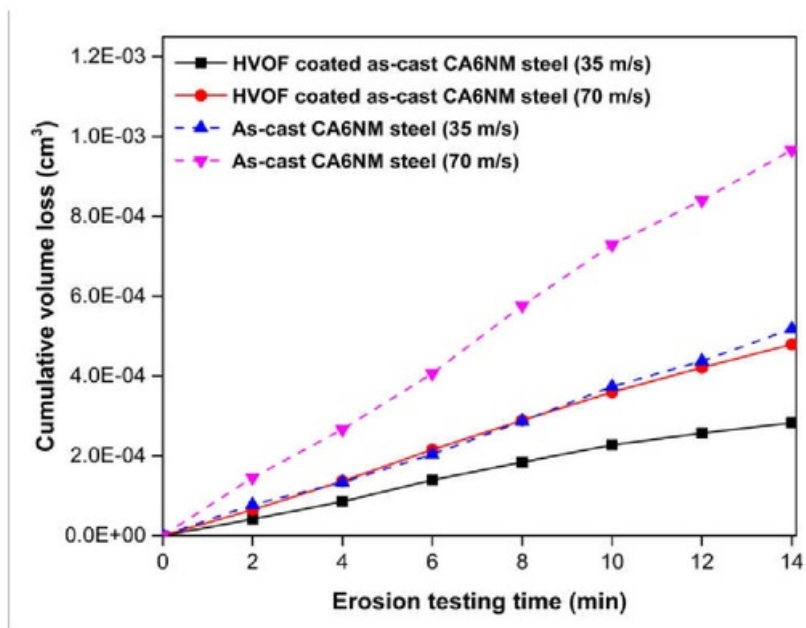


Fig. 4.24. Cumulative volume loss of as cast CA6NM steel and HVOF coated steel as a function of erosion time (14 minutes) at 90° impingement angle for 35 and 70 m/s impact velocity.

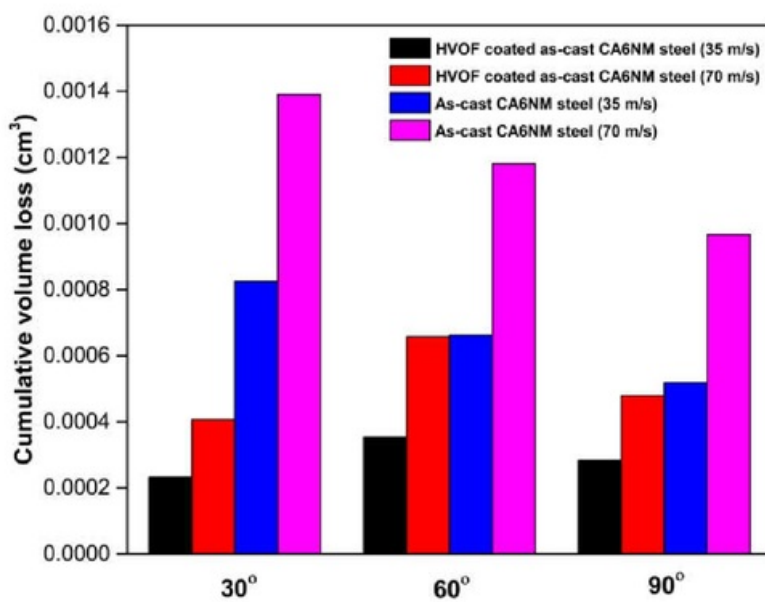


Fig. 4.25. Comparison of cumulative volume loss of as-cast CA6NM steel and HVOF coated steel at 30°, 60° and 90° impingement angles for 35 and 70 m/s impact velocity.

4.3.6. Analysis of eroded HVOF sprayed coating surface

The FESEM micrographs of eroded surfaces of HVOF coated CA6NM steel substrate at 30° impingement angle on different locations for 35 and 70 m/s impact velocity are shown in Fig. 4.26 and Fig. 4.27. It was observed that material removal took place by micro cutting and microploughing, same is observed by several researchers [28,30]. Removal of splats is also noticed, which is mainly due to large tangential force acting on the splats due to the impinging particle striking at a low impact angle, which resulted in the detachment of the splats. However, samples eroded at 70 m/s impact velocity (Fig. 4.27) shows severe erosion features in comparison to the samples eroded at 35 m/s (Fig. 4.26).

The FESEM micrographs of eroded surfaces of HVOF coated CA6NM steel substrate at 60° impingement angle on different location for 35 and 70 m/s impact velocity are shown in Fig. 4.28 and Fig. 4.29. In the case of 60° impingement angle, material removal takes place due to the mixed mode of micro cutting and removal of a single grain of WC [31]. The lips and craters can be seen in HVOF coated steel eroded at 35 m/s (Fig. 4.28). The FESEM micrograph of HVOF coated CA6NM steel eroded at 70 m/s also show the lips and craters (Fig. 4.29). However, it is more severe than 35 m/s sample.

The FESEM micrographs of eroded surfaces of HVOF coated CA6NM steel substrate at 90° impingement angle on different location for 35 and 70 m/s impact velocity are shown in Fig. 4.30 and Fig. 4.31. At high impact angle, material removal took place by removal of a single grain of WC. Impinging erodent particle removes the binder phase from the surface and it results into the accumulation of plastic strain in WC particles and eventually cracks are generated in-between WC grains, which results in the removal of single WC particle [32]. Samples eroded at 70 m/s show severe erosion features in comparison to the one eroded at 35 m/s.

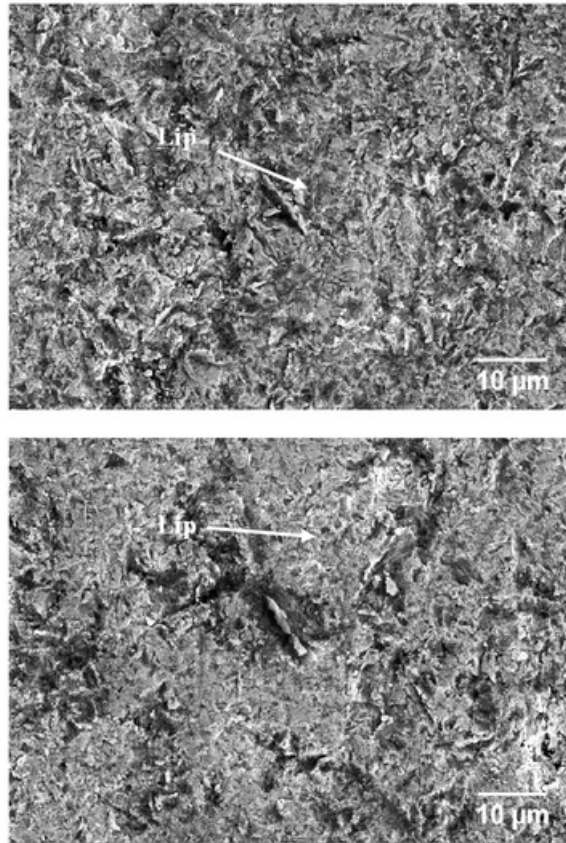


Fig. 4.26. FESEM micrograph of eroded surface of HVOF coating at 30° impingement angle on different locations for 35 m/s impact velocity

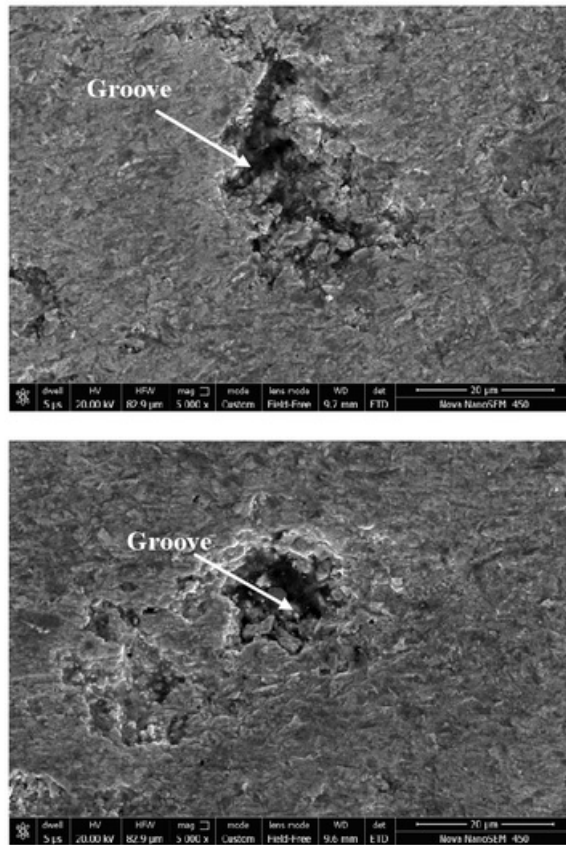


Fig. 4.27. FESEM micrograph of eroded surface of HVOF coating at 30° impingement angle on different locations for 70 m/s impact velocity

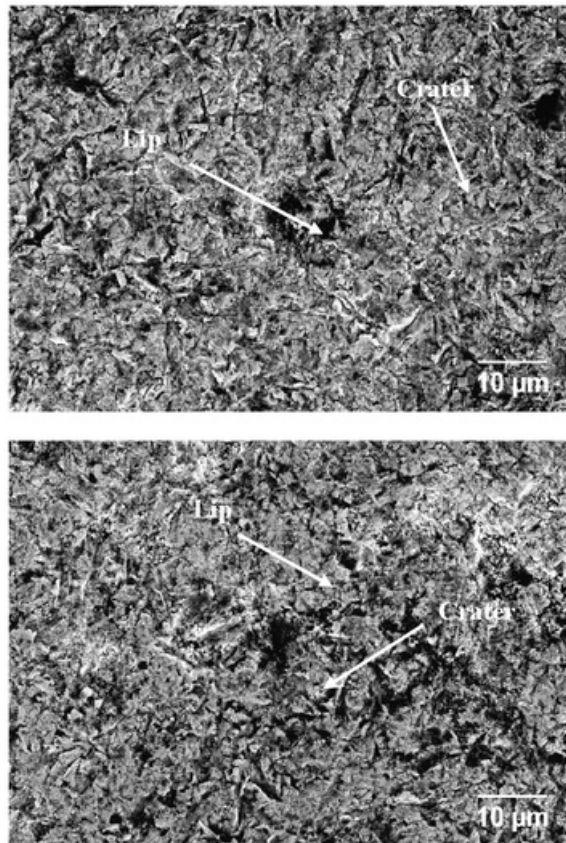


Fig. 4.28. FESEM micrograph of eroded surface of HVOF coating at 60° impingement angle on different locations for 35 m/s impact velocity

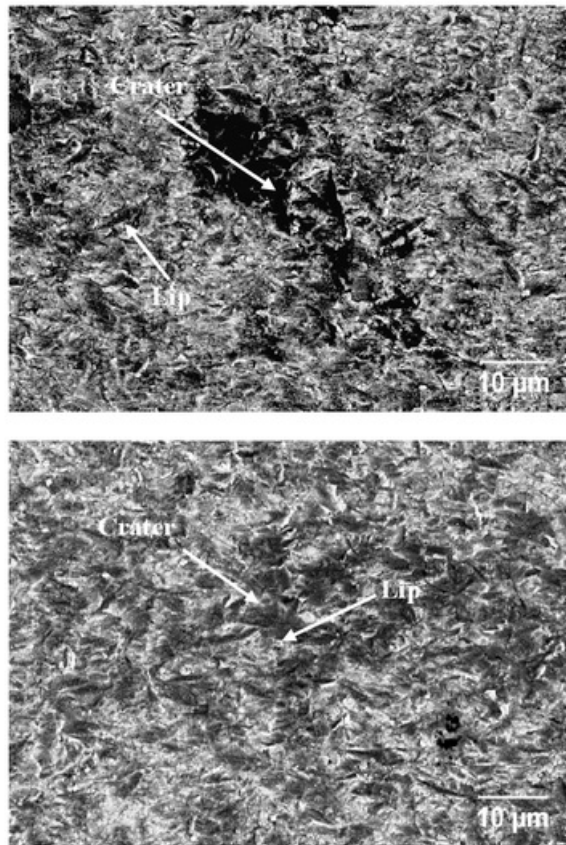


Fig. 4.29. FESEM micrograph of eroded surface of HVOF coating at 60° impingement angle on different locations for 70 m/s impact velocity

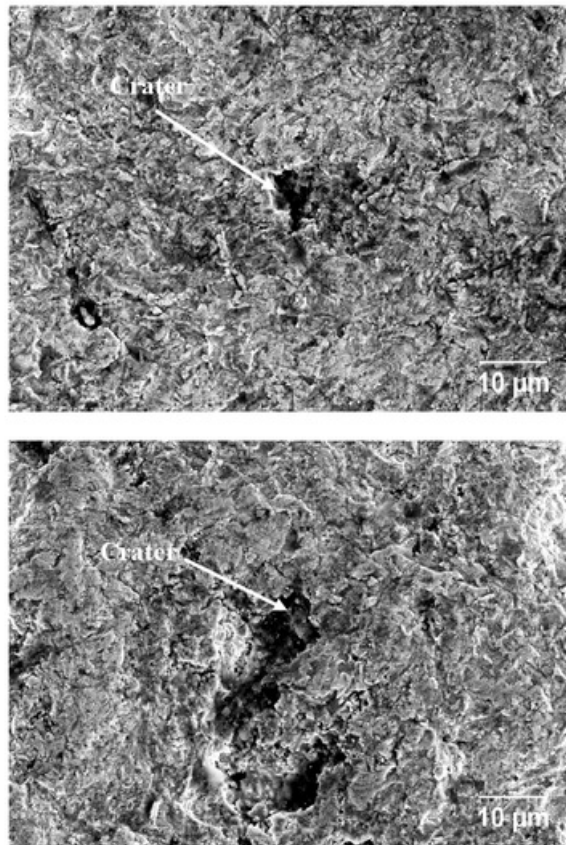


Fig. 4.30. FESEM micrograph of eroded surface of HVOF coating at 90° impingement angle on different locations for 35 m/s impact velocity

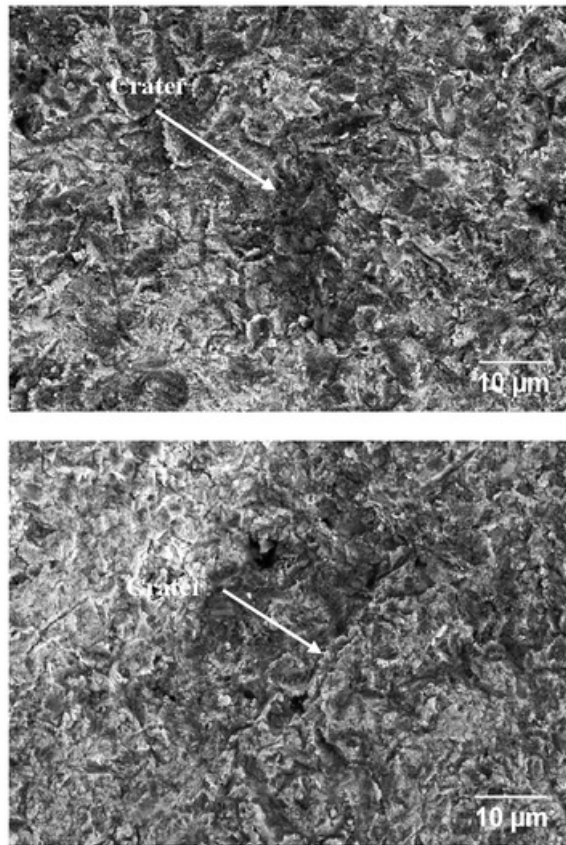


Fig. 4.31. FESEM micrograph of eroded surface of HVOF coating at 90° impingement angle on different locations for 70 m/s impact velocity

4.4. Characterization and Erosive Wear Study of HVOF Sprayed WC-10Co-4Cr Coating on CA6NM Steel

4.4.1. Feedstock powder characterization

The morphology of the feedstock powder used in HVOF spraying is shown in Fig. 4.32. The morphology of feedstock powder was found to be spherical, which provides excellent fluidity and stability during spraying. Powder also possesses porous nature, which helps in uniform coating.

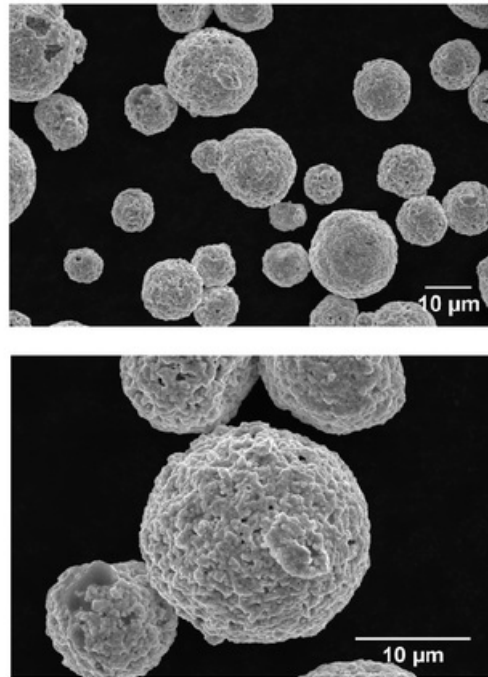


Fig. 4.32. Morphology of WC-10Co-4Cr feedstock powder used in HVOF spraying

4.4.2. XRD Study of feedstock powder and HVOF sprayed coating

The X-ray diffraction patterns for the surface of the HVOF sprayed WC-10Co-4Cr coating and the feedstock powder is shown in Fig. 4.33. There is no significant difference observed between the diffraction pattern of the feedstock powder and that of the coating [33], both the powder and coating contained WC as the primary phase. Traces of $\text{Co}_3\text{W}_3\text{C}$ and Co phases were also noticed. Traces of W_2C phase is also observed in HVOF sprayed coating, which indicates that there is very little or negligible decarburization in the coating. In HVOF

coating, higher particle velocity and lower particle temperature during spraying are the main factors which result in a lower degree of decarburization [34,35]. The retention of WC retention was found to be 96.00 %.

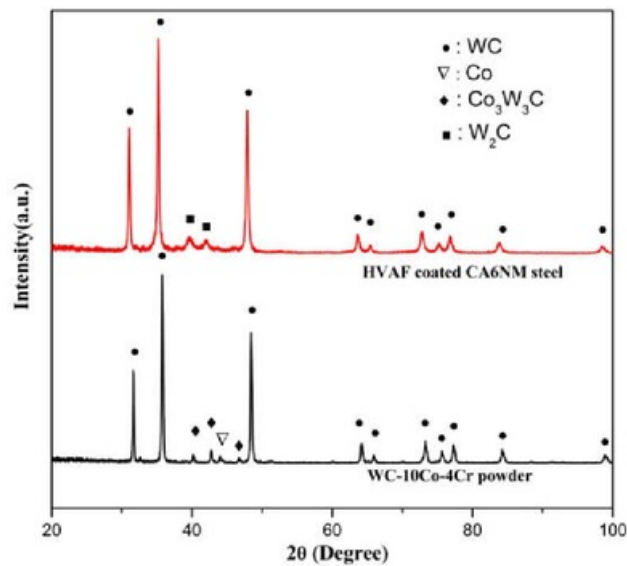


Fig. 4.33. XRD pattern of feedstock powder and HVOF sprayed WC-10Co-4Cr coating on CA6NM steel

4.4.3. Cross-sectional microstructure of HVOF sprayed coating

The cross-sectional FESEM micrograph of the HVOF sprayed WC-10Co-4Cr coating on the CA6NM steel has been shown in Fig. 4.34. Even at lower magnification (Fig. 4.34(a)), coating-substrate interface, coating, and the substrate can be seen clearly. It is observed that coating has a homogeneous structure, which is dense and well bonded to the substrate. At higher magnification, (Fig. 4.34(b)) porosity present in the coating can be observed. It is also observed that WC grains appear blocky in shape without any deformation and dissolution. Therefore, it can be inferred that the Co-Cr metallic binder was wholly or partially melted, while the WC-particles mostly remained in the solid state during spraying. This clearly indicates that very little decomposition of WC has taken place during spraying. Unlike HVOF sprayed WC-10Co-4Cr coating, no lamellar morphology is observed in HVOF sprayed

coating, which indicates that less decarburization of WC has taken place. Although minute pores are visible in the coating, it is less porous than HVOF sprayed WC-10Co-4Cr coatings. The reason being for this is shorter particle residence time in the HVOF jet, which lowers the oxidation of particles. The thickness, as-sprayed surface roughness, porosity and density of the coating are presented in Table 4.5.

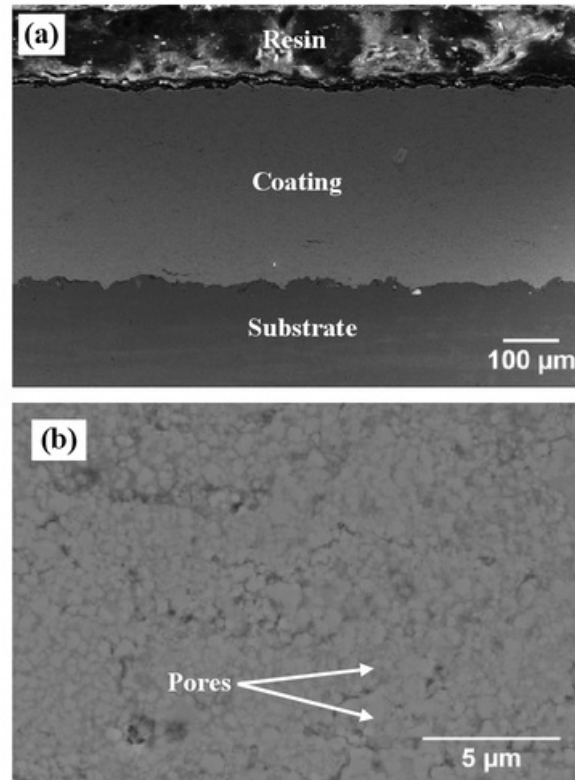


Fig. 4.34. Cross-sectional FESEM micrographs of HVOF coated CA6NM steel (a) At lower magnification, (b) At higher magnification

4.4.4. Cross-sectional micro hardness and fracture toughness of HVOF sprayed coating

The average and the standard deviation value of indentation fracture toughness, cross-sectional microhardness, and surface roughness Ra values of investigated samples are reported in Table 4.6. The fracture toughness value was calculated at the polished cross

Table 4.5 Thickness, as sprayed coating surface roughness, porosity and density of HVOF sprayed WC-10Co-4Cr coating on CA6NM steel

HVOF coating data	CA6NM steel
Coating Thickness (μm)	341 ± 6
As-sprayed surface roughness Ra (μm)	2.61 ± 0.42
Porosity (vol. %)	0.98 ± 0.25
Density (g/cm^3)	13.53

section of the coating. It was observed that cracks are generated parallel to the coating–substrate interface, as shown in Fig. 4.35. Cracks were not observed in the perpendicular direction which attributed to the anisotropic behavior of coating. The microhardness of the coatings was also measured along the depth from the coating to the substrate. The microhardness values of coating were found to be in the range of 1285–1352 Hv. It was observed that microhardness value oscillates in a narrow range (1285–1352), which is mainly due to low porosity and uniform microstructure of the coating. Surface roughness for coated and uncoated steel after polishing are measured before starting erosion testing, to provide a uniform initial condition for erosion.

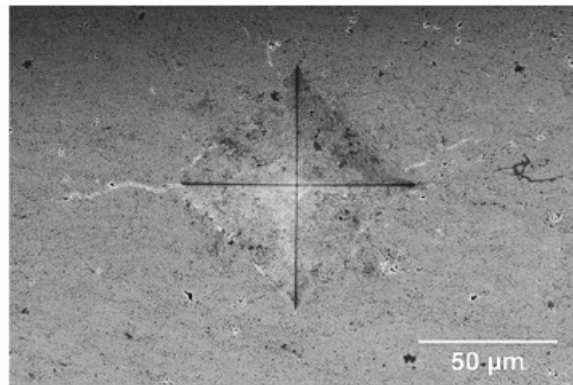


Fig. 4.35. Indentation and crack micrograph on the HVOF sprayed WC-10Co-4Cr coating cross section of CA6NM steel.

4.4.5. Effect of HVOF sprayed WC-10Co-4Cr coating on solid particle erosion resistance of CA6NM steel

Cumulative volume loss of HVOF coated CA6NM steel as a function of erosion time (up to 14 minutes with interval of 2 minutes) at 30°, 60° and 90° impact angles for 35 and 70 m/s impact velocity is shown in Fig. 4.36 to Fig. 4.38 respectively. It can be seen that in all the

Table 4.6 Microhardness and fracture toughness of HVOF sprayed WC-10Co-4Cr coating on CA6NM steel.

	Indentation fracture toughness (MPa m ^{1/2})	Cross-sectional microhardness (HV _{0.3})
WC-10Co-4Cr coating	6.60 ± 0.21	1327 ± 26

cases cumulative volume loss increases linearly with increasing the erosion time. From all the figures, it is observed that coated steel shows better erosion resistance than uncoated steel. Figure 4.39 shows the comparison of cumulative volume loss of uncoated and HVOF coated CA6NM steel at 30°, 60° and 90° impingement angles for 35 and 70 m/s impact velocity. The uncoated steel exhibit the ductile mode of erosion because the volumetric erosion rate continuously decreases with increasing impact angle and reaches a minimum at 90°. HVOF coating on the other hand showed the mixed mode of ductile and brittle erosion. The reason being that volumetric steady-state erosion rate is maximum at 60° impact angle, then decreases at 90° and 30° impact angle. The improvement in erosion rate of cast CA6NM steel after HVOF coating is given in Table 4.7. It is observed that there is around 65 to 84 % improvement in erosion resistance after application of HVOF coating.

Table 4.7 Improvement in erosion resistance of cast CA6NM steel at 30°, 60° and 90° impact angles after application of HVOF coating.

Sample	Process conditions	Erosion resistance improvement (%)					
		(30° angle)		(60° angle)		(90° angle)	
		35 m/s	70 m/s	35 m/s	70 m/s	35 m/s	70 m/s
Cast steel	-	-	-	-	-	-	-
HVOF	Cast steel + HVOF sprayed WC-10Co-4Cr coating	84%	83%	67%	67%	65%	67%

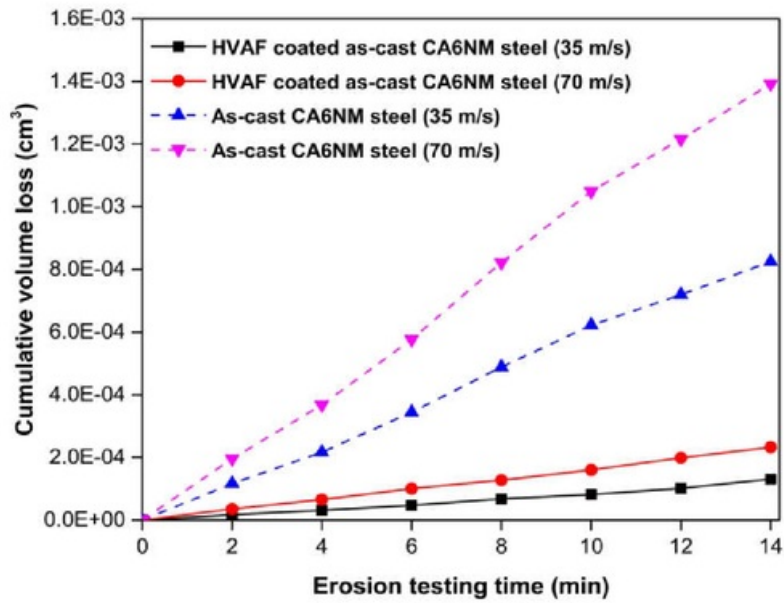


Fig. 4.36. Cumulative volume loss of as cast CA6NM steel and HVOF coated steel as a function of erosion time (14 minutes) at 30° impingement angle for 35 and 70 m/s impact velocity.

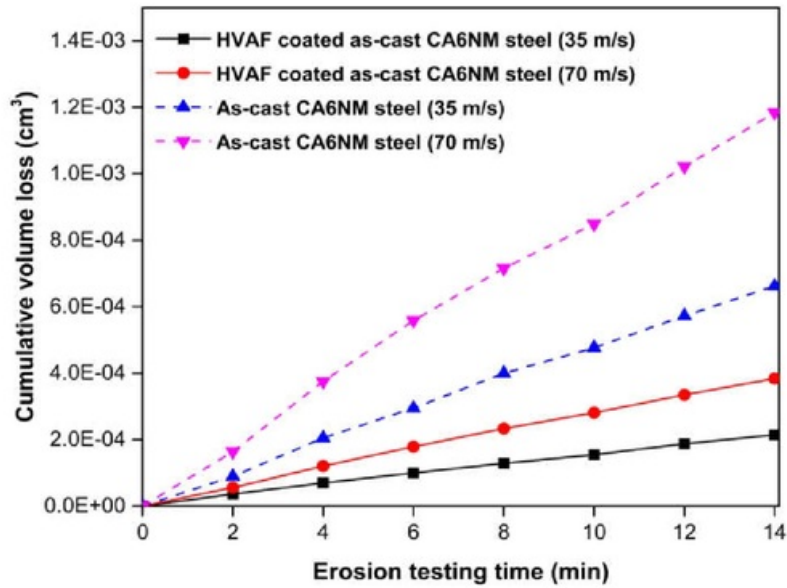


Fig. 4.37. Cumulative volume loss of as cast CA6NM steel and HVOF coated steel as a function of erosion time (14 minutes) at 60° impingement angle for 35 and 70 m/s impact velocity.

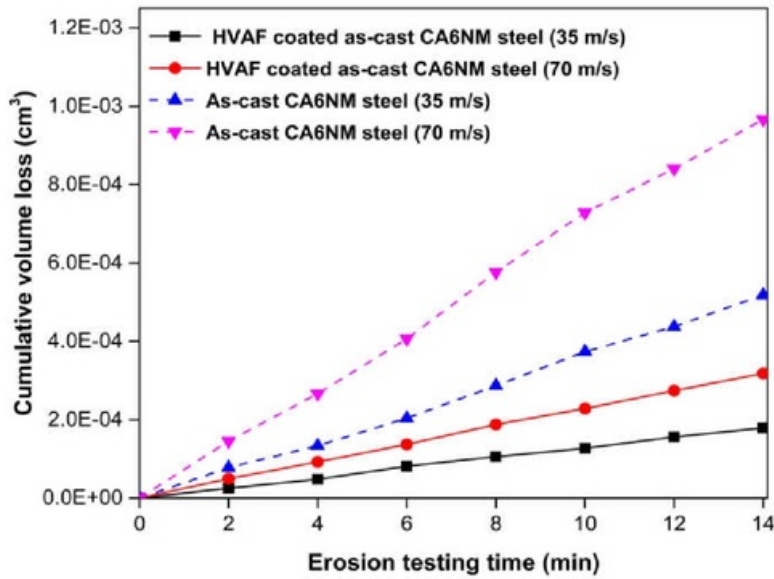


Fig. 4.38. Cumulative volume loss of as cast CA6NM steel and HVOF coated steel as a function of erosion time (14 minutes) at 90° impingement angle for 35 and 70 m/s impact velocity.

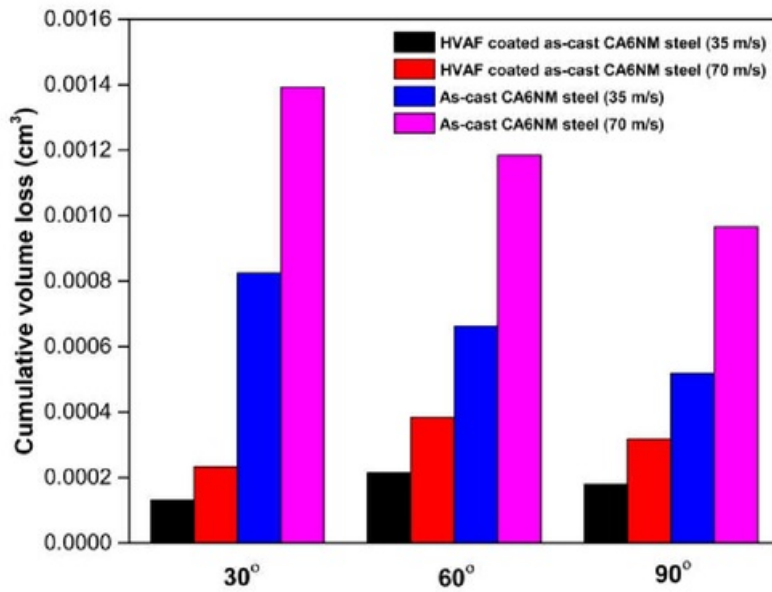


Fig. 4.39. Comparison of cumulative volume loss of as-cast CA6NM steel and HVOF coated steel at 30°, 60° and 90° impingement angles for 35 and 70 m/s impact velocity.

4.4.6. Analysis of steady state eroded HVAF sprayed coating surface

The FESEM micrographs of eroded surfaces of HVAF coated as cast CA6NM steel at 30° impingement angle for 35 and 70 m/s impact velocity are shown in Fig. 4.40 and Fig. 4.41. It is observed that coating is mainly removed by cutting and ploughing action. HVAF coating eroded at 70 m/s impact velocity shows large ploughs and lips (Fig. 4.41) compared to HVAF coating eroded at 35 m/s impact velocity (Fig. 4.40).

The FESEM micrographs of eroded surfaces of HVAF coated as cast CA6NM steel at 60° impingement angle for 35 and 70 m/s impact velocity are shown in Fig. 4.42 and Fig. 4.43. It is observed that coating is removed by the ploughing and removal of single grain of WC. The erosion features observed in samples eroded at 70 m/s is more severe than one observed at 35 m/s.

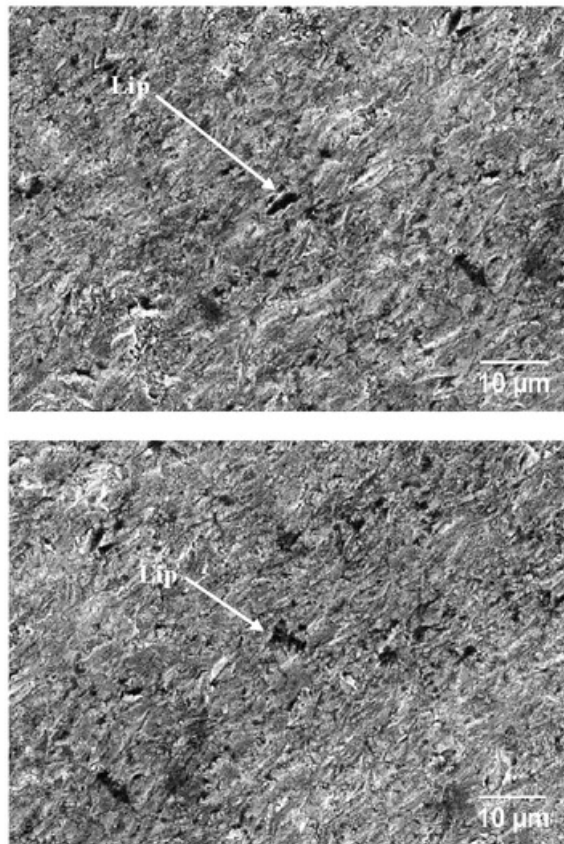


Fig. 4.40. FESEM micrograph of eroded surface of HVAF coating at 30° impingement angle on different locations for 35 m/s impact velocity

Fig. 4.44 and Fig. 4.45 shows the FESEM micrographs of the eroded surfaces of HVAF coated as cast CA6NM steel at 90° impingement angle for 35 and 70 m/s impact velocity. Eroded surface of HVAF coated steel revealed the large numbers of craters formed mainly due to removal of single grain of WC.

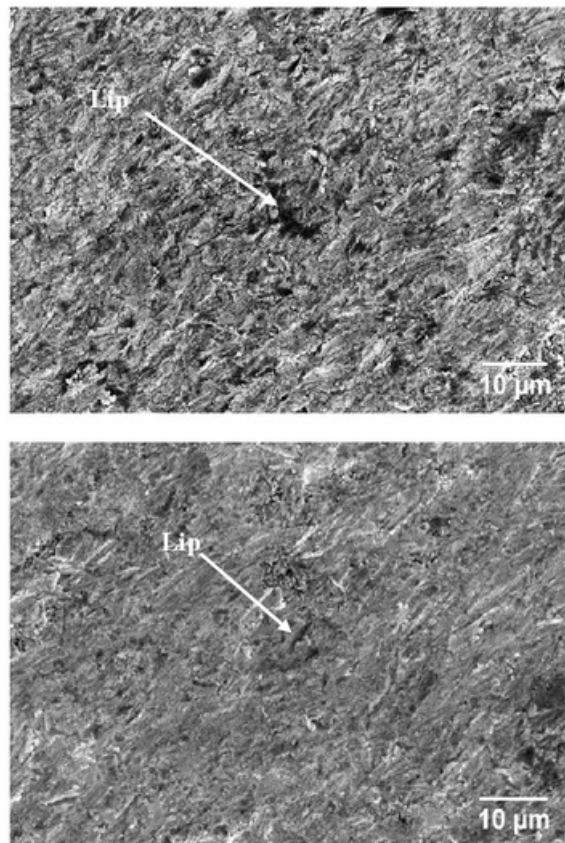


Fig. 4.41. FESEM micrograph of eroded surface of HVAF coating at 30° impingement angle on different locations for 70 m/s impact velocity

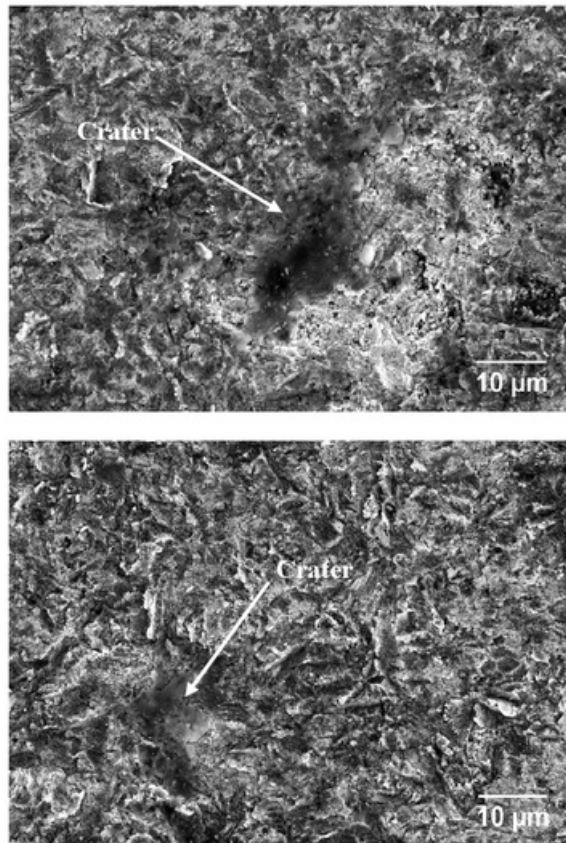


Fig. 4.42. FESEM micrograph of eroded surface of HVOF coating at 60° impingement angle on different locations for 35 m/s impact velocity

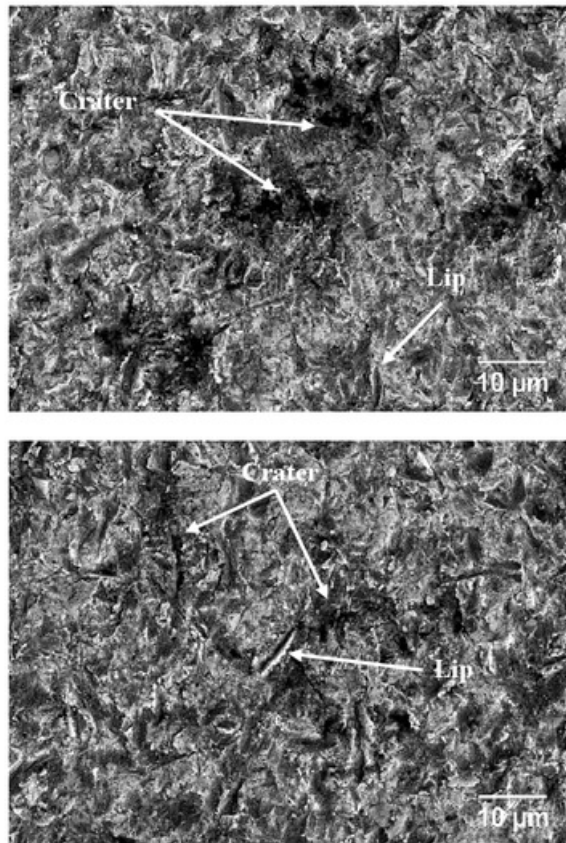


Fig. 4.43. FESEM micrograph of eroded surface of HVOF coating at 60° impingement angle on different locations for 70 m/s impact velocity

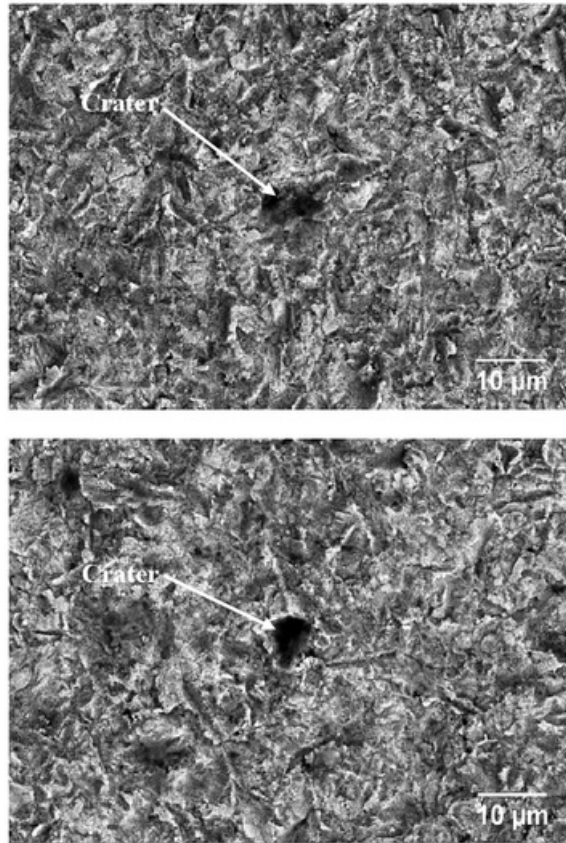


Fig. 4.44. FESEM micrograph of eroded surface of HVOF coating at 90° impingement angle on different locations for 35 m/s impact velocity

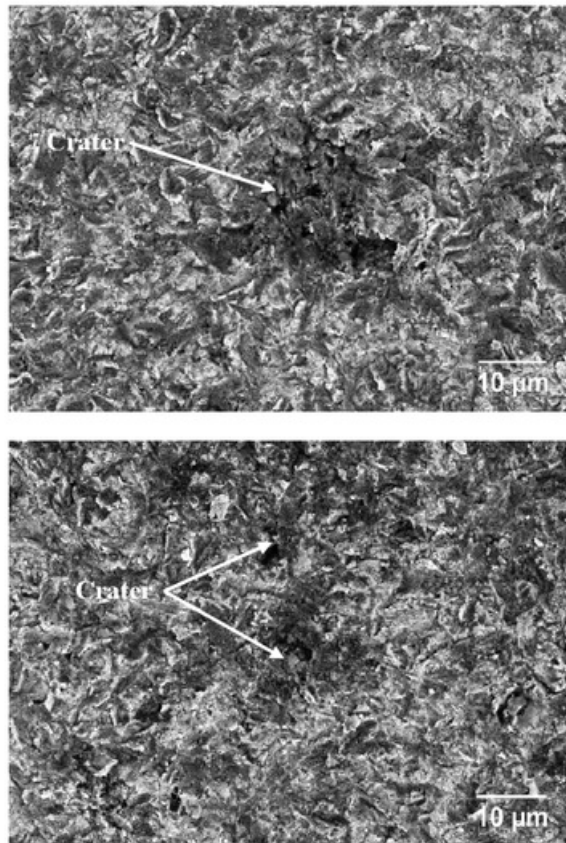


Fig. 4.45. FESEM micrograph of eroded surface of HVOF coating at 90° impingement angle on different locations for 70 m/s impact velocity

CHAPTER 5

Conclusions and Suggestions for Future Work

The conclusions of the experimental work performed in this study and suggestions for future work are presented in this chapter.

5.1. Conclusions

The important conclusions drawn from the present investigation are divided into three parts and they are as follows:

(i) Cast CA6NM steel:

1. CA6NM steel shows lath martensite with delta ferrite as a secondary phase.
2. Maximum cumulative volume loss in the case of CA6NM steel was observed at 30° impingement angle followed by 60° and 90°, which points to the fact that material has eroded in ductile manner.
3. It was also observed that cumulative volume loss at 30°, 60° and 90° impingement angles for 35 m/s impact velocity is lower than that observed at 70 m/s impact velocity, which is mainly due to the higher kinetic energy of impacting particles at higher impact velocity.

(ii) HVOF sprayed WC-10Co-4Cr coating on CA6NM steel:

1. The XRD analysis of surface of HVOF sprayed WC-10Co-4Cr coating revealed that considerable amount of decarburization of WC into W₂C has taken place. WC retention was found to be 87.47 %.
2. The polished cross-sectional microstructure of HVOF sprayed WC-10Co-4Cr coating showed a homogeneous and well-bonded coating with laminar structure.
3. The fracture toughness of coating was found to be on lower side due to presence of porosity in coating.
4. Application of HVOF coating significantly improved the erosion resistance of CA6NM steel. Higher cumulative volume loss is observed at 35 m/s impact velocity in comparison to 70 m/s impact velocity.

5. Maximum cumulative volume loss was observed at 60° impingement angle followed by 90° and 30, which points to fact that material has eroded in mixed mode (ductile & brittle).
6. After the application of HVOF coating 44 to 72 % improvement in erosion resistance was observed in uncoated steel.

(iii) HVAF sprayed WC-10Co-4Cr coating on CA6NM steel:

1. The XRD analysis of surface of HVAF sprayed WC-10Co-4Cr coating revealed that very little amount of decarburization of WC into W₂C has taken place. WC retention was found to be 96.00 %.
2. The polished cross-sectional microstructure of HVAF sprayed WC-10Co-4Cr coating shows a homogeneous, well-bonded structure with low porosity.
3. The fracture toughness of coating was found to be higher side which is due to lower porosity,
4. The HVAF-sprayed WC-10Co-4Cr coating enhanced the erosion resistance of the CA6NM steel. This may be attributed to its higher hardness of coating as compared to the uncoated steel.
5. Higher cumulative volume loss is observed at 70m/s impact velocity in comparison to 35 m/s impact velocity. This is attributed to the higher kinetic energy of erodent in the case of 70m/s impact velocity.
6. The percentage improvement in erosion resistance after application of HVAF coating on CA6NM steel is higher than HVOF coating.
7. After the application of HVAF coating 65 to 84 % improvement in erosion resistance was observed in uncoated steel.

APPENDICES

Appendix I

(Solid particle erosion experimental data of uncoated CAGNM steel substrate)

(i) Cumulative volume loss at 30° impact angle

Test duration (min)	35 m/s Impact velocity			70 m/s Impact velocity		
	Wt. loss (mg)	Vol. loss (cm ³)	Cum. Vol. loss (cm ³)	Wt. loss (mg)	Vol. loss (cm ³)	Cum. Vol. loss (cm ³)
2	0.9	0.0001169	1.17E-04	1.51	0.000196104	1.96E-04
4	0.77	0.0001	2.17E-04	1.32	0.000171429	3.68E-04
6	0.98	0.0001273	3.44E-04	1.61	0.000209091	5.77E-04
8	1.11	0.0001442	4.88E-04	1.89	0.000245455	8.22E-04
10	1.03	0.0001338	6.22E-04	1.75	0.000227273	1.05E-03
12	0.75	9.74E-05	7.19E-04	1.28	0.000166234	1.22E-03
14	0.81	0.0001052	8.25E-04	1.36	0.000176623	1.39E-03

(ii) Cumulative volume loss at 60° impact angle

Test duration (min)	35 m/s Impact velocity			70 m/s Impact velocity		
	Wt. loss (mg)	Vol. loss (cm ³)	Cum. Vol. loss (cm ³)	Wt. loss (mg)	Vol. loss (cm ³)	Cum. Vol. loss (cm ³)
2	0.69	8.961E-05	8.96E-05	1.26	0.0001636	1.64E-04
4	0.89	0.0001156	2.05E-04	1.63	0.0002117	3.75E-04
6	0.69	8.961E-05	2.95E-04	1.41	0.0001831	5.58E-04
8	0.81	0.0001052	4.00E-04	1.21	0.0001571	7.16E-04
10	0.59	7.662E-05	4.77E-04	1.03	0.0001338	8.49E-04
12	0.74	9.61E-05	5.73E-04	1.33	0.0001727	1.02E-03
14	0.69	8.961E-05	6.62E-04	1.25	0.0001623	1.18E-03

(iii) Cumulative volume loss at 90° impact angle

Test duration (min)	35 m/s Impact velocity			70 m/s Impact velocity		
	Wt. loss (mg)	Vol. loss (cm ³)	Cum. Vol. loss (cm ³)	Wt. loss (mg)	Vol. loss (cm ³)	Cum. Vol. loss (cm ³)
2	0.6	7.79221E-05	7.79E-05	1.12	0.0001455	1.45E-04
4	0.43	5.58442E-05	1.34E-04	0.93	0.0001208	2.66E-04
6	0.54	7.01299E-05	2.04E-04	1.08	0.0001403	4.06E-04
8	0.64	8.31169E-05	2.87E-04	1.31	0.0001701	5.77E-04
10	0.67	8.7013E-05	3.74E-04	1.17	0.0001519	7.29E-04
12	0.49	6.36364E-05	4.38E-04	0.86	0.0001117	8.40E-04
14	0.62	8.05195E-05	5.18E-04	0.97	0.000126	9.66E-04

Appendix II

(Solid particle erosion experimental data of HVOF coated CA6NM steel substrate)

(iv) Cumulative volume loss at 30° impact angle

Test duration (min)	35 m/s Impact velocity			70 m/s Impact velocity		
	Wt. loss (mg)	Vol. loss (cm ³)	Cum. Vol. loss (cm ³)	Wt. loss (mg)	Vol. loss (cm ³)	Cum. Vol. loss (cm ³)
2	0.39	3.37E-05	3.37E-05	0.72	6.23E-05	6.23E-05
4	0.46	3.98E-05	7.35E-05	0.78	6.75E-05	1.30E-04
6	0.35	3.03E-05	1.04E-04	0.6	5.19E-05	1.82E-04
8	0.49	4.24E-05	1.46E-04	0.85	7.35E-05	2.55E-04
10	0.34	2.94E-05	1.76E-04	0.58	5.02E-05	3.05E-04
12	0.36	3.11E-05	2.07E-04	0.63	5.45E-05	3.60E-04
14	0.3	2.59E-05	2.33E-04	0.54	4.67E-05	4.07E-04

(v) Cumulative volume loss at 60° impact angle

Test duration (min)	35 m/s Impact velocity			70 m/s Impact velocity		
	Wt. loss (mg)	Vol. loss (cm ³)	Cum. Vol. loss (cm ³)	Wt. loss (mg)	Vol. loss (cm ³)	Cum. Vol. loss (cm ³)
2	0.51	4.41E-05	4.41E-05	1.1	9.52E-05	9.52E-05
4	0.67	5.80E-05	1.02E-04	1.22	1.06E-04	2.01E-04
6	0.62	5.36E-05	1.56E-04	1.1	9.52E-05	2.96E-04
8	0.7	6.06E-05	2.16E-04	1.3	1.12E-04	4.08E-04
10	0.53	4.58E-05	2.62E-04	0.95	8.22E-05	4.90E-04
12	0.52	4.50E-05	3.07E-04	1.01	8.74E-05	5.78E-04
14	0.54	4.67E-05	3.54E-04	0.92	7.95E-05	6.57E-04

7

(vi) Cumulative volume loss at 90° impact angle

Test duration (min)	35 m/s Impact velocity			70 m/s Impact velocity		
	Wt. loss (mg)	Vol. loss (cm ³)	Cum. Vol. loss (cm ³)	Wt. loss (mg)	Vol. loss (cm ³)	Cum. Vol. loss (cm ³)
2	0.48	4.15E-05	4.15E-05	0.98	8.48E-05	8.48E-05
4	0.51	4.41E-05	8.56E-05	0.95	8.22E-05	1.67E-04
6	0.62	5.36E-05	1.39E-04	0.98	8.48E-05	2.52E-04
8	0.52	4.50E-05	1.84E-04	1.11	9.60E-05	3.48E-04
10	0.5	4.33E-05	2.28E-04	1.03	8.91E-05	4.37E-04
12	0.34	2.94E-05	2.57E-04	0.87	7.53E-05	5.12E-04
14	0.3	2.59E-05	2.83E-04	0.8	6.92E-05	5.81E-04

2

Appendix III

(Solid particle erosion experimental data of HVAF coated CA6NM steel substrates)

(vii) Cumulative volume loss at 30° impact angle

Test duration (min)	35 m/s Impact velocity			70 m/s Impact velocity		
	Wt. loss (mg)	Vol. loss (cm ³)	Cum. Vol. loss (cm ³)	Wt. loss (mg)	Vol. loss (cm ³)	Cum. Vol. loss (cm ³)
2	0.23	1.67E-05	1.70E-05	0.48	3.54E-05	3.55E-05
4	0.19	1.41E-05	3.10E-05	0.41	3.03E-05	6.58E-05
6	0.22	1.62E-05	4.73E-05	0.47	3.47E-05	1.01E-04
8	0.28	2.06E-05	6.80E-05	0.37	2.73E-05	1.28E-04
10	0.19	1.4E-05	8.20E-05	0.44	3.25E-05	1.60E-04
12	0.26	1.92E-05	1.01E-04	0.52	3.84E-05	1.99E-04
14	0.4	2.95E-05	1.31E-04	0.46	3.39E-05	2.33E-04

(viii) Cumulative volume loss at 60° impact angle

Test duration (min)	35 m/s Impact velocity			70 m/s Impact velocity		
	Wt. loss (mg)	Vol. loss (cm ³)	Cum. Vol. loss (cm ³)	Wt. loss (mg)	Vol. loss (cm ³)	Cum. Vol. loss (cm ³)
2	0.49	3.62E-05	3.62E-05	0.75	5.54E-05	5.54E-05
4	0.45	3.32E-05	6.95E-05	0.88	6.50E-05	1.20E-04
6	0.41	3.03E-05	9.98E-05	0.79	5.83E-05	1.79E-04
8	0.39	2.88E-05	1.29E-04	0.74	5.46E-05	2.34E-04
10	0.35	2.58E-05	1.54E-04	0.64	4.73E-05	2.81E-04
12	0.45	3.32E-05	1.88E-04	0.73	5.39E-05	3.35E-04
14	0.36	2.66E-05	2.14E-04	0.66	4.87E-05	3.84E-04

7

(ix) Cumulative volume loss at 90° impact angle

Test duration (min)	35 m/s Impact velocity			70 m/s Impact velocity		
	Wt. loss(mg)	Vol. loss (cm ³)	Cum. Vol. loss (cm ³)	Wt. loss(mg)	Vol. loss (cm ³)	Cum. Vol. loss (cm ³)
2	0.34	2.51E-05	2.51E-05	0.67	4.95E-05	4.95E-05
4	0.31	2.29E-05	4.80E-05	0.58	4.28E-05	9.24E-05
6	0.45	3.32E-05	8.13E-05	0.6	4.43E-05	1.37E-04
8	0.33	2.43E-05	1.06E-04	0.69	5.09E-05	1.88E-04
10	0.29	2.14E-05	1.27E-04	0.55	4.06E-05	2.28E-04
12	0.39	2.88E-05	1.56E-04	0.62	4.58E-05	2.74E-04
14	0.31	2.29E-05	1.79E-04	0.59	4.36E-05	3.18E-04

Appendix IV

1 (List of Publications)

International Journal Publications

1. **Anurag Hamilton, Ashok Sharma, Upender Pandel**, "Solid particle erosion resistance of HVOF sprayed WC-10Co-4Cr coating on CA6NM steel" *Surface Review and Letters*, Vol. 25, No. 2 (2018)

DOI: 10.1142/S0218625X18500117 (*SCI Indexed*)

2. **Anurag Hamilton, Ashok Sharma, Upender Pandel**, "Effect of Impingement Angle on Erosion Resistance of HVOF Sprayed WC-10Co-4Cr Coating on CA6NM Steel" *Key Engineering Materials* Vol. 751, pp 79-83

DOI:10.4028/www.scientific.net/KEM.751.79 (Proceeding of 9th International Conference on Materials Science and Technology, Bangkok) (*Scopus Indexed*)

Other publication

1. **Anurag Hamilton, Ashok Sharma, Upender Pandel**, "Different methods to combat erosion in hydro turbine" presented in National workshop on Mechanical Failures (MF-2015) at BRCM CET Bahal, Haryana, 11-12 September, 2015.

Award

1. Winner of **Thai parkerizing Best student paper Runner-up award** and award price of 20000 Bhat at The 9th International conference on Materials Science and Technology, Bangkok (14th-15th Dec. 2016) for the paper in Surface engineering and Heat treatment session entitled "Effect of Impingement Angle on Erosion Resistance of HVOF Sprayed WC-10Co-4Cr Coating on CA6NM Steel"

thesis

ORIGINALITY REPORT

% **33**

SIMILARITY INDEX

% **8**

INTERNET SOURCES

% **13**

PUBLICATIONS

% **20**

STUDENT PAPERS

PRIMARY SOURCES

1 Submitted to Lemna Manhattan Preparatory School % **18**
Student Paper

2 mnit.ac.in % **4**
Internet Source

3 kumar, Avnish, Ashok Sharma, and S.K. Goel. "Erosion behaviour of WC–10Co–4Cr coating on 23-8-N nitronic steel by HVOF thermal spraying", Applied Surface Science, 2016. % **2**
Publication

4 Manish Roy. "Elevated temperature erosive wear of metallic materials", Journal of Physics D Applied Physics, 03/21/2006 % **1**
Publication

5 Kumar Goyal, Deepak, Harpreet Singh, Harmesh Kumar, and Varinder Sahni. "Slurry erosion behaviour of HVOF sprayed WC–10Co–4Cr and Al₂O₃+13TiO₂ coatings on a turbine steel", Wear, 2012. % **1**
Publication

6 Handbook of Manufacturing Engineering and

Technology, 2015.

Publication

% 1

7

Rout, A. K., and A. Satapathy. "Study on mechanical and erosion wear performance of granite filled glass-epoxy hybrid composites", Proceedings of the Institution of Mechanical Engineers Part L Journal of Materials Design and Applications, 2013.

Publication

<% 1

8

nacomm2013.org

Internet Source

<% 1

9

docslide.us

Internet Source

<% 1

10

Thermal Spray Fundamentals, 2014.

Publication

<% 1

11

Submitted to University of Sheffield

Student Paper

<% 1

12

Wang, Qun, Shiyong Zhang, Yingliang Cheng, Jing Xiang, Xinqi Zhao, and Guibin Yang. "Wear and corrosion performance of WC-10Co4Cr coatings deposited by different HVOF and HVOF spraying processes", Surface and Coatings Technology, 2013.

Publication

<% 1

13

espace.curtin.edu.au

Internet Source

<% 1

14

Hong, Sheng, Yuping Wu, Yugui Zheng, Bo

Wang, Wenwen Gao, Gaiye Li, Guobing Ying, and Jinran Lin. "Effect of Spray Parameters on the Corrosion Behavior of HVOF Sprayed WC-Co-Cr Coatings", Journal of Materials Engineering and Performance, 2014.

Publication

<% 1

15

Li, Chang-Jiu, and Guan-Jun Yang. "Relationships between feedstock structure, particle parameter, coating deposition, microstructure and properties for thermally sprayed conventional and nanostructured WC-Co", International Journal of Refractory Metals and Hard Materials, 2013.

Publication

<% 1

16

QIAN, SHIJIE, KUIYING CHEN, RONG LIU, and MING LIANG. "MODELING STUDY OF SOLID PARTICLE EROSION WITH CONSIDERATION OF PARTICLE VELOCITY DEPENDENT MODEL PARAMETERS", International Journal of Modeling Simulation and Scientific Computing, 2016.

Publication

<% 1

17

Yadav, Abhay Shankar, and S.B. Mishra. "Slurry erosive wear study of d-gun sprayed coatings on SAE 431", 2013 International Conference on Control Computing Communication and Materials (ICCCCM), 2013.

Publication

<% 1

18

file.scirp.org

Internet Source

<% 1

19

Selokar, Ashish, Ravi Kant, D.B. Goel, and U. Prakash. "Solid Particle Erosion Behaviour of Martensitic and Nitrogen Alloyed Austenitic Stainless Steel", *Advanced Materials Research*, 2014.

Publication

<% 1

20

Sahoo, R., B.B. Jha, T.K. Sahoo, and S. Mantry. "Effect of Microstructural Degradation on Solid Particle Erosion Behavior of 2.25Cr-1Mo Steel", *Tribology Transactions*, 2014.

Publication

<% 1

21

Wang, Qun, Zhaoxi Tang, and Limei Cha. "Cavitation and Sand Slurry Erosion Resistances of WC-10Co-4Cr Coatings", *Journal of Materials Engineering and Performance*, 2015.

Publication

<% 1

22

www.diva-portal.org

Internet Source

<% 1

23

Hong, Sheng, Yuping Wu, Jianfeng Zhang, Yugui Zheng, Yujiao Qin, and Jinran Lin. "Ultrasonic cavitation erosion of high-velocity oxygen-fuel (HVOF) sprayed near-nanostructured WC-10Co-4Cr coating in NaCl solution", *Ultrasonics Sonochemistry*,

<% 1

2015.

Publication

24

Encyclopedia of Tribology, 2013.

Publication

<% 1

25

Zoei, Maedeh Sadat, Mohammad Hosein Sadeghi, and Mehdi Salehi. "Effect of grinding parameters on the wear resistance and residual stress of HVOF-deposited WC-10Co-4Cr coating", Surface and Coatings Technology, 2016.

Publication

<% 1

EXCLUDE QUOTES ON

EXCLUDE MATCHES < 5 WORDS

EXCLUDE
BIBLIOGRAPHY ON

MALAVIYA NATIONAL INSTITUTE OF TECHNOLOGY JAIPUR

FORM FOR SUBMITTING FOUR/FIVE SOFT BOUND COPIES OF PH.D. THESIS

ID No.: 2014RMT9060

Name (in Hindi): अनुराग हॅमिल्टन

Name in English: ANURAG HAMILTON As per the
qualifying degree certificate, for printing it on degree certificate, failing which certificate will not
be printed (attested copy of the same should be enclosed):

Category: Research Scholar (T/A)/Foreign
 National/QIP/Sponsored/Institute Staff/ Project Staff/
 External/ Institute Teacher/Research Assistant
(Strike out the one not applicable)

Department/Centre: Department of Metallurgical & Materials Engg.

Date of joining: _____

Date of registration: 19/07/2014

Title of the thesis in Hindi & English: (Please write in
legible letters and as per the format of synopsis and thesis)

Characterization and Fracture Behaviour Study of Carbide Based
Thermal Spray Coatings on Steel.

Address for communication: 40-B, Abhaygarh Scheme, Opp. K.V. No.1
AFS, Jodhpur. (Rajasthan)

Email / Phone No. : a.hamilton2107@gmail.com, Sunnyy8@gmail.com, 9413855498

Name of Supervisor: Prof. Dr. Ashok Sharma

Co-supervisor (if any): Prof. Dr. Upender Pandey

External Supervisor Name with address: _____

In case of candidate whose registration expired beyond six years from the date of registration
for Ph.D., please state:

- i) whether extension has been granted : Yes/NO YES NO
and if yes – The date upto which extension has been granted: NO
Office letter No., date and Authority granting Extension. _____

Enclosed clearance certificate from: (i) Accounts section (ii) Students

Accounts Unit/ Hostel Coordinating Unit.

All the copies of the thesis prepared strictly in accordance with the instructions
for guidance of the candidate regarding format of thesis issued by the Institute:

DECLARATION CERTIFICATE

I, ANURAG HAMILTON declare that this thesis titled Characterization and Erosion Behaviour Study of Corrosion Based Thermal Spray Coatings on Steel.
And the work presented in it is my own. The work has been carried out under the supervision of Prof. Dr. Ashok Sharma & Prof. Dr. Upender Khandel. I confirm that:

1. This work was done wholly or mainly while in candidature for a Ph.D. degree at MNIT Jaipur.
2. Where any part of this thesis has previously been submitted for a degree or any other qualification at MNIT Jaipur or any other institution, this has been clearly stated.
3. Where I have consulted the published work of others, this is clearly attributed.
4. Where I have quoted from the works of others, the source is always given. With the exception of such quotations, this thesis is entirely my own work
5. I have acknowledged all main sources of help.
6. Where the thesis is based on work done by myself, jointly with others, I have made clear exactly what was done by others and what I have contributed myself.

HAMILTON A.
Signature of the candidate Date: 18/07/17

DECLARATION CERTIFICATE

1. I am satisfied that the thesis presented by Mr. ANURAG HAMILTON worthy of consideration for the award of the degree of Doctor of philosophy and is a record of the original bonafide research work carried out by him under my guidance and supervision and that the results contained in it have not been submitted in part or full to any other university or Institute for award of any degree/diploma.
2. I certify that he/she has pursued the prescribed course of research.
3. Plagiarism report enclosed.

[Signature]
(Signature)
Supervisor(s) of the student
Dept. Mech. & Mat. Engg.

Remarks/ Recommendations of the guiding Supervisor(s) authorizing the Academic Office to receive four/ five copies of thesis.

[Signature]
Signature of the Supervisor:

[Signature]
Signature of the Co-supervisor (if any):

Date: 18/07/17

FOR OFFICIAL USE ONLY

Synopsis and Thesis submitted to Department along with the clearance forms, plagiarism report, declaration certificate and attested copy of the qualifying degree certificate on 17-07-2017.

[Signature]
(Signature of Department Office Staff)

Clearance forms, plagiarism report, declaration certificate, Synopsis and thesis received in Academic Section on _____

Assistant Registrar
(Academic)

MALAVIYA NATIONAL INSTITUTE OF TECHNOLOGY JAIPUR
FORMAT TO DEFEND THE THESIS WHILE ON LEAVE BY THE Ph.D. STUDENT

PART A

TO BE FILLED BY THE STUDENT

1. Name of the Candidate ANURAG HAMILTON 2. ID Number 2014RMT9060
 3. Mobile No.: 9413855498 4. Email ID: a.hamilton2107@gmail.com, Sunnyy8@gmail.com
 5. Ph.D. topic Characterization and Erosion Behaviour Study of Carbon Based
 6. Name of Supervisor Prof. Dr. Ashok Sharma 7. Dept. Thermal Spray Coating of Steel
 8. Full Time/Part Time FT
 9. Date of registration in Ph.D. Programme 19/07/2014
 10. Type: Sponsored/Self Finance/Institute Assistant/QIP/TEQIP Assistantship/JRF/SRF Assistantship from other sources (Please)
 11. Date of award of Ph.D. Candidacy 09/07/2015
 12. Date of submission of thesis 17/07/17
 13. Details of course work completed:-

Semester	Session	Course Code	Title	Credit	Grade	Overall CGPA
I st	14-15	MET-90D	Research Methodology & Design of Exp.	03	BB	8.0
I st	14-15	MTT-653	Structural Metallurgy of Ferrous Mat.	03	BC	
II nd	14-15	MTT-660	Frontiers of Mechanical working	03	AB	
 						

14. Details of Grade awarded in Progress Report.

Progress Report	Semester											
	1	2	3	4	5	6	7	8	9	10	11	12
Submitted (YES/NO)	Y	Y	Y	Y	Y	Y	 					
Details (Satisfactory/Unsatisfactory) Mention in the form of SSSS, SSSX, SSXX, SXXX, XXXX	SSSS	SSSS	SSSS	SSSS	SSSS	SSSS	 					

Date: 17-07-2017

Hamilton A.
Signature of Student

PART-B
FOR OFFICIAL USE ONLY

Recommendation of the Supervisor; Recommended/Not recommended

Date: 17-07-2017

Sharma A.

Signature of Supervisor

Recommendation of DPGC Convener; Recommended/Not recommended

P. C. Mehrotra
Signature of Convener DPGC


Signature of Associate Dean (PG)

Dealing assistant (Academic Section)


Turnitin Originality Report

Characterization and Erosion Behaviour
Study of Carbide Based Thermal Spray
Coatings on Steel by Anurg Hamilton

From Table (Ph.D)

 Similarity Index 15%	Similarity by Source Internet Sources: 8% Publications: 12% Student Papers: 1%
---	--

Processed on 07-Jul-2017 12:39 AM
CDT
ID: 829447162

Word Count: 19188

sources:

- 1 4% match (Internet from 02-Oct-2014)
http://mnit.ac.in/new/cms/uploads/2014/05/admission_brochure_final.pdf

- 2 2% match (publications)
[kumar, Avnish, Ashok Sharma, and S.K. Goel. "Erosion behaviour of WC–10Co–4Cr coating on 23-8-N nitronic steel by HVOF thermal spraying". Applied Surface Science, 2016.](#)

- 3 1% match (publications)
[Kumar Goyal, Deepak, Harpreet Singh, Harmesh Kumar, and Varinder Sahni. "Slurry erosion behaviour of HVOF sprayed WCâ€"10Coâ€"4Cr and Al2O3+13TiO2 coatings on a turbine steel". Wear, 2012.](#)

- 4 1% match (publications)
[Handbook of Manufacturing Engineering and Technology, 2015.](#)

- 5 1% match (Internet from 19-Feb-2017)
https://espace.curtin.edu.au/bitstream/handle/20.500.11937/1410/195896_Rahman%202013-.pdf?isAllowed=y&sequence=2

- 6 1% match (publications)
[Hong, Sheng, Yuping Wu, Yuguang Zheng, Bo Wang, Wenwen Gao, Gaiye Li, Guobing Ying, and Jinran Lin. "Effect of Spray Parameters on the Corrosion Behavior of HVOF Sprayed WC-Co-Cr Coatings". Journal of Materials Engineering and Performance, 2014.](#)

- 7 < 1% match (Internet from 01-Jul-2014)
http://nacomm2013.org/Papers/117-inacomm2013_submission_121.pdf

- 8 < 1% match (publications)
[QIAN, SHIJIE, KUIYING CHEN, RONG LIU, and MING LIANG. "MODELING STUDY OF SOLID PARTICLE EROSION WITH CONSIDERATION OF PARTICLE VELOCITY DEPENDENT MODEL PARAMETERS". International Journal of Modeling Simulation and Scientific Computing, 2016.](#)

- 9 < 1% match (publications)
[Rout, A. K., and A. Satapathy. "Study on mechanical and erosion wear performance of granite filled glass-epoxy hybrid composites". Proceedings of the Institution of Mechanical Engineers Part L Journal of Materials Design and Applications, 2013.](#)

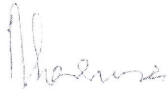
MALAVIYA NATIONAL INSTITUTE OF TECHNOLOGY, JAIPUR

Department of Metallurgical and Materials Engineering

05-04-2017

Notice

Pre Ph.D. open seminar of Mr. Anurag Hamilton (2014RMT9060) will be conducted on 21/04/2017 at 11:00 am in the HOD office. All the DREC members are requested to attend the same. The title of his thesis is "**Characterization and Erosion Behaviour Study of Carbide based Thermal Spray Coatings on steel**". All interested faculty members and students are also cordially invited to attend the open seminar.



Dr. Ashok Sharma
Professor & Supervisor



Dr. Upender Pandel
Professor & Co-Supervisor

Copy to:

1. Dean, Academic Affairs
2. Dr. R. K. Duchaniya, DPGC Convener
3. Prof. A. K. Bhargava, HOD & DREC Member
4. Prof. Upender Pandel, Co- Supervisor & DREC Member
5. Dr. S. K. Gupta, DREC Member
6. Mr. Anurag Hamilton (ID:2014RMT9060)
7. Department Notice Board

MALAVIYA NATIONAL INSTITUTE OF TECHNOLOGY JAIPUR
OFFICE OF DEAN ACADEMIC

Application for Refund of Institute Caution Money after Final Clearance/Admission Withdrawal
To be filled in by student in CAPITAL LETTERS

Name: ANURAG HAMILTON..... Father's Name: H. H. LALL.....
 ID No. 2014RMT1902 Semester 6th..... B. Tech./B.Arch./M.Tech./Ph.D./M.Sc. M.Planning/MBA
 Date of Birth 21/07/89..... Institute Admission Date 19/07/14..... Institute Leaving Date.....
 Address for Communication 40-B, ABHAYGARH SCHEME, OPP. K.V. NO. 1
APS, JODHPUR.....
 Phone No. (O)..... (R)..... Mobile No. 9413855498.....
 Day Scholar/Hosteller..... Hosteller..... Category: General/ST/SC/OBC/Girls..... GEN.....
 Date of Occupying Hostel..... Date of Vacating Hostel.....
 Name & Signature of Hostel Authority:

List of outstanding dues (on Institute Leaving Date)

S. No.	Type	Amount (Rs.)	Name & Signature
1.	Library	<u>NIL</u>	Asst. Librarian <u>[Signature]</u>
2.	Hostel Mess	<u>NIL</u>	Hostel Incharge <u>[Signature]</u>
3.	Games & Sports	<u>NIL</u>	Sports Officer <u>[Signature]</u>
4.	Dean Student Affairs*	<u>NIL</u>	Dealing Asst. <u>[Signature]</u>
5.	Scholarship/Assistantship		Dealing Asst.
6.	Dean Academic Affairs		Dealing Asst.

* ID Card is to be surrendered at DSA office otherwise ID Card Fee Rs. 100/- is to be charged.

Signature of Student [Signature]..... Date: 13/07/17.....

For Office use only

Student may be relieved from the Institute and Institute Caution Money/Security Deposit may be refunded

Checked from the fees register page No. year Institute Caution Money/
Security deposit is to be refunded to Shri/Ms. ID No.

Account Section may kindly prepare the cheque from Rs. in favour of the student.

Dealing Assistant

Assistant Registrar

Dean Academic

Dy. Registrar (Accounts)

Form : Fee Challan

:

Fee

Advance Paid	0.00
Adm Proc Fee (RS)	1000.00
Tuition Fee (USD/RS)	7500.00
Total Fee	14800.00
Development (RS)	1500.00
Library/Book Bank (RS)	500.00
Computer / Internet (RS)	1800.00
Sports CA Society (RS)	1000.00
Student Welfare (RS)	500.00
Ind Tr & Placement (RS)	500.00
Examination (RS)	500.00
Insurance (RS)	0.00
Inst Caution Dep (RS)	0.00
Security Deposite (RS)	0.00
Alumni Ass Memb (RS)	0.00
Identity CC (RS)	0.00

General

StudentID	2014RMT9060
Student Name	ANURAG HAMILTON
Challan No	2016/107218
Date:	2016-12-27
DD No.	online
DD Amt	14800.00
Semester	6
F Year	2016-17
Status	Posted



THE MAHARAJA SAYAJIRAO UNIVERSITY OF BARODA

Whereas

Anurag Hamilton

*Of the Faculty of Technology and Engineering
has pursued a course of study prescribed by the
University in Material Technology and
passed the requisite Examination in the*

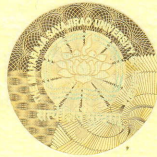
First Class

*Now therefore this is to certify that he has this day
been duly admitted by the Senate to the Degree of.*

Master of Engineering

(Metallurgical and Materials Engineering)

*Given under my hand this Twenty Fourth Day of
December two thousand thirteen*



Chancellor

CHAPTER 1

Introduction

1.1. Background

Hydropower plants play a vital role in fulfilling the India's domestic energy requirements. It is the most substantial and economical source compared to other sources of energy [1–7]. The Himalayan rivers provide a huge potential for hydropower generation due to its steep gradient and topography [8–10]. However, due to geographically fragile and young mountains, the amount of silt in flowing river water increases to alarmingly high level during the monsoon season [11–14].

Consequently, silt contents exceed up to 50 kg of silt per cubic meter of water, which is above the permissible limit (1 kg of silt per cubic meter of water) [15]. Hence, the silt particles (700–1000 HV) present in the water interacts with the surface of the hydro turbine and causes serious damage to hydro turbine components due to silt erosion [16]. Fig. 1.1 shows the damaged hydro turbine components due to silt erosion. In particular, blades, guide vanes, bearing bodies and nozzles, etc. bears high risks of being damaged by silt particles [17,18]. Various materials used for the construction of hydro turbine component is given in Table 1.1.

The gradual removal of material from underwater parts changes the profile of turbine, which reduces the lifespan of the hydro turbine and its overall efficiency [19,20]. The silt erosion intensity depends on the (i) particle variable: particle size, shape, and hardness. (ii) Impingement variable: velocity of silt and fluid, impact angle, concentration, flow media and (iii) base material variables: microstructure and mechanical properties [3,5,21–27]. Among these, base material properties play a paramount role, as it is the only variable that can easily minimize the erosion up to greater extent.

The silt erosion menace can be controlled by three approaches: (i) effective de-silting arrangement (ii) developing silt resistance equipment design and (iii) surface engineering route [19]. However, during the monsoon season, it becomes challenging to stop the interaction of silt with turbine even after application of de-silting arrangement and incorporating silt resistance equipment design [15,28]. Hence, the application of surface

engineering is the most viable alternative. Different researchers [29–31] have suggested various surface engineering routes to enhance the properties of turbine steel. However, it has been found that the deposition of thermal spray coatings can significantly improve the erosion performance of the hydroturbine steel [32–34].

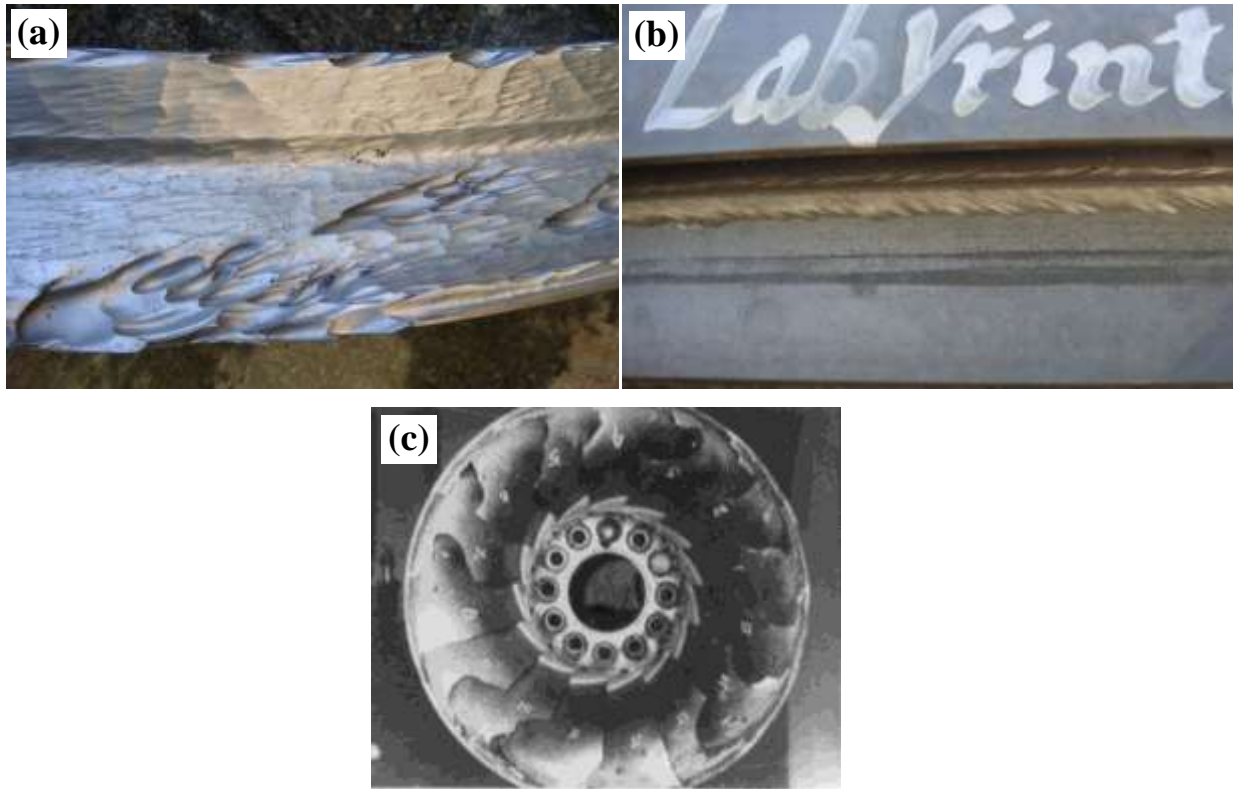


Fig. 1.1. Eroded Hydroturbine components of Nathpa Jhakri Hydro Power Station, SJVN Limited, Jhakri, India.

Table 1.1 Materials used for the construction of hydroturbine components.

Sr.No.	Component	Material
1.	Runner	13%Cr, 4% Ni stainless steel
2.	Labyrinth seals	13%Cr, 4%Ni or 18%Cr, 10%Ni stainless steel
3.	Guide vane	13%Cr, 4% Ni stainless steel
4.	Liners for top cover and pivot ring	18%Cr, 10%Ni stainless steel
5.	Fasteners in water path	Stainless steel
6.	Tubes for bearing coolers	Cupro-Nickel (80% Cu-20%Ni)
7.	Rubber seals	Neoprene synthetic rubber

Thermal spray coatings are versatile means of depositing coating with high inter-splat strength, better adhesive strength, low porosity and oxide contents [35,36]. Various types of feedstock powders [37–39] have been attempted by different investigators to improve the erosion resistance of hydroturbine components. It has been found that WC-Co-Cr based coating gives the exceptional erosion performance compared to other type of powders [39–42], It is due to the presence of hard WC particle in a tough and ductile Co-Cr matrix [43–45]. Corrosion resistance of the coating is also enhanced by the presence of chromium (Cr) in the metallic binder (Co-Cr) phase [46]. Presently, high-velocity oxy-fuel (HVOF) process (flame temperature-2800°C, particle velocity-200-1000 m/s) is widely used for developing erosion resistant coating on hydroturbine steel [34,45,47,48]. However, in this process decarburization of WC to W_2C takes place, which deteriorates the erosion resistance of the coating [49–53]. Recently, high-velocity air fuel (HVOF) system is gaining much attention among the researchers [54–61]. This process operates at a much lower combustion temperature (flame temperature-1950°C, particle velocity-600-1250m/s) using compressed air (not oxygen) for combustion [59,62–64]. Which significantly decreases the decarburization of WC and produces a homogeneous and dense coating [65–67]. HVOF technique also reduces the production cost of coatings by using compressed air instead of pure oxygen [57,68–70]. Therefore, there is a scope to explore the possibility of HVOF sprayed coating in erosion resistance application like hydroturbine. In literature, application of HVOF coating on CA6NM hydro turbine steel as a solution to silt erosion problem has not been addressed. Hence, in this present work, HVOF and HVOF sprayed WC-10Co-4Cr coating was deposited on a CA6NM steel substrate. A detailed microstructural and phase compositional study was carried out on the coatings. Mechanical properties of the coatings were also evaluated. Consequently, their erosion resistance was assessed using solid particle erosion test at various impingement angles and velocities. The percentage improvement in erosion resistance of CA6NM steel after application of HVOF and HVOF coating was also discussed.

1.2. Objectives of the Study

The primary aim of this study was to prevent the silt erosion of hydroturbine steel by developing suitable carbide based thermal spray coatings. To achieve the primary objective, the following specific objectives were carried out:

1. Study of erosion behavior of as-cast CA6NM steel at different impingement angles and velocities.

2. Study of HVOF processed WC-10Co-4Cr coating characteristics on the as-cast CA6NM substrate.
3. Evaluate and compare the erosion resistance of HVOF sprayed WC-10Co-4Cr coating on as-cast CA6NM steel with the uncoated CA6NM steel.
4. Study of HVAF processed WC-10Co-4Cr coating characteristics on the as-cast CA6NM substrate.
5. Evaluate and compare the erosion resistance of HVAF sprayed WC-10Co-4Cr coating on as-cast CA6NM steel with the uncoated CA6NM steel.

1.3. Outline of the Thesis

The thesis has been organized into five chapters, references and appendix as follows:

Chapter 1 provides an introduction to the basic background of the research including objectives of the research as well as the outline of the thesis.

Chapter 2 presents a comprehensive review of available literature. The chapter begins with a brief introduction about hydropower plant and types of turbine. It discusses the silt erosion problem faced by hydro turbine components. Types of erosive wear (solid particle, slurry, cavitation and liquid impingement erosion) are also described in brief. The mechanism of erosion is a complex phenomenon and governed by various factors. The various contributing factors for erosion such as cutting by silt particles, cavitation, subsurface damages, plastic deformation, fatigue, and synergy are also discussed. Erosion dependent variables have been categorized into three categories: particle variable, impingement variable, base material variables. Each variable is discussed in detail to gain insight into their effect on erosion behaviour.

The principle of thermal spraying and different types of thermal spraying process used for hydroturbine application are discussed. Various properties and microstructure features of thermal spray coatings are also discussed. The primary focus was paid to HVOF and HVAF spraying techniques due to their versatile advantages in term of coating deposition. WC-Co based cermet coatings are presented as a novel method for protecting the hydroturbine components. Hard WC particles in the coating provide high hardness and wear resistance while the metal binder (Co) offers the sufficient coating toughness, which in turn, results in higher erosion resistance. This chapter also covers the erosion performance of various WC-Co/WC-Co-Cr coatings deposited by HVOF and HVAF thermal spraying. After an extensive review of the available literature, research gap has been described at the end of the chapter.

Chapter 3 describes the materials, equipment, and methodology employed to complete the present study. The chapter is divided into three sections.

The first part discusses the selection of base material, evaluation of mechanical properties of steel and its characterization. The second part of the study focuses on thermal spray coatings. Different WC-10Co-4Cr powder was used in HVOF and HVAF spraying to achieve the maximum benefits. The sprayed coatings were characterized in terms of coating roughness, phases present, index of carbide retention, cross-sectional microstructure, microhardness, coating porosity, density and fracture toughness. The third section of the chapter provides a detailed description about erosion tester used to evaluate the erosion behavior of uncoated and coated steel.

Chapter 4 presents the results and discussions of the experimental work performed in this study and their discussion. This chapter is divided into four sections.

The **first section** discusses the characterization of as-cast CA6NM steel. The CA6NM steel was characterized in terms of microstructure, phases and mechanical properties followed by detailed discussion.

The **second section** deals with erosion performance of as-cast CA6NM steel at different impingement angles and velocities.

The **third section** discusses the characterization of HVOF sprayed WC-10Co-4Cr coated CA6NM steel and its erosion performance at different impingement angles and velocities.

The **last section** focuses on HVAF sprayed WC-10Co-4Cr coating on CA6NM steel and its characterization. It also discusses erosion performance at different impingement angles and velocities.

Chapter 5 presents the conclusions of the experimental work performed in this study and suggestions for future work in the area.

References

Appendix I presents the solid particle erosion experimental data of uncoated CA6NM steel substrate.

Appendix II presents the solid particle erosion experimental data of HVOF coated CA6NM steel substrate.

Appendix III presents the solid particle erosion experimental data of HVAF coated CA6NM steel substrate.

Publications arising from this work and reprint of published paper are attached at the end of this thesis.

CHAPTER 2

Literature Review

This chapter contains a comprehensive review of the literature related to hydropower plant, types of turbine, types of erosion, erosion dependent variables and erosion mechanism. Thermal spray technique and their role in combating erosion are also discussed. The studies related to erosion performance of thermal spray coating developed using high-velocity oxy-fuel (HVOF), and high-velocity air fuel (HVOF) processes are also added. After a comprehensive review of the available literature, research gap has been described at the end of the chapter.

2.1. Hydropower Plant and its Functioning

Hydropower plants play a vital role in fulfilling growing energy requirements worldwide. Hydropower plants utilize the potential energy of the stored water to generate electricity [1,3,5,14]. In India, Himalayan rivers provide a great potential for hydropower generation due to its steep gradient and topography [9,19]. India ranks fifth in terms of exploitable hydro-potential on the global scale [71]. Currently, the total installed capacity in India including all resources is about 330 KMW, in which the share of hydro energy is 13.5 %. List of the major hydropower plants situated in India are shown in Table 2.1 [72]. A schematic layout of a hydropower plant is shown in Fig. 2.1. Hydro turbine is the heart of the hydropower plant. The hydraulic energy of the flowing water is transformed into mechanical energy through hydroturbine blades, and this energy is transmitted to generator shaft, in this way a hydropower plant generates electricity. Generated electricity is transferred to electrical grid based on requirement [73,74].

2.1.1. Types of hydro turbine

Hydroturbines can be divided into two categories as impulse and reaction turbines [75].

(a) Impulse turbine

Table 2.1 List of the major hydropower plants in India.

Sr. No.	Name of hydropower plant	State	Installed capacity
1	Tehri Dam	Uttarakhand	2400 MW
2	Koyna Dam	Maharashtra	1960 MW
3	Srisaillam Dam	Andhra Pradesh	1670 MW
4	Nathpa Jhakri	Himachal Pradesh	1500 MW
5	Sardar Sarovar	Gujarat	1450 MW
6	Bhakra Dam	Punjab	1325 MW
7	Indira Sagar Dam	Madhya Pradesh	1000 MW
8	Kalinadi	Karnataka	1240 MW
9	Nagarjunasagar Dam	Andhra Pradesh	965 MW
10	Idukki Dam	Kerala	780 MW

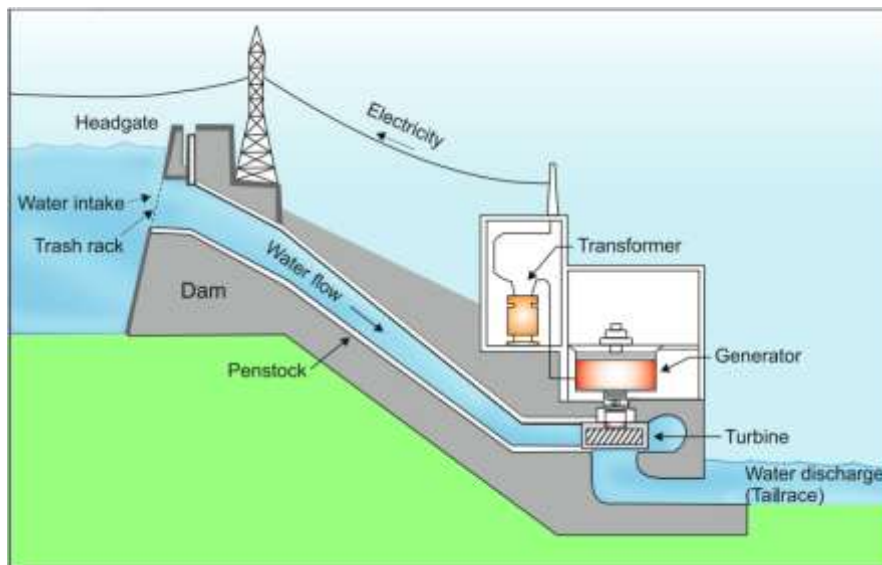


Fig. 2.1. Layout of hydropower plant, adapted from [76–78].

In impulse turbine velocity of moving water is used to move the runner. An impulse turbine finds application in high head and low flow applications. The water stream strikes each bucket on the runner. The mechanism of Impulse turbine used in hydropower plant is shown in Fig. 2.2. A well-known example of Pelton wheel is the impulse turbine. In the case of Pelton wheel, the entire head (velocity head, elevation head, and pressure head) of the

flowing water is transformed into velocity head at the exit of supply nozzle. The force of individual jets of water striking the buckets generates the torque which rotates the turbine shaft [77,78]

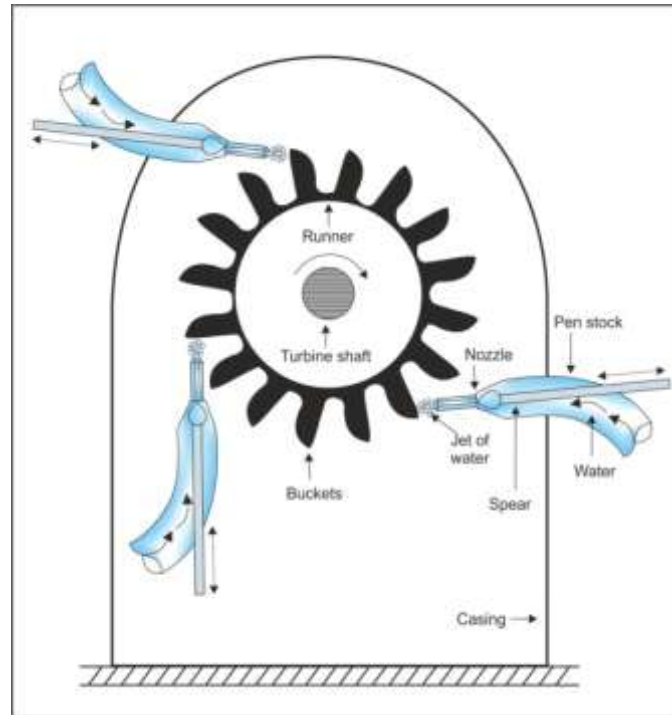


Fig. 2.2. Schematic layout of impulse turbine, adapted from [76–78].

(b) Reaction turbine

In a reaction turbine combined the action of pressure and moving water is used to generate power. The runner is implanted in such a way that water stream flows over the turbine blades. Unlike impulse turbine, in the case of reaction turbines, the water completely fills the passageways through which it flows. The water is directed into the rotor with the help of inlet guide vanes with a tangential component of velocity [79]. The reaction turbines find application in hydropower plants with lower head and higher flows. Francis and Kaplan turbines are the two main types of reaction turbine. In Francis turbine, the blades have a unique curved feature which is designed to generate maximum performance from the turbine. The mechanism of Francis turbine is shown in Fig. 2.3. Kaplan turbine is popularly known as the propeller turbine because there runner/blades resembles the propeller of a ship. Mechanism of Kaplan turbine is illustrated in Fig. 2.4. In the case of Kaplan turbine, optimum efficiency is generated at different pressure condition because of adjustable blades. Therefore, Kaplan turbine can operate under a low head condition and gain optimum efficiencies, which is not feasible in the case of Francis turbines [78].

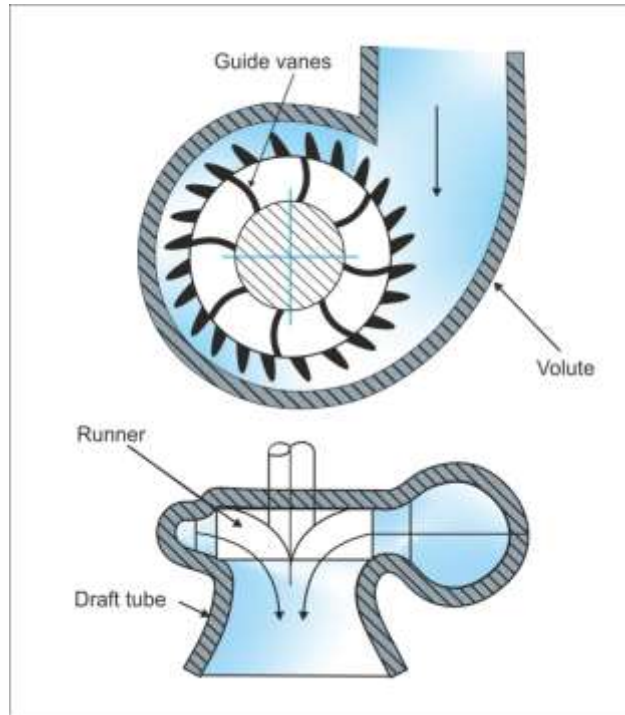


Fig. 2.3. Schematic layout of Francis turbine, adapted from [76–78].

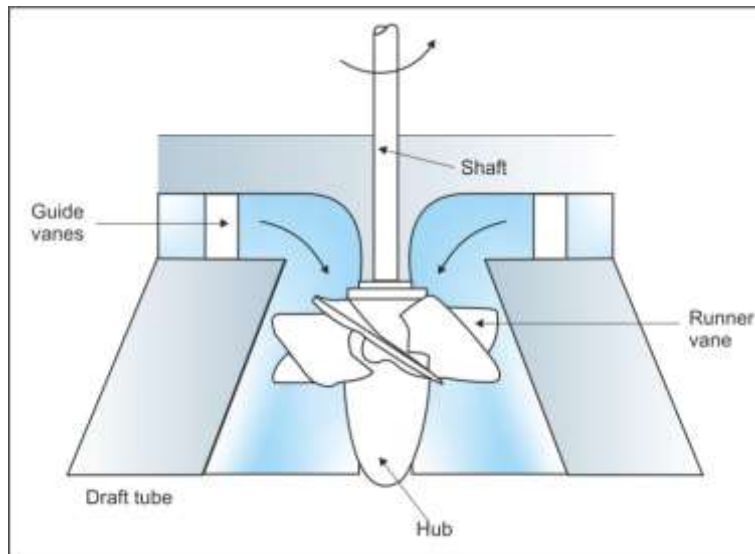


Fig. 2.4. Schematic layout of Kaplan turbine, adapted from [76–78].

2.1.2. Silt erosion problem in hydroturbine components

Although hydropower is the most important and cheapest renewable source of energy, hydropower plants encounter problems like silt erosion, which reduces its operational capabilities [6,19,39,80,81]. In general purpose, turbines are designed for clear water. However, during monsoon season it becomes nearly impossible to avoid interaction of silt and turbine components [82]. This leads to the severe problem of silt erosion [8,15].

Hydroturbine consists of static and moving parts [18,83]. Both of them are exposed to erosion. Spiral casing, draft tube, etc. are classified as static parts. Runner, guide vanes, shafts, etc. comes under moving parts. The high-velocity fluid (10 to 150 m/s) coming from reservoir contains clay, silt and sand particles [9,14,20]. Table 2.2 shows the classification of river sediment [84]. In order to stop them from entering the hydro turbine, desilting arrangements are put in place. However, during monsoon season, it becomes impossible to prevent the interaction of silt particles with Hydro turbine components. These silt particles contains quartz (70-80%) which measures 7 on Moh's scale and result in erosion [9]. Hydroturbine is found to undergo significant erosion when they are exposed to rivers that exceed 1 kg of silt per cubic meter of water. The problem is particularly severe in Himalayan rivers where the silt content during the rainy season exceeds 50 kg of silt per cubic meter of water [16]. Silt erosion in hydro turbine components reduces the performance and efficiency of hydropower turbines but at the same time also causes the problem of maintenance and operation [85]. In the case of Pelton turbine operating in the Himalayan region, the erosion rate of 3.4 mm/year has been recorded for the buckets and needles and the buckets, which resulted in a reduction of around 1.21% in the efficiency of the hydro turbine [4,20].

Table 2.2 Classification of river sediment

Particle	Clay	Silt	Sand	Gravel	Cobbles	Bounders
Size (mm)	<0.002	0.002-0.06	0.06- 2	2-60	60-250	>250

2.2. Types of Erosive Wear

According to ASTM G40-15 Standard [86], erosion wear is defined as progressive loss of material from a surface of material due to mechanical interaction between that surface and fluid, a multi-component fluid or impinging liquid or solid particles. The erosive wear is mainly classified into four types according to the interaction of target material and impinging particle as shown in Fig. 2.5

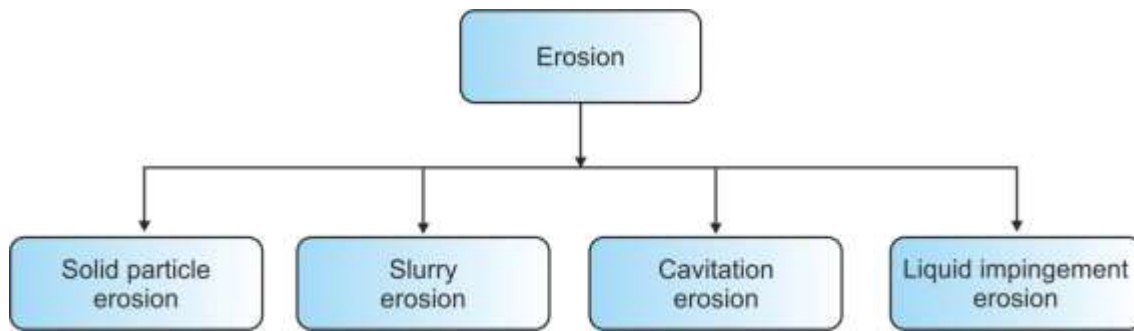


Fig. 2.5 Classification of erosion.

2.2.1. Solid particle erosion

The solid particle erosion (SPE) may be defined as loss of material arising from the continuous impact of solid particles traveling at substantial velocities [87–90]. The response of the material to SPE by solid particles is influenced by the properties of the material such as the hardness and microstructure [91–93]. SPE in practical conditions includes a macroscopic scooping appearance, increased surface roughening and thinning of components [90,94–96]. Fig. 2.6 shows the schematic layout of solid particle erosion mechanism. Solid particle erosion is a result of the impact of solid particles on the solid surface, resulting in part of the surface been taken out due to higher hardness of impacting particle [24,97]. This type of erosion is commonly found in hydroturbine blades, soot blowers, and cyclone separators [98,99].

2.2.2. Slurry erosion

The slurry erosion may be defined as the loss of material from the surface due to the interaction of hard solid particles suspended in liquid moving at considerable velocities with the surface [82,100–102]. The slurry is defined as an insoluble mixture of solid particles suspended in liquid with certain consistency so that it can be transported or pumped [103–105]. Slurry erosion is a serious problem for the operation, maintenance and reliability of slurry equipment used in solid-liquid hydro transportation systems, coal liquefaction plants and hydroelectric power stations [106–108].

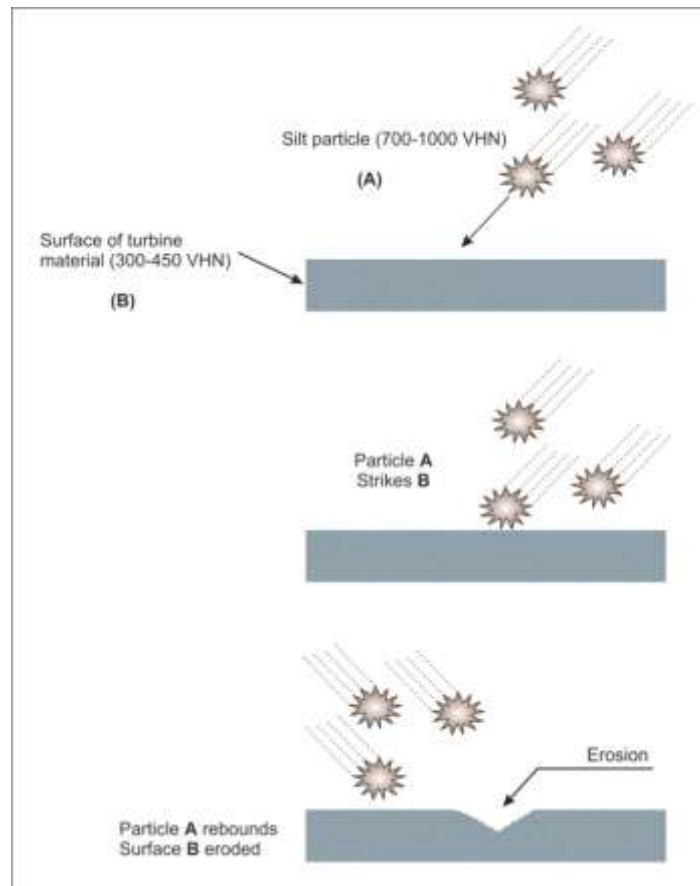


Fig. 2.6 Schematic layout of solid particle erosion mechanism, adapted from [109].

2.2.3. Cavitation erosion

The word "cavitation" was first used by Froude, Barnaby, and Parsons in connection with the propeller breakdown of early steamships [110]. Cavitation erosion is the mechanical degradation of the surface of material due to the continuous collapse of bubbles in a surrounding liquid. Bubbles in the liquid are formed when the partial pressure of gases dissolved in a fluid decrease, due to a vibration or to a turbulent [111,112]. When the partial pressure increases these bubbles explode and generate high-intensity shock waves [113,114]. These shock waves penetrate the surface and material is removed from the surface. Cavitation erosion leads to degradation of surface roughness which further increases the cavitation phenomenon [115,116]. The severity of the cavitation damage is much more increased when silt particles are present in the liquid; this is observed in hydroturbines [117]. Cavitation erosion is also observed in fluid propulsion devices like pumps, ship propellers, and valves [118].

2.2.4. Liquid impingement erosion

Liquid impingement erosion (LIE) may be defined as the continuous removal of material from a solid surface due to continued exposure to impingement by liquid drops or jets [119,120]. The impact pressure of liquid drops or jets exceeds the target material elastic limit and material is deformed permanently, which leads to material removal [16]. LIE is observed in low-pressure steam turbine and piping. Pipes made from materials that rely on the formation of the passive oxide film for corrosion resistance are a greater risk of LIE. The mechanical action of the liquid drops or jets removes the protective oxide film from the surface. This repeated action can perforate pipe elbows when velocity is high [121].

2.3. Mechanisms of Erosion in Hydroturbine

The erosion mechanism of hydro turbine components is a convoluted phenomenon and is dictated by various contributing factors [85,122]. Schematic layout of the various damaging factors responsible for the erosion damages is shown in Fig. 2.7. Silt erosion takes place due to following mechanisms:

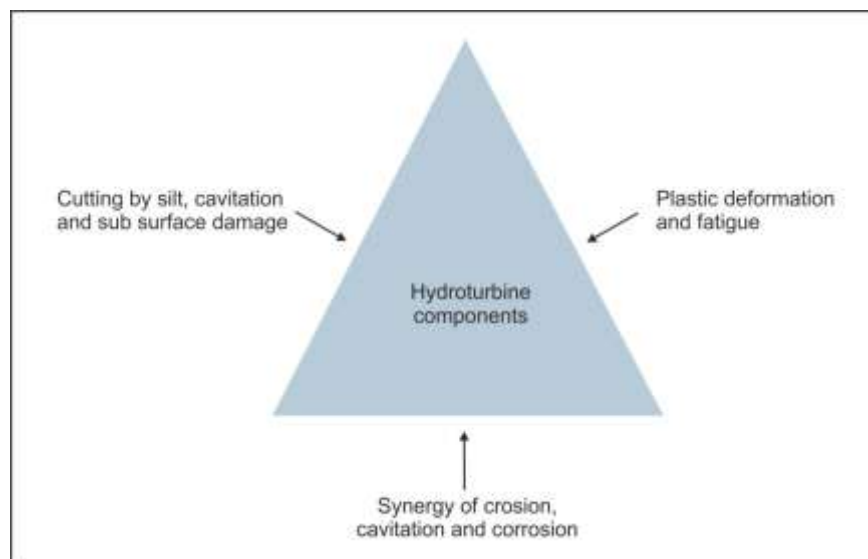


Fig. 2.7 Schematic diagram showing mechanisms of silt erosion.

(a) Cutting by silt particles, cavitation and subsurface damages

Erosion by hard silt particles is highly depended upon the impingement angle at which the silt particles impact on the target surface. At shallow impingement angles, silt erosion takes place due to the formation of lips and surface ploughs [21,22]. These erosion features are formed because impacting silt particles at shallow angles strike the surface with tangential force, which results in the formation of ploughs and lips in the direction of the particle movement

[123]. The target material which is extruded from surface form lips on the edges of the ploughs which is in work hardened state [124,125]. The extent of work hardening increases with time and further impingement, which results in embrittlement and subsequent removal of extruded surface. At high impingement angle, the impact of silt particles is almost perpendicular to the surface of the material. This provides bigger indentation force, and the erodent penetrates into the surface resulting in the formation of craters [126]. The schematic diagram showing the development of lips and crater on the surface of the material is shown in Fig. 2.8 and 2.9.

Formation of ploughs and craters on the surface of hydroturbine due to silt erosion alters the surface profile of the hydroturbine surface. Which results in the excessive generation of bubbles [127]. These air bubbles explode near the surface of the material and generate high-intensity shock waves (70 MPa). These shock waves try to pervade into the body of the hydroturbine component and cause severe damages at the surface as well as in the interior of the underwater parts as presented in Fig. 2.10. Impacting high energy silt particle and the explosion of bubbles transfer their energy into the material. Which results into nucleation of cracks at sensitive locations like inclusions and coarse precipitates [128]. These cracks travel through the parts of the hydroturbine component leading to accelerated failure and the total problem of material removal by silt erosion is compounded.

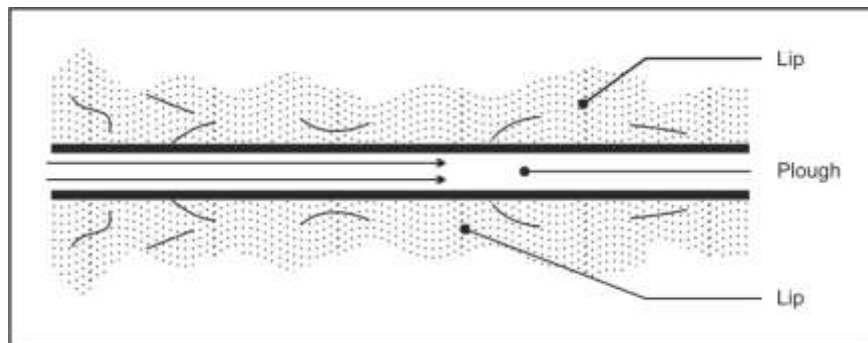


Fig. 2.8 Schematic diagram showing formation of lips.

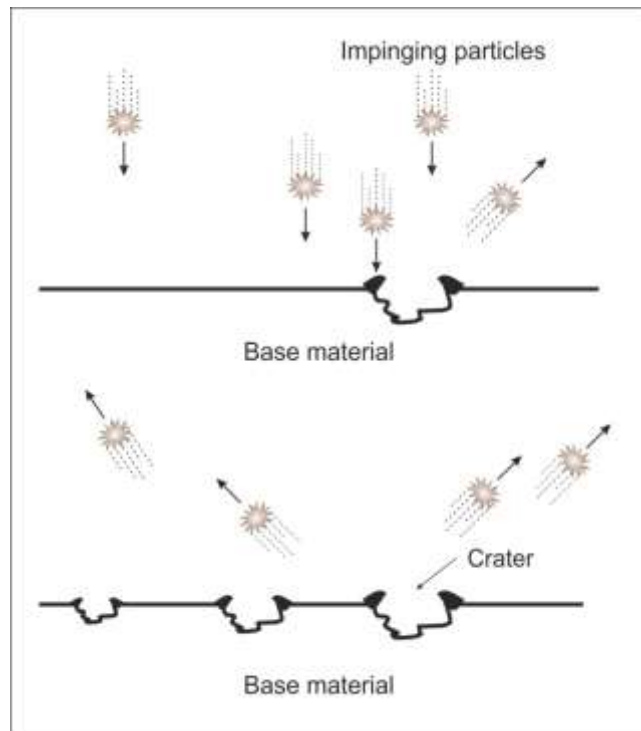


Fig. 2.9 Schematic diagram showing formation of craters.

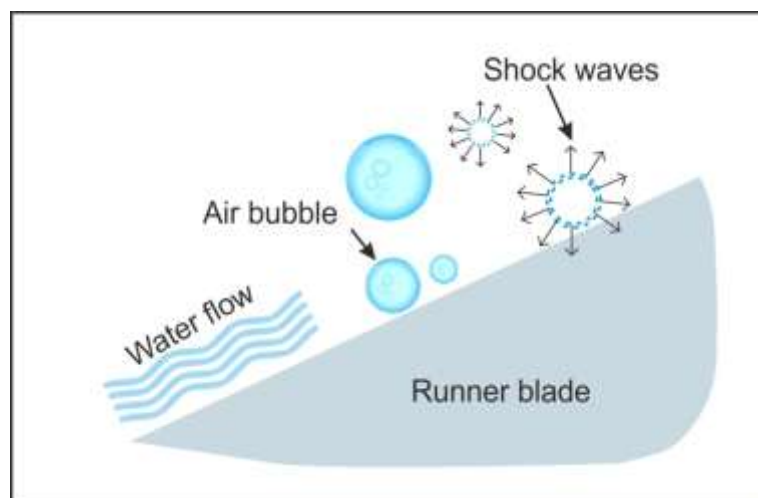


Fig. 2.10 Mechanism of cavitation in hydroturbine.

(b) Plastic deformation and Fatigue

Plastic deformation and fatigue also play an important role in hydroturbine material failure [129]. The extensive pressure generated by water streams results in the distortion of blade profile, which leads to turbulence and rapid damage. When a material with coarse grain size and low thickness is given significant deformation, the grains develop a tendency to separate from each other. This results in the formation of a so-called ‘honeycomb structure,’ in which

one can observe various grain segments having a tendency to separate from each other [130]. Plastic deformation greatly influences the mechanism of failure of underwater parts [11]. Therefore, it is important to select a blade material which possesses high strength and fine grain sizes. Fatigue also plays a significant role in the hydroturbine material failure. The regular impact of silt and water on hydroturbine components develops cyclic stress, which leads to fatigue damage [27].

(c) Synergy of erosion, cavitation and corrosion

In actual service condition, all the parameters mentioned above act together. This results in much higher erosion rate than the sum of erosion due to silt and liquid separately. It is often referred to as the synergetic erosion. Medium silt content causes four times higher erosion than the cavitation in clean water (without silt), and the combined effect of cavitation and erosion is 16 times greater than cavitation alone [131]. The particle entrainment in the cavitating medium increases the concentration of bubble nuclei and consequently promotes the occurrence of cavitation. The repeated bubble formation and collapsing may cause the rupture of the electrochemically formed protective passive film which results in decreased corrosion resistance of the metal [132].

2.4. Factors Influencing Erosion

There are various factors or variables that influence the erosion of material [27,102]. Their classification is as follows

- (i) Impingement variables: impingement angle, the velocity of silt and fluid, flux rate or concentration, the medium of flow [22,133–135].
- (ii) Particle variables: particle size, shape and hardness [136,137].
- (iii) Base material variables: microstructure, mechanical properties such as hardness, ductility, work hardening behavior and physical properties like specific heat, melting point, and density [128,138].

2.4.1. Impingement variables

The features of impingement variables include impingement angle, the velocity of water carrying silt, temperature, media of the flow, and turbulence.

(a) Impingement angle

The impingement angle is defined as the geometrical angle between a specimen surface and a nozzle axis. Erosion behavior of material strongly depends upon its nature. Ductile, brittle and composite material have different erosion behavior at different impingement angles

[22,139,140]. Finnie et al. [141] reported that ductile material suffers maximum erosion at an impact angle of about 20° and offer good erosion resistance at normal incidence angle, On the other hand, brittle materials suffer severe erosion under normal impact (90°) but provide excellent erosion resistance at a low angle [142] as demonstrated in Fig. 2.11

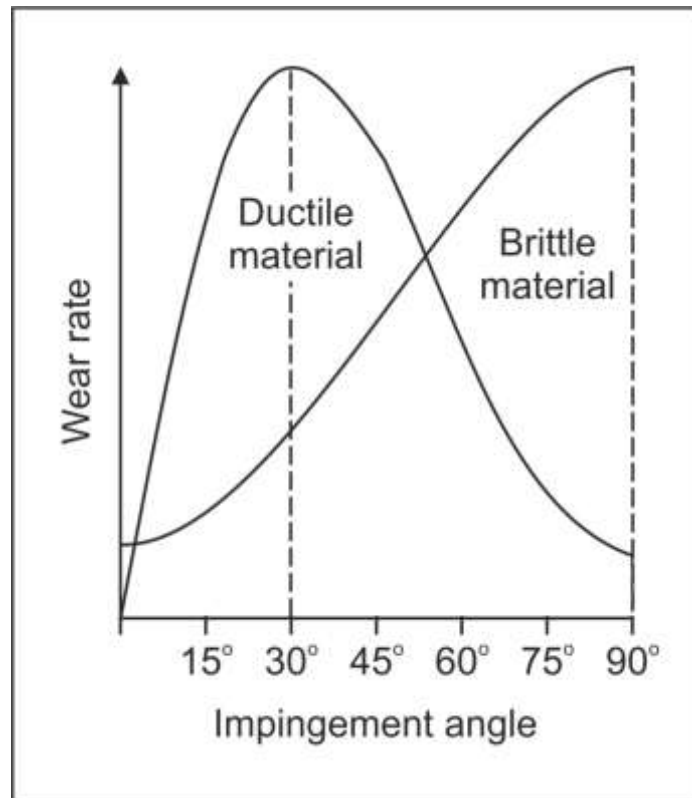


Fig. 2.11. The relationship between the impingement angle and the erosion rate for ductile and brittle material [141].

(b) Velocity of water and silt

The intensity of erosion is proportional to the cube of the velocity of water, carrying silt particles in a suspended condition. Material damage due to cutting and plastic deformation occurs at the same time, and the ratio of these damage mechanisms is depended on the velocity of the particle and the impingement angle together with other parameters [143]. Up to specific velocity, also referred as critical velocity or threshold velocity, the particle cannot skid on the surface because friction and cutting action does not take place. As the velocity increases higher than critical velocity, cutting component increases, which amplify the erosion rate drastically [15]. Fig. 2.12 shows the erosion versus time for type 1020 steel at 30 m/s and 70 m/s impingement velocity [144]. The relation between erosion and velocity of the particle is

$$\text{Erosion} \propto \text{Velocity}^n$$

Where the values of exponent ‘n’ depend on the material and other operating conditions. Considering the impact of particles due to kinetic energy, as the cause of material removal. Theoretically, the value of n is 3 [23,145,146].

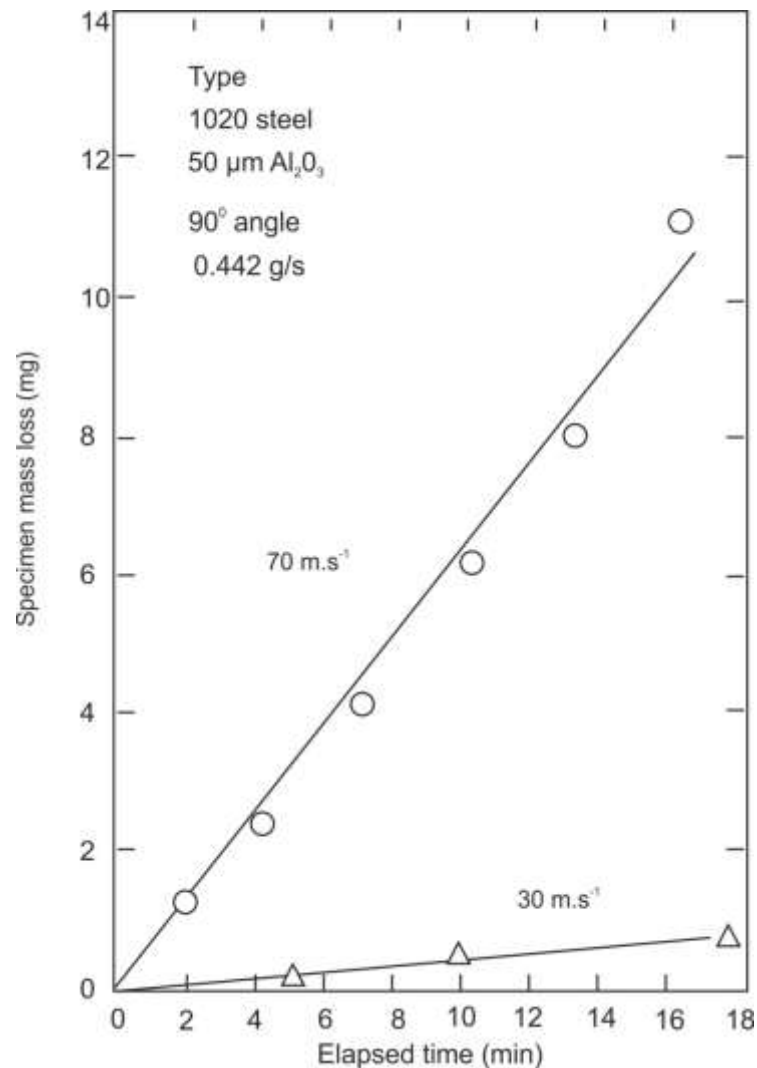


Fig. 2.12 Schematic diagram showing erosion versus time for type 1020 steel at 30 m/s and 70 m/s impingement velocity [144].

2.4.2. Particle variables

(a) Size and shape of the particle

The intensity of erosion is directly proportional to the impinging particles size. Particle sizes above 0.2 to 0.25 mm are extremely harmful. It has been found that large size silt particles (above 0.25 mm) even with hardness lesser than five on Moh’s scale cause wear [14,81,85]. Similarly, fine silt even with size less than 0.05 to 0.1 mm, containing quartz wears out the underwater parts. The fine silt can also be dangerous if the turbine is operating under the high head. Angular and sharp particles cause severe erosion in comparison to rounded ones [3].

Experiments by Bahadur et al. [147] have also shown variation in the erosion due to particle shape. Feng et al. [148] have reported that the shape and kinetic energy of solid particles are the dominant parameters in case of erosion of ductile materials.

(b) Hardness of particle

The intensity of the erosion is also directly proportional to the hardness of particles [149–152]. Those particles which have a hardness value above five on Moh's scale are considered harmful. Incidentally, most of the Himalayan silt contains more than 70 % Quartz particles on average with hardness value 7 in Moh's scale (700-1000VHN) [153]. Hence, the hardness of the particle is a highly influencing factor in the erosion rate. Tsai et al. [154] observed that the erosion of steels has increased by 40-100 times by SiC particles compared to that of coal. Levy et al. [155] have found that soft particles like calcite and apatite cause less wear due to breaking-up of particles during impact.

(c) Concentration

The silt concentration is one of the dominating factor influencing erosive wear rates. Concentration is the total mass (or volume) of impacting particles present in the unit mass (or volume) of the fluid. Turenne et al. [156] reported that wear increases with sand concentration because of the higher amount of erodent particles impinge on the surface of the sample. Padhy et. al. [4] concluded that the erosive wear rate increases with an increase in the silt concentration irrespective of the silt size. Sometimes, concentration is also called particle flux rate, or the mass of the impacting material per unit area and time. It can also be represented in terms of percentage of particles in a given fluid mass (or volume). Especially for river sedimentation, concentration is usually expressed in grams per liter (g/l). However, often parts per million (ppm) by weight is used, which is equivalent to mg/l, with the approximation of 1,000 ppm equal to 1 kg/m³ of water being normal usage.

2.4.3. Base material variables

The selection of material for the turbine components is strongly dependent on material variables [3,5]. The hardness of the material, its chemical composition, microstructure and its work hardening property influence the intensity of erosion. The choice of the material for a particular component is to be made considering its ability to meet the functional requirements like impact strength and ability to withstand cyclic loading in addition to its wear resistance [130].

(a) Microstructure

Microstructure plays a significant role in determining the erosion resistance of the material [21]. Adherence to the composition alone is not sufficient to impart proper erosion resistance. Salik et al. [157] performed erosion studies on AISI 1045 steel in the annealed, normalized, spheroidized, austempered, water quenched and tempered conditions. It was observed that the metallurgical changes affected the erosion resistance more significantly than the change in hardness. Green et al. [158] investigated the erosion of plain carbon steels. They found that erosion rate decreased with increasing cementite volume in pearlitic steels of constant lamellar spacing. Clark et al. [159] reported that ferritic structures in low carbon steels displayed lower erosion resistance. However, at comparable low hardness levels, the 0.35–0.45% carbon steels displayed much superior erosion resistance than the lower carbon materials. The erosion resistance was found to increase with growing share of pearlite in the structure. Suchanek et al. [25] found that the erosion resistance of quenched carbon and low alloy steels increased with the increase in C content. It was attributed to the presence of M_7C_3 and $M_{23}C_6$ complex carbides in the microstructure.

(b) Mechanical Properties

Erosion wear strongly depends on material mechanical properties. Since the erosion mechanism involves the formation of wide and deep ploughs containing lips at their edges, the various mechanical properties of the target material become an important parameter in affecting erosion. Various studies have shown that hardness is perhaps the most important property as it provides resistance to indentation and scratching by hard particles [3,21]. Thus for high erosion resistance, a material of high hardness with some definite amount of ductility is perhaps the best choice. Ductility and hardness have a roughly inverse relationship, increasing one invariably reduce the other. Naim et al. [160] found in 18% maraging steel that erosion increases with the increasing hardness at constant ductility, which was in conflict with the results of Finnie et al. [141], who showed that erosion decreases with increasing hardness. Naim et al. [160] also noted an increase in erosion rate as the ductility is reduced by cold working primarily at constant strength. In actual service, the erodent particles impact on the target surface and hence the impact energy should also play a major role.

2.5. Evolution of Hydroturbine Material

Till now various grades of steels have been developed for hydroturbine application [14,85]. The selection of materials for the hydraulic turbine is based on the criteria and requirements as listed in Table 2.3 Initially; turbine components were made of cast iron, which was later

replaced by cast steel and riveted plates due to the higher requirement of strength and toughness. In 1950's the Cast steel was replaced by fabricated steel. After this 18Cr8Ni Austenitic steel was developed which offered good resistance to corrosion and cavitation, however, their fatigue and creep resistance are poor. They still find application in small hydropower plants. Martensitic steel 13Cr1Ni was developed as a replacement for 18Cr8Ni, but due to lower Ni content hardness and toughness of steel was on the lower side which in turn results in reduced corrosion, cavitation, and sand erosion resistance [85]. In 1960 CA6NM (ASTM -A743) steel was developed. It is also known as 13Cr-4Ni MSS. It showed better erosion and corrosion resistance than all the steels developed before for hydro turbine application [161]. The reason for its better properties is owed to strength-to-toughness ratio. Currently, it finds wide application in the construction of hydroturbine components such as guide vanes, needle, nozzles, and labyrinth. A higher chromium content 16Cr-5Ni was also developed for salt water application. It has similar strength, higher erosion and corrosion resistance such as CA6NM steel [31].

Table 2.3 Requirements and criteria for the selection process of turbine material.

Requirements to be fulfilled	Criteria for the choice of material
. Operational Condition	Static load, Dynamic load, Temperature And Corrosion/Abrasion/Erosion/Cavitation
Operational Requirement	Reliability, Maintainability and Life time
Production feasibility	Weldability, Availability in market and Machinability
Price and delivery time	Material cost, labor cost and Delivery time

2.6. Martensitic Stainless Steel

The name 'martensite' comes from the German scientist 'Martens.' Martensitic grades of stainless steel were developed to provide a group of stainless steels which are corrosion resistant and hardenable by heat treatment [162]. They are similar to the carbon steels or low alloy steels, and they have a body-centered tetragonal crystal lattice, and they are classified as a hard ferro magnetic. Carbon percentage plays a major role in martensitic stainless steel. With a suitable heat treatment, the desired hardness and strength can be achieved in martensitic stainless steels since the strength of the steel obtained by the heat treatment

depends on the carbon content [163]. If the content of carbon is on the higher side, there is an increase in strength and hardness but a decrease in both ductility and toughness. The most widely used MSS grades are CA6NM, CB7Cu1, and CB7Cu2. CA6NM cast steel was initially developed at the George Fischer steel foundry to have a high impact strength, good weldability, and corrosion with a low carbon content. Temper embrittlement is reduced by adding molybdenum while increasing the nickel content achieves a microstructure free of δ -ferrite. However, in actual practice, some δ -ferrite is retained in cast structure [164].

The most commonly used grades of CA6NM are:

- CA6NM Gr A487 Class A
- CA6NM Gr A487 Class B
- CA6NM Gr A743

CA6NM Grade A743 is widely used for the construction of hydroturbine components. It also has an excellent corrosion resistance. A743 denotes the pressure code employed by the oil industry [165].

2.6.1. Effect of alloying elements

The effect of alloying elements present in martensitic stainless steel can be expressed as chromium (Cr) equivalent if they stabilize ferrite and nickel (Ni) equivalent if they stabilize the austenite. The Schaeffler diagram is used to predict the structure of stainless steel based on the function of Ni and Cr equivalent as shown in Fig. 2.13. The general effects of the alloying elements in martensitic stainless steel are as follows:

Chromium is the most important alloying element in the stainless steel and acts as a ferrite stabilizer. Chromium also increases the resistance to oxidation at high temperatures and erosion resistance. It is mainly responsible for the excellent corrosion resistance.

Nickel is a strong austenite stabilizer and facilitates the formation of austenite at room temperature. It is a non-carbide forming element and improves impact toughness and fatigue resistance in combination with Cr and Mo. Nickel is the only alloying element that increases hardness, tensile strength and toughness of the steel without any loss of ductility.

Carbon is a strong austenitizing and enhances the strength by interstitial solid solution hardening. If present in a greater amount, forms chromium carbides thus depleting Cr in the matrix and hence reduce the corrosion resistance. It also reduces the ductility, impact toughness, and weldability of the steel.

Manganese is also austenite stabilizer and can replace Ni to some extent. It is weak carbide former and favorably affects the forgeability and weldability. However greater contents of

Mn (>2%) results in an increased tendency towards cracking and distortion during quenching. Similar to Cr, it enhances segregation of the impurities to the grain boundary and induces temper embrittlement.

Molybdenum is pronounced carbide former and a ferrite stabilizer. It can induce secondary hardening during the tempering of quenched steel. The addition of Mo produces fine-grained steels, improves fatigue strength and can delay temper embrittlement. Molybdenum increases the resistance towards crevice condition in chloride atmosphere and pitting corrosion.

Silicon is a non-carbide former in steel and eliminates stress corrosion in Cr-Ni austenitic steels. Silicon, beyond 0.40%, causes a marked decrease in ductility in plain carbon steels [166,167].

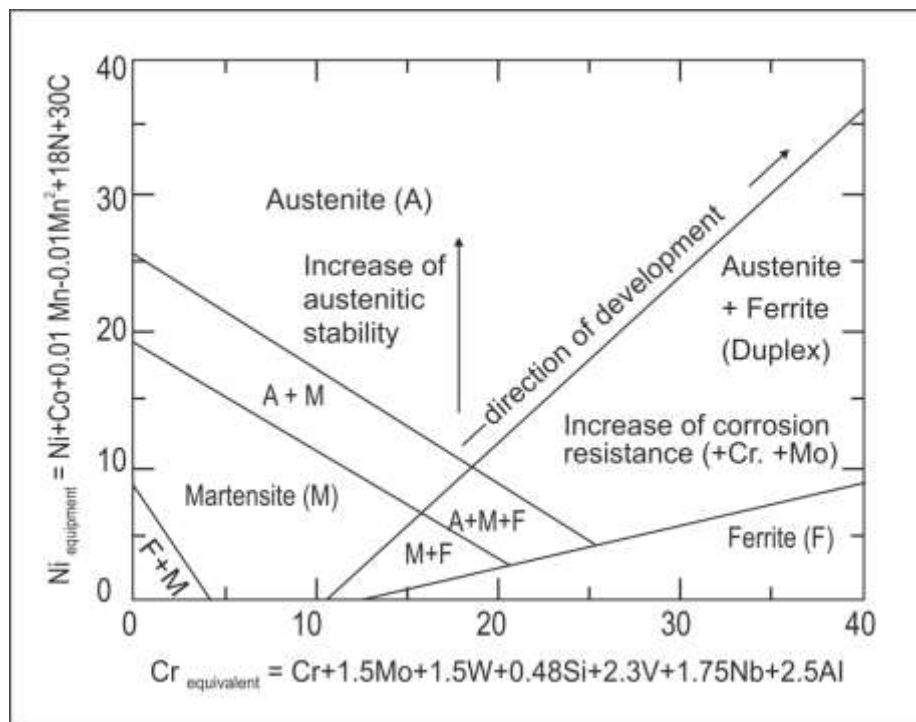


Fig. 2.13. Modified Schaeffler diagram [168].

2.7. Thermal spray process

Thermal spray process was invented by a young Swiss inventor named Dr. Max Schoop in 1911 [169]. Thermal spraying is a class of processes in which molten metal is deposited on a substrate by spraying [170]. Thermal spray coating processes differ from other conventional coating methods as it is not atomistic processes (individual ions or atoms attached to a surface). Instead, metallic, ceramic, cermet materials in the form of wire, rod or powder, are fed to a torch or gun with which they are heated to near or somewhat above their melting point [40,171]. Schematic diagram showing process of thermal spray coating is shown in Fig.

2.14. The resulting molten or nearly molten droplets of material are accelerated in a gas stream and projected against the surface to be coated. On impact, particles are flattened and solidified to form a disk-shaped structure called “splat” [172]. Overlapping “splats” on the substrate build up a coating of any desired thickness [173,174]. Schematic diagram showing process of coating deposition is shown in Fig. 2.15. The total coating thickness is usually generated in multiple passes of the coating device. The bonding between the substrate and coating is formed through mechanical interlocking [175].

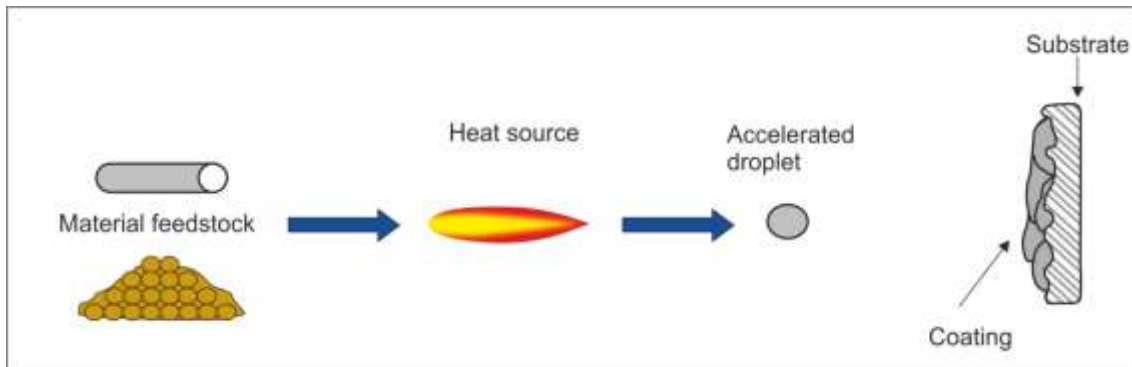


Fig. 2.14 Schematic diagram showing process of thermal spray coating.

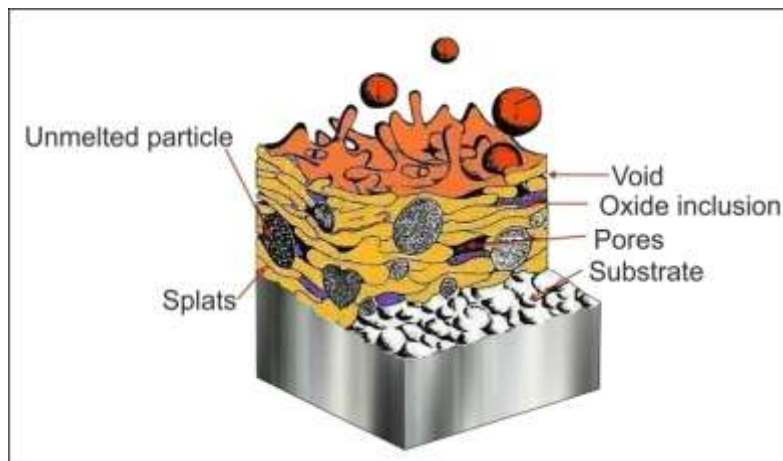


Fig. 2.15 Schematic diagram showing the process of coating deposition.

2.7.1. Various types of thermal spray process

There are different types of thermal spray techniques [176–179] that are developed till date and put into practice. The most widely used thermal spraying processes for erosion resistance application are as follow:

- (a) Plasma spraying
- (b) Detonation gun spraying (D-gun)
- (c) High-velocity oxy-fuel spraying (HVOF)
- (d) High-velocity air-fuel spraying (HVOF)

Thermal spray process is also classified according to process temperature and velocity that they employ, as shown in Fig. 2.16. HVOF and D-gun are industrially established thermal spray processes [180]. However, they lead to inferior coating properties which deteriorates the erosion resistance. Recent investigations have shown that high-velocity air fuel (HVOF) spraying is a rapidly emerging thermal spray technology for depositing surface coatings to combat wear, erosion and high-temperature corrosion and has challenged the D-Gun and HVOF process [60,61,181]. The comparison of the thermal spray processes and their essential characteristics [182] are given in Table 2.4.

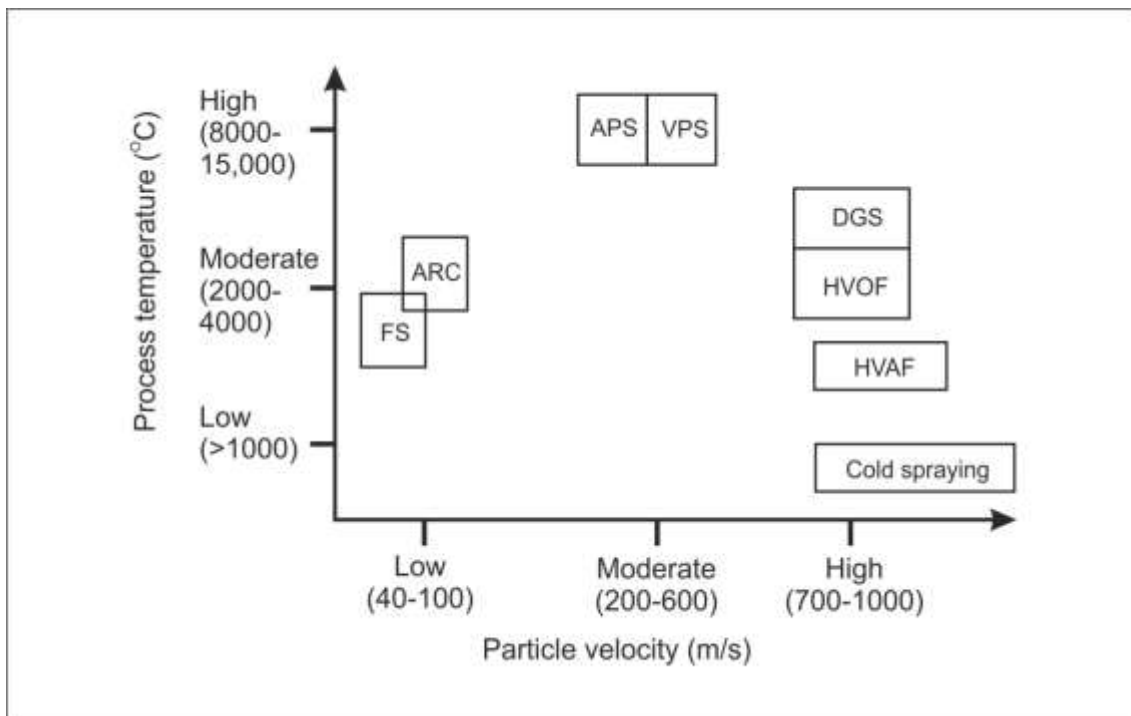


Fig. 2.16 Classification of thermal spray process according to process temperature and velocity [182].

Table 2.4 Comparison of thermal spray process and coating characteristics [182,183].

Attributes	Plasma	D-gun	HVOF	HVOF
Propellant/media	Inert gas	Detonation shock waves	Combustion jet	Combustion jet
Gas types	Ar, He, H ₂ , N ₂	O ₂ , C ₂ H ₂	C ₃ H ₆ , C ₃ H ₈ , C ₂ H ₂ , CH ₄ , C ₁₂ H ₂₆ , LPG, O ₂	C ₃ H ₆ , C ₃ H ₈ , air

Flame or exit plasma temperature, °C	8300	3900	3300	1900-1950
Particle velocity, m/s	200-800	910	200-1000	600-1250
Material feed rate, g/min	50-150	17	15-50	400 max
Density range, %	90 – 95	> 95	> 95	> 95
Bond strength, MPa	<68	82	68	>70
Oxides	Moderate to coarse	Small	Moderate to dispersed	Negligible

(a) **Plasma spraying**

In the plasma spray process, the electrical discharge between the cathode and anode heats up the working gas. This working gas expands in the atmosphere and generates plasma jet stream [98,183]. The thermal energy of the electric arc is used to melt the particles, and they are sprayed upon the substrate [177,184]. The working gas is usually a mixture of some gases like Ar+He+H₂ or Ar+He+N₂ [185]. The main advantage of the plasma spraying process is the high flame temperature that is generated depending on the gas used, and the operating energy often reaches 720 MJ [178]. The high temperature of the spray torch and the rapid cooling of deposits result in complex chemical transformations, which leads to the formation of metastable phases within the coatings, which are undesirable. The presence of oxygen is found to promote the nucleation of oxy carbides and extensive decarburization which are undesirable for erosion resistance point of view. The disadvantages of plasma spray process are the higher cost and complexity of the process. The plasma spray process [182] is shown schematically in Fig. 2.17.

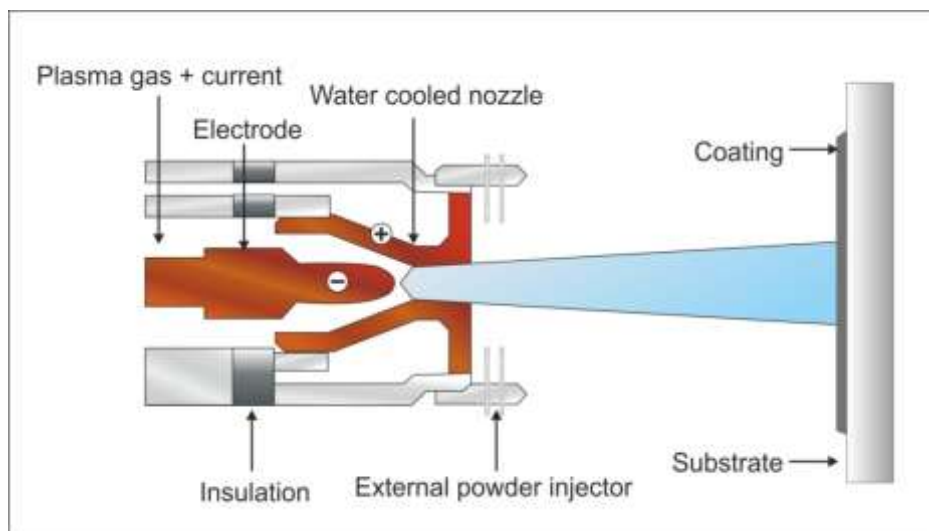


Fig. 2.17. Schematic diagram of plasma spray process adapted from [182].

(b) Detonation gun (D-Gun) spraying

The detonation gun process is invented in 1955 by Praxair Surface Technologies, Inc [186]. In D-Gun spray process mixture of Oxygen, Fuel and feedstock powder is introduced in long tube/barrel and is ignited by the spark plug. The resulting high-pressure shock waves (detonation wave) heats and accelerated the entrained powder particles in the barrel. These particles then accelerate out of the barrel and impact the component on which coating has to be deposited [177,187,188]. Depending upon the proportion of the combustion gases, the temperature of the hot gas stream can be as high as 3900°C. In D-gun spraying processes decomposition of the carbide based coating is minimized in comparison to plasma spraying due to lower heat enthalpy and shorter duration involved in the coating process [189,190]. The detonation gun spray process [182] is shown in Fig. 2.18.

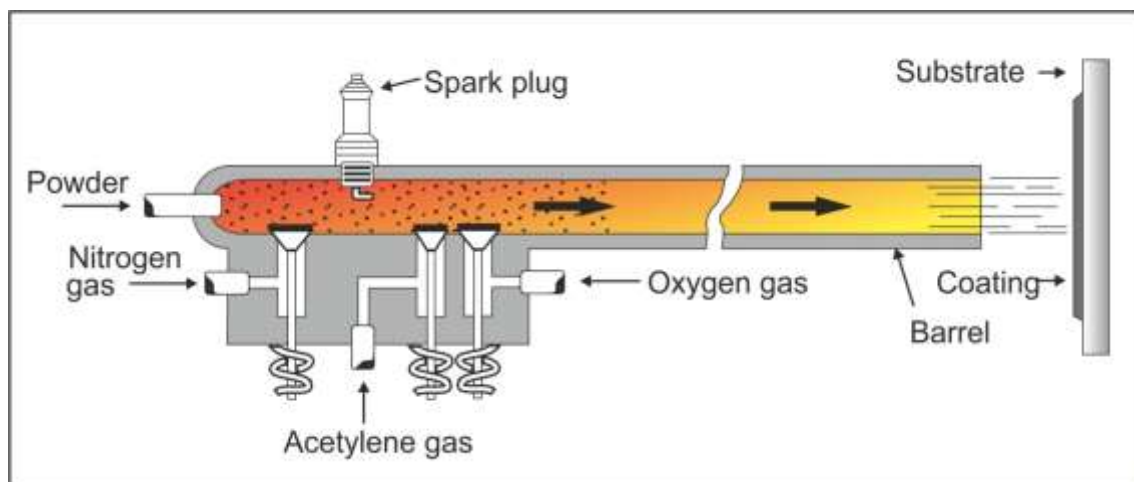


Fig. 2.18. Schematic diagram of detonation Gun (D-Gun) spraying process, adapted from [182].

(c) High-velocity oxy-fuel (HVOF) spray process

The high-velocity oxy fuel process is one of the most popular and industrially established thermal spray processes and has been widely adopted by many industries since the mid-1980s [191,192]. Currently, this process finds wide application in erosion resistance application of hydro turbine [34,42,47,193]. The HVOF coating process uses significantly lower deposition temperatures relative to air plasma spraying and D-Gun spraying methods [194,195]. Additionally, the higher particle velocity of HVOF spraying during deposition provides several advantages such as lower porosity, high mechanical interlocking, high adhesion strength and high hardness [196,197]. In the HVOF process, the combustion fuel and oxygen are led to the combustion chamber together with the spray powder. The resulting flame

expands supersonically through the nozzle. The speed of particle impact on the substrate is much greater, resulting in improved coating characteristics [198]. The powder may be fed axially or radially into the combustion chamber or supplied through a side nozzle and is melted and accelerated by the flame [176]. The main factors influencing the formation of HVOF thermal spray coatings are the fuel used and process parameters such as oxygen to fuel ratio, spray distance, and powder feed rate [199]. The high-velocity oxy-fuel spray process spray process is shown in Fig. 2.19.

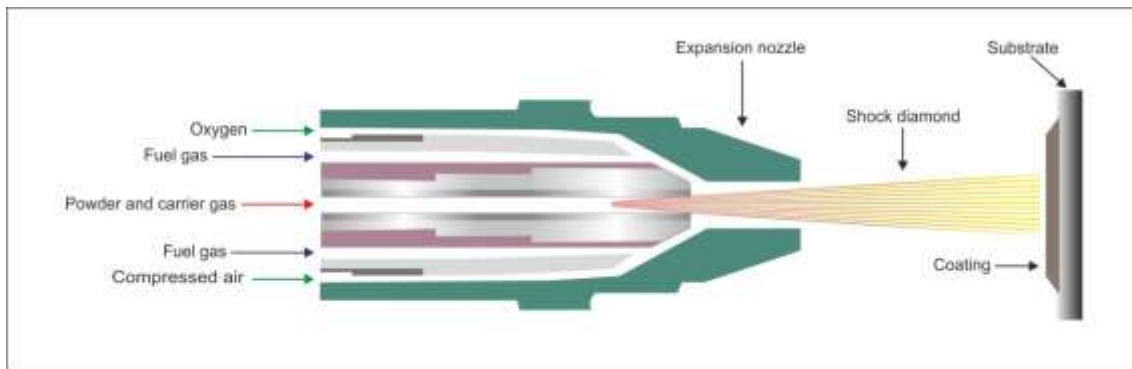


Fig. 2.19 Schematic diagram showing high-velocity oxy-fuel spray process, adapted from [200].

(d) High-velocity air-fuel (HVAF) spray process

The HVAF process is a fast emerging process, and it's a modification of the HVOF process [57,201]. In this process, coatings are sprayed with compressed air systems rather than oxygen since the former lead to lower contact time of spray particles with the flame and lower temperatures of materials, both of which lead to less decarburization of WC [54,56]. In the HVAF the spray particles are heated below the material melting point, thus remaining in a solid state during coating deposition [202,203]. In order to form a good-quality coating, they are accelerated to rather a high velocity (600-1250 m/s). Propane is the primary fuel gas in thermal spraying. However, propylene gas is used instead of propane to increase the gas temperature when spraying high-melting point materials. Compressed air provides cooling of the gun. When partially melted particles are impacting to the substrate, thermally softened particles undergoes intensive plastic deformation, forming a non-porous coating. Deformation of the substrate during particle impact results in a good coating bonding due to mechanical bonding at the substrate-particle interface [55,203,204]. The high-velocity oxy-fuel spray process spray process is shown in Fig. 2.20.

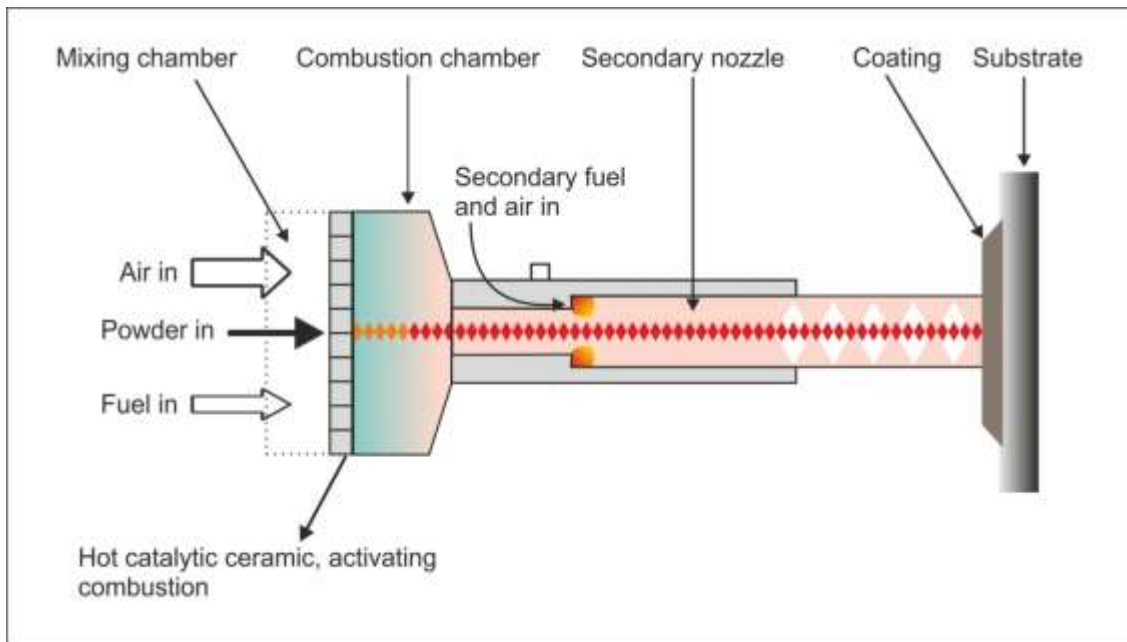


Fig. 2.20 Schematic diagram showing high-velocity air-fuel spray, adapted from [205].

2.7.2. WC-Co based coating for erosion resistance application

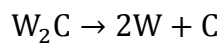
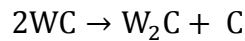
The selection of coating powder for erosion resistance application depends upon the severity and erosion environment. For hydroturbine application coating with high hardness and toughness is required, in order to resist the impact of hard silt particles [39]. In the past, Several different types [48,206,207] of coating powders have been attempted by various researchers to improve erosion resistance of turbine blades. However, It has been observed that WC-Co based cermet coating gives excellent erosion performance in comparison to other type of powders [42], which is due to the presence of hard WC particle in a tough and ductile Co-Cr matrix [208]. Cermet materials (ceramic and metal) in the form of coatings find wide application in hydro turbine components due to their combination of abrasion, erosion and corrosion resistance.

The addition of chromium to the cobalt binder has shown significant improvement in the erosion and corrosion resistance of the coating. Several attempts [34,42] have been made to reduce the erosion damage to hydroturbine underwater components by deposition of cermet coatings. Extensive works have been done on evaluation of different properties and performance of thermally sprayed cermet coatings. Most of these studies are around WC-Co coatings produced by various thermal spray techniques.

2.7.3. Decarburization in carbide based cermets

To obtain cermet coatings for erosion resistance application, it is necessary that they must possess adequate microstructure and inter-splat bonding [209]. The interfacial nature and

quality of coatings are significantly affected by decarburization and formation of W_2C phase [210]. Decarburization of WC leads into metastable phases which are brittle and undesirable, the presence of these phases reduce the erosion resistance [211,212]. The decomposition of WC is a two-step mechanism; the first reaction involves the decomposition of WC to W_2C followed by the oxidation assisted decarburization of W_2C to metallic tungsten [196,213,214].



The overall reaction is kinetically driven i.e. dependent on time and temperature, making the degree of decarburization sensitive to the process flame temperature and flame velocity. In HVOF process higher decarburization of WC is observed in comparison to HVAF process, which is mainly attributed to a higher temperature and in flight time. Higher process temperature leads to melting of WC particles which result into higher decarburization. In HVAF process higher velocity and lower flame temperature are used because of that particle in flight time is less and less decarburization of particles takes place [63,204,215].

2.7.4. Thermal spray coating properties for erosion resistant applications

Several properties are required for erosion resistance application and are as follow.

(a) Microstructural properties

The microstructure of coating can be observed by optical or electron microscope, and is a good indicator of the quality of the coating [204,216]. The microstructure of coating consists of laminar splats of WC particle in Co-Cr matrix [219]. Coating porosity is also a good indication of the quality of the coating [220,221]. In HVAF process lower porosity is generated which results in higher density, which in turn results in better erosion resistance. Medium coating porosity (1 - 5%) and high porosity coatings (in the range of 5 - 10%) of the same hardness deposited by different techniques (HVOF, D-gun, and Plasma spraying). The cross-sectional microstructure of WC-10Co-4Cr coating sprayed by HVOF and HVAF techniques are shown in Fig. 2.21, where the differences in porosity and interlamellar oxidation level in HVOF and HVAF coating can be seen. Therefore, HVAF coated steel shows higher erosion resistance than HVOF coated steel.

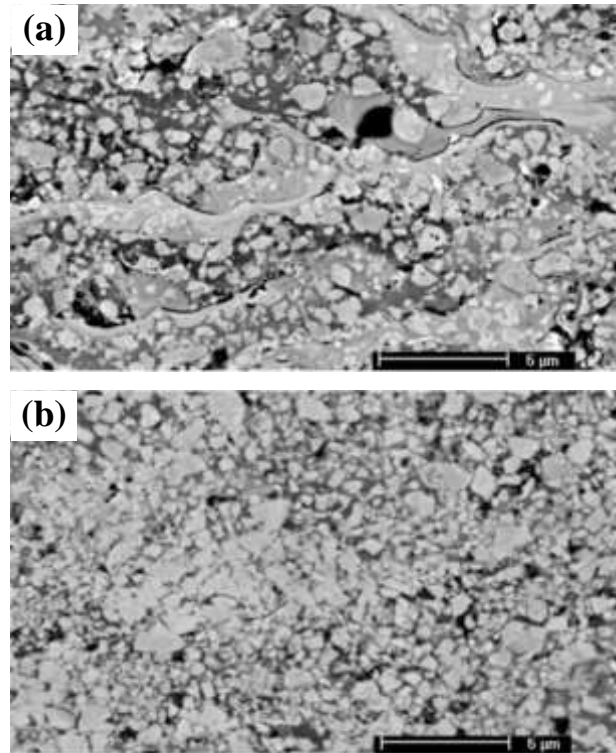


Fig. 2.21. Cross-sectional microstructure of WC-10Co-4Cr coating processed by (a) HVOF spraying, (b) HVAF spraying [64].

(b) Mechanical properties

The quality of thermal spray coatings and its erosion performance are strongly dependent upon its hardness. When coating hardness is higher than erodent hardness, then erosion does not take place. However, when the hardness of erodent is greater than coating micro cutting of the coating surface may take place [34]. Therefore high coating hardness is essential for getting better erosion resistance. Hardness improvement due to the formation of brittle phase W_2C is undesirable and result in lowering of erosion resistance. The toughness of a coating material is also an important mechanical characteristic since fracture determines the erosion resistance against the impacted erodent particles at different impact angles. Lima et al. [222] reported that the fracture toughness is the most relevant property corresponding to the erosion resistance of WC-Co spray coatings in comparison to the hardness. Thakur et al. [223] also observed that fracture toughness and hardness has a strong influence on the erosion behaviour of WC-CoCr nano-structured coating. At low impact angle of 15° and 30° , the micro cutting is more prominent, while at a normal impact angle of 90° , direct and fatigue fracture dominant. In conclusion, both high fracture toughness, hardness along with tensile adhesion strength of the coating are necessary at all erosion conditions of impact angles. At low impact

angle, high hardness and fracture toughness are required. At high impact angle of 90°, high toughness and low hardness are required to improve the erosion resistance.

2.7.5. Erosion performance of HVOF and HVAF sprayed WC-Co coatings

Thakur et. al. [223] investigated the slurry erosion behavior of HVOF sprayed WC–Co–Cr cermet coatings with two different WC grain sizes. Slurry erosion testing was performed using a pot-type slurry erosion tester to evaluate slurry erosion resistance of the coatings. It was observed that WC–Co–Cr cermet coating deposited with fine grain WC provides higher slurry erosion resistance as compared to conventional cermet coating. Goyal et al. [42] have conducted a slurry erosion studies on HVOF deposited WC-10Co-4Cr and $\text{Al}_2\text{O}_3 + 13\text{TiO}_2$ coatings on CF8M turbine. The bare steel and $\text{Al}_2\text{O}_3 + 13\text{TiO}_2$ coating showed the ductile and brittle mechanisms respectively whereas WC-10Co-4Cr coating exhibited mixed behavior (mainly ductile). It was observed that WC–10Co–4Cr coating was found to be useful to increase the slurry erosion resistance of steel remarkably. Santana et. al. [41] studied the solid particle erosion behaviour of high-velocity oxygen fuel (HVOF) sprayed WC-12Co and WC-10Co-4Cr coatings. The erosion tests were conducted at 30° and 90° impact angles using SiC particles It has been found that the WC-10Co-4Cr coating exhibited a higher erosive wear resistance as compared to the WC-12Co coating. Wang et. al.[66] studied the cavitation and slurry erosion resistances of high-velocity oxygen fuel (HVOF) and high-velocity air fuel (HVAF) sprayed WC-10Co-4Cr coatings. They observed that the HVAF-sprayed WC-10Co-4Cr coating has a lower degree of decarburization and better hardness, fracture toughness, porosity, cavitation and sand slurry erosion resistances than that of HVOF-sprayed WC-10Co-4Cr coatings respectively. Kumar et al. [34] studied the solid particle erosion performance of HVOF sprayed WC-10Co-4Cr coating on as-cast and solution treated Nitronic steel substrate. It is observed that coating on solution treated substrate was superior to cast substrate. The reason being that coating has dense and well-bonded structure with low porosity, less decarburization, and inter-splat oxidation. Higher erosion resistance of coated solution treated 23-8-N nitronic steel was attributed to combination of high fracture toughness and hardness of coating including optimum mechanical properties of the substrate.

2.8. Identification of Research Gap

Currently, HVOF process is widely used in hydropower plants for spraying WC-10Co-4Cr coating on CA6NM steel. However, this process leads to decarburization of WC into W_2C . Which reduces the erosion performance of the coating. The HVAF process is a fast emerging process, and it has potential to replace the HVOF coating for the hydroturbine application.

Most of the research done on HVAF coating is done to evaluate its wear performance. However, erosion studies of HVAF sprayed WC-10Co-4Cr coating on CA6NM steel for hydro turbine application is not addressed in the literature. Hence, in the present investigation, solid particle erosion performance of HVAF sprayed WC-10Co-4Cr coating on CA6NM steel at three different impingement angles, and two different impingement velocities were studied.

CHAPTER 3

Materials and Methods

This chapter describes the materials, equipment, and methodology employed to complete the present study. The chapter is divided into three sections. The first part discusses the selection of base material, evaluation of mechanical properties of steel and its characterization by field-emission scanning electron microscopy (FESEM) and X-Ray diffraction (XRD) methods. The second part of the study focuses on thermal spray coatings. It discusses feedstock powder selection, HVOF, HVAF coating deposition procedure and their respective process parameters. Feedstock powder characterization was carried out using FESEM and XRD. Both the coatings were characterized in terms of cross-sectional microstructure, porosity, volume fractions, phases, microhardness, fracture toughness and tensile adhesion. The last section of the chapter provides a detailed description of air jet erosion tester used to evaluate the erosion behavior of uncoated and coated steel.

3.1 Selection of Base Material

As-cast CA6NM martensitic stainless steel (ASTM A743 grade) is used as a substrate material for coating deposition and erosion behavior study. It finds wide application in the construction of hydroturbine components. The optimum combination of strength and ductility makes it a potential candidate for application in hydroturbine components [224]. The steel was received in as-cast condition from M/s Star Wire (India) Ltd., Ballabgarh (Haryana) in the form of 250 mm x 250 mm x 50 mm plate. As-cast steel test block was machined, and samples of 25 mm x 25 mm x 5 mm & 25 mm x 20 mm x 5 mm were prepared using wire-cut electric discharge machine (EDM) for erosion testing. Plates of 103 mm x 50 mm x 5 mm was also cut from the same test block for coating deposition. The chemical composition of the steel is given in Table 3.1.

Table 3.1 Chemical composition of as-cast CA6NM steel (wt %).

C	Cr	Ni	Mn	Si	Mo	S	P	Fe
0.06	11.88	3.65	0.61	0.45	0.61	0.002	0.028	Bal.

3.2 CA6NM Martensitic Stainless Steel Characterization

Mechanical properties and microstructure of steel have an enormous effect on its erosion performance. Therefore, It is necessary to characterize the martensitic steel before conducting the erosion testing and proceeding for coating deposition. It will help to study the correlation of structure properties and erosion performance of the martensitic steel. In the present investigation, following methods of the martensitic steel characterization and techniques were used:

- (i) X-Ray diffraction (XRD)
- (ii) Microhardness and roughness testing
- (iii) Tensile and Charpy impact testing
- (iv) Density measurement
- (v) Optical and FESEM analysis

3.2.1. XRD analysis

To identify the phase composition, the XRD pattern of martensitic steel was recorded with X'Pert Powder PANalytical with Cu K α radiation. It was operated at an applied voltage of 45 kV with 40 mA current. The XRD was used with a step size 0.02° and a step time of 0.6 s in the angle range 20° to 120°.

3.2.2. Microhardness and roughness testing

Vickers Microhardness of martensitic steel was measured using INNOVATEST (NEXUS 4000) hardness tester under a 300 g load with 10 s dwell time. Average of ten readings were reported. To provide similar erosion conditions samples were mirror polished and surface roughness was measured using a surface roughness tester (Surftest SJ 301, Mitutoyo).

3.2.3. Tensile and Charpy impact testing

Standard cylindrical tensile specimens were prepared with a gauge length of 20 mm and gauge diameter of 4 mm according to ASTM E8/E8M-15a [225] specifications as shown in Fig. 3.1. The tensile tests were performed on H25KTinius Olsen machine with a crosshead speed of 1 mm/min. Standard Charpy impact specimens of dimension 10 mm \times 10 mm \times 55 mm were prepared as per ASTM E23-12c [226] (V-notch) specification as shown in Fig. 3.2. Both the tests were conducted at room temperature, and an average of three samples are reported.

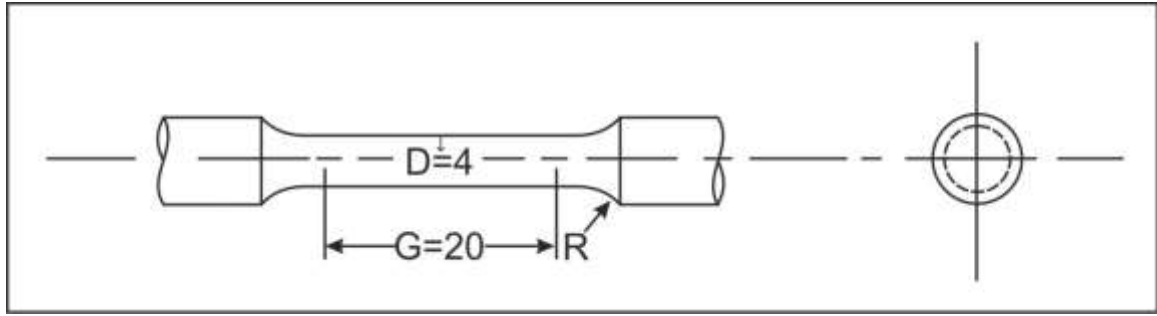


Fig. 3.1. Tensile test specimen as per ASTM E8/E8M-15a specification (all dimensions in mm) [225].

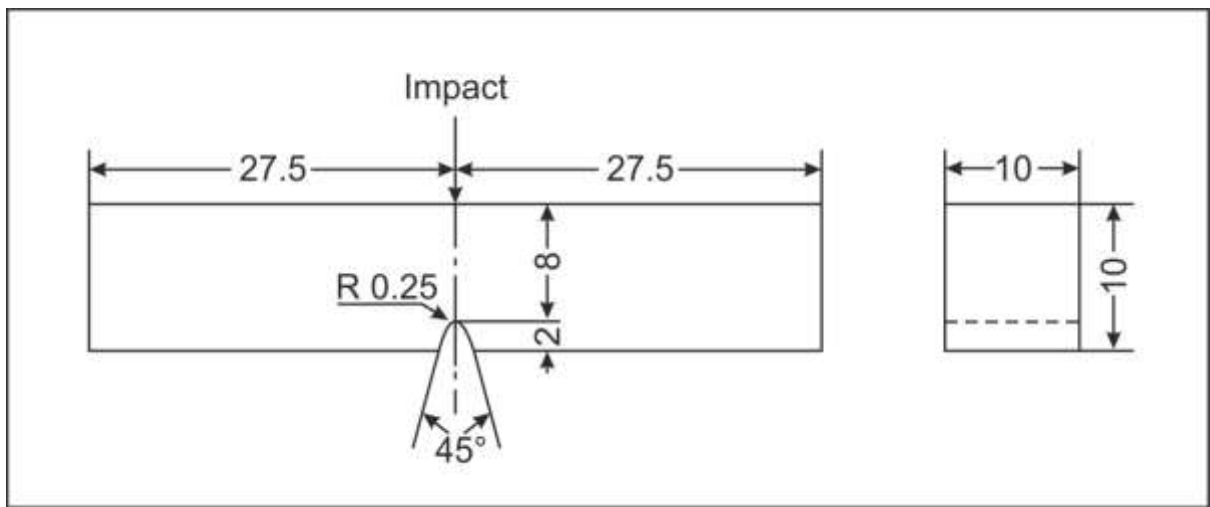


Fig. 3.2. Charpy V-notch impact test specimen as per ASTM E23-12c specification (all dimensions in mm) [226].

3.2.4. Density measurement

The experimental density of martensitic steel was measured as per ASTM B962-15 [144] Standard using Archimedes principle.

3.2.5. Optical and FESEM analysis

The microstructure of martensitic steel was examined using an inverted metallurgical microscope (Model: SuXma- Met 1, Conation Technologies) and field emission scanning electron microscope (NOVA Nano 450). FESEM operated at 20 kV. The samples were mirror polished and etched using picral (5 gm picric acid, 5 ml HCL and 95 ml ethanol) in both the cases.

-

3.3. Thermal Spray Coating

To overcome the problem of silt erosion in hydro turbine components, surface engineering route was selected. Thermal spray coating was deposited on as-cast CA6NM martensitic steel using HVOF and HVAF process. WC-10Co-4Cr powders were used for deposition as it results in significant improvement in hardness of the surface.

3.3.1. Selection of feedstock powders

Successful deposition of thermal spray coating is mainly dependent upon two factors i.e. thermal and kinetic energy. Either has to be dominant to achieve uniform coating. In HVOF spraying higher flame temperature and lower particle velocity is used, which accounts for high thermal and low kinetic energy [209]. On the other hand, HVAF process employs higher velocity and low flame temperature, which results in high kinetic and low thermal energy. HVOF focuses more on thermal energy and HVAF on Kinetic energy [67]. However, due to the application of higher thermal energy in HVOF process oxidation of WC takes place and it results in decarburization of the coating [53,208,227]. Finer the size of powder higher is the oxidation due to high surface to volume ratio which causes decarburization of WC into the molten binder at higher flame temperature [228,229]. Taking that into account a coarser powder is generally used for HVOF coating. In HVAF spraying finer powder is preferred as coarser powders need higher kinetic energy to deform and get deposited on the surface. At the same time as there is no risk of decarburization, finer powders are preferred as finer powder leads to better properties [52].

Therefore, two different sizes of WC-10Co-4Cr powder were used for HVOF and HVAF thermal spraying to achieve the greater deposition efficiency. Coarse agglomerated and sintered powder with particle size of -45 to $+15$ μm was used for HVOF thermal spraying. Fine powder (AMPERIT[®] 556.059, agglomerated and sintered) with the nominal particle size of -30 to $+5$ μm was used for HVAF spraying.

3.3.2. HVOF thermal spraying

Grit blasting was performed on the substrate before coating to remove any contamination from the surface of the substrate and also create a rough surface to increase the mechanical interlocking of the sprayed coating to the substrate. WC-10Co-4Cr powder was sprayed on martensitic steel plates (103 mm x 50 mm x 5 mm) using HVOF thermal spray system at M/s Metalizing Export Company Jodhpur India using Hypojet-HP2100 HVOF gun. The HVOF thermal spray unit mainly consists of three parts: (i) gasses control panel, (ii) powder feeder, and (iii) spray gun. The complete HVOF unit is shown in Fig. 3.3. Oxygen gas and liquid

petroleum gas (LPG) were used for the combustion and producing chemical energy for maintaining the temperature of the throat of the gun, where WC-10Co-4Cr powder remains in the semi-molten state. The pressure of gases was controlled by the control panel, which also indicates the discharge rate. Nitrogen gas is used for the cover atmosphere during spraying. Powder to be sprayed was filled in powder feeder and carried to the spray gun with the compressed air and nitrogen gas through the hoses. The HVOF process parameters are specified in Table 3.2. These process parameters were suggested by the coating manufacturer.

Table 3.2. HVOF process parameters.

Parameters	Value
Fuel	LPG
Spray distance (mm)	160-180
Powder feed rate (g/min)	40
Oxygen flow rate (l/min) & Oxygen pressure (MPa)	300 - 320 & 0.98
Air flow rate (l/min) & Air pressure (MPa)	440 & 0.5
Fuel flow rate (l/min) & Fuel pressure (MPa)	80 - 85 & 0.44
Deposition rate ($\mu\text{m}/\text{pass}$)	25-30
Carrier gas flow rate (SCFH)	10-15
Step size (mm)	3.5
Number of passes	13



(a) HVOF spraying gun



(b) Oxygen cylinder



(c) Powder feeder



(d) Gas control panel

Fig. 3.3. HVOF thermal spray coating unit at Metalizing Export Company, India

3.3.3. HVAF thermal spraying

Before spraying, the substrate was grit blasted by M3 HVAF gun (Uniquecoat Technologies USA). WC-10Co-4Cr powder was sprayed onto martensitic steel plates (103 mm x 50 mm x 5 mm) at M/s PTC Innovation Sweden using the same gun that was used for grit blasting the substrate. HVAF thermal spray system is shown in Fig. 3.4. Samples were mounted on a 300 mm round rotating carousel during spraying. The HVAF gun was placed in front of the samples at a stand-off/spray distance of 300 mm to give a horizontal spray jet. Propane was used as the primary combustion fuel gas (fuel 1) as well as secondary combustion gas (fuel 2). Nitrogen was used as the powder carrier gas, and compressed air jets were used to cool the samples during spraying. The HVAF process parameters are specified in Table 3.3. The optimum process parameters were suggested by coating manufacturer and are used industrially.

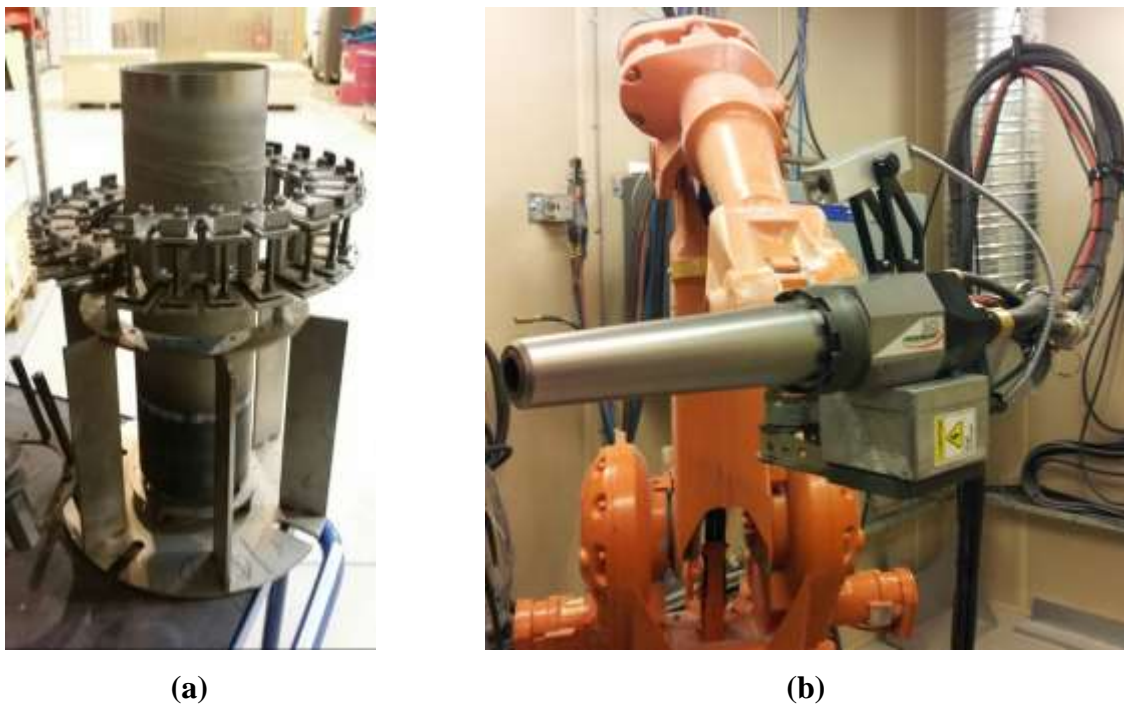


Fig. 3.4. (a) Round rotating carousel used for sample mounting, (b) HVAF thermal spray system (HVAF M3, Uniquecoat) at PTC Innovation, Sweden.

Table 3.3 HVAF process parameters.

Parameters	Value
Fuel 1 and Fuel 2	Propane
Spray distance (mm)	300
Gun traverse velocity (m/min)	100
Step size (mm)	5
Powder feed rate (g/min)	200
Nitrogen carrier gas flow (l/min)	60
Air pressure (MPa)	0.80
Fuel 1 pressure (MPa)	0.69
Fuel 2 pressure (MPa)	0.72
Deposition Rate ($\mu\text{m}/\text{pass}$)	20
Number of passes	17

3.4. Feedstock Powder Characterization

Characteristics of feedstock powder play a major role in the microstructure and performance of the coatings. Characterization of powder was conducted as follows:

- (i) FESEM for morphology analysis.
- (ii) XRD was used to determine constituent phases in the feedstock powders

PANalytical instrument was used to perform the XRD analysis in the angle range of 20° to 100° with a step size 0.02° and a step time of 0.6 s.

3.5. Coating Characterization

Erosion performance of HVOF and HVAF coating is strongly dependent on coating Microstructural features. Examination of microstructural features is important to analyze the quality of coatings. In the present study, following methods of coating characterization and techniques were used:

3.5.1. Coating roughness

The surface roughness of as-sprayed thermal sprayed coating gives important insight into the coating process and its quality. After deposition of WC-10Co-4Cr coating on CA6NM martensitic steel using HVOF and HVAF process, as-sprayed surface roughness was measured using surface roughness tester (Model: SJ410, Mitutoyo). To achieve uniform

starting condition before erosion, all the samples were mirror polished, and surface roughness was measured using the same tester.

3.5.2. XRD analysis

XRD was utilized to analyze the phases present in HVOF and HVAF sprayed WC-10Co-4Cr coating over an angle range of 20° to 100°. The index of carbide retention (I) in coating was calculated by the integral intensities of (100) peak of WC (I_{WC}) at $2\theta = 35.6^\circ$ and the (101) peak of W_2C (I_{W_2C}) at $2\theta = 39.6^\circ$. It gives the value of WC retention against the formation of W_2C phase in coating. It is calculated using equation [230] as given below:

$$I = \frac{I_{WC}}{(I_{WC} + I_{W_2C})} \quad (3.1)$$

3.5.3. FESEM & EDS analysis

To characterize the microstructure of coating, samples were cut using the linear precision saw and hot mounted in resin powder (PhenoCure, BUEHLER) using the automatic mounting press (SimpliMet 3000, BUEHLER). Mounted samples were polished to 1 μm finish. The polished cross section of the coating was observed using FESEM to analyze the microstructure of coating. EDS analysis is used to analyze the phases present in the coating. The coating thickness was measured using FESEM images taken at low magnification (200X) on polished cross-sections.

3.5.4. Coating density and porosity

Image analysis was done on cross-sectional FESEM micrograph (10,000X) of the coating to evaluate volume fraction of the WC, binder (Co-Cr) and porosity. The density of the coating was calculated by the volume fraction of the WC and binder (Co-Cr). The density of the WC ($\rho_{WC} = 15.7 \text{ g/cm}^3$) and binder ($\rho_{Co-Cr} = 8.6 \text{ g/cm}^3$) was taken to calculate the density of the coating [34,217].

3.5.5. Microhardness

Vickers micro Hardness measurements of HVOF and HVAF sprayed coating were performed on the polished transverse section of the coatings with INNOVATEST (NEXUS 4000) hardness tester at 300 g load with 10 s dwell time.

3.5.6. Fracture toughness

The fracture toughness of coating was determined by the indentation method. A Vickers indenter was used on metallographically prepared cross sections of coating with a 5 kg load with 10 s dwell time. The indenter was loaded such that the two indent diagonals were

parallel and perpendicular to the substrate/coating interface respectively. The length of the cracks, both parallel and normal to the substrate-coating interface, produced by the indentation technique was measured using FESEM micrograph.

The fracture toughness (K_c) of the coatings was determined by the indentation method using the Evans and Wilshaw equation [232] as given below:

$$K_c = 0.079 \frac{P}{a^{3/2}} \log 4.5 \left(\frac{a}{c} \right) \quad (3.2)$$

Where 'P' applied indentation load (mN), and 'a' and 'c' correspond to the length of the indentation half-diagonal (μm) and crack length from the center of the indent (μm), respectively as shown in Fig. 3.5.

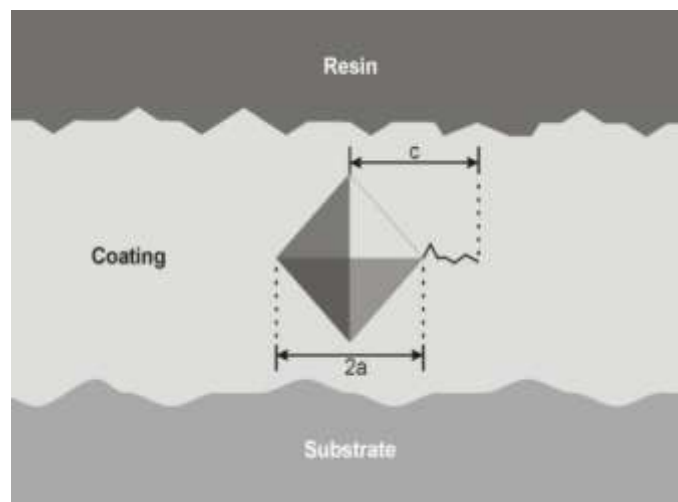


Fig. 3.5. Schematic depiction of the Vickers indentation and crack geometry.

3.5.7. Tensile adhesion

The tensile adhesion of thermal spray coating was measured using ASTM C633-13 [233] standard. In this test, two cylindrical sample were glued together in which one sample is coated and other remained uncoated. Tensile load is applied on the samples and the strength to part the samples is calculated as tensile adhesion of samples as shown in Fig. 3.6 [234,235].

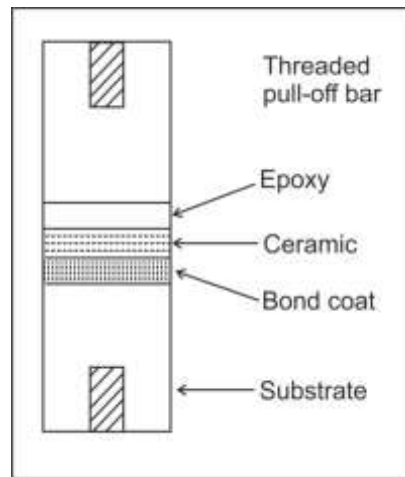


Fig. 3.6. Schematic diagram showing tensile adhesion test.

3.6. Solid Particle Erosion Testing

The erosion behavior of as-cast and coated CA6NM steel were evaluated using air jet erosion tester (Model: TR, DUCOM Bangalore). Erosion test was performed as per ASTM G-76-13 [236] test standard. Schematic diagram of the air jet erosion tester [34] used for these experiments is shown in Fig. 3.7. The erosion test parameters utilized in the present study are provided in Table 3.4. In this erosion tester, the abrasive particles were accelerated from a nozzle by using a compressed air stream that caused them to impact on the surface of the material. Figure 3.8 shows the FESEM micrograph of alumina particle (50 μm) used for erosion testing; it was observed that particles are flaky and angular in shape. To provide an initial standard surface condition before erosion test, all specimen were abraded using 0/0, 1/0, 2/0, 3/0, and 4/0 grades of emery paper. Cloth wheel polishing was done to obtain a mirror finish using a diamond paste. Each sample was removed after every 2 min to determine the mass loss. The impingement angles used for the tests were 30°, 60° and 90°. These angles were selected to evaluate the behaviour of these materials at low, intermediate and high impingement angles. A particle velocity of 35 m/s and 70 m/s is used to replicate severe erosion condition, and an abrasive flow rate of 2 g/min were used to conduct the tests. Particle velocity was measured with an accuracy of $\pm 2\text{m/s}$, using the double disc rotating method [95,237,238] as shown in Fig. 3.9.

In this apparatus, two disks are attached to a common rotating shaft. A radial slot is cut on top disk, and the lower disk is coated with thin layer of paint. A stream of erodent is allowed to strike on top disk for 10 minutes, and elliptical shape scar is formed on the bottom disk, which is measured using a protractor. Velocity is measured using formula as given below

$$V = [H \times N] \times [360/A] \quad (3.3)$$

Where H = Distance between disks in m (0.03)

N = Revolution per second of double disk system (5000/60)

A = Angle of Incidence

The abrasive flow rate was measured by collecting the abrasive in a container during 1 min. Before and after the tests, each specimen was weighed using a digital balance with an accuracy of 0.0001 g to observe the difference in weight loss for each test. The weight loss was converted into volume loss to obtain the precise data because the WC-10Co-4Cr coating and substrate possess different densities. Micrographs of the eroded surfaces were obtained using an FESEM to analyze the specimens and to identify the possible erosion mechanisms.

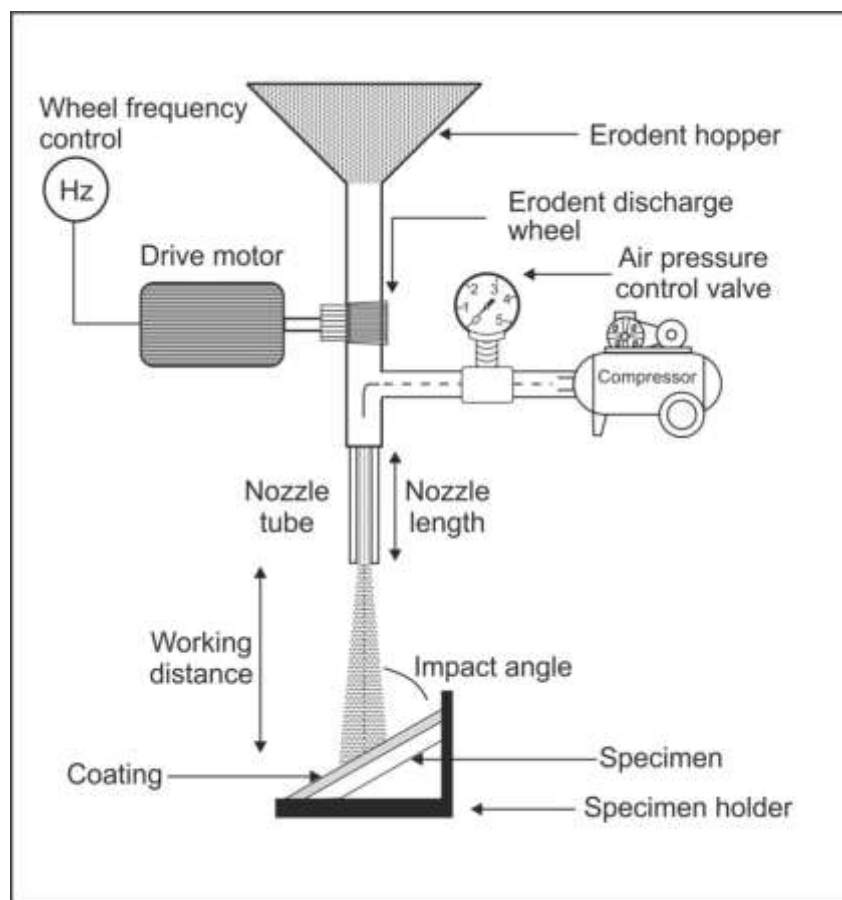


Fig. 3.7. Schematic view of air jet erosion tester used for solid particle erosion testing

[34].

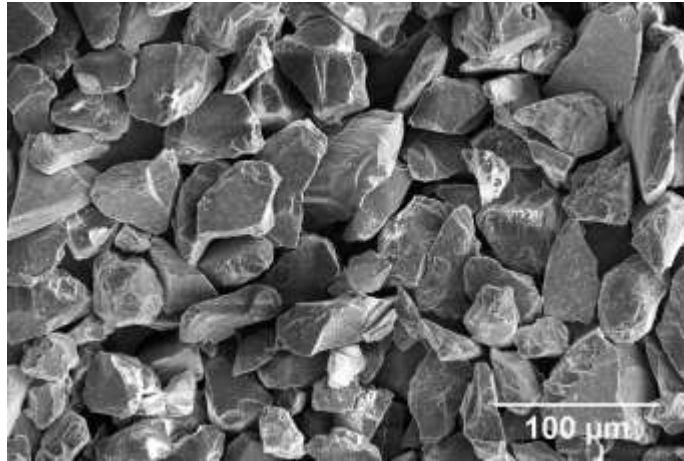


Fig. 3.8. Morphology of alumina particles.

Table 3.4 Parameters used in solid particle erosion testing.

Erodent particle	Alumina
Average erodent particle size	50 μm
Impact velocity	35 & 70 m/s
Erodent discharge	2 gm/min
Test gas	compressed air
Standoff distance	10 mm
Nozzle diameter	1.5 mm
Impingement angle	30°, 60° and 90°
Test duration	Cycles of 2 min
Test temperature	Room temperature
Sample size	(25x25x5) and (25x20x5) mm

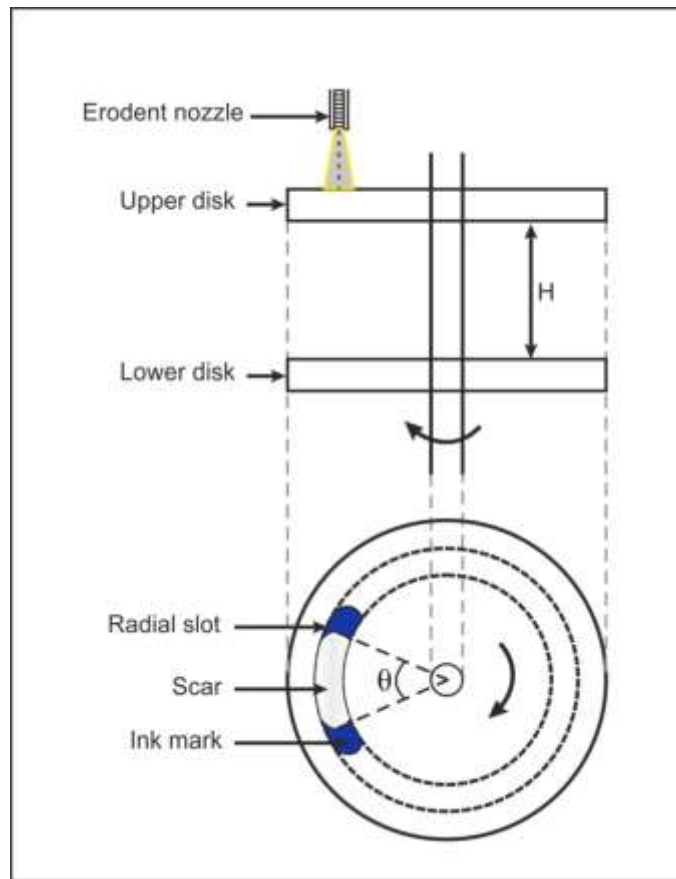


Fig. 3.9. Schematic diagram of the double disk apparatus.

CHAPTER 4

Results and Discussions

The results of the experimental work performed in this study and their discussion are presented in this chapter. This chapter is divided into four sections. The first section discusses the characterization of CA6NM steel. The second section deals with erosion performance of CA6NM steel at different impingement angles and velocities. The third section discusses the characterization of HVOF sprayed WC-10Co-4Cr coated CA6NM steel and its erosion performance at different impingement angles and velocities. The last section focuses on HVAF sprayed WC-10Co-4Cr coating on CA6NM steel and its characterization. It also discusses erosion performance at different impingement angles and velocities.

4.1. Characterization of CA6NM Steel

Erosion performance of steel mainly depends upon its microstructure and mechanical properties. Evaluation of microstructure and properties are necessary to gain insight into erosion behavior of steel. In this section microstructure, XRD study, mechanical properties of CA6NM steel are presented.

4.1.1. Microstructure and XRD study

The optical and FESEM microstructure of as-cast CA6NM steel is illustrated in Fig. 4.1 (a,b). The microstructure of as-cast CA6NM steel consisted of lath martensitic needles. Apart from them, the structure also exhibited the presence of delta ferrite [15,28]. X-ray diffraction patterns of the as-cast CA6NM is shown in Figure 4.2. The diffraction pattern showed peaks of martensite.

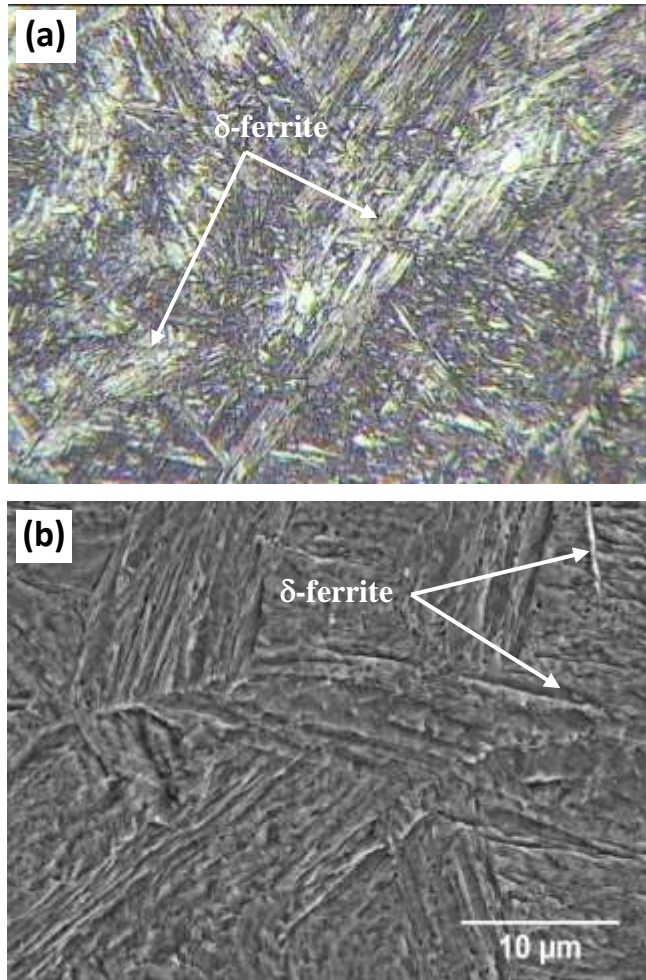


Fig. 4.1. (a) Optical and (b) FESEM micrograph of as-cast CA6NM steel.

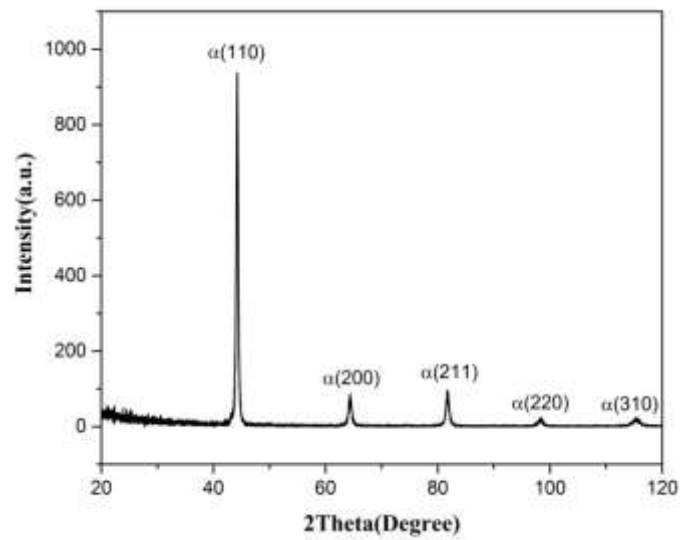


Fig. 4.2. XRD pattern of as-cast CA6NM steel

4.1.2. Mechanical properties and density

Analysis of mechanical properties of steel is important in understanding its erosion behavior. Table 4.1 shows the mechanical properties and density of as-cast CA6NM steel. It was observed that steel in cast condition contains an optimum combination of strength and ductility.

Table 4.1 Mechanical properties and density of as-cast CA6NM steel.

Mechanical Properties	Cast CA6NM steel
Microhardness (HV _{0.3})	338 ± 29
YS (MPa)	652 ± 48
UTS (MPa)	892 ± 66
Ductility (% elongation)	13 ± 4
Impact energy (J)	42 ± 8
Density (g/cm ³)	7.70

4.1.3. Fractography of tensile and Charpy specimen

Tensile fractographs of as-cast CA6NM steel at lower and higher magnifications are shown in Fig 4.3. The fracture surface of the as-cast CA6NM steel was ductile, and dimples can be seen on the fractured surface, which points to the fact that plastic deformation had taken place before fracture.

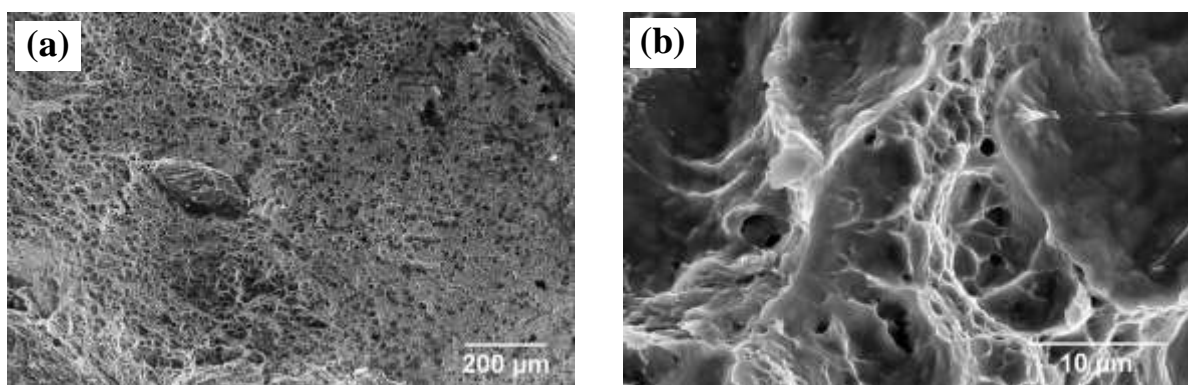


Fig. 4.3. FESEM fractographs of a tensile specimen of as-cast CA6NM steel (a) lower magnification (150 X) and (b) higher magnification (5000 X).

The FESEM fractographs of Charpy V-notch fractured samples of as-cast CA6NM steel is given in Fig. 4.4 at lower and higher magnification respectively. Fracture surface showed ductile features. It mainly composed of dimples, which points to relatively high toughness

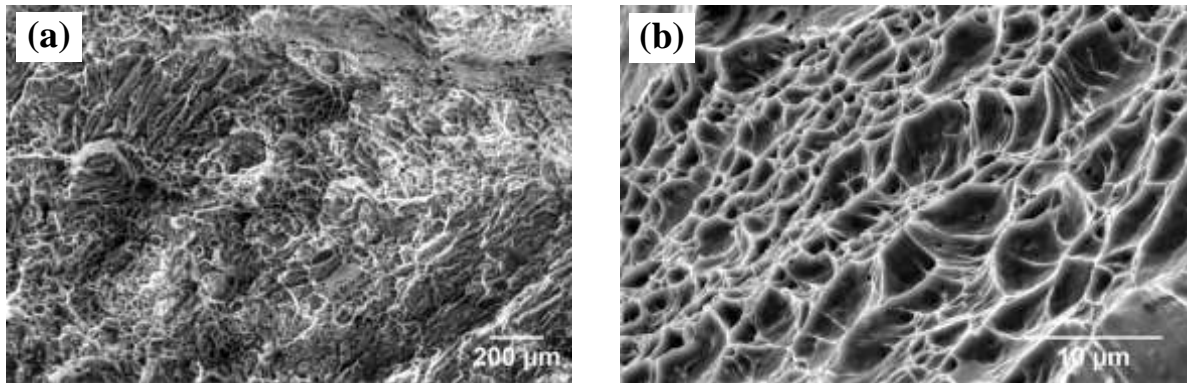


Fig. 4.4. FESEM fractographs of Charpy impact specimen of Cast CA6NM steel (a) lower magnification (100 X) and (b) higher magnification (5000 X).

4.2. Erosion Performance of CA6NM Steel

Erosion performance of CA6NM steel was evaluated at 35 m/s and 70 m/s impingement velocities and three different impingement angles (30°, 60° and 90°) using alumina as erodent. Effect of impingement angle on cumulative volume loss and FESEM images of eroded surfaces are presented in this section.

4.2.1. Effect of impingement angle on formation of erosion scar

Erosion mechanism of material is dependent upon the angle of impingement between erodent and surface of the sample. Variation in the angle of impingement results into a change of erosion scar morphology. Schematic diagram showing the interaction of erodent with the surface at different impingement angles is shown in Fig. 4.5. It was observed that as the impingement angle rose from 30° to 90°, vertical component of the kinetic energy of impacting particle increases. This results in a decrease of area of contact between erodent and surface, thus reducing the size of erosion scar that formed on the surface of the samples. Photographs of the erosion scar formed on samples at 30°, 60° and 90° impingement angles and their respective sample holders are shown in Fig. 4.6. The sample size used for 30° impingement angle is 25 mm x 20 mm x 5 mm. While for 60° and 90° impingement angle the sample size is 25 mm x 25 mm x 5 mm. The smaller size of 30° impingement angle sample prevents the contact of sample and nozzle during retrieving and placing of the sample in the holder. The center region of the eroded scar (Region"1") showed the region of erosion, and

on its periphery, it surrounded by a region of elastically loaded material (Region "2") [239]. At 30° impingement angle, the contact area of erodent with the substrate was high, and erosion scar of an ellipsoid shape covering the entire length of the sample was observed. At 60° impingement angle material was eroded forming a perfect ellipsoid shape depression, it was due to the lower contact area than that of 30° impingement angle. Whereas at 90° impingement angle, the contact area of erodent with the surface was lowest and it created a perfect circular shape depression.

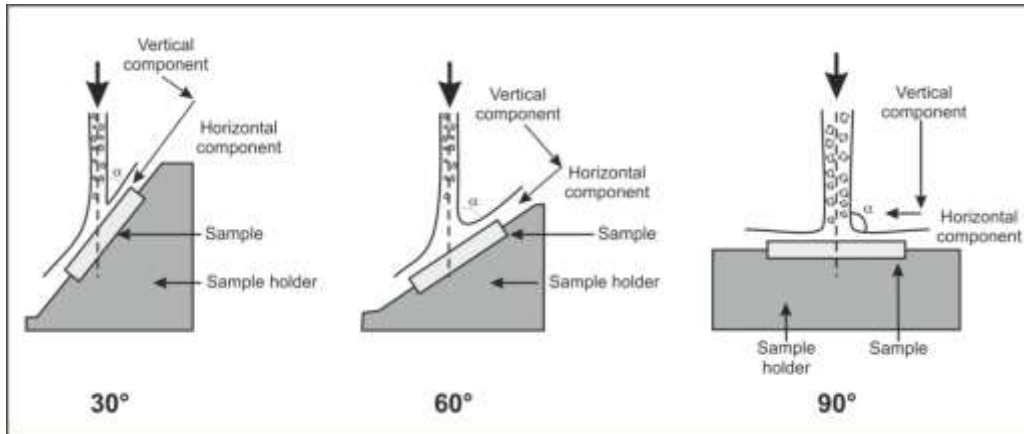


Fig. 4.5. Schematic diagram showing interaction of erodent with surface of sample at (a) 30°, (b) 60° and (c) 90° impingement angle.

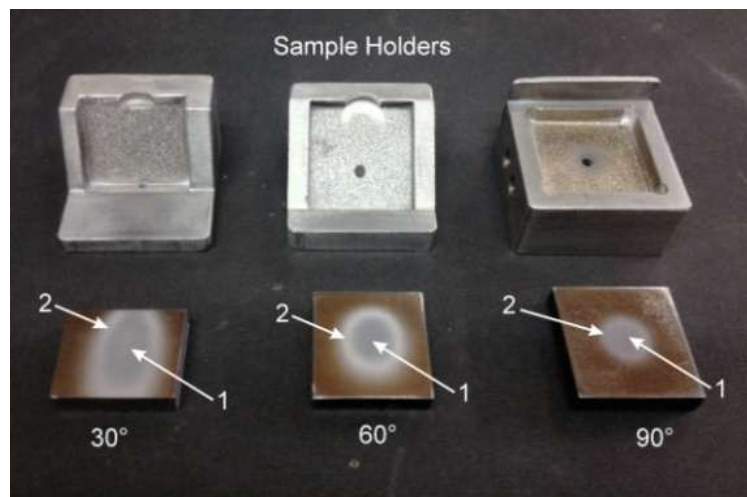


Fig. 4.6. Photographs of the erosion scar formed on eroded samples at 30°, 60° and 90° impingement angles and their respective sample holder.

4.2.2. Effect of impingement angles and velocities on cumulative volume loss

Cumulative volume loss of the as-cast CA6NM steel as a function of erosion time at 30°, 60° and 90° impingement angle for 35 m/s and 70 m/s impingement velocities are shown in Fig. 4.7 to Fig. 4.9. It was observed that cumulative volume loss increased linearly with increase in erosion time. It can be observed that cumulative volume loss at 30°, 60° and 90° impingement angles for 35 m/s impingement velocity was lower than that observed at 70 m/s impingement velocity. It was mainly due to the higher kinetic energy of impacting particles at higher impact velocities. The relationship between cumulative volume loss and impingement angles for as-cast CA6NM steel is shown in Fig. 4.10. It was noticed that cumulative volume loss continuously decreased with increasing impingement angle and reached a minimum at 90° angle. Maximum cumulative volume loss was observed at 30° impingement angle, which points to the fact that the material eroded in a ductile manner, the same behavior was also observed by other researchers [240–242] in earlier investigations on ductile materials.

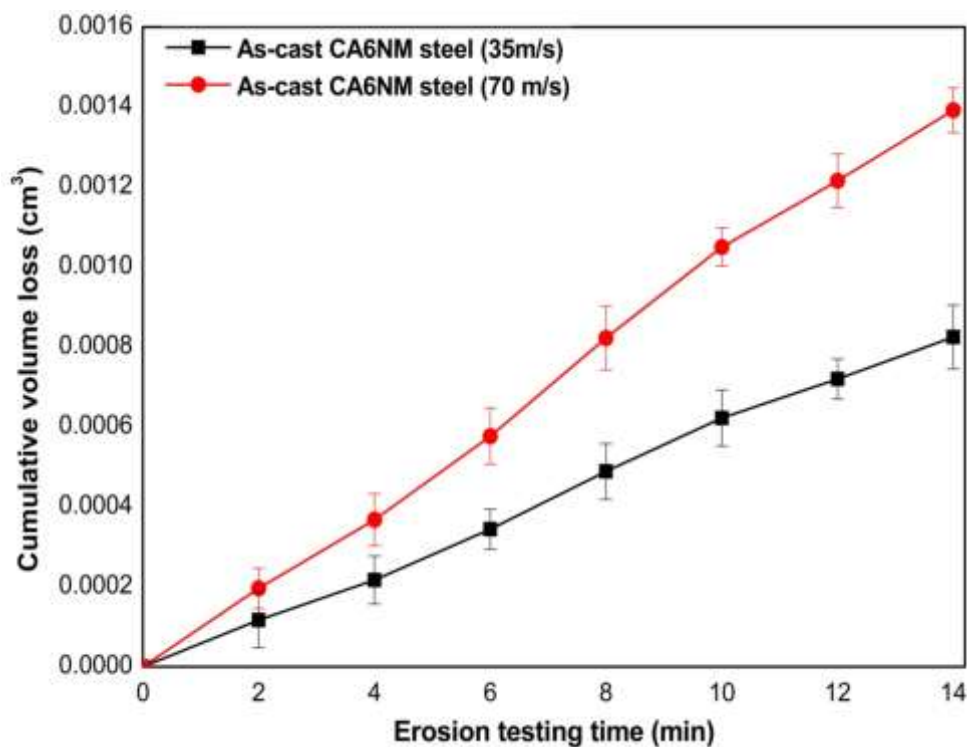


Fig. 4.7. Cumulative volume loss of as-cast CA6NM steel as a function of erosion time at 30° impingement angle for 35 m/s and 70 m/s impingement velocities.

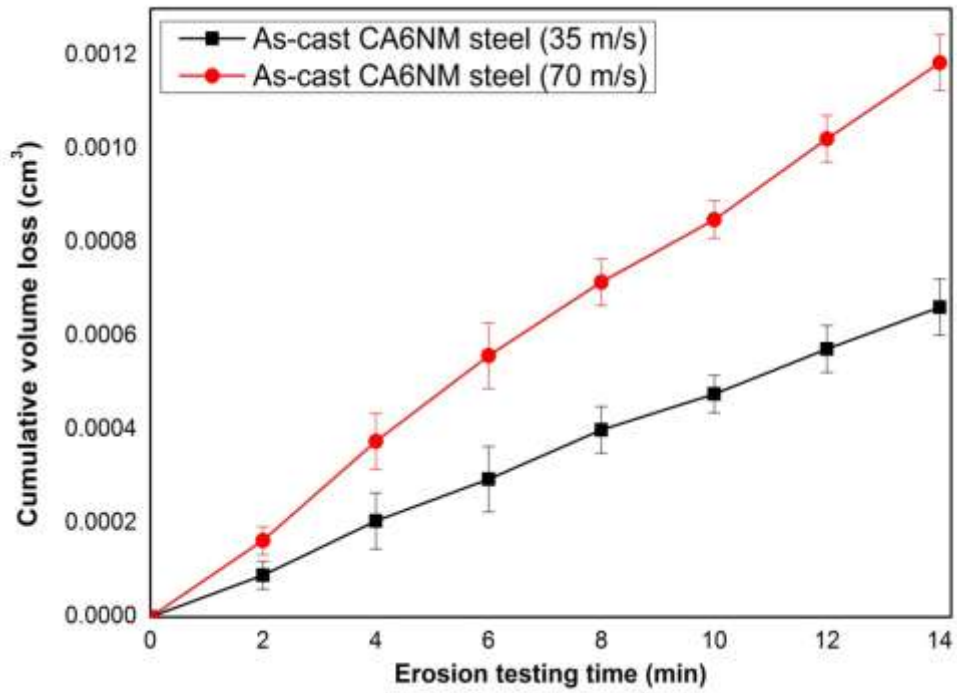


Fig. 4.8. Cumulative volume loss of as-cast CA6NM steel as a function of erosion time at 60° impingement angle for 35 m/s and 70 m/s impingement velocities.

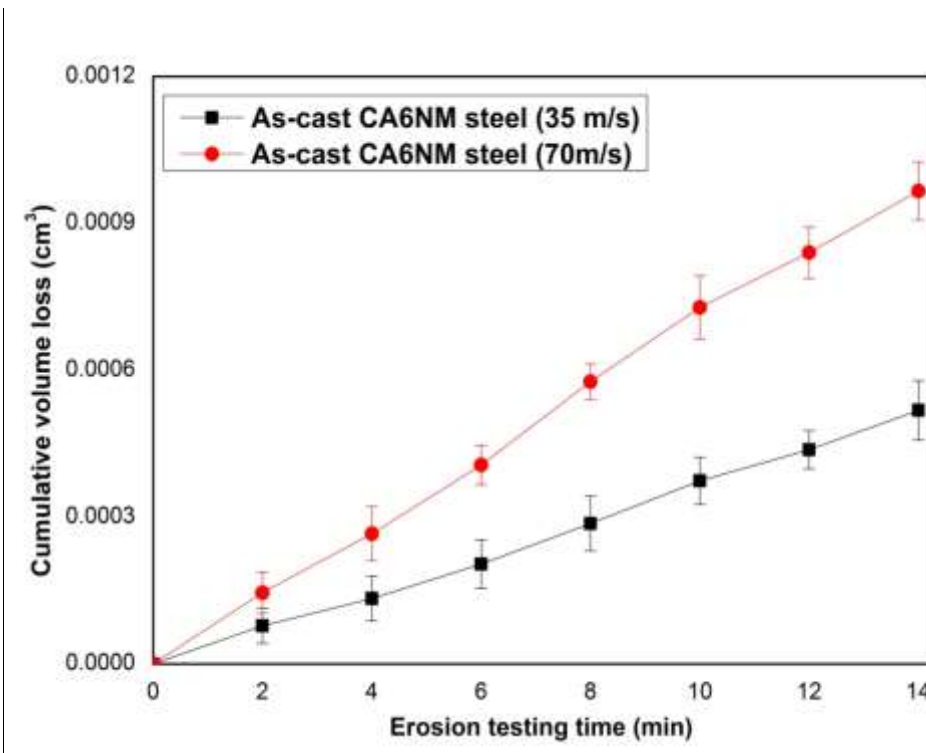


Fig. 4.9. Cumulative volume loss of as-cast CA6NM steel as a function of erosion time at 90° impingement angle for 35 m/s and 70 m/s impingement velocities.

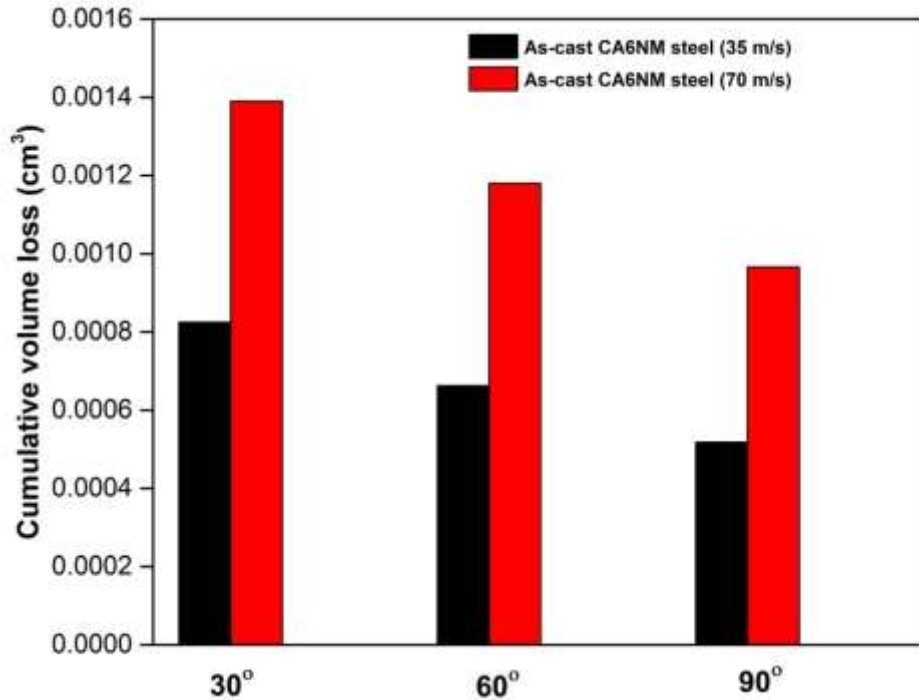


Fig. 4.10. Comparison of cumulative volume loss of as-cast CA6NM steel at 30°, 60° and 90° impingement angles for 35 m/s and 70 m/s impingement velocity.

4.2.3. Erosion mechanism and FESEM analysis of eroded surfaces

Analysis of FESEM micrographs of the eroded surface is important to understand the erosion features. FESEM micrograph of CA6NM steel before erosion is shown in Fig. 4.11. FESEM micrographs of eroded surfaces of as-cast CA6NM steel at 30° impingement angle on a different location for 35 m/s and 70 m/s impingement velocity are shown in Fig. 4.12 and Fig. 4.13 respectively. In the case of 30° impingement angle, the horizontal component (shear force) of the kinetic energy of the impinging particles was higher than vertical component (normal force) [243], as shown in Fig. 4.5. Thus, the force to slide on the surface was higher than the force to penetrate the surface, which resulted in the formation of lips on the surface of the steel [244]. Figure 4.12 showed the formation of lips on the surface of the steel. Similar erosion features were also observed in samples eroded at 70 m/s impingement velocity (Fig. 4.13). However, it was more prominent in comparison to the one observed in 35 m/s eroded samples.

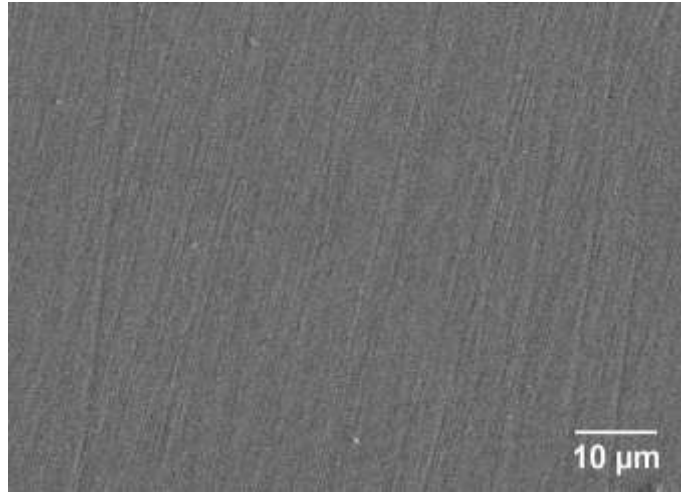


Fig. 4.11. FESEM micrograph of as-cast CA6NM steel before erosion.

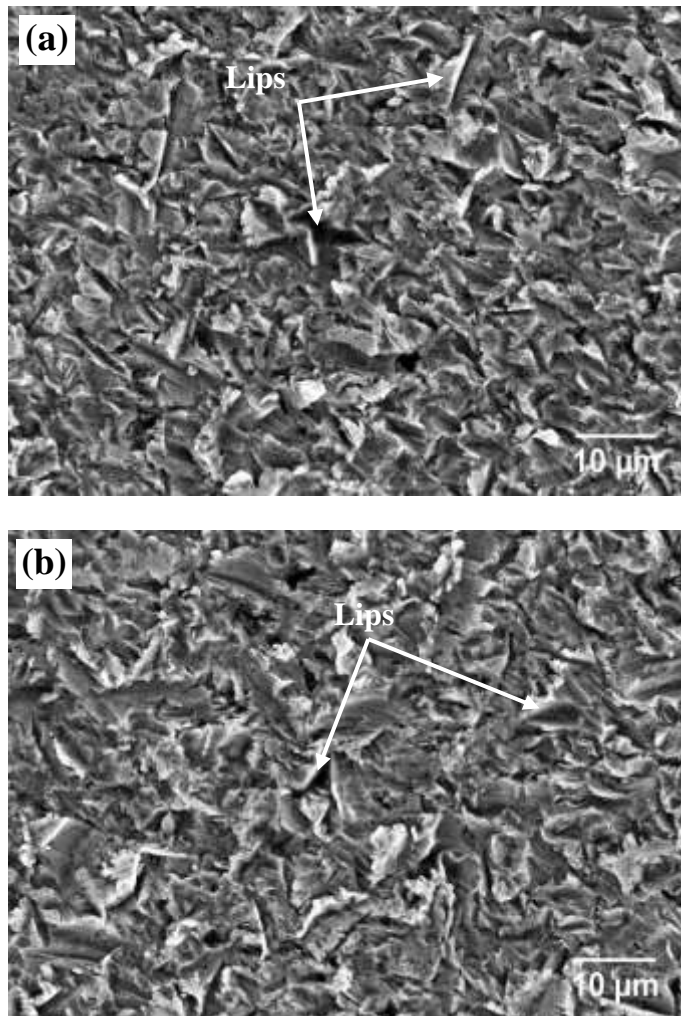


Fig. 4.12. FESEM micrographs of eroded surfaces of as-cast CA6NM steel at 30° impingement angle on different locations for 35 m/s impingement velocity.

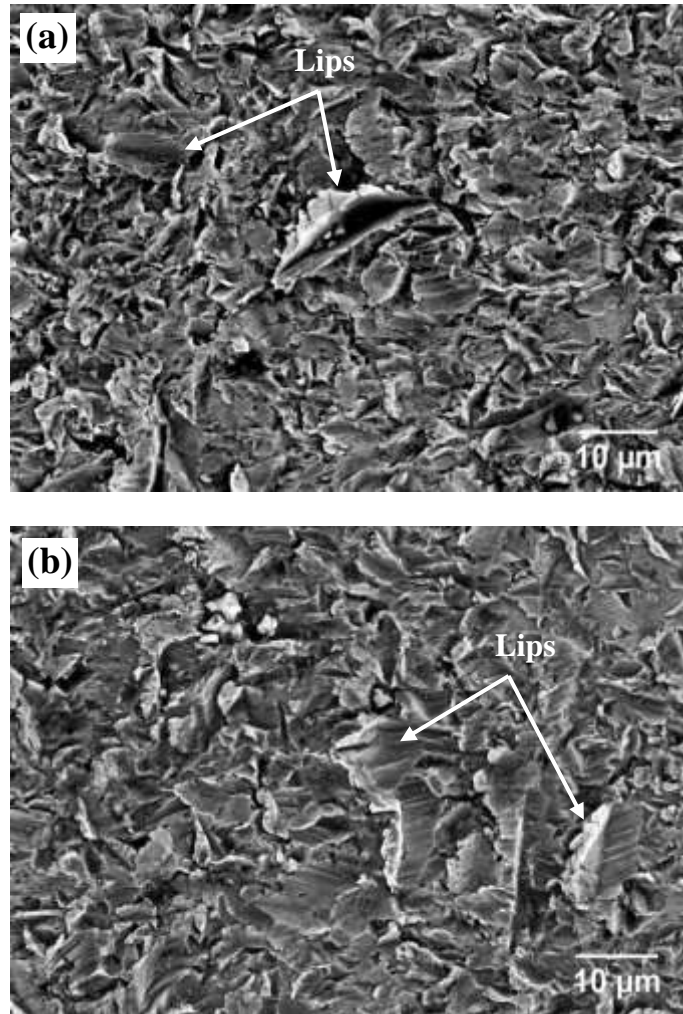


Fig. 4.13. FESEM micrographs of eroded surfaces of as-cast CA6NM steel at 30° impingement angle on different locations for 70 m/s impingement velocity.

Figure 4.14 and Fig. 4.15 shows the FESEM micrographs of eroded surfaces of as-cast CA6NM steel at 60° impingement angle on two different locations for 35 m/s and 70 m/s impingement velocity. For medium impingement angle (60°), the horizontal component (shear force) of the kinetic energy of the impinging particles and the vertical component (normal force) were close to equal, as shown in Fig. 4.5. Therefore, the material removal mainly took place due to combined action of cutting and extrusion, which resulted in the formation of lips and craters. The eroded surfaces showed the formation of lips and craters. It indicated that material was removed by the combination of cutting and extrusion. However, the erosion features were less prominent in samples eroded at 35 m/s impingement velocity in comparison to the sample eroded at 70 m/s impingement velocity.

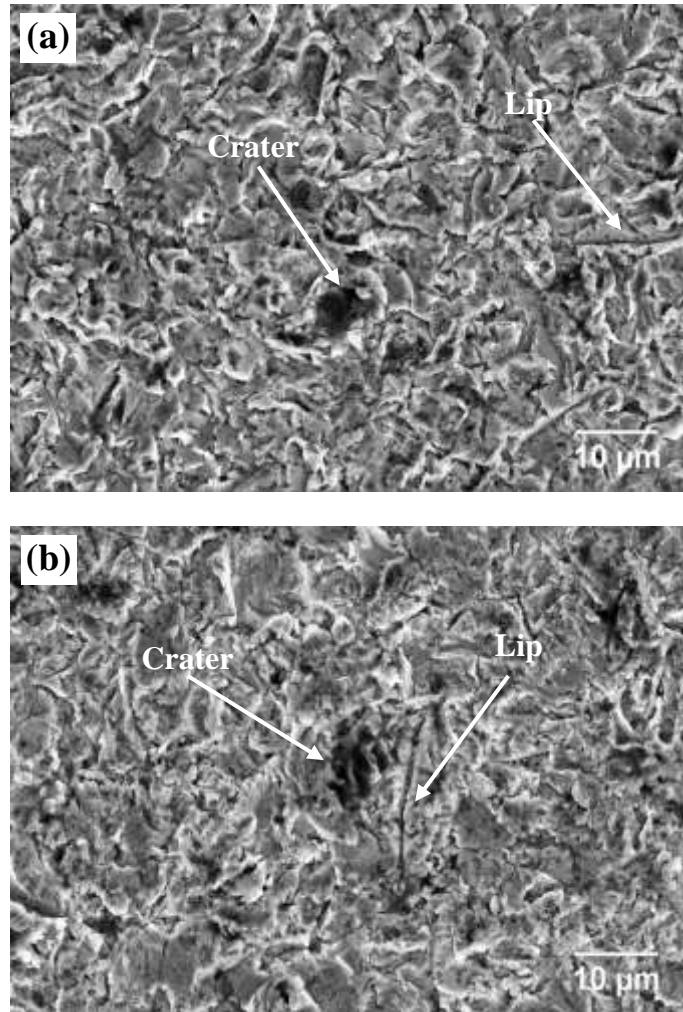


Fig. 4.14 FESEM micrographs of eroded surfaces of as-cast CA6NM steel at 60° impingement angle on different locations for 35 m/s impingement velocity.

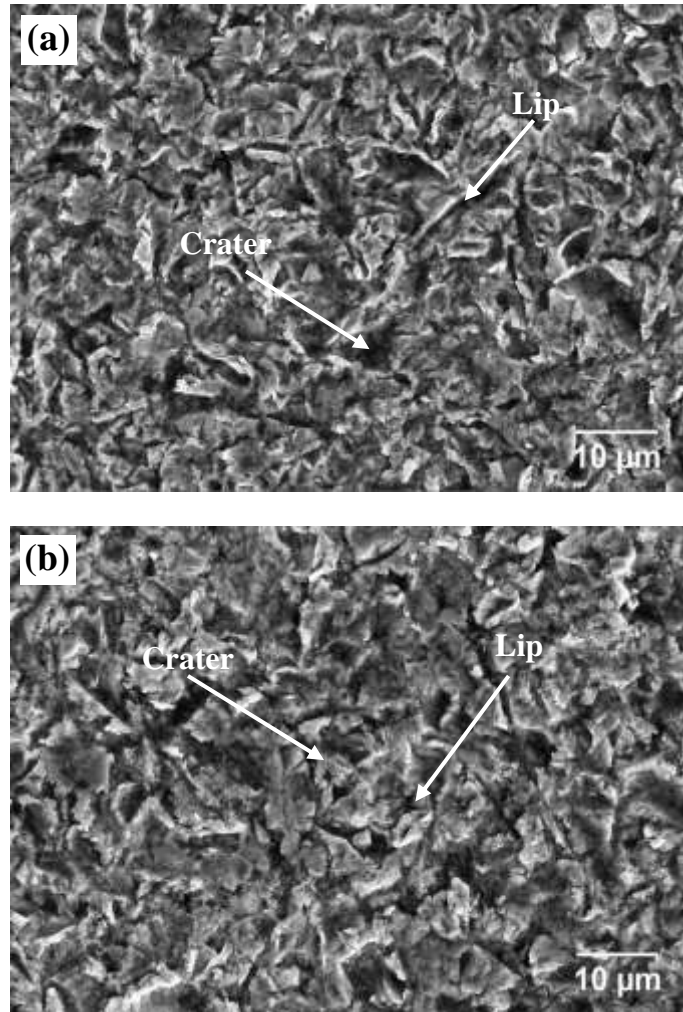


Fig. 4.15 FESEM micrographs of eroded surfaces of as-cast CA6NM steel at 60° impingement angle on different locations for 70 m/s impingement velocity.

FESEM micrographs of eroded surfaces of as-cast CA6NM steel at 90° impingement angle on two different locations for 35 m/s and 70 m/s impingement velocity are shown in Fig. 4.16 and Fig. 4.17 respectively. For the high impingement angle (90°), the vertical component (Normal force) of the kinetic energy was higher than horizontal component (shear force), as shown in Fig. 4.5. It provided bigger indented force, and erodent penetrates into the surface resulting in the formation of craters [244]. At 90° impingement angle, extrusion of the sample took place, and formation of craters were observed in samples [28]. However, craters were small in the case of samples eroded at 35 m/s impingement velocity.

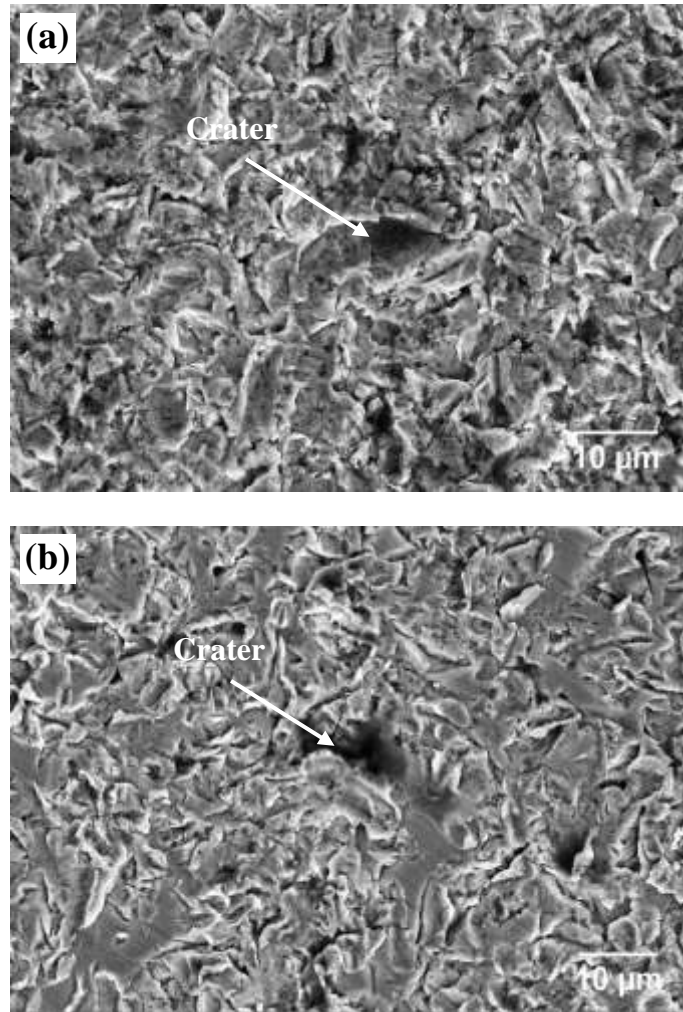


Fig. 4.16 FESEM micrographs of eroded surfaces of as-cast CA6NM steel at 90° impingement angle on different locations for 35 m/s impingement velocity.

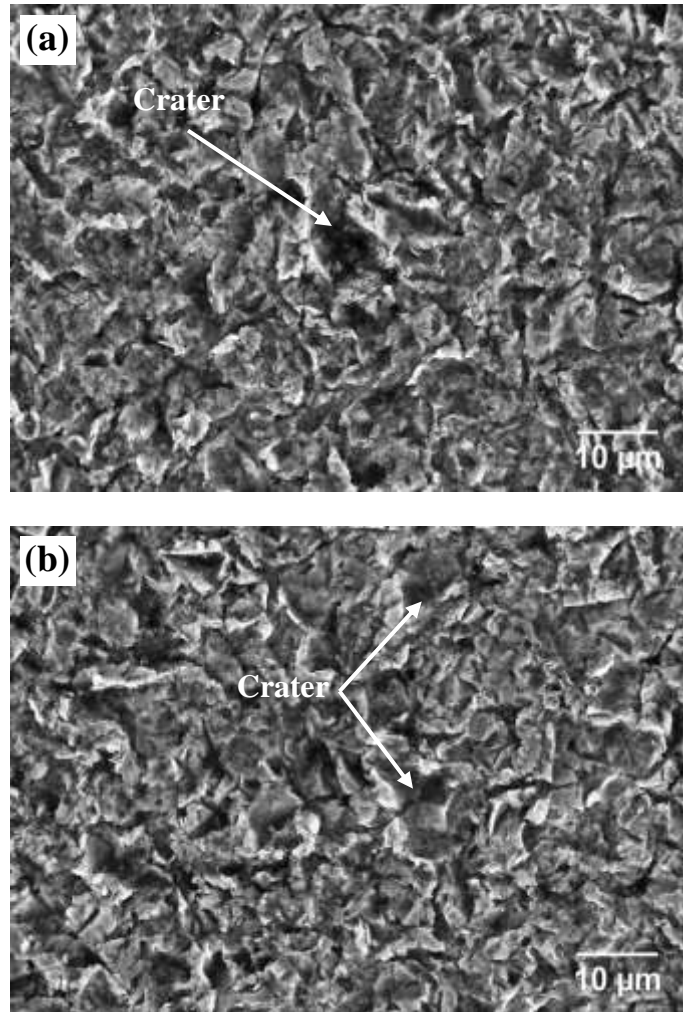


Fig. 4.17 FESEM micrographs of eroded surfaces of as-cast CA6NM steel at 90° impingement angle on different locations for 70 m/s impingement velocity.

FESEM micrographs taken under all the above condition showed that extensive plastic deformation occurred on the surface of the CA6NM steel. It was also observed that all the impingement angles erosion exhibited less prominent erosion features at 35 m/s impingement velocity compared to 70 m/s. This phenomenon was mainly attributed to lower kinetic energy of erodent particles in the case of 35 m/s impingement velocity.

4.3. Characterization and Erosive Wear Study of HVOF Sprayed WC-10Co-4Cr Coating on CA6NM Steel

4.3.1. Feedstock powder characterization

Fig. 4.18 (a, b) shows the morphology of the WC-10Co-4Cr feedstock powder used in HVOF spraying. The morphology of feedstock powder was found to be spherical. The spherical morphology improves the feedability and sprayability of powder during spraying. The spherical morphology also reduces the moisture absorption and helps in uniform heating of powder. Feedstock powder also exhibits porous nature (Fig. 4.18(b)). The porous powders do not shatter during impact on the surface, as the kinetic energy is converted into crushing the powder. This leads to homogenous and well-bonded coating.

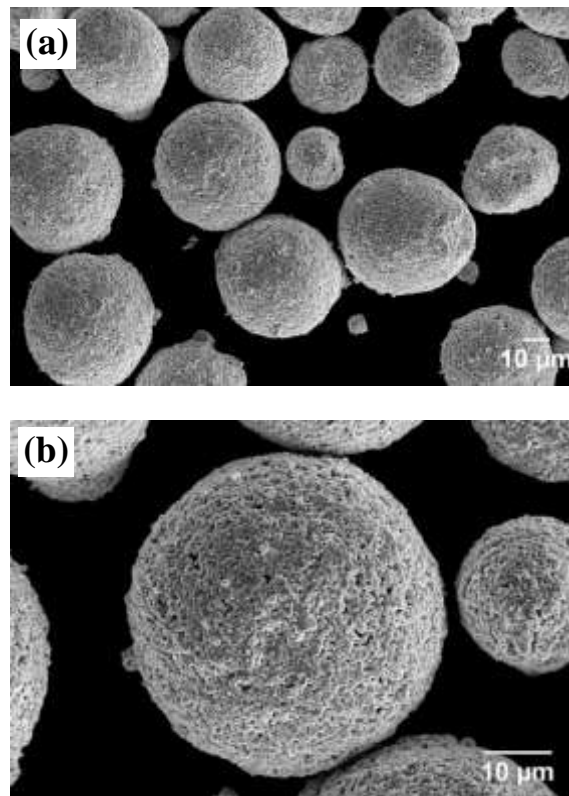


Fig. 4.18. FESEM micrograph of WC-10Co-4Cr feedstock powder used in HVOF spraying (a) Lower magnification (2000 X) and (b) Higher magnification (5000 X).

4.3.2. XRD Study of feedstock powder and HVOF sprayed coating

The X-ray diffraction patterns for the surface of the HVOF sprayed WC-10Co-4Cr coating, and the feedstock powder is shown in Fig. 4.19. Diffraction peaks of feedstock powder correspond to mainly WC with a minor peak of Co. WC was found to be a primary phase, a small amount of ternary carbides $(Co, Cr)_3W_3C$ (M_6C type) are also noticed. After HVOF

spraying, some changes in XRD pattern was observed. WC was found to be a primary phase. Moreover, a new phase W_2C was also observed. This was formed due to decarburization of WC phase during spraying [245]. Higher flame temperature and lower particle velocity during HVOF process increase the particle in-flight time, which in turn, resulted in decarburization of WC into W_2C [41,51,53]. The retention of WC retention was found to be 87.47 %.

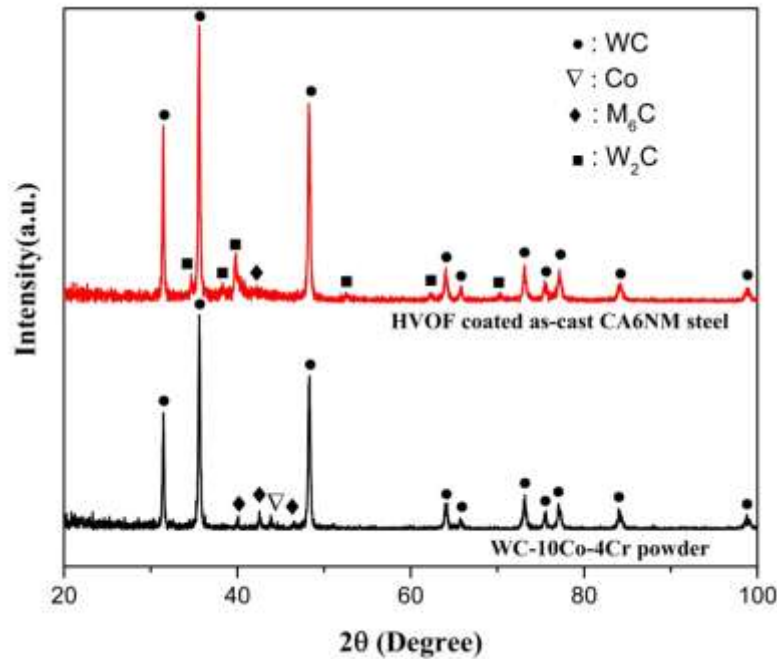


Fig. 4.19. XRD pattern of WC-10Co-4Cr feedstock powder and HVOF sprayed WC-10Co-4Cr coating on CA6NM steel.

4.3.3. Cross-sectional microstructure of HVOF sprayed coating

The cross-sectional FESEM micrographs of the HVOF sprayed WC-10Co-4Cr coating on the CA6NM steel is shown in Fig. 4.20. At lower magnification (Fig. 4.20(a)) coating-substrate bonding can be seen clearly. It was observed that coating had a homogeneous laminar structure bonded to the substrate. The thickness, as-sprayed surface roughness and density of the coating are presented in Table 4.2. At higher magnification (Fig. 4.20(b)) pores and interlaminar oxidation can be seen.

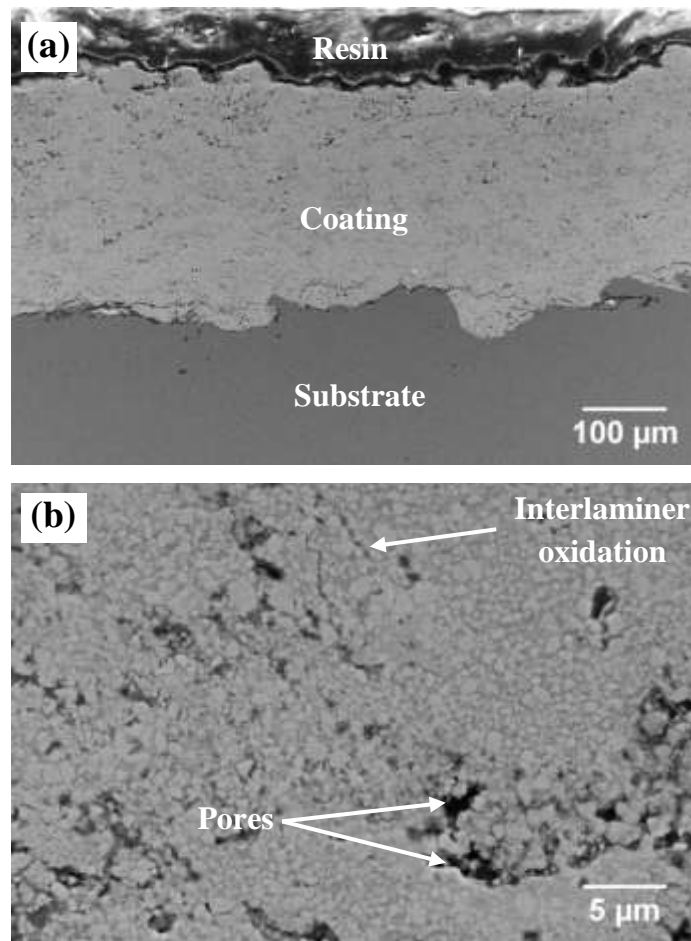


Fig. 4.20. Cross-sectional FESEM micrographs of HVOF sprayed WC-10Co-4Cr coating (a) At lower magnification and (b) At higher magnification.

Table 4.2 Thickness, as-sprayed coating surface roughness, porosity and density of HVOF sprayed WC-10Co-4Cr coating on CA6NM steel

HVOF coating data	CA6NM steel
Coating Thickness (μm)	307 ± 7
As-sprayed surface roughness Ra (μm)	4.76 ± 0.40
Porosity (vol. %)	4.29 ± 0.8
Density (g/cm^3)	11.56

4.3.4. Cross-sectional micro hardness, indentation fracture toughness and tensile adhesion of HVOF sprayed coating

Cross-sectional microhardness, indentation fracture toughness and tensile adhesion values of HVOF sprayed WC-10Co-4Cr coating on CA6NM steel is given in Table. 4.3. The microhardness of the coatings was measured along the depth from the coating to the

substrate. The fracture toughness value was calculated at the polished cross section of the coating. It was observed that cracks are generated parallel to the coating–substrate interface, as shown in Fig. 4.21. Cracks were not observed in the perpendicular direction, which is attributed to the anisotropic behavior of coating. In the case of tensile adhesion, it was observed that some pull off coating had taken place during rupture.

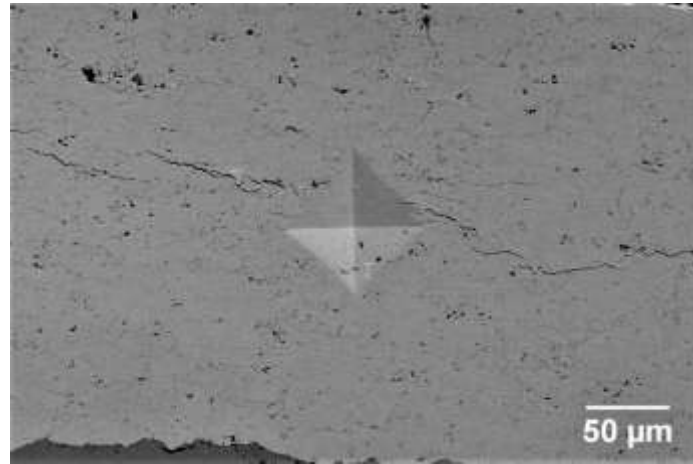


Fig. 4.21. Indentation and crack micrograph on the HVOF sprayed WC-10Co-4Cr coating cross section of CA6NM steel.

Table 4.3 Indentation fracture toughness, Microhardness and tensile adhesion of HVOF sprayed WC-10Co-4Cr coating on CA6NM steel.

	Indentation fracture toughness (MPa m^{1/2})	Cross-sectional microhardness (HV_{0.3})	Tensile adhesion (MPa)
WC-10Co-4Cr coating	2.31 ± 0.19	1107 ± 41	72

4.3.5. Effect of HVOF sprayed WC-10Co-4Cr coating on erosion resistance of CA6NM steel substrate

Fig. 4.22 to Fig. 4.24 shows the variation in cumulative volume loss of uncoated and HVOF coated CA6NM steel as a function of erosion time at 30°, 60° and 90° impingement angles respectively. It can be seen that in all the cases cumulative volume loss increases linearly with increasing the erosion time. It was also observed that HVOF sprayed WC-10Co-4Cr coating on CA6NM steel showed lower cumulative volume loss compared to uncoated steel

under all the impingement angles. Comparison of cumulative volume loss of uncoated and HVOF coated CA6NM steel at 30°, 60° and 90° impingement angles for 35 m/s and 70 m/s impingement velocities is shown in Fig. 4.25. The uncoated steel showed the ductile mode of erosion behavior as highest cumulative volume loss was observed at 30° impingement angle. However, in the case of HVOF coating highest cumulative volume loss was observed at 60° impingement angle, followed by 90° and 30°. This mode is neither ductile (highest cumulative volume loss at 30°) nor brittle (highest cumulative volume loss at 90°). Hence, this behavior was called mixed mode of erosion, and it was in accordance with earlier findings. Mixed mode of erosion was mainly attributed to composite nature of the coating. The hard WC particle provides brittleness, and soft Co-Cr matrix gives ductile character to the coating. The percentage improvement in erosion resistance after application of HVOF coating on as-cast CA6NM steel is shown in Table 4.4. It was observed that improvement of 44 to 72 % in erosion resistance occurred after application of HVOF coating.

Table 4.4 Improvement in erosion resistance of as-cast CA6NM steel at 30°, 60° and 90° impingement angles after application of HVOF coating.

Sample	Process conditions	Erosion resistance improvement (%)					
		(30° angle)		(60° angle)		(90° angle)	
		35 m/s	70 m/s	35 m/s	70 m/s	35 m/s	70 m/s
Cast steel	-	-	-	-	-	-	-
HVOF	Cast steel + HVOF sprayed WC-10Co-4Cr coating	72%	70%	46%	44%	45%	44%

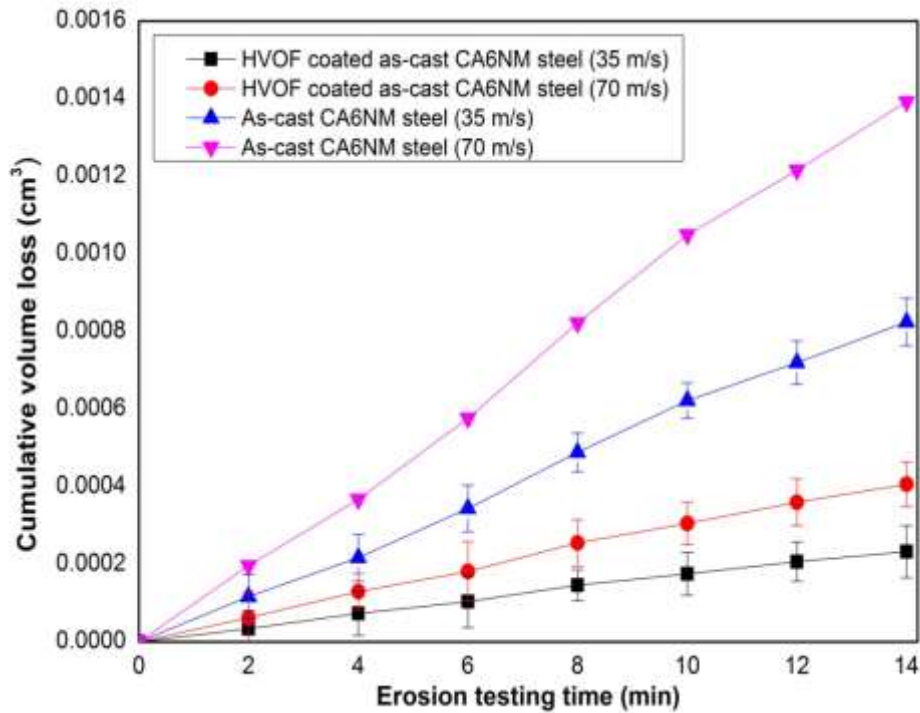


Fig. 4.22. Cumulative volume loss of as-cast CA6NM steel and HVOF coated steel as a function of erosion time at 30° impingement angle for 35 m/s and 70 m/s impingement velocities.

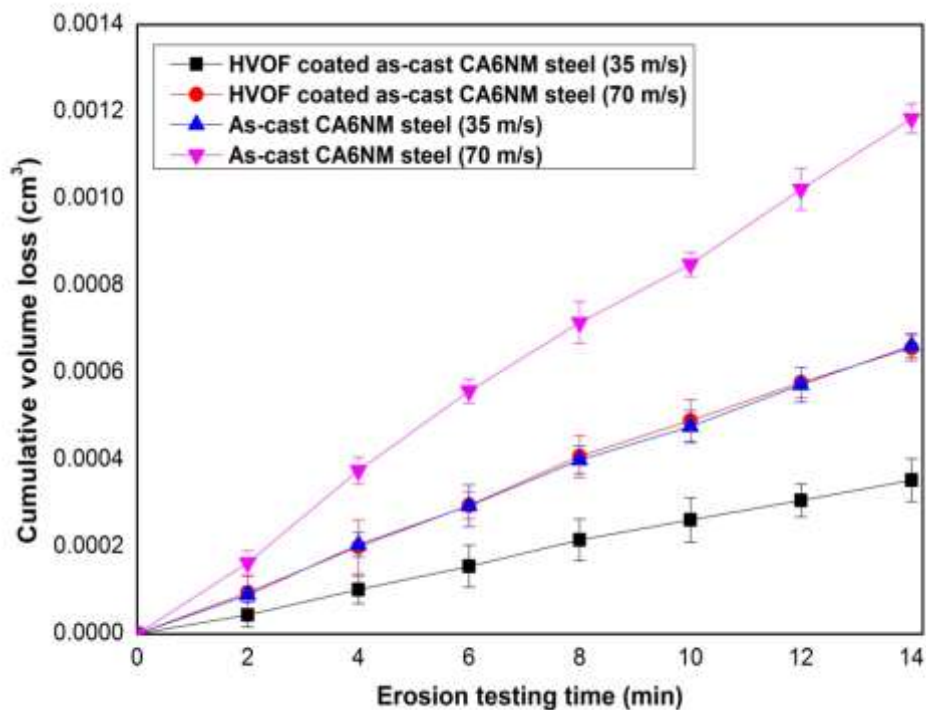


Fig. 4.23. Cumulative volume loss of as-cast CA6NM steel and HVOF coated steel as a function of erosion time at 60° impingement angle for 35 m/s and 70 m/s impingement velocities.

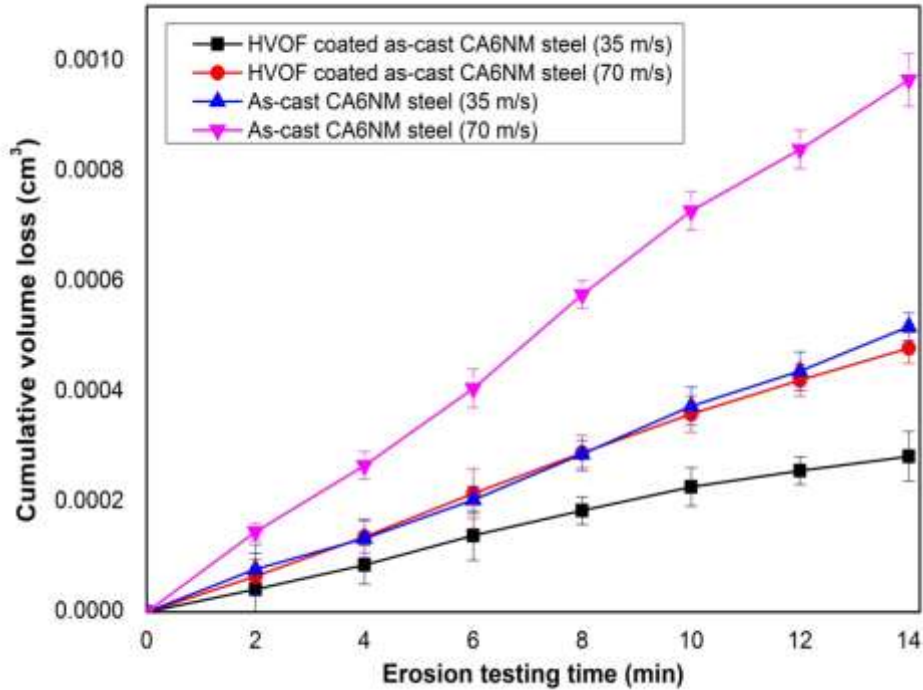


Fig. 4.24. Cumulative volume loss of as-cast CA6NM steel and HVOF coated steel as a function of erosion time at 90° impingement angle for 35 m/s and 70 m/s impingement velocities.

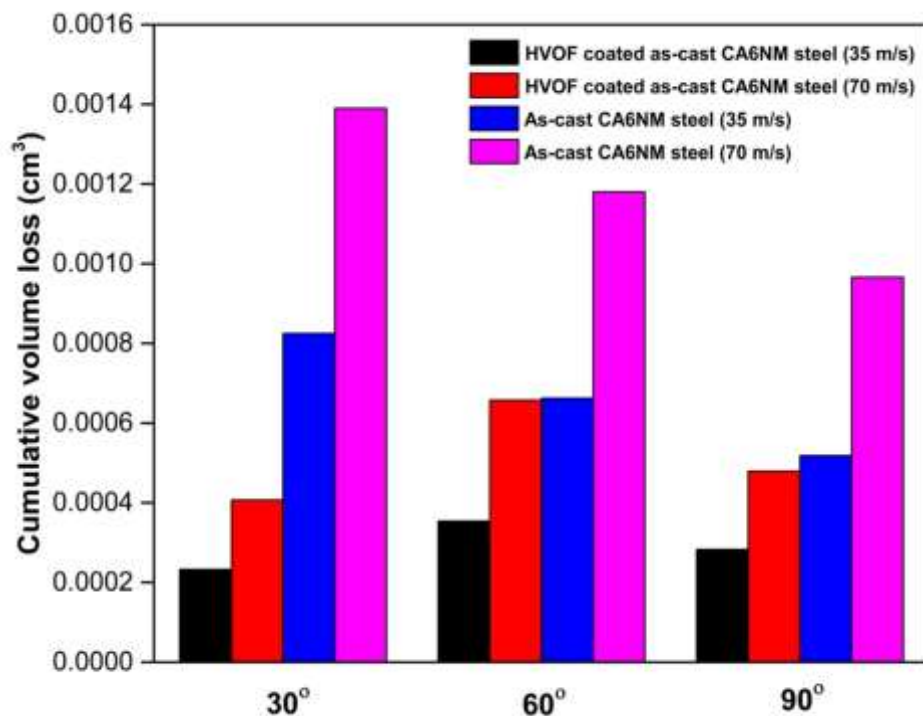


Fig. 4.25. Comparison of cumulative volume loss of as-cast CA6NM steel and HVOF coated steel at 30°, 60° and 90° impingement angles for 35 m/s and 70 m/s impingement velocities.

4.3.6. Analysis of eroded HVOF sprayed coating surface

The FESEM micrographs of eroded surfaces of HVOF coated CA6NM steel substrate at 30° impingement angle on different locations for 35 m/s and 70 m/s impingement velocities are shown in Fig. 4.27 and Fig. 4.28. FESEM micrograph of HVOF coated CA6NM steel before erosion is shown in Fig. 4.26. It was observed that material removal took place by micro cutting and microplooughing, same is observed by several researchers [148,239,246] at these impingement angles. Removal of splats was also noticed, which is mainly due to the large tangential force acting on the splats due to the impinging particle striking at a low impingement angle, this resulted in the detachment of the splats from the surface [35,223,247]. However, samples eroded at 70 m/s impingement velocity (Fig. 4.28) showed severe erosion features in comparison to the samples eroded at 35 m/s (Fig. 4.27).

The FESEM micrographs of eroded surfaces of HVOF coated CA6NM steel substrate at 60° impingement angle on a different location for 35 m/s and 70 m/s impingement velocities is shown in Fig. 4.29 and Fig. 4.30. In the case of 60° impingement angle, material removal took place due to the mixed mode of micro cutting and removal of a single grain of WC [248]. The lips and craters can be seen in HVOF coated steel eroded at 35 m/s (Fig. 4.29). The FESEM micrograph of HVOF coated CA6NM steel eroded at 70 m/s also showed the lips and craters (Fig. 4.30). However, it was more severe than 35 m/s sample.

The FESEM micrographs of eroded surfaces of HVOF coated CA6NM steel substrate at 90° impingement angle on a different location for 35 m/s and 70 m/s impingement velocities are shown in Fig. 4.31 and Fig. 4.32. At high impingement angle, material removal took place by removal of a single grain of WC. Impinging erodent particle removed the binder phase from the surface, and it resulted in the accumulation of plastic strain in WC particles. Eventually, cracks were generated in-between WC grains, which resulted in the removal of single WC particle [184,220,249]. Samples eroded at 70 m/s showed severe erosion features in comparison to the one eroded at 35 m/s.

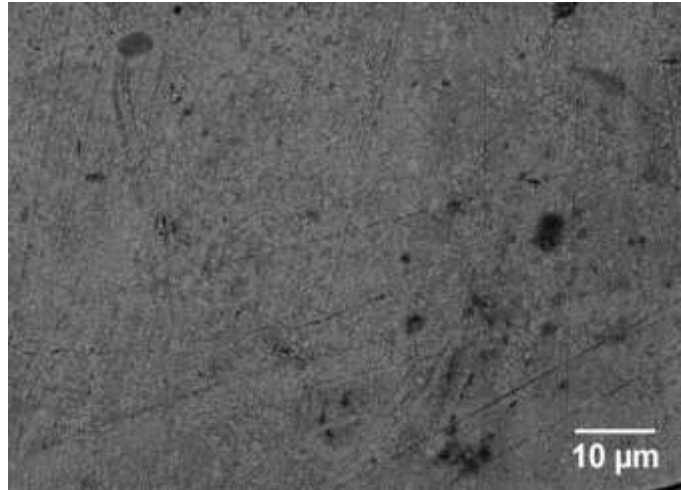


Fig. 4.26. FESEM micrograph of HVOF coated CA6NM steel before erosion.

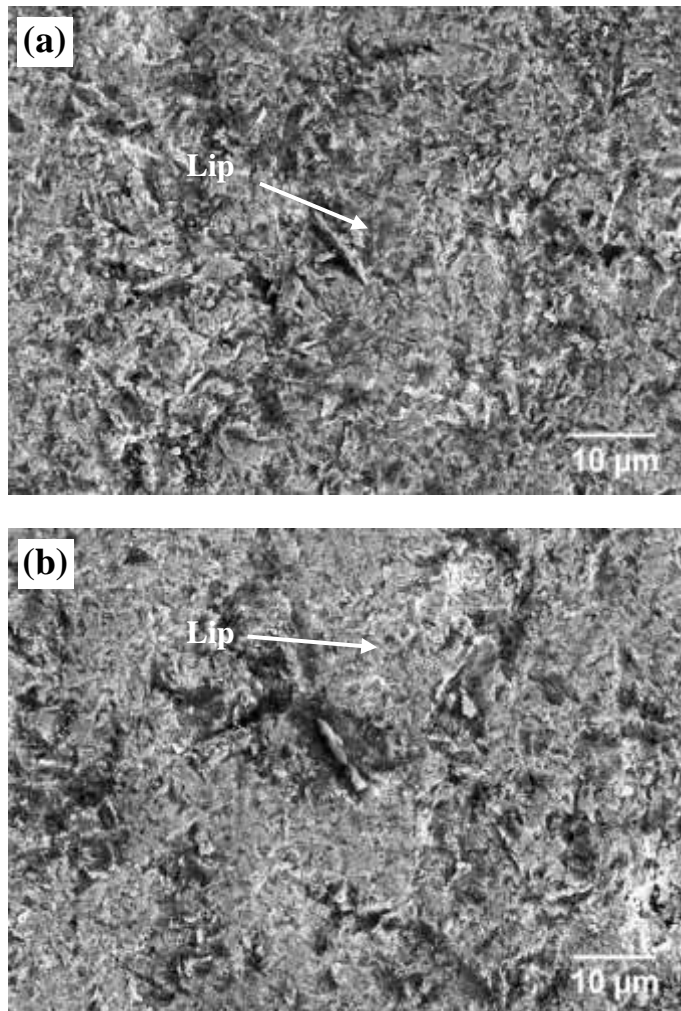


Fig. 4.27. FESEM micrograph of eroded surface of HVOF coating at 30° impingement angle on different locations for 35 m/s impingement velocity.

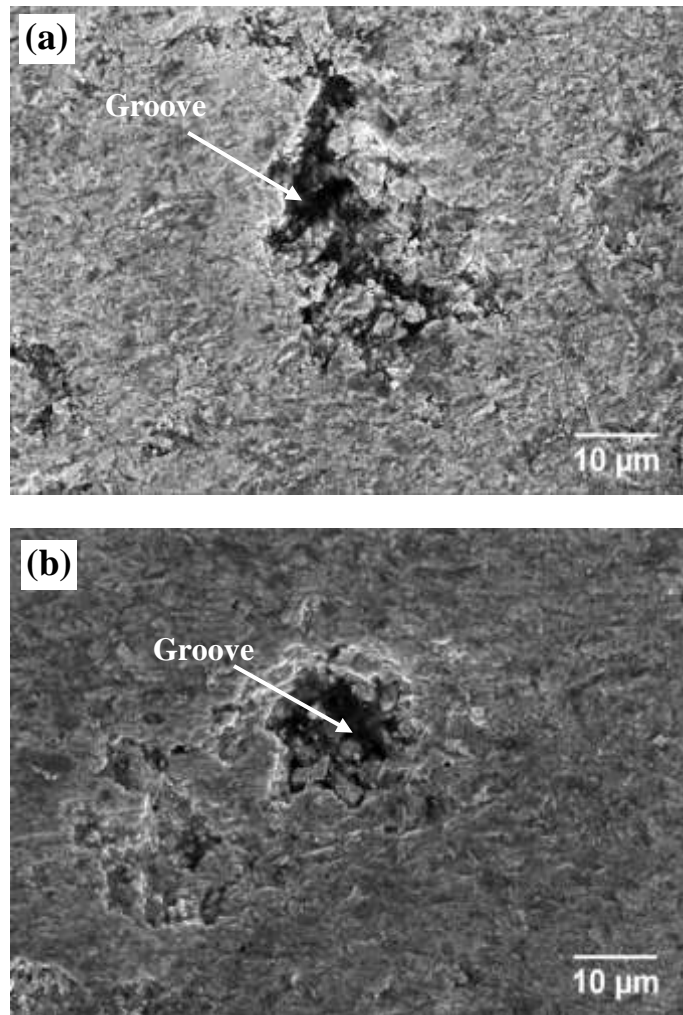


Fig. 4.28. FESEM micrograph of eroded surface of HVOF coating at 30° impingement angle on different locations for 70 m/s impingement velocity.

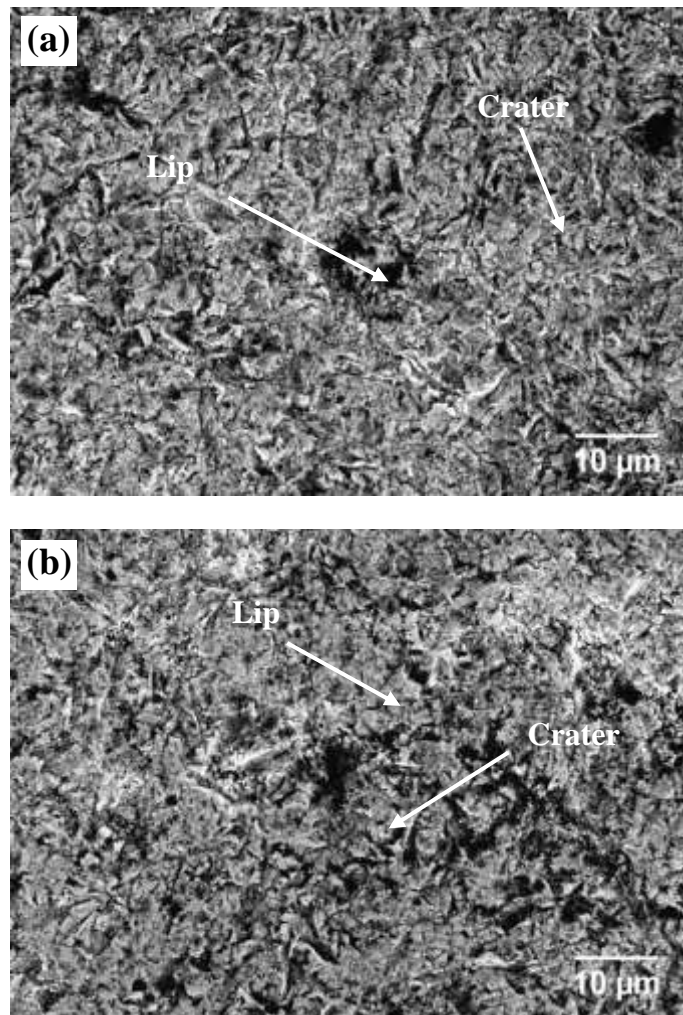


Fig. 4.29. FESEM micrograph of eroded surface of HVOF coating at 60° impingement angle on different locations for 35 m/s impingement velocity.

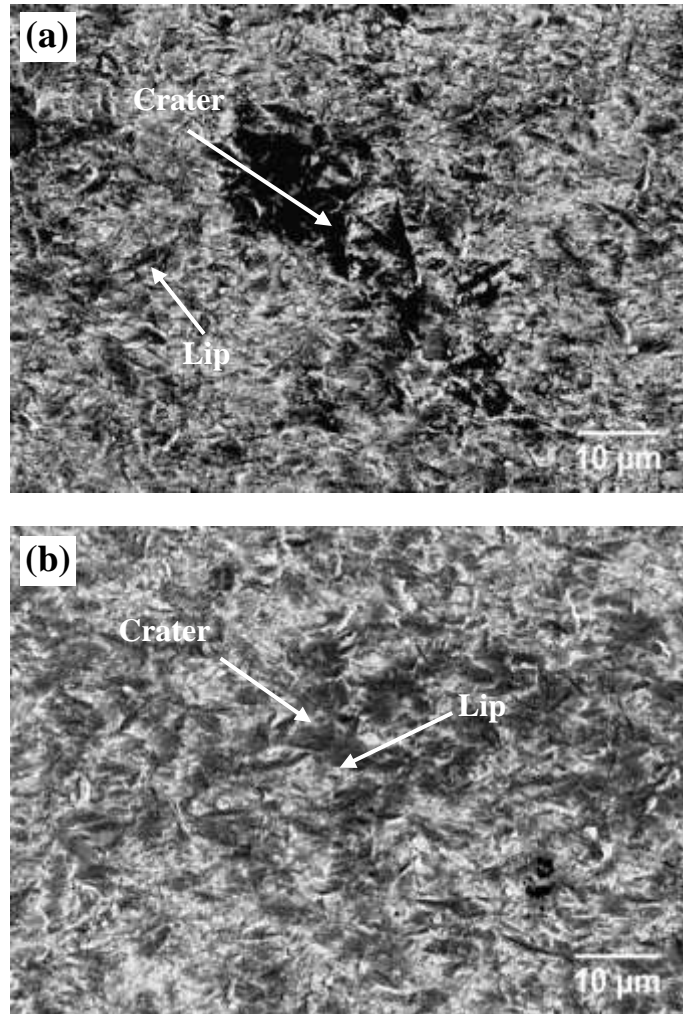


Fig. 4.30. FESEM micrograph of eroded surface of HVOF coating at 60° impingement angle on different locations for 70 m/s impingement velocity.

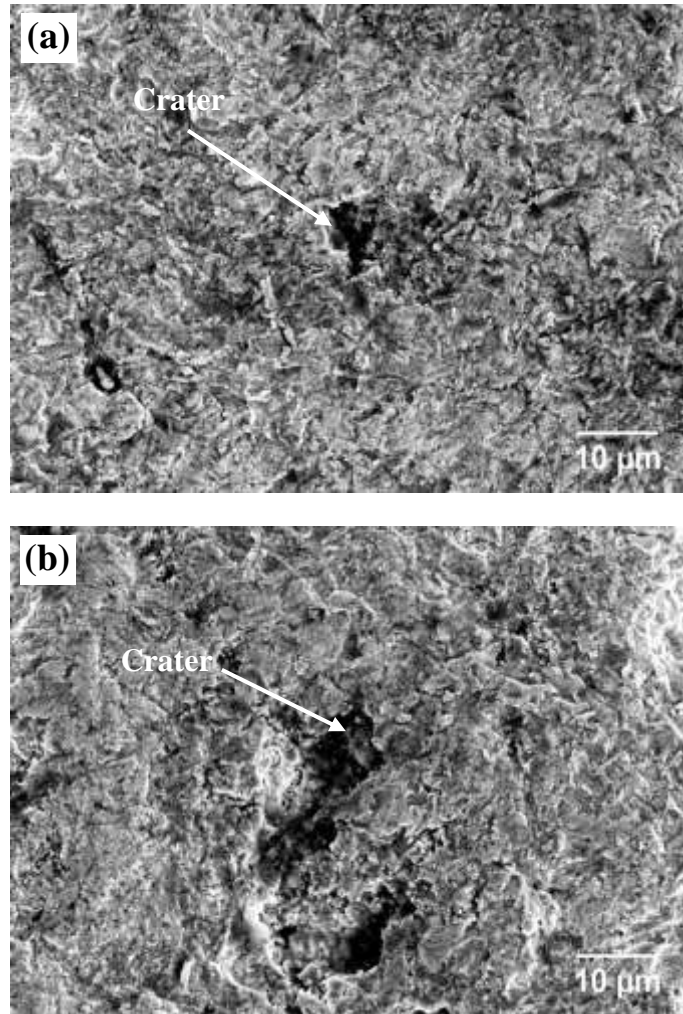


Fig. 4.31. FESEM micrograph of eroded surface of HVOF coating at 90° impingement angle on different locations for 35 m/s impingement velocity.

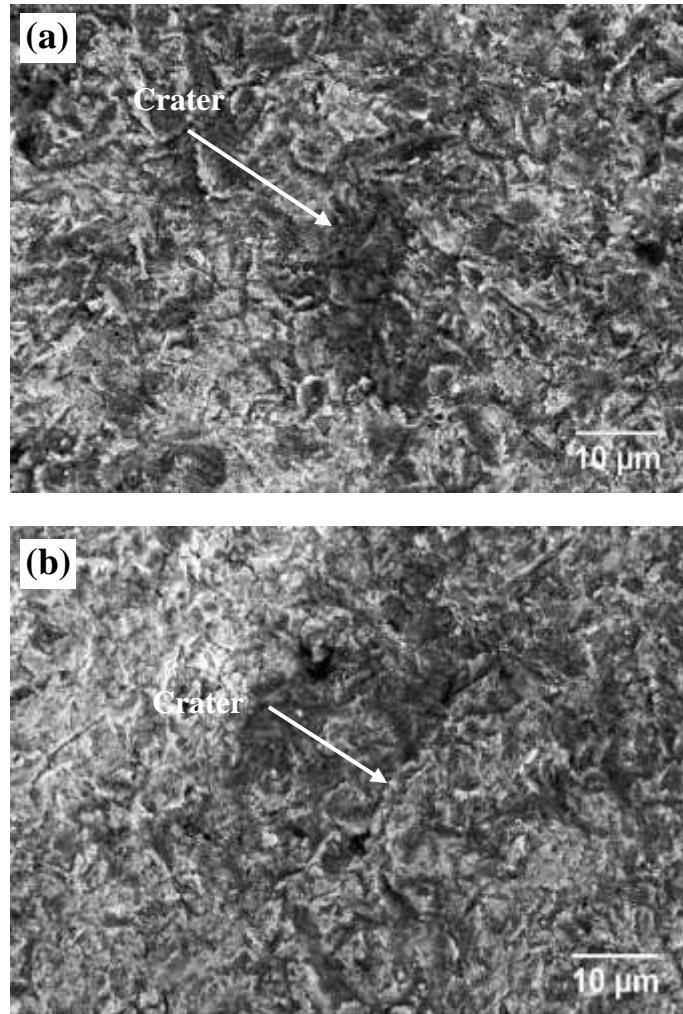


Fig. 4.32. FESEM micrograph of eroded surface of HVOF coating at 90° impingement angle on different locations for 70 m/s impingement velocity.

4.4. Characterization and Erosive Wear Study of HVOF Sprayed WC-10Co-4Cr Coating on CA6NM Steel

4.4.1. Feedstock powder characterization

The morphology of the feedstock powder used in HVOF spraying is shown in Fig. 4.33. The morphology of feedstock powder was found to be spherical, which provides excellent fluidity and stability during spraying. The powder also possesses porous nature, which helps in a uniform coating.

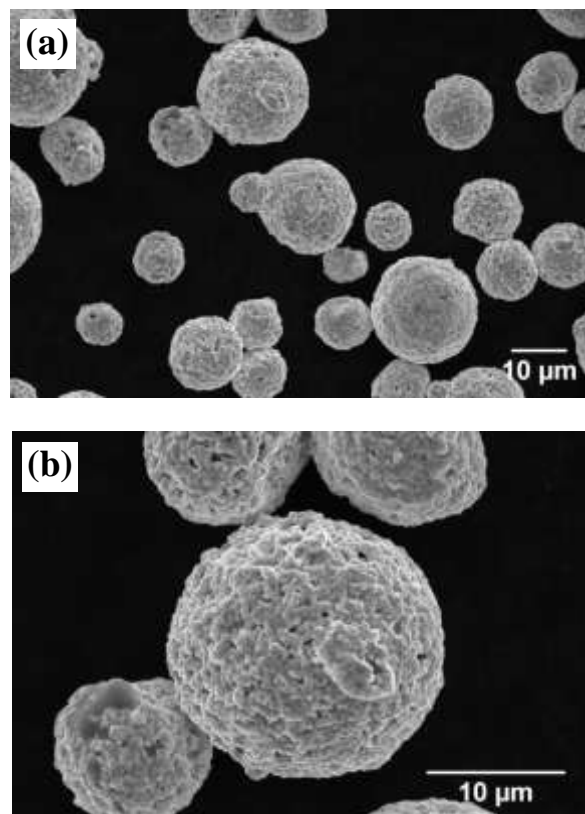


Fig. 4.33. Morphology of WC-10Co-4Cr feedstock powder used in HVOF spraying (a) Lower magnification (2000 X) and (b) Higher magnification (5000 X).

4.4.2. XRD study of feedstock powder and HVOF sprayed coating

The X-ray diffraction patterns for the surface of the HVOF sprayed WC-10Co-4Cr coating, and the feedstock powder is shown in Fig. 4.34. There was no significant difference observed between the diffraction pattern of the feedstock powder and the coating [66]. Both the powder and coating contained WC as the primary phase. However, traces of $\text{Co}_3\text{W}_3\text{C}$ and Co phases were also noticed [66]. Traces of W_2C phase is also observed in HVOF sprayed

coating, which indicated that there was very little or negligible decarburization in the coating [65]. In HVAF coating, higher particle velocity and lower particle temperature during spraying were the main factors which resulted in a lower degree of decarburization [204,215,250]. The retention of WC retention was found after coating deposition via HVAF route was 96.00 %.

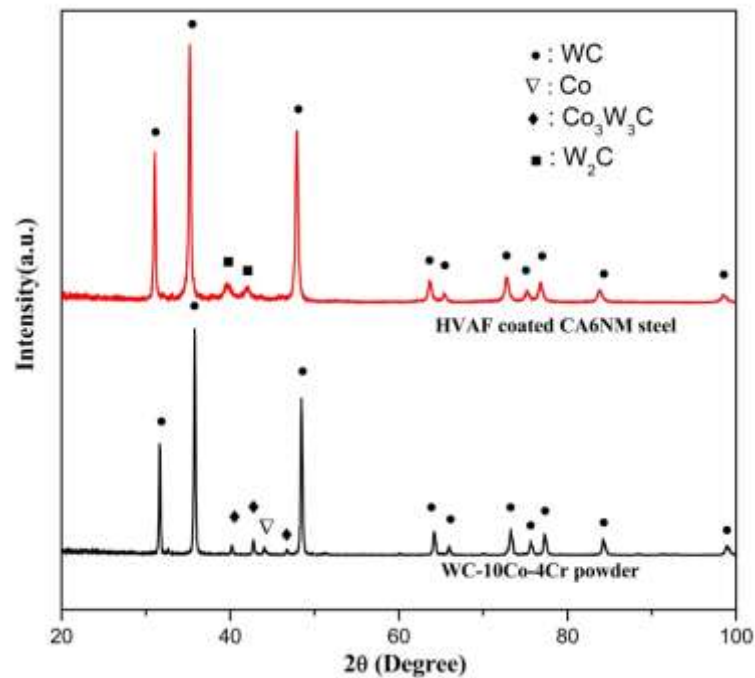


Fig. 4.34. XRD pattern of feedstock powder and HVAF sprayed WC-10Co-4Cr coating on CA6NM steel.

4.4.3. Cross-sectional microstructure of HVAF sprayed coating

The cross-sectional FESEM micrograph of the HVAF sprayed WC-10Co-4Cr coating on the CA6NM steel is shown in Fig. 4.35. Even at lower magnification (Fig. 4.35 (a)), coating-substrate interface bonding can be seen clearly. It was observed that coating had a homogeneous structure, which was dense and well bonded to the substrate. At higher magnification, (Fig. 4.35 (b)) porosity present in the coating can be observed. It was also observed that WC grains appeared in blocky shape without any deformation and dissolution. Therefore, it can be inferred that the Co-Cr metallic binder was wholly or partially melted, while the WC-particles mostly remained in the solid state during spraying. This indicated that very little decomposition of WC had taken place during spraying. Unlike HVOF sprayed WC-10Co-4Cr coating, no lamellar morphology was observed in HVAF sprayed coating, which indicated that less decarburization of WC took place. Although minute pores are

visible in the coating, it is less porous than HVOF sprayed WC-10Co-4Cr coatings. The reason being for this is shorter particle residence time in the HVOF jet, which lowered the oxidation of particles. The thickness, as-sprayed surface roughness, porosity and density of the coating are presented in Table 4.5.

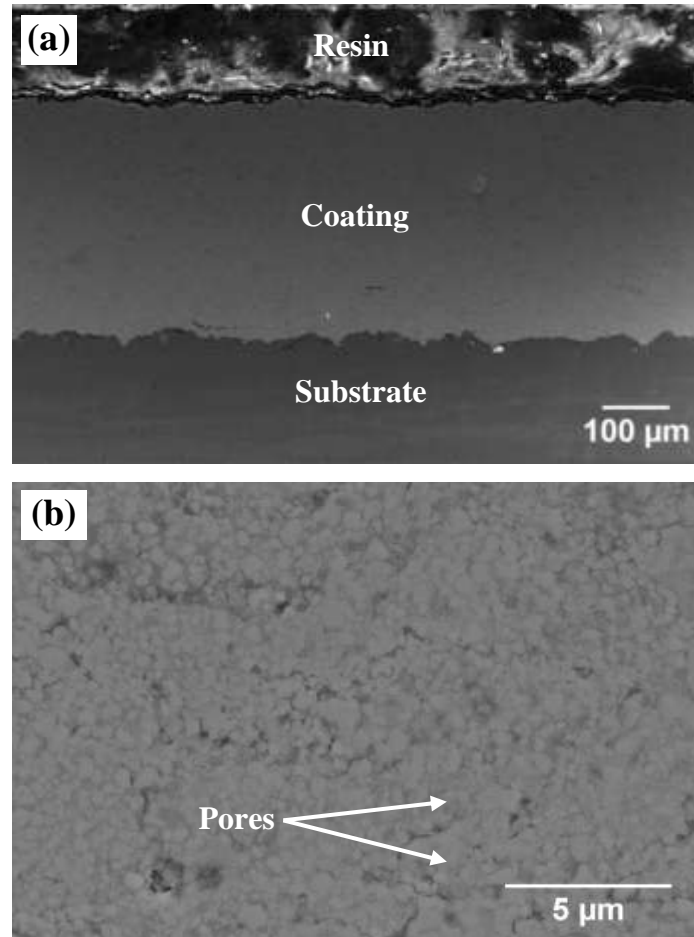


Fig. 4.35. Cross-sectional FESEM micrographs of HVOF coated CA6NM steel (a) At lower magnification (200 X) and (b) At higher magnification (10000 X).

Table 4.5 Thickness, as-sprayed coating surface roughness, porosity and density of HVOF sprayed WC-10Co-4Cr coating on CA6NM steel.

HVOF coating data	CA6NM steel
Coating Thickness (μm)	341 ± 6
As-sprayed surface roughness Ra (μm)	2.61 ± 0.42
Porosity (vol. %)	0.98 ± 0.25
Density (g/cm^3)	13.53

4.4.4. Cross-sectional microhardness, fracture toughness and tensile adhesion of HVAF sprayed coating

The values of indentation fracture toughness, cross-sectional microhardness and tensile adhesion of investigated samples are reported in Table 4.6. The fracture toughness value was calculated at the polished cross section of the coating. It was observed that cracks were generated parallel to the coating–substrate interface, as shown in Fig. 4.36. Cracks were not observed in the perpendicular direction which attributed to the anisotropic behavior of coating. The microhardness of the coatings was also measured along the depth from the coating to the substrate. The microhardness values of coating were found to be in the range of 1285–1352 Hv. It was observed that microhardness value oscillates in a narrow range (1285–1352), which is mainly due to low porosity and uniform microstructure of the coating. Surface roughness for coated and uncoated steel after polishing is measured before starting erosion testing, to provide a uniform initial condition for erosion. In the case of tensile adhesion, it was observed that rupture had taken place at the interface between uncoated substrate and glue, while coating remained intact. This point to the fact that actual tensile adhesion of coating is higher because industrial available glue has maximum strength of around 83 MPa.

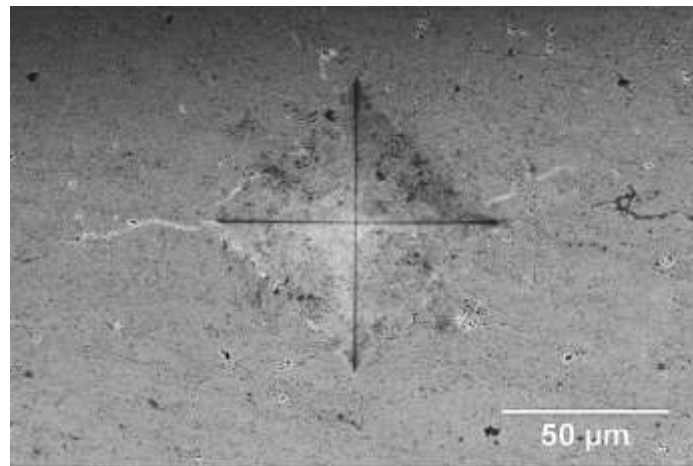


Fig. 4.36. Indentation and crack micrograph on the HVAF sprayed WC-10Co-4Cr coating cross section of CA6NM steel.

Table 4.6 Indentation fracture toughness, Microhardness and tensile adhesion of HVAF sprayed WC-10Co-4Cr coating on CA6NM steel.

	Indentation fracture toughness (MPa m^{1/2})	Cross-sectional microhardness (HV_{0.3})	Tensile adhesion (MPa)
WC-10Co-4Cr coating	6.60 ± 0.21	1327 ± 26	83

4.4.5. Effect of HVAF sprayed WC-10Co-4Cr coating on solid particle erosion resistance of CA6NM steel

Cumulative volume loss of HVAF coated CA6NM steel as a function of erosion time at 30°, 60° and 90° impingement angles for 35 m/s and 70 m/s impingement velocity is shown in Fig. 4.37 to Fig. 4.39 respectively. It can be seen that in all the cases cumulative volume loss increases linearly with increasing the erosion time. From all the figures (Fig. 4.37 to 4.39), it was observed that coated steel showed better erosion resistance than uncoated steel. Figure 4.40 shows the comparison of cumulative volume loss of uncoated and HVAF coated CA6NM steel at 30°, 60° and 90° impingement angles for 35 m/s and 70 m/s impingement velocity. The uncoated steel exhibited the ductile mode of erosion because the volumetric erosion rate continuously decreased with rising impingement angle and reached a minimum at 90°. HVAF coating, on the other hand, showed the mixed mode of ductile and brittle erosion [251]. The reason being that volumetric erosion rate was maximum at 60° impact angle, then decreases at 90° and 30° impact angle. The improvement in erosion rate of as-cast CA6NM steel after HVAF coating is given in Table 4.7. Improvement of 65 to 84 % in erosion resistance was observed after application of HVAF coating.

Table 4.7 Improvement in erosion resistance of as-cast CA6NM steel at 30°, 60° and 90° impingement angles after application of HVOF coating.

Sample	Process conditions	Erosion resistance improvement (%)					
		(30° angle)		(60° angle)		(90° angle)	
		35 m/s	70 m/s	35 m/s	70 m/s	35 m/s	70 m/s
Cast steel	-	-	-	-	-	-	-
HVOF	Cast steel + HVOF sprayed WC-10Co-4Cr coating	84%	83%	67%	67%	65%	67%

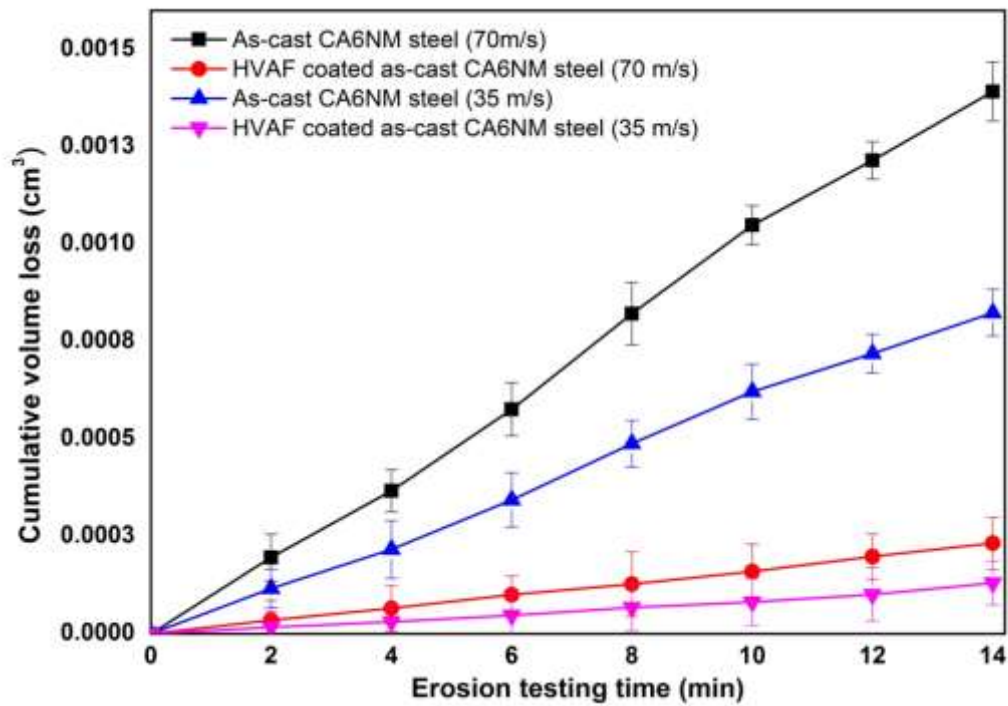


Fig. 4.37. Cumulative volume loss of as-cast CA6NM steel and HVOF coated steel as a function of erosion time at 30° impingement angle for 35 m/s and 70 m/s impingement velocities.

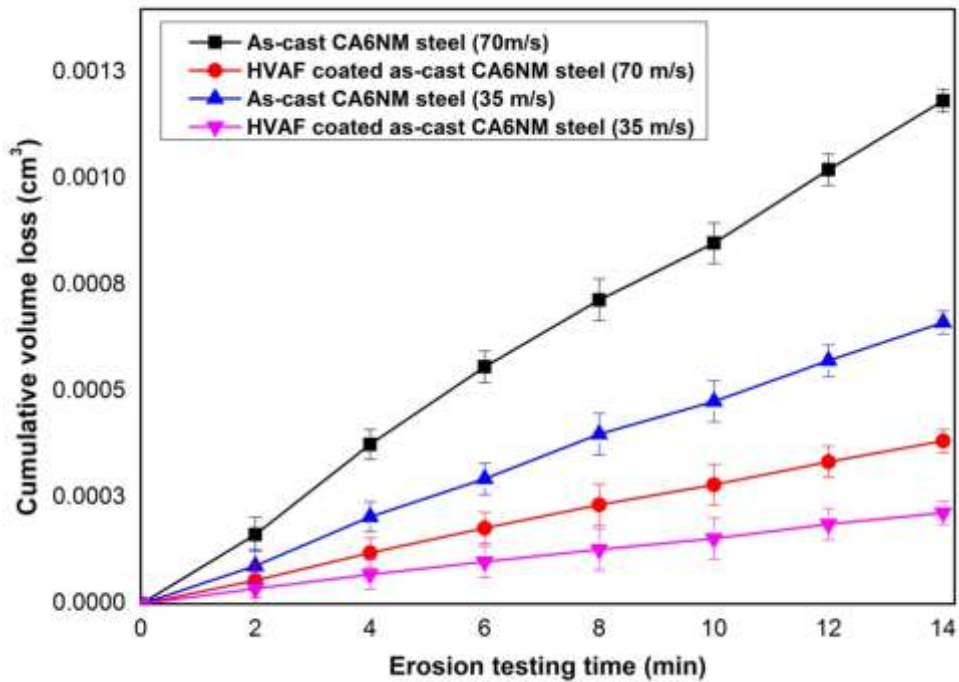


Fig. 4.38. Cumulative volume loss of as-cast CA6NM steel and HVAF coated steel as a function of erosion time at 60° impingement angle for 35 m/s and 70 m/s impingement velocities.

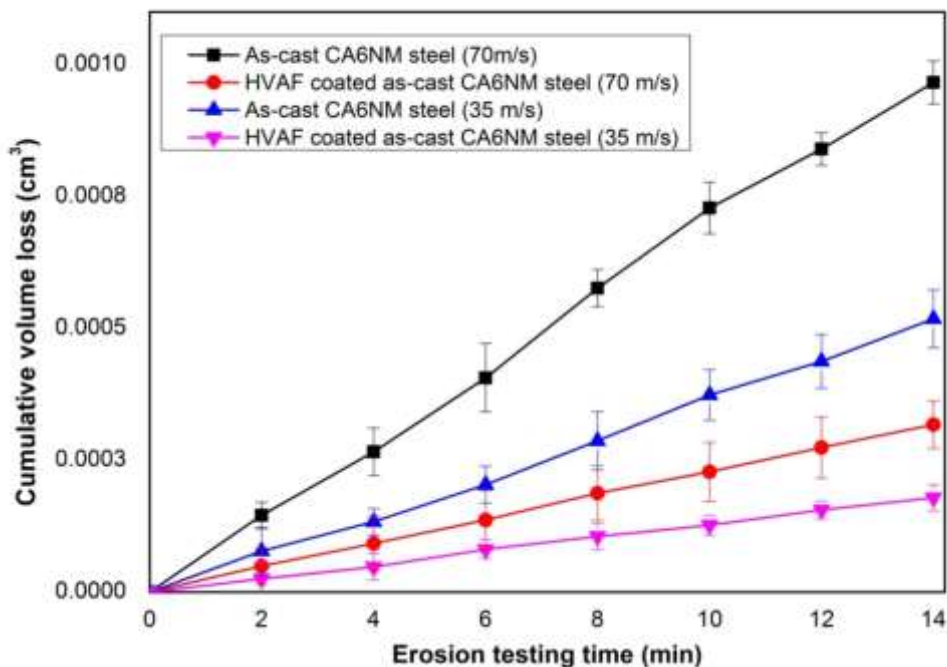


Fig. 4.39. Cumulative volume loss of as-cast CA6NM steel and HVAF coated steel as a function of erosion time at 90° impingement angle for 35 m/s and 70 m/s impingement velocities.

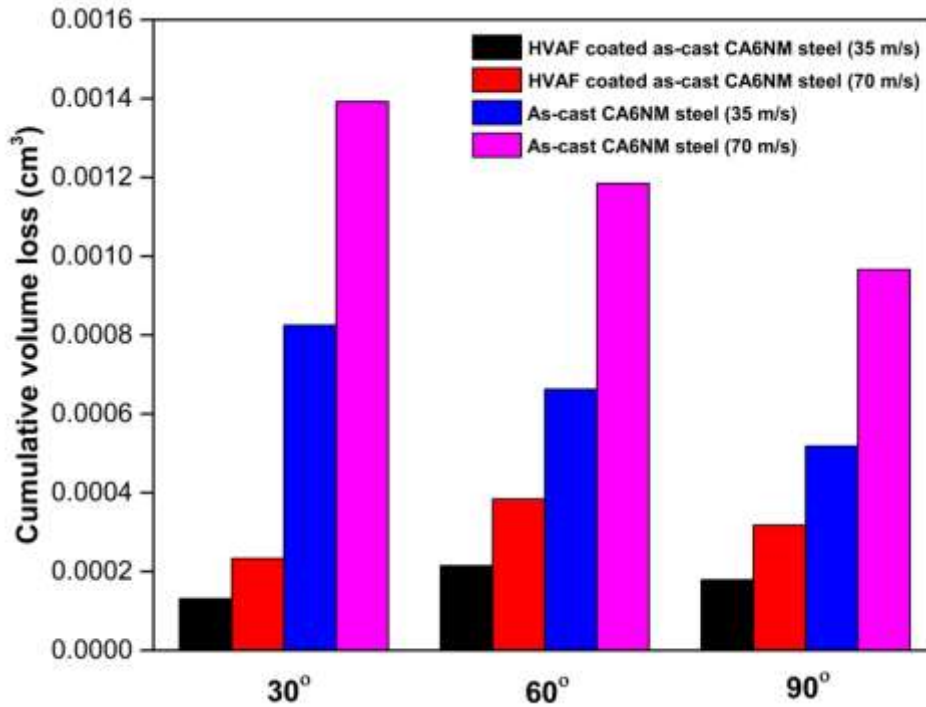


Fig. 4.40. Comparison of cumulative volume loss of as-cast CA6NM steel and HVOF coated steel at 30°, 60° and 90° impingement angles for 35 m/s and 70 m/s impingement velocities.

4.4.6. Analysis of eroded HVOF sprayed coating surface

The FESEM micrographs of eroded surfaces of HVOF coated as-cast CA6NM steel at 30° impingement angle for 35 m/s and 70 m/s impingement velocities are shown in Fig. 4.42 and Fig. 4.43. FESEM micrograph of HVOF coated CA6NM steel before erosion is shown in Fig. 4.41. It is observed that coating mainly removed by cutting and ploughing action [252]. HVOF coating eroded at 70 m/s impingement velocity showed large ploughs and lips (Fig. 4.43) compared to HVOF coating eroded at 35 m/s impingement velocity (Fig. 4.42).

The FESEM micrographs of eroded surfaces of HVOF coated as-cast CA6NM steel at 60° impingement angle for 35 m/s and 70 m/s impingement velocities are shown in Fig. 4.44 and Fig. 4.45. It was observed that coating removed by the ploughing and removal of a single grain of WC [253,254]. The erosion features observed in samples eroded at 70 m/s is more severe than one observed at 35 m/s. Fig. 4.46 and Fig. 4.47 shows the FESEM micrographs of the eroded surfaces of HVOF coated as-cast CA6NM steel at 90° impingement angle for 35 m/s and 70 m/s impingement velocities. Eroded surface of HVOF coated steel revealed the large numbers of craters formed mainly due to the removal of a single grain of WC.

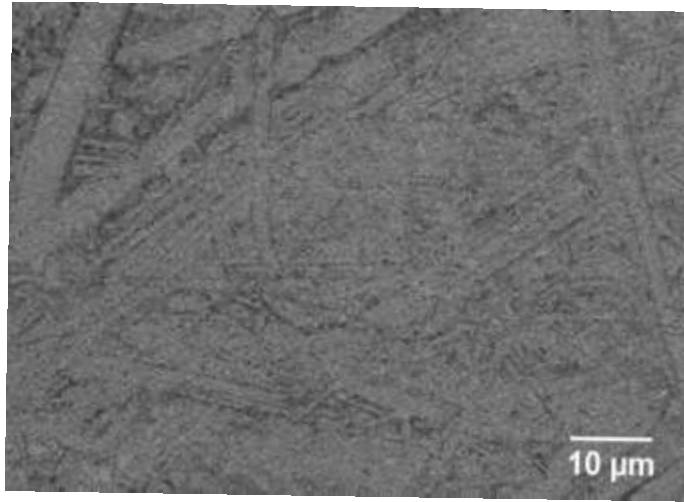


Fig. 4.41. FESEM micrograph of HVOF coated CA6NM steel before erosion.

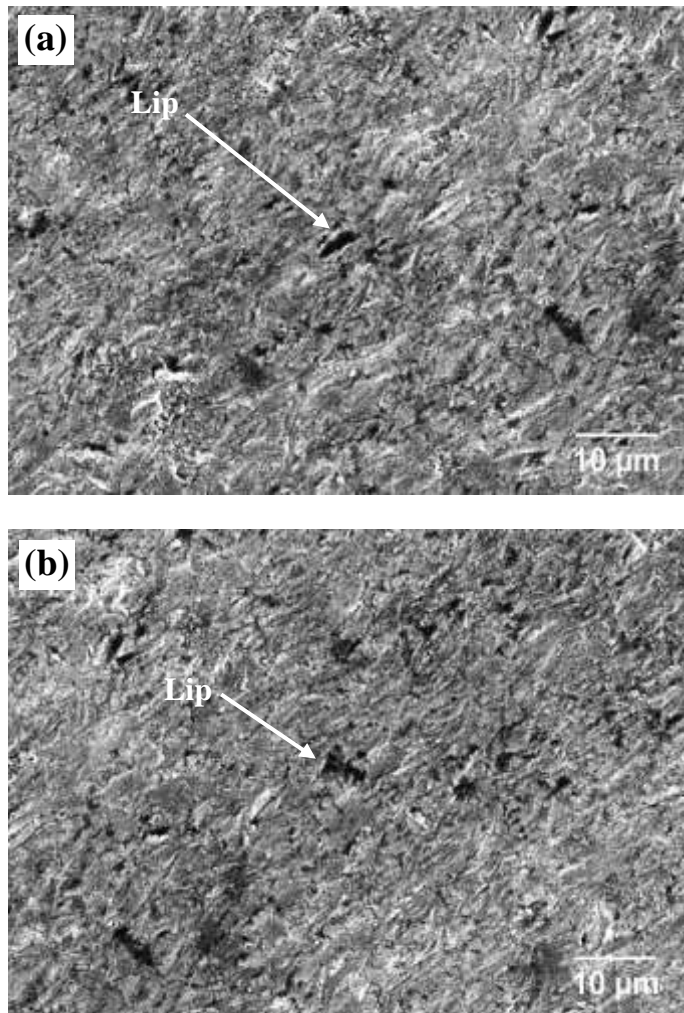


Fig. 4.42. FESEM micrograph of eroded surface of HVOF coating at 30° impingement angle on different locations for 35 m/s impingement velocity.

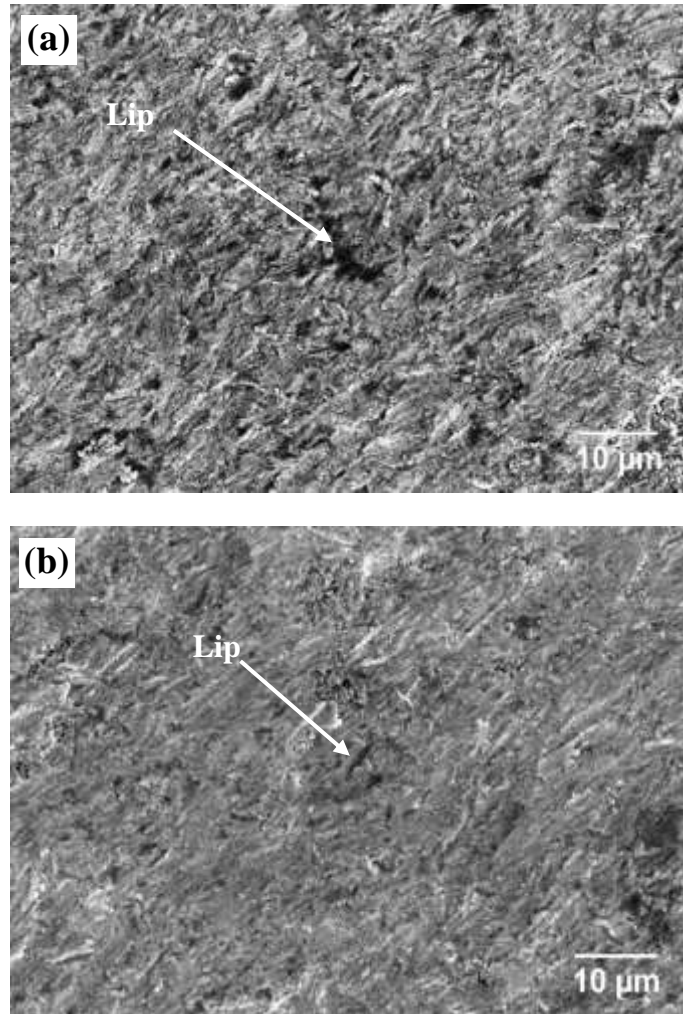


Fig. 4.43. FESEM micrograph of eroded surface of HVAF coating at 30° impingement angle on different locations for 70 m/s impingement velocity.

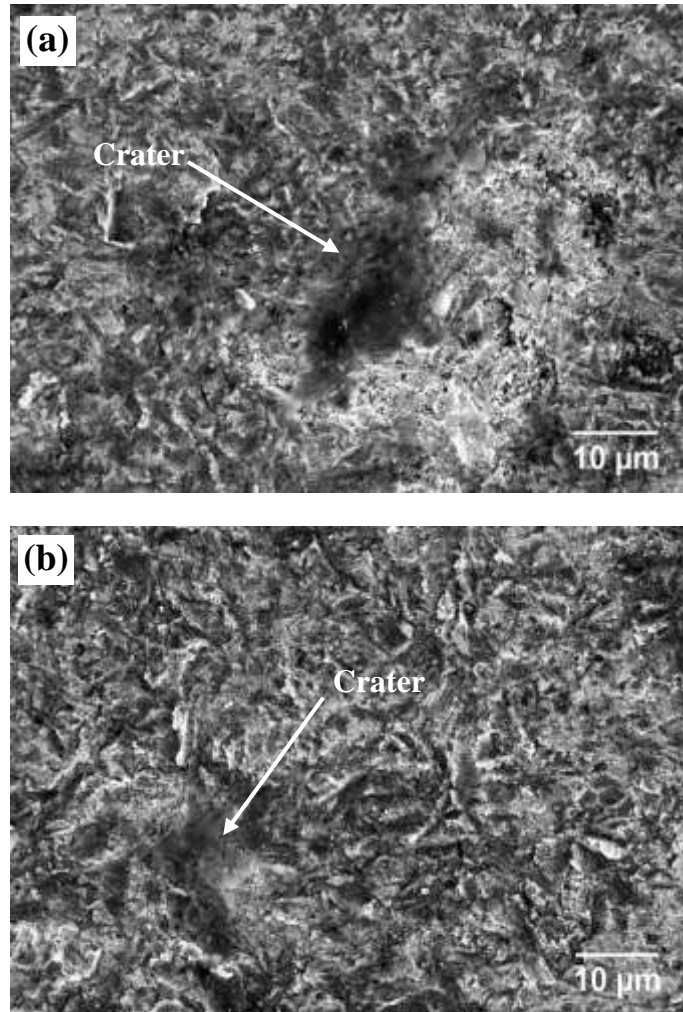


Fig. 4.44. FESEM micrograph of eroded surface of HVAF coating at 60° impingement angle on different locations for 35 m/s impingement velocity.

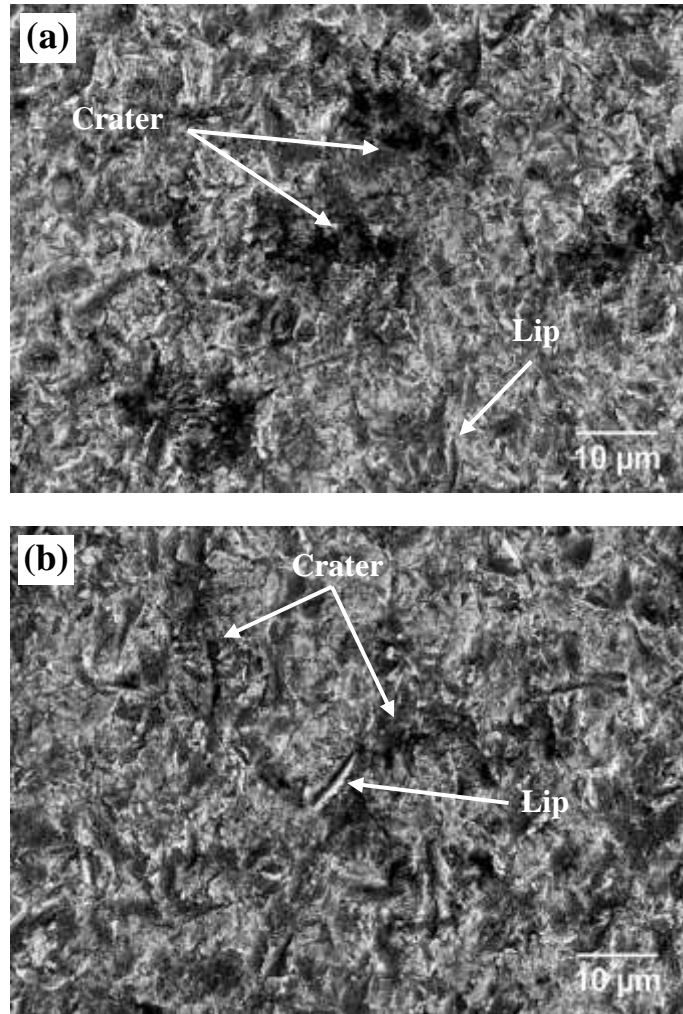


Fig. 4.45. FESEM micrograph of eroded surface of HVAF coating at 60° impingement angle on different locations for 70 m/s impingement velocity.

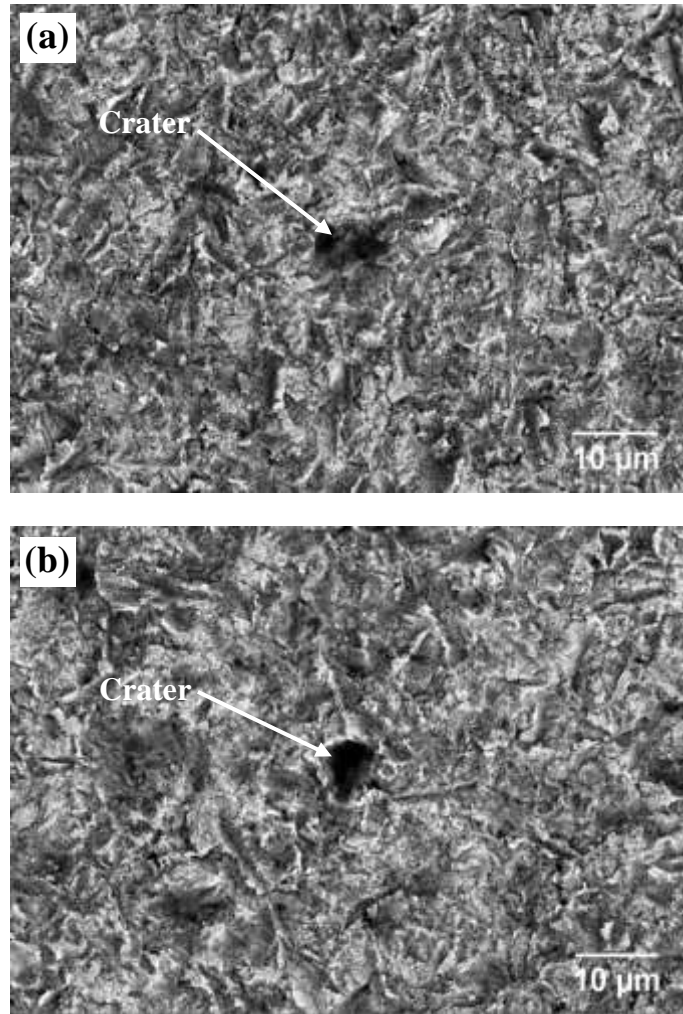


Fig. 4.46. FESEM micrograph of eroded surface of HVOF coating at 90° impingement angle on different locations for 35 m/s impingement velocity.

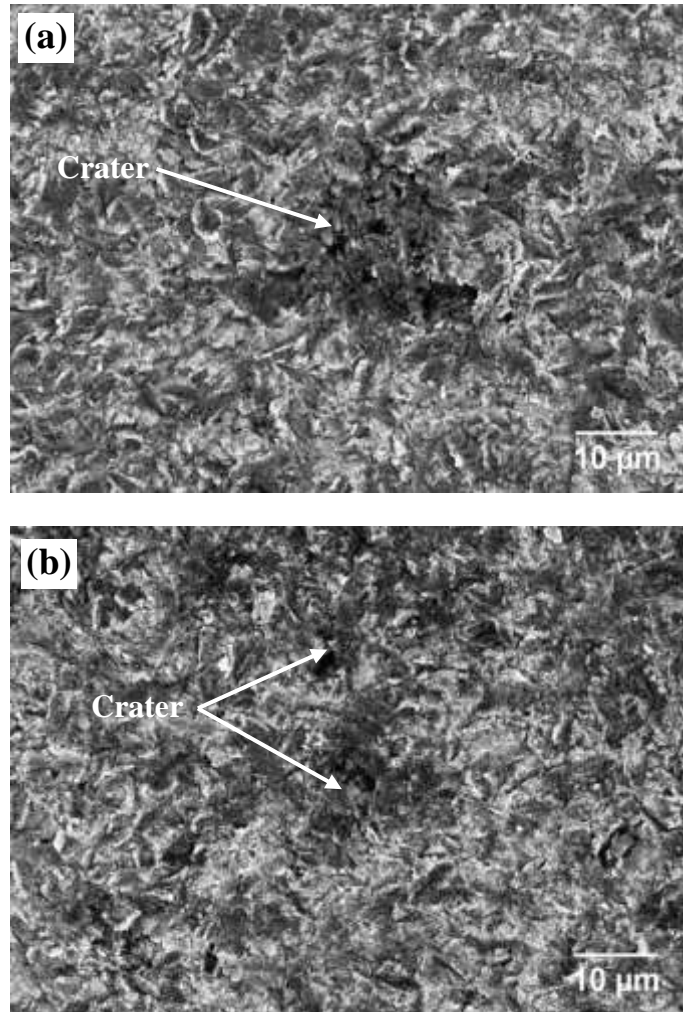


Fig. 4.47. FESEM micrograph of eroded surface of HVAF coating at 90° impingement angle on different locations for 70 m/s impingement velocity.

CHAPTER 5

Conclusions and Suggestions for Future Work

The conclusions of the experimental work performed in this study and suggestions for future work are presented in this chapter.

5.1. Conclusions

The important conclusions drawn from the present investigation are divided into three parts, and they are as follows:

(i) Cast CA6NM steel:

1. CA6NM steel shows lath martensite with delta ferrite as a secondary phase.
2. Maximum cumulative volume loss in the case of CA6NM steel was observed at 30° impingement angle followed by 60° and 90°, which points to the fact that material has eroded in a ductile manner.
3. It was also noted that cumulative volume loss at 30°, 60° and 90° impingement angles for 35 m/s impingement velocity is lower than that observed at 70 m/s impingement velocity, Which is mainly due to the higher kinetic energy of impacting particles at higher impingement velocity.

(ii) HVOF sprayed WC-10Co-4Cr coating on CA6NM steel:

1. The XRD analysis of the surface of HVOF sprayed WC-10Co-4Cr coating revealed that decarburization of WC into W_2C had taken place. WC retention was found to be 87.47 %.
2. The polished cross-sectional microstructure of HVOF sprayed WC-10Co-4Cr coating showed a uniform and well-bonded coating with laminar structure.
3. The fracture toughness and tensile adhesion of coating was found to be on lower side due to the presence of porosity in the coating.
4. Application of HVOF coating significantly improved the erosion resistance of CA6NM steel. Higher cumulative volume loss is observed at 70 m/s impingement velocity in comparison to 35 m/s impingement velocity.

5. Maximum cumulative volume loss was observed at 60° impingement angle followed by 90° and 30°, which points to the fact that material has eroded in mixed mode (ductile & brittle).
6. After the application of HVOF coating 44 to 72 % improvement in erosion resistance was observed in uncoated steel.

(iii) HVAF sprayed WC-10Co-4Cr coating on CA6NM steel:

1. The XRD analysis of the surface of HVAF sprayed WC-10Co-4Cr coating revealed that very little amount of decarburization of WC into W₂C had taken place. WC retention was found to be 96.00 %.
2. The polished cross-sectional microstructure of HVAF sprayed WC-10Co-4Cr coating shows a uniform, well-bonded structure with low porosity.
3. The fracture toughness of coating was found to be higher side which is due to lower porosity,
4. The HVAF-sprayed WC-10Co-4Cr coating enhanced the erosion resistance of the CA6NM steel. This may be attributed to its higher hardness of coating as compared to the uncoated steel.
5. Higher cumulative volume loss is observed at 70 m/s impingement velocity in comparison to 35 m/s impingement velocity. This is attributed to the higher kinetic energy of erodent in the case of 70m/s impact velocity.
6. The percentage improvement in erosion resistance after application of HVAF coating on CA6NM steel is higher than HVOF coating.
7. After the application of HVAF coating 65 to 84 % improvement in erosion resistance was observed in uncoated steel.
8. Tensile adhesion of HVAF sprayed coatings was found to be higher than HVOF coatings, which is mainly attributed to lower porosity and decarburization of WC particle.

HVAF sprayed WC-10Co-4Cr coating demonstrated significant improvement in erosion resistance as compared to HVOF sprayed WC-10Co-4Cr coating. Both HVOF and HVAF thermal spray coatings on CA6NM steel substrate have potential to prevent the erosion damages in hydroturbine components. However, HVAF coated steel may resist the erosion of hydroturbine components for a longer period.

5.2. Suggestions for Future Work

There are the following suggestions for future work.

1. Post-spray modification of thermal spray coating such as laser remelting, heat treatment should also be carry out to further improve erosion resistance of coated steel.
2. The nano-structured coating may also be attempted to further increase the erosion resistance.
3. HVAF sprayed steel have shown better erosion resistance than HVOF sprayed coating. Process parameters such as air to fuel ratio, powder feed rate, spraying distance may be varied to increase the deposition efficiency further.
4. Thermal spray coatings can be attempted on heat treated steel substrate and relation of substrate properties on final properties of coating can be studied.

References

- [1] U. Dorji, R. Ghomashchi, Hydro turbine failure mechanisms: An overview, *Eng. Fail. Anal.* 44 (2014) 136–147.
- [2] B. Singh, O. Gunnar, B. Thapa, Sediment erosion in hydro turbines and its effect on the flow around guide vanes of Francis turbine, *Renew. Sustain. Energy Rev.* 49 (2015) 1100–1113.
- [3] A. Kumar, G. Tripathi, A. Hamilton, A. Sharma, Effect of Heat Treatment on Microstructure , Mechanical Properties and Erosion Behaviour of Cast 21-4-N Nitronic Steel, *Mater. Sci. Eng.* 121 (2016) 1–5.
- [4] M.K. Padhy, R.P. Saini, Effect of size and concentration of silt particles on erosion of Pelton turbine buckets, *Energy.* 34 (2009) 1477–1483.
- [5] A. Kumar, A. Sharma, S.K. Goel, Effect of heat treatment on microstructure , mechanical properties and erosion resistance of cast 23-8-N nitronic steel, *Mater. Sci. Eng. A.* 637 (2015) 56–62.
- [6] S. Khurana, Navtej, H. Singh, Effect of cavitation on hydraulic turbines- A review, *Int. J. Curr. Eng. Technol.* 2 (2012) 172–177.
- [7] R. Koirala, B. Thapa, H.P. Neopane, B. Zhu, B. Chhetry, Sediment erosion in guide vanes of Francis turbine: A case study of Kaligandaki Hydropower Plant, Nepal, *Wear.* 362–363 (2016) 53–60.
- [8] B.S. Mann, High-energy particle impact wear resistance of hard coatings and their application in hydroturbines, (2000) 140–146.
- [9] S. Kumar, Estimation of Silt Erosion in Hydro Turbine, *Int. J. Eng. Res. Technol.* 4 (2015) 65–68.
- [10] M. Singh, J. Banerjee, P.L. Patel, H. Tiwari, Effect of silt erosion on Francis turbine: a case study of Maneri Bhali Stage-II, Uttarakhand, India, *ISH J. Hydraul. Eng.* (2012) 37–41.
- [11] A.K. Chauhan, D.B. Goel, S. Prakash, Solid particle erosion behaviour of 13Cr-4Ni and 21Cr-4Ni-N steels, *J. Alloys Compd.* 467 (2009) 459–464.
- [12] M. Singh, J. Banerjee, P.L. Patel, H. Tiwari, Effect of silt erosion on Francis turbine: a case study of Maneri Bhali Stage-II, Uttarakhand, India, *ISH J. Hydraul. Eng.* (2012) 1–10.
- [13] S. Khurana, Varun, A. Kumar, Silt erosion study on the performance of an impulse

- turbine in small hydropower, *Int. J. Ambient Energy*. 750 (2015) 1–8.
- [14] G.P.Patel, P. Singh, P. Kulshreshtha, V. Atreya, J. Singh, Silt erosion, *Int. Conf. Hydropower Sustain. Dev.* (2015) 563–568.
- [15] D.B. Goel, Metallurgy of erosion of underwater parts in hydro electric projects, in: *Metall. Eros. Underw. Parts Hydro Electr. Proj., Proceedings of the 3rd International Conference on Silting problems in Hydropower Projects*, 2008.
- [16] H.S. Grewal, H. Singh, A. Agrawal, Understanding Liquid Impingement erosion behaviour of nickel-alumina based thermal spray coatings, *Wear*. 301 (2013) 424–433.
- [17] A. Luna-ramírez, A. Campos-amezcua, O. Dorantes-gómez, Z. Mazur-czerwiec, R. Muñoz-quezada, Failure analysis of runner blades in a Francis hydraulic turbine — Case study, *EFA*. 59 (2016) 314–325.
- [18] R.P. Singh, Silt damage control measures for underwater parts-Nathpa Jhakri hydro power station-Case study of a success story, *Water Energy Int.* 66 (2009) 36–42.
- [19] S. Khurana, K. Kumar, A. Kumar, Silt erosion in hydro turbines- A review, *Int. J. Mech. Prod. Eng.* 1 (2012) 34–38.
- [20] M.K. Padhy, R.P. Saini, Study of silt erosion mechanism in Pelton turbine buckets, *Energy*. 39 (2012) 286–293.
- [21] A. Islam, T. Alam, Z.N. Farhat, A. Mohamed, A. Alfantazi, Effect of microstructure on the erosion behavior of carbon steel, *Wear*. 332–333 (2015) 1080–1089.
- [22] A. Islam, Z.N. Farhat, Effect of impact angle and velocity on erosion of API X42 pipeline steel under high abrasive feed rate, *Wear*. 311 (2014) 180–190.
- [23] Y.I. Oka, H. Ohnogi, T. Hosokawa, M. Matsumura, The impact angle dependence of erosion damage caused by solid particle impact, *Wear*. 203–204 (1997) 573–579.
- [24] M. Divakar, V.K. Agarwal, S.N. Singh, Effect of the material surface hardness on the erosion of AISI316, *Wear*. 259 (2005) 110–117.
- [25] E.Z. Jan Suchanek, Vladimir Kuklik, Influence of microstructure on erosion resistance of steels, *Wear*. 267 (2009) 2092–2099.
- [26] Y.C. B. Sun, J. Fan, D. Wen, An experimental study of slurry erosion involving tensile stress for pressure pipe manifold, *Tribol. Int.* 82 (2015) 280–286.
- [27] G.F. Truscott, A literature survey on abrasive wear in hydraulic machinery, *Wear*. 20 (1972) 29–50.
- [28] A.K. Chauhan, D.B. Goel, S. Prakash, Erosion behaviour of hydro turbine steels, *Bull. Mater. Sci.* 31 (2008) 115–120.
- [29] T. Manisekaran, M. Kamaraj, S.M. Sharrif, S. V. Joshi, Slurry erosion studies on

- surface modified 13Cr-4Ni steels: Effect of angle of impingement and particle size, *J. Mater. Eng. Perform.* 16 (2007) 567–572.
- [30] S.A. Romo, J.F. Santa, J.E. Giraldo, A. Toro, Cavitation and high-velocity slurry erosion resistance of welded Stellite 6 alloy, *Tribol. Int.* 47 (2012) 16–24.
- [31] S.S. Basha, V.M. Periasamy, M. Kamaraj, S.M. Shariff, Improvement of Slurry Erosion Wear Resistance of 16Cr-5Ni Martensite Stainless Steel by LSA and LTH, 22 (2013) 3689–3698.
- [32] S.Y. Cui, Q. Miao, W.P. Liang, B.Z. Huang, Z. Ding, B.W. Chen, Slurry Erosion Behavior of F6NM Stainless Steel and High-Velocity Oxygen Fuel-Sprayed WC-10Co-4Cr Coating, *J. Therm. Spray Technol.* 26 (2017) 473–482.
- [33] J.F. Santa, J.C. Baena, A. Toro, Slurry erosion of thermal spray coatings and stainless steels for hydraulic machinery, *Wear.* 263 (2007) 258–264.
- [34] Avnish Kumar, Ashok Sharma, S.K. Goel, Erosion behaviour of WC-10Co-4Cr coating on 23-8-N nitronic steel by HVOF thermal spraying, *Appl. Surf. Sci.* 370 (2016).
- [35] H. Wang, X. Wang, X. Song, X. Liu, X. Liu, Sliding wear behavior of nanostructured WC – Co – Cr coatings, *Appl. Surf. Sci.* 355 (2015) 453–460.
- [36] Z.H. Masuku, P.A. Olubambi, J.H. Potgieter, B.A. Obadele, Tribological and Corrosion Behavior of HVOF-Sprayed WC-Co-Based Composite Coatings in Simulated Mine Water Environments, *Tribol. Trans.* 58 (2015).
- [37] S. Bhandari, H. Singh, Slurry Erosion Behaviour of Detonation Gun Spray Al_2O_3 Accelerated Conditions, *Tribol Lett.* 45 (2012) 319–331.
- [38] G. Singh, S. Bhandari, Slurry erosion comparison of d-gun sprayed stellite- 6, Cr_3C_2 -25NiCr coatings and substrate 13Cr4Ni under hydro accelerated condition, *Int. J. Adv. Res. Eng. Technol.* (2013) 210–222.
- [39] H. Singh, K. Goyal, D.K. Goyal, Slurry Erosion Behaviour of Plasma Thermal Sprayed (50 %) WC-Co-Cr and Ni-Cr-B-Si Coatings of Different Thickness on CA6NM Turbine Steel Material, 2 (2014) 81–92.
- [40] G. Bolelli, L.M. Berger, M. Bonetti, L. Lusvardi, Comparative study of the dry sliding wear behaviour of HVOF-sprayed WC-(W,Cr)₂C-Ni and WC-CoCr hardmetal coatings, *Wear.* 309 (2014) 96–111.
- [41] Y.Y. Santana, J.G. La Barbera-sosa, A. Bencomo, J. Lesage, D. Chicot, E. Bemporad, M.H. Staia, Influence of mechanical properties of tungsten carbide – cobalt thermal spray coatings on their solid particle erosion behaviour, 28 (2012) 237–244.
- [42] D. Kumar, H. Singh, H. Kumar, V. Sahni, Slurry erosion behaviour of HVOF sprayed

- WC -10Co - 4Cr and Al₂O₃ + 13TiO₂ coatings on a turbine steel, *Wear*. 289 (2012) 46–57.
- [43] H.L.D.V. Lovelock, Powder/processing/structure relationships in WC-Co thermal spray coatings: A review of the published literature, *J. Therm. Spray Technol.* 7 (1998) 357–373.
- [44] D.A. Stewart, P.H. Shipway, D.G. McCartney, Abrasive wear behaviour of conventional and nanocomposite HVOF-sprayed WC-Co coatings, *Wear*. 225–229 (1999) 789–798.
- [45] M. Jafari, M.H. Enayati, M. Salehi, S.M. Nahvi, C.G. Park, Comparison between oxidation kinetics of HVOF sprayed WC-12Co and WC-10Co-4Cr coatings, *Int. J. Refract. Met. Hard Mater.* 41 (2013) 78–84.
- [46] L. Zhao, M. Maurer, F. Fischer, E. Lugscheider, Study of HVOF spraying of WC-CoCr using on-line particle monitoring, *Surf. Coatings Technol.* 185 (2004) 160–165.
- [47] D. A. Karandikar, HVOF coatings to combat hydro abrasive erosion, *Int. Conf. Hydropower Sustain. Dev.* (2015) 171–179.
- [48] D.K. Goyal, H. Singh, H. Kumar, V. Sahni, Slurry Erosive Wear Evaluation of HVOF-Spray Cr₂O₃ Coating on Some Turbine Steels, 21 (2012) 838–851.
- [49] H. Liao, B. Normand, C. Coddet, Influence of coating microstructure on the abrasive wear resistance of WC/Co cermet coatings, *Surf. Coatings Technol.* 124 (2000) 235–242.
- [50] D.A. Stewart, P.H. Shipway, Microstructural evolution in thermally sprayed WC - Co coatings : comparison between nanocomposite and conventional starting powders, *Acta Mater.* 48 (2000) 1593–1604.
- [51] B.H. Kear, G. Skandan, R.K. Sadangi, factors controlling decarburization in hvof sprayed nano- WC/Co hardcoatings, *Scr. Mater.* 44 (2001) 1703–1707.
- [52] D. Fu, H. Xiong, Q. Wang, Microstructure Evolution and Its Effect on the Wear Performance of HVOF-Sprayed Conventional WC-Co Coating, *J. Mater. Eng. Perform.* 1 (2016).
- [53] P. Chivavibul, M. Watanabe, S. Kuroda, K. Shinoda, Effects of carbide size and Co content on the microstructure and mechanical properties of HVOF-sprayed WC-Co coatings, *Surf. Coatings Technol.* 202 (2007) 509–521.
- [54] I. Hulka, D. Utu, V.A. Serban, M.L. Dan, V. Matikainen, P. Vuoristo, Corrosion Behavior of WC-FeCrAl Coatings Deposited by HVOF and HVOF Thermal Spraying Methods, *Chem. Bull. "POLITEHNICA" Univ. (Timisoara)*. 61(75) (2016).

- [55] C. Lyphout, S. Björklund, Internal Diameter HVOF Spraying for Wear and Corrosion Applications, *J. Therm. Spray Technol.* 24 (2014) 235–243.
- [56] S. Matthews, B. James, M. Hyland, The role of microstructure in the mechanism of high velocity erosion of Cr₃C₂-NiCr thermal spray coatings: Part 1 - As-sprayed coatings, *Surf. Coatings Technol.* 203 (2009) 1086–1093.
- [57] S.B. E. Sadeghimeresht, N. Markocsan, P. Nylén, Corrosion performance of bi-layer NiCr₂C₃-NiCr HVOF thermal spray, *Appl. Surf. Sci.* 369 (2016) 470–481.
- [58] A. Milanti, V. Matikainen, H. Koivuluoto, G. Bolelli, L. Lusvarghi, P. Vuoristo, Effect of spraying parameters on the microstructural and corrosion properties of HVOF-sprayed Fe-Cr-Ni-B-C coatings, *Surf. Coatings Technol.* 277 (2015) 81–90.
- [59] C. Lyphout, K. Sato, S. Houdkova, E. Smazalova, L. Lusvarghi, G. Bolelli, P. Sassatelli, Tribological Properties of Hard Metal Coatings Sprayed by High-Velocity Air Fuel Process, *J. Therm. Spray Technol.* 25 (2016) 331–345.
- [60] H. Myalska, G. Moskal, K. Szymański, Microstructure and properties of WC-Co coatings, modified by sub-microcrystalline carbides, obtained by different methods of high velocity spray processes, *Surf. Coatings Technol.* 260 (2014) 303–309.
- [61] H. Myalska, K. Szymański, G. Moskal, Microstructure and properties of WC-Co HVOF coatings obtained from standard, superfine and modified by sub-micrometric carbide powders, *Arch. Metall. Mater.* 60 (2015).
- [62] X.P.Z. S.L. Liu, Microstructure and properties of AC-HVOF sprayed Ni60WC composite coating, *J. Alloys Compd.* 480 (2009) 254–258.
- [63] L. Jacobs, M.M. Hyland, M. De Bonte, Comparative Study of WC-Cermet Coatings Sprayed via the HVOF and the HVOF Process, 7 (1998) 213–218.
- [64] Q. Wang, S. Zhang, Y. Cheng, J. Xiang, X. Zhao, G. Yang, Wear and corrosion performance of WC-10Co4Cr coatings deposited by different HVOF and HVOF spraying processes, *Surf. Coatings Technol.* 218 (2013) 127–136.
- [65] G.Q.G. S.L. Liu, X.P. Zheng, Influence of nano-WC-12Co powder addition in WC-10Co-4Cr AC-HVOF sprayed, *Wear.* 269 (2010) 362–367.
- [66] Q. Wang, Z. Tang, L. Cha, Cavitation and Sand Slurry Erosion Resistances of WC-10Co-4Cr Coatings, *J. Mater. Eng. Perform.* 24 (2015) 2435–2443.
- [67] V. Matikainen, H. Koivuluoto, A. Milanti, P. Vuoristo, Advanced coatings by novel high-kinetic thermal spray processes, *T. Tek. Mater.* (2015) 46–50.
- [68] K.N. I. Hulka, V.A. Şerban, I. Secoşan, P. Vuoristo, Wear properties of CrC-37WC-18M coatings deposited by HVOF and HVOF, *Surf. Coat. Technol.* 210 (2012) 15–20.

- [69] R.Q. Guo, C. Zhang, Q. Chen, Y. Yang, N. Li, L. Liu, Study of structure and corrosion resistance of Fe-based amorphous coatings prepared by HVAF and HVOF, *Corros. Sci.* 53 (2011) 2351–2356.
- [70] H.M. Shenglin Liu, Dongbai Sun, Zishuan Fan, Hong-ying Yu, The influence of HVAF powder feedstock characteristics on the sliding wear, *Surf. Coat. Technol.* 202 (2008) 4893–4900.
- [71] G.P. Patel, P. Singh, P. Kulshreshtha, V. Atreya, J. Singh, Silt erosion, in: *Int. Conf. Hydropower Sustain. Dev.*, (2015) 563–568.
- [72] R.K. Kumar, M. Kamaraj, P. Samapthkumaran, S. Seetharamu, Abrasion and erosion characteristics of hydro turbine materials and HVOF processed tungsten carbide coatings, in: *Metall. Probl. Power Proj. India*, (2013) 30–37.
- [73] N. Kishor, R.P. Saini, S.P. Singh, A review on hydropower plant models and control, *Renew. Sustain. Energy Rev.* 11, (2007) 776–796.
- [74] L. Gudukeya, I. Madanhire, Efficiency improvement of pelton wheel and cross-flow turbines in micro-hydro power plants: case study, *Int. J. Eng. Comput. Sci.* 2 (2013) 416–432.
- [75] M. Kumar, A. Nikhade, Cavitation in Kaplan Turbines – A Review, *J. Mater. Sci. Mech. Eng.* 2 (2015) 425–429.
- [76] V.K. Mehta, R. Mehta, *Principles of power system: Including generation, transmission, distribution, switchgear and protection*, S. Chand Limited, New Delhi, India, 2005.
- [77] R.K. Bansal, *A textbook of fluid mechanics and hydraulic machines*, 9th ed., Laxmi Publications, New Delhi, India, 2017.
- [78] R.K. Rajput, *A Textbook of Hydraulic Machines In SI Units*, 3rd ed., S. Chand Limited, New Delhi, India, (2006).
- [79] H. Brekke, Y.L. Wu, B.Y. Cai, Design of hydraulic machinery working in sand laden water, in: *Abras. Eros. Corros. Hydraul. Mach.*, 2nd ed., Imperial College Press, (2003) 155–233.
- [80] I.F.P. A.M. Morales, J.A.E. J. Loboguerrero, J.A. Medina, Development of a test rig to evaluate abrasive wear on Pelton turbine nozzles. A case study of Chivor hydropower, *Wear.* 372–373 (2017) 208–215.
- [81] B.V. S. Kumar, Estimation of silt erosion in hydro turbine, *Int. J. Eng. Res. Technol.* 4 (2015) 65–68.
- [82] H.S. Grewal, H.S. Arora, A. Agrawal, H. Singh, S. Mukherjee, Slurry erosion of

- thermal spray coatings: Effect of sand concentration, *Procedia Eng.* 68 (2013) 484–490.
- [83] A. Hamed, W. Tabakoff, R. Wenglarz, Erosion and deposition in turbomachinery, *J. Propuls. Power.* 22, (2006) 350–360.
- [84] T.R. Bajracharya, B. Acharya, C.B. Joshi, R.P. Saini, O.G. Dahlhaug, Sand erosion of Pelton turbine nozzles and buckets : A case study of Chilime Hydropower Plant, *Wear.* 264 (2008) 177–184.
- [85] M. Padhy, P. Senapati, Turbine blade materials used for the power plants exposed to high silt erosion – A review, in: *ICHPSD-2015*, 2015: pp. 114–122.
- [86] ASTM G40-15, Standard Terminology Relating to Wear and Erosion, (2015) 1–9.
- [87] J. Roberto, T. Branco, R. Gansert, S. Sampath, C.C. Berndt, H. Herman, Solid Particle Erosion of Plasma Sprayed Ceramic Coatings, 7 (2004) 147–153.
- [88] E. Bousser, L. Martinu, J.E. Klemberg-Sapieha, Solid particle erosion mechanisms of hard protective coatings, *Surf. Coatings Technol.* 235 (2013) 383–393.
- [89] E. Bousser, L. Martinu, J.E. Klemberg-Sapieha, Solid particle erosion mechanisms of protective coatings for aerospace applications, *Surf. Coatings Technol.* 257 (2014) 165–181.
- [90] T.H. Kosel, Solid Particle Erosion, in: *ASM Handb. Vol. 18 Frict. Lubr. Wear Technol.*, 10th Editi, ASM International, (1992) 199–213.
- [91] J. Malik, I.H. Toor, W.H. Ahmed, Z.M. Gasem, M.A. Habib, H.M. Badr, Evaluating the Effect of Hardness on Erosion Characteristics of Aluminum and Steels, *JMEPEG.* 23 (2014) 2274–2282.
- [92] B.A. Lindsley, A.R. Marder, Solid particle erosion of an Fe–Fe₃C metal matrix composite, *Metall. Mater. Trans. A.* 29 (1998) 1071–1079.
- [93] S. Yerramareddy, Effect of operational variables , microstructure and mechanical properties on the erosion of Ti-6Al-4V, *Wear.* 42 (1991) 253–263.
- [94] F. Cernuschi, C. Guardamagna, S. Capelli, L. Lorenzoni, D.E. Mack, A. Moscatelli, Solid particle erosion of standard and advanced thermal barrier coatings, *Wear*, (2016) 348–349.
- [95] E. Avcu, S. Fidan, Y. Yıldiran, T. Sınmazçelik, E. Avcu, S. Fidan, Y. Yıldiran, T. Sınmazçelik, Solid particle erosion behaviour of Ti6Al4V alloy Solid particle erosion behaviour of Ti6Al4V alloy, *Tribol. - Mater. Surfaces Interfaces.* 5831 (2017).
- [96] F. Cernuschi, C. Guardamagna, S. Capelli, L. Lorenzoni, D.E. Mack, A. Moscatelli, Solid particle erosion of standard and advanced thermal barrier coatings, *Wear.* 348–

- 349 (2016) 43–51.
- [97] A.P. Harsha, U.S. Tewari, B. Venkatraman, Solid particle erosion behaviour of various polyaryletherketone composites, *Wear*. 254 (2003) 693–712.
- [98] S.B. Mishra, S. Prakash, K. Chandra, Studies on erosion behaviour of plasma sprayed coatings on a Ni-based superalloy, *Wear*. 260 (2006) 422–432.
- [99] G. Sundararajan, The solid particle erosion of metallic materials: The rationalization of the influence of material variables, *Wear*. 186187 (1995) 129–144.
- [100] A. Singh, R.L. Viridi, K. Goyal, To study the slurry erosion behaviour of hard faced alloy SS304, *Manuf. Sci. Technol.* 2 (2014) 111–115.
- [101] A. V. Levy, G. Hickey, Liquid-solid particle slurry erosion of steels, *Wear*. 117 (1987) 129–146.
- [102] C.S. Ramesh, R. Keshavamurthy, B.H. Channabasappa, S. Pramod, Influence of heat treatment on slurry erosive wear resistance of Al6061 alloy, *Mater. Des.* 30 (2009) 3713–3722.
- [103] A.A. Noon, M.H. Kim, Erosion wear on centrifugal pump casing due to slurry flow, *Wear*, (2016) 103–111.
- [104] J.E. Miller, Slurry Erosion, in: *ASM Handb. Vol. 18 Frict. Lubr. Wear Technol.*, ASM International, (1992) 233–235.
- [105] H.M. Clark, The influence of the flow field in slurry erosion, *Wear*. 152 (1992) 223–240.
- [106] S. Purkayastha, D. Kumar Dwivedi, Slurry erosion performance of CeO₂-modified Ni–WC coatings, *Ind. Lubr. Tribol.* 66 (2014) 533–537.
- [107] S.R. More, B.D. Nandre, G.R. Desale, Development of Pot Tester to Simulate the Erosion Wear due to Solid-Liquid Mixture, 2 (2014) 6–12.
- [108] A. V. Levy, P. Yau, Erosion of steels in liquid slurries, *Wear*. 98 (1984) 163–182.
- [109] J. Stokes, Surface engineering and wear, in: *Theory Appl. HVOF Therm. Spray Process*, Dublin City University, 2008.
- [110] J.H. Wu, W.J. Gou, Critical size effect of sand particles on cavitation damage, *J. Hydrodyn.* 25 (2013) 165–166.
- [111] S. LI, Cavitation enhancement of silt erosio- An envisaged micro model, *Wear*. (2006) 1145–1150.
- [112] X. Escaler, E. Egusquiza, M. Farhat, F. Avellan, M. Coussirat, Detection of cavitation in hydraulic turbines, *Mech. Syst. Signal Process.* 20 (2006) 983–1007.
- [113] L. Thakur, N. Arora, A study on erosive wear behavior of HVOF sprayed

- nanostructured WC-CoCr coatings, *J. Mech. Sci. Technol.* 27 (2013) 1461–1467.
doi:10.1007/s12206-013-0326-1.
- [114] D.S.L. Ning Qiu, Leqin Wang, Suhuan Wu, Research on cavitation erosion and wear resistance, *Eng. Fail. Anal.* 55 (2015) 208–233.
- [115] S. Hong, Y. Wu, J. Zhang, Y. Zheng, Y. Qin, W. Gao, G. Li, Cavitation Erosion Behavior and Mechanism of HVOF Sprayed WC-10Co-4Cr Coating in 3.5 wt% NaCl Solution, *Trans. Indian Inst. Met.* 68 (2014) 151–159.
- [116] R. Singh, S.K. Tiwari, S.K. Mishra, Cavitation erosion in hydraulic turbine components and mitigation by coatings: Current status and future needs, *J. Mater. Eng. Perform.* 21 (2012) 1539–1551.
- [117] L.A. Espitia, A. Toro, Cavitation resistance, microstructure and surface topography of materials used for hydraulic components, *Tribol. Int.* 43 (2010) 2037–2045.
- [118] B.K. Pant, V. Arya, B.S. Mann, Cavitation erosion characteristics of nitrocarburized and HPDL-treated martensitic stainless steels, *J. Mater. Eng. Perform.* 21 (2012) 1051–1055.
- [119] H.X. Hu, S.L. Jiang, Y.S. Tao, T.Y. Xiong, Y.G. Zheng, Cavitation erosion and jet impingement erosion mechanism of cold sprayed Ni-Al₂O₃ coating, *Nucl. Eng. Des.* 241 (2011) 4929–4937.
- [120] S. Hattori, M. Takinami, Comparison of cavitation erosion rate with liquid impingement erosion rate, *Wear.* 269 (2010) 310–316.
- [121] ASTM G73-10, Standard test method for liquid impingement erosion using rotating apparatus, ASTM International, West Conshohocken, PA, (2010).
- [122] N. Andrews, L. Giourntas, A.M. Galloway, A. Pearson, Effect of impact angle on the slurry erosion-corrosion of Stellite 6 and SS316, *Wear.* 320, (2014) 143–151.
- [123] D.C. Wen, Particle erosion of SUS403 tempered martensitic stainless steel, *ISIJ Int.* 46, (2006) 728–733.
- [124] Q.B. Nguyen, V.B. Nguyen, C.Y.H. Lim, Q.T. Trinh, S. Sankaranarayanan, Effect of impact angle and testing time on erosion of stainless steel at higher velocities, *Wear.* 321 (2014) 87–93.
- [125] J.R. Laguna-Camacho, A. Marquina-Chavez, J.V. Mendez-Mendez, M. Vite-Torres, E.A. Gallardo-Hernandez, Solid particle erosion of AISI 304, 316 and 420 stainless steels, *Wear.* 301 (2013) 398–405.
- [126] H.S. Grewal, A. Agrawal, H. Singh, Identifying Erosion Mechanism : A Novel Approach, *Tribol Lett.* (2013) 1–7.

- [127] A.K. Chauhan, Cavitation erosion resistance of 13/4 and 21-4-N steels, *Sadhana*. 38, (2013) 25–35.
- [128] M.K. Padhy, R.P. Saini, A review on silt erosion in hydro turbines, *Renew. Sustain. Energy Rev.* 12, (2008) 1974–1987.
- [129] L.P. McCabe, G. A. Sargent, H. Conrad, Effect of microstructure on the erosion of steel by solid particles, *Wear*. 105, (1985) 257–277.
- [130] D.B. Goel, Metallurgy of erosion of under water parts in hydro electric projects, in: 3rd Int. Conf. Silting Probl. Hydro Power Proj., New Delhi, 2008: pp. 1–10.
- [131] H.J. Amarendra, G.P. Chaudhari, S.K. Nath, Synergy of cavitation and slurry erosion in the slurry pot tester, *Wear*. 290–291 (2012) 25–31.
- [132] R. Singh, S.K. Tiwari, S.K. Mishra, Cavitation erosion in hydraulic turbine components and mitigation by coatings: Current status and future needs, *J. Mater. Eng. Perform.* 21, (2012) 1539–1551.
- [133] M. Lindgren, J. Perolainen, Slurry pot investigation of the influence of erodent characteristics on the erosion resistance of austenitic and duplex stainless steel grades, *Wear*. 319, (2014) 38–48.
- [134] T. Frosell, M. Fripp, E. Gutmark, Investigation of slurry concentration effects on solid particle erosion rate for an impinging jet, *Wear*. 342–343, (2015) 33–43.
- [135] M.K. Sharma, G.S. Grewal, A.K. Singh, Silt erosion in Indian hydroelectric projects- Laboratory studies of thermal spray coatings over hydro turbine components, *Hydrovision.*, (2007) 1–12.
- [136] S. Kumar, J.S. Ratol, Effects of tribological parameters on slurry erosion behaviour of uncoated and coated materials: A review, *Mater. Eng.* 20, (2013) 119–131.
- [137] O. Gohardani, Impact of erosion testing aspects on current and future flight conditions, *Prog. Aerosp. Sci.* 47, (2011) 280–303.
- [138] S. Yerramareddy, S. Bahadur, Effect of operational variables, microstructure and mechanical properties on the erosion of Ti-6Al-4V, *Wear*. 42, (1991) 253–263.
- [139] Y.M. Abd-Elrhman, A. Abouel-Kasem, K.M. Emara, S.M. Ahmed, Effect of Impact Angle on Slurry Erosion Behavior and Mechanisms of Carburized AISI 5117 Steel, *J. Tribol.* 136 (2013) 11106.
- [140] E. Rodríguez, M. Flores, A. Pérez, R.D. Mercado-solis, R. González, Erosive wear by silica sand on AISI H13 and 4140 steels, *Wear*. 267 (2009) 2109–2115.
- [141] I. Finnie, Erosion of surface by solid particles, *Wear*. 3 (1960) 87–103.
- [142] A.M.A.M. Paul C. Okonkwo, R.A. Shakoor, Essam Ahmed, Erosive wear

- performance of API X42 pipeline steel, *Eng. Fail. Anal. J.* 60 (2016) 86–95.
- [143] P.C. Okonkwo, A.M.A. Mohamed, E. Ahmed, Influence of particle velocities and impact angles on the erosion mechanisms of AISI 1018 steel, *Adv. Mater. Lett.* 6 (2015) 653–659.
- [144] ASTM B962-13, Standard test methods for density of compacted or sintered powder metallurgy (PM) products using archimedes' principle, ASTM International, West Conshohocken, PA, (2013).
- [145] G.R. Desale, B.K. Gandhi, S.C. Jain, Particle size effects on the slurry erosion of aluminium alloy (AA 6063), *Wear.* 266 (2009) 1066–1071.
- [146] B.A. Lindsley, A.R. Marder, The effect of velocity on the solid particle erosion rate of alloys, *Wear.* (1999) 510–516.
- [147] S. Bahadur, R. Badruddin, Erodent particle characterization and the effect of particle size and shape on erosion, *Wear.* 138 (1990) 189–208.
- [148] Z. Feng, A. Ball, The erosion of four materials using seven erodents — towards an understanding, *Wear.* (1999) 674–684.
- [149] C.I. Walker, M. Hambe, Influence of particle shape on slurry wear of white iron, *Wear.* 333, (2015) 1021–1027.
- [150] M. Lindgren, R. Suihkonen, J. Vuorinen, Erosive wear of various stainless steel grades used as impeller blade materials in high temperature aqueous slurry, *Wear.* 328–329, (2015) 391–400.
- [151] N. Ojala, K. Valtonen, A. Antikainen, A. Kemppainen, J. Minkkinen, O. Oja, et al., Wear performance of quenched wear resistant steels in abrasive slurry erosion, *Wear.* 354–355, (2016) 21–31.
- [152] S. Chatterjee, T.K. Pal, Solid particle erosion behaviour of hardfacing deposits on cast iron-Influence of deposit microstructure and erodent particles, *Wear.* 261, (2006) 1069–1079.
- [153] S. Kumar, B. Varshney, Estimation of silt erosion in hydro turbine, *Int. J. Eng. Res. Technol.* 4, (2015) 65–68.
- [154] W. Tsai, J.A.C. Humphrey, I. Cornet, A. V Levy, Experimental measurement of accelerated erosion in a slurry pot tester, *Wear.* 68 (1981) 289–303.
- [155] A. V Levy, P. Chik, The effects of erodent erosion of steel composition and shape on the, *Wear.* 89 (1983) 151–162.
- [156] S. Turenne, M. Fiset, J. Masounave, The effect of sand concentration materials by a slurry jet, *Wear.* 133 (1989) 95–106.

- [157] J. Salik, D. Buckley, W.A. Brainard, The effect of mechanical surface and heat treatments on the erosion resistance of 6061 aluminum alloy, *Wear*. 65 (1981) 351–358.
- [158] G. Green, R. Taggart, D. Polonis, Influence of microstructure on the erosion of plain carbon steels, *Metallography*. 212 (1981) 191–212.
- [159] H.M. Clark, R.J. Llewellyn, Assessment of the erosion resistance of steels used for slurry handling and transport in mineral processing applications, *Wear*. 250 (2001) 32–44.
- [160] M. Naim and S. Bahadur, The significance of the erosion parameter and the mechanisms of erosion in single-particle impacts, *Wear* 94, (1984) 219–232.
- [161] W.J.P. Casas, S.L. Henke, N. Novicki, Fracture toughness of CA6NM alloy, quenched and tempered, and of its welded joint without PWHT, *Weld. Int.* 23 (2009) 166–172.
- [162] R. Ganesan, Improving the quality of high alloy CA6NM stainless steel castings, 2015.
- [163] C. García De Andrés, G. Caruana, L.F. Alvarez, Control of $M_{23}C_6$ carbides in 0.45C–13Cr martensitic stainless steel by means of three representative heat treatment parameters, *Mater. Sci. Eng. A241*. (1998) 211–215.
- [164] A.N. Isfahany, H. Saghafian, G. Borhani, The effect of heat treatment on mechanical properties and corrosion behavior of AISI420 martensitic stainless steel, *J. Alloys Compd.* 509 (2011) 3931–3936.
- [165] A. Trudel, M. Lvesque, M. Brochu, Microstructural effects on the fatigue crack growth resistance of a stainless steel CA6NM weld, *Eng. Fract. Mech.* 115 (2014) 60–72.
- [166] S.H. Avner, *Introduction to Physical Metallurgy*, 2nd ed., McGraw Hill Education, 2008.
- [167] High performance stainless steel, <http://www.outokumpu.com/>, (2017).
- [168] G.S. J. Menzel, W. Kirschner, High nitrogen containing Ni-free austenitic steels for medical applications, *ISIJ Int.* 36 (1996) 893–900.
- [169] S. Siegmann, C. Abert, 100 years of thermal spray: About the inventor Max Ulrich Schoop, *Surf. Coatings Technol.* 220 (2013) 3–13.
- [170] L.M. Berger, Application of hardmetals as thermal spray coatings, *Int. J. Refract. Met. Hard Mater.* 49 (2015) 350–364.
- [171] A. Vackel, G. Dwivedi, S. Sampath, Structurally Integrated, Damage-Tolerant, Thermal Spray Coatings, *Jom.* 67 (2015) 1540–1553.
- [172] P. Fauchais, M. Fukumoto, A. Vardelle, M. Vardelle, Knowledge Concerning Splat Formation: An Invited Review, *J. Therm. Spray Technol.* 13 (2004) 337–360.

- [173] S.J. Matthews, B.J. James, M.M. Hyland, Microstructural influence on erosion behaviour of thermal spray coatings, *Mater. Charact.* 58 (2007) 59–64.
- [174] C. Li, A. Ohmori, Relationships between the microstructure and properties of thermally sprayed deposits, *J. Therm. Spray Technol.* 11 (2002) 365–374.
- [175] Y. Wang, C. Li, A. Ohmori, Influence of substrate roughness on the bonding mechanisms of high velocity oxy-fuel sprayed coatings, 485 (2005) 141–147.
- [176] M.M. El Rayes, H.S. Abdo, K.A. Khalil, Erosion - Corrosion of cermet coating, *Int. J. Electrochem. Sci.* 8 (2013) 1117–1137.
- [177] M. Singla, H. Singh, V. Chawla, Thermal Sprayed CNT Reinforced Nanocomposite Coatings—A Review, *J. Miner. Mater.* 10 (2011) 717–726.
- [178] R.J. Talib, S. Saad, M.R.M. Toff, H. Hashim, Thermal Spray Processes Combustion Electric Wire Plasma, *Solid State Sci. Technol.* 11 (2003) 109–117.
- [179] Y.G. Yingqing Fu, Tianxiang Peng, Deming Yang, Chengqi Sun, Yuzhen Chen, HVOF sprayed Al–Cu–Cr quasicrystalline coatings from coarse feedstock powders, *Surf. Coat. Technol.* 252 (2014) 29–34.
- [180] C.J. Li, G.J. Yang, Relationships between feedstock structure, particle parameter, coating deposition, microstructure and properties for thermally sprayed conventional and nanostructured WC-Co, *Int. J. Refract. Met. Hard Mater.* 39, (2013) 2–17.
- [181] Z. Geng, S. Hou, G. Shi, D. Duan, S. Li, Tribological behaviour at various temperatures of WC-Co coatings prepared using different thermal spraying techniques, *Tribology Int.* 104, (2016) 36–44.
- [182] J.R. Davis, *Handbook of thermal spray technology*, 1st ed., ASM International, 2004.
- [183] J. Robert C. Tucker, *ASM Handbook, Volume 5A: Thermal Spray Technology*, 1st ed., ASM International, 2013.
- [184] J.S.S. Ayyappan Susila Praveen, J. Sarangan, S. Suresh, Erosion wear behaviour of plasma sprayed NiCrSiBA₂O₃, *Int. J. Refract. Hard Mater.* 52 (2015) 209–218.
- [185] T. Troczynski, S. Cockcroft, H. Wong, Thermal Barrier Coatings for Heta Engines, *Key Eng. Mater.* 122–124 (1996) 451–462.
- [186] S. Kamal, R. Jayaganthan, S. Prakash, High temperature oxidation studies of detonation-gun-sprayed Cr₃C₂-NiCr coating on Fe- and Ni-based superalloys in air under cyclic condition at 900 C, *J. Alloys Compd.* 472 (2009) 378–389.
- [187] M. Kaur, H. Singh, S. Prakash, Surface engineering analysis of detonation-gun sprayed Cr₃C₂-NiCr coating under high-temperature oxidation and oxidation-erosion environments, *Surf. Coatings Technol.* 206 (2011) 530–541.

- [188] A.K. Chauhan, D.B. Goel, S. Prakash, Erosive wear of a surface coated hydroturbine steel, *Bull. Mater. Sci.*, 33 (2010) 483–489.
- [189] G. Sundararajan, K.U.M. Prasad, D.S. Rao, S. V. Joshi, A Comparative Study of Tribological Behavior of Plasma and D-Gun Sprayed Coatings under Different Wear Modes, *J. Mater. Eng. Perform.* 7 (1998) 343–351.
- [190] G. Sundararajan, P.S. Babu, Detonation sprayed WC-Co coatings: Unique aspects of their structure and mechanical behaviour, *Trans. Indian Inst. Met.* 62 (2009) 95–103.
- [191] E.F. Bernhard Wielage, Andreas Wank, Hanna Pokhmurska, Thomas Grund, Christian Rupprecht, Guido Reisel, Development and trends in HVOF spraying technology, *Surf. Coat. Technol.* 201 (2006) 2032–2037.
- [192] S.P. Hazoor Singh Sidhu, Buta Singh Sidhu, Mechanical and microstructural properties of HVOF sprayed WC–Co and Cr₃C₂–NiCr coatings on the boiler tube steels using LPG as the fuel gas, *J. Mater. Process. Technol.* 171 (2006) 77–82.
- [193] S. Sharma, Erosive wear study of rare earth-modified hvof-sprayed coatings using design of experiment, *J. Therm. Spray Technol.* 21 (2012) 49–62.
- [194] C. Li, H. Yang, H. Li, Effect of gas conditions on HVOF flame and properties of WC-Co coatings, *Mater. Manuf. Process.* 14 (1999) 383–395.
- [195] G.-J.Y. Chang-Jiu Li, Relationships between feedstock structure, particle parameter, coating deposition, microstructure and properties for thermally sprayed conventional and nanostructured WC–Co, *Int. J. Refract. Met. Hard Mater.* 39 (2013) 2–17.
- [196] A.O. Qiaoqin Yang, Tetsuya Senda, Effect of carbide grain size on microstructure and sliding wear behavior of HVOF-sprayed WC–12% Co coatings, *Wear.* 254 (2003) 23–34.
- [197] T.F. Weber, High-Velocity Oxy-Fuel Spraying, *Mater. Sci. Forum.* 163–165 (1994) 573–578.
- [198] M. Li, D. Shi, P.D. Christofides, Diamond Jet hybrid HVOF thermal spray: Gas-phase and particle behavior modeling and feedback control design, *Ind. Eng. Chem. Res.* 43 (2004) 3632–3652.
- [199] R.J.K. Wood, Tribology of thermal sprayed WC-Co coatings, *Int. J. Refract. Met. Hard Mater.* 28 (2010) 82–94.
- [200] Sulzer Metco (<https://www.sulzer.com/>), An introduction to thermal spray, (2013) 1–24.
- [201] P.N. E. Sadeghimeresht, H. Hooshyar, N. Markocsan, S. Joshi, Oxidation behavior of HVAF-sprayed NiCoCrAlY coating in H₂-H₂O environment, *Oxid. Met.* 86 (2016)

- 299–314.
- [202] A. Milanti, H. Koivuluoto, P. Vuoristo, Influence of the Spray Gun Type on Microstructure and Properties of HVOF Sprayed Fe-Based Corrosion Resistant Coatings, *J. Therm. Spray Technol.* 24 (2015) 1312–1322.
- [203] H.R. Ma, J.W. Li, J. Jiao, C.T. Chang, G. Wang, J. Shen, X.M. Wang, R.W. Li, Wear resistance of Fe-based amorphous coatings prepared by AC-HVOF and HVOF, *Mater. Sci. Technol.* 33 (2017) 65–71.
- [204] G. Bolelli, T. Börner, A. Milanti, L. Lusvarghi, J. Laurila, H. Koivuluoto, K. Niemi, P. Vuoristo, Tribological behavior of HVOF- and HVOF-sprayed composite coatings based on Fe-Alloy + WC-12% Co, *Surf. Coatings Technol.* 248 (2014) 104–112.
- [205] A. Verstak, V. Baranovski, AC-HVOF sprayed tungsten carbide : Properties and applications, in: *Therm. Spray Sci. Innov. Appl. ASM Int.*, pp. 643–648., (2006).
- [206] H.S. Grewal, A. Agrawal, H. Singh, B.A. Shollock, Slurry Erosion Performance of Ni-Al₂O₃ Based Thermal-Sprayed Coatings : Effect of Angle of Impingement, 23 (2014) 389–401.
- [207] H.S. Grewal, A. Agrawal, H. Singh, Slurry erosion performance of Ni – Al₂O₃ based composite coatings, *Tribology Int.* 66 (2013) 296–306.
- [208] A. Lekatou, D. Sioulas, A.E. Karantzalis, D. Grimanelis, A comparative study on the microstructure and surface property evaluation of coatings produced from nanostructured and conventional WC-Co powders HVOF-sprayed on Al7075, *Surf. Coatings Technol.* 276 (2015) 539–556.
- [209] T.C. Hanson, C.M. Hackett, G.S. Settles, Independent Control of HVOF Particle Velocity and Temperature, *J. Therm. Spray Technol.* 11 (2002) 75–85.
- [210] J. Nerz, B. Kushner, A. Rotolico, Microstructural evaluation of tungsten carbide-cobalt coatings, *J. Therm. Spray Technol.* 1 (1992) 147–152.
- [211] C. Verdon, A. Karimi, J. Martin, A study of high velocity oxy-fuel thermally sprayed tungsten carbide based coatings . Part 1 : Microstructures, *Mater. Sci. Eng. A.* 246 (1998) 11–24.
- [212] D. Lou, J. Hellman, D. Luhulima, J. Liimatainen, V.K. Lindroos, Interactions between tungsten carbide (WC) particulates and metal matrix in WC-reinforced composites, *Mater. Sci. Eng. A.* 340 (2003) 155–162.
- [213] D. Kekes, P. Psyllaki, M. Vardavoulias, Tribology in Industry Wear Micro-Mechanisms of Composite WC-Co / Cr - NiCrFeBSiC Coatings . Part I : Dry Sliding, 36 (2014) 361–374.

- [214] R.J.K.W. J. Barber, B.G. Mellor, The development of sub-surface damage during high energy solid particle erosion of a thermally sprayed WC–Co–Cr coating J., *Wear*. 259 (2005) 125–134.
- [215] Q. Wang, S. Zhang, Y. Cheng, J. Xiang, X. Zhao, G. Yang, Wear and corrosion performance of WC-10Co4Cr coatings deposited by different HVOF and HVAF spraying processes, *Surf. Coatings Technol.* 218 (2013) 127–136
- [216] J.L. Sheng Hong, YupingWu, Yugui Zheng, BoWang, Wenwen Gao , Microstructure and electrochemical properties of nanostructured WC–10Co–4Cr coating prepared by HVOF spraying, *Surf. Coat. Technol.* 235 (2013) 582–588.
- [217] G. Bolelli, L.M. Berger, T. B??rner, H. Koivuluoto, L. Lusvarghi, C. Lyphout, N. Markocsan, V. Matikainen, P. Nyl, P. Sassatelli, R. Trache, P. Vuoristo, Tribology of HVOF- and HVAF-sprayed WC-10Co4Cr hardmetal coatings: A comparative assessment, *Surf. Coatings Technol.* 265 (2015) 125–144.
- [218] I. Hussainova, Effect of microstructure on the erosive wear of titanium carbide-based cermets, *Wear*. 255 (2003) 121–128.
- [219] M. Xie, S. Zhang, Mingxi Li, Comparative investigation on HVOF sprayed carbide-based coatings, *Appl. Surf. Sci.* 273 (2013) 799– 805.
- [220] J.K.N. Murthy, K. Satya Prasad, K. Gopinath, B. Venkataraman, Characterisation of HVOF sprayed Cr₃C₂-50(Ni20Cr) coating and the influence of binder properties on solid particle erosion behaviour, *Surf. Coatings Technol.* 204 (2010) 3975–3985.
- [221] M. Kovaleva, Y. Tyurin, N. Vasilik, O. Kolisnichenko, M. Prozorova, M. Arsenko, Effect of processing parameters on the microstructure and properties of WC – 10Co – 4Cr coatings formed by a new multi-chamber gas-dynamic accelerator, *Ceram. Int.* 41 (2015) 15067–15074.
- [222] M.M. Lima, C. Godoy, P.J. Modenesi, J.C. Avelar-Batista, A. Davison, A. Matthews, Coating fracture toughness determined by Vickers indentation: an important parameter in cavitation erosion resistance of WC–Co thermally sprayed coatings, *Surf. Coatings Technol.* 177–178 (2004) 489–496.
- [223] R.S. Lalit Thakur, N. Arora, R. Jayaganthan, An investigation on erosion behavior of HVOF sprayed WC–CoCr coatings, *Appl. Surf. Sci.* 258 (2011) 1225–1234.
- [224] S. Bhandari, H. Singh, H.K. Kansal, Slurry erosion studies of hydroturbine steels under hydroaccelerated conditions, 226 (2014) 239–250.
- [225] ASTM E8/E8M - 15a, Standard test methods for tension testing of metallic materials, ASTM International, West Conshohocken, PA, (2015).

- [226] ASTM E 23-12c, Standard test methods for notched bar impact testing of metallic materials, ASTM International, West Conshohocken, PA, (2012).
- [227] G.G. H. Wang, X. Song, C. Wei, Y. Gao, Abrasion resistance enhancement of ultrafine-structured WC-Co coating fabricated by using in situ synthesized composite powder, *J. Mater. Sci. Technol.* 29 (2013) 1067–1073.
- [228] H. Myalska, K. Szymaski, G. Moskal, Microstructure and properties of WC-Co HVAF coatings obtained from standard, superfine and modified by sub-micrometric carbide powders, *Arch. Metall. Mater.* 60 (2015) 759–766.
- [229] M. Jafari, M.H. Enayati, M. Salehi, S.M. Nahvi, S.N. Hosseini, C.G. Park, Influence of Nickel-Coated Nanostructured WC-Co Powders on Microstructural and Tribological Properties of HVOF Coatings, *J. Therm. Spray Technol.* 23 (2014) 1456–1469.
- [230] C. Bartuli, T. Valente, F. Cipri, E. Bemporad, M. Tului, Parametric Study of an HVOF Process for the Deposition of Nanostructured WC-Co Coatings, *J. Therm. Spray Technol.* 14 (2005) 187–195.
- [231] G. Bolelli, L. Berger, T. Börner, H. Koivuluoto, L. Lusvarghi, C. Lyphout, N. Markocsan, V. Matikainen, P. Nylén, P. Sassatelli, R. Trache, P. Vuoristo, Tribology of HVOF- and HVAF-sprayed WC – 10Co4Cr hardmetal coatings : A comparative assessment, *Surf. Coat. Technol.* 265 (2015) 125–144.
- [232] A.G. Evans, T.R. Wilshaw, Quasi-static solid particle damage in brittle solids-1. Observations, Analysis and Implications, *Acta Metall.* 24 (1976).
- [233] ASTM C633-13, Standard Test Method for Adhesion or Cohesion Strength of Thermal Spray Coatings 1, 3 (2001) 1–7.
- [234] S. Kuroda, J. Kawakita, T. Fukushima, S. Tobe, Importance of the adhesion of HVOF sprayed coatings for aqueous corrosion resistance, *ITSC, Therm. Spray 2001 New Surfaces a New Millennium.* 44 (2001) 1123–1129.
- [235] C.R.C. Lima, J.M. Guilemany, Adhesion improvements of Thermal Barrier Coatings with HVOF thermally sprayed bond coats, *Surf. Coat. Technol.* 201 (2007) 4694–4701.
- [236] ASTM G76-13, Standard Test Method for Conducting Erosion Tests by Solid Particle Impingement Using Gas Jets 1, (2013) 1–6.
- [237] H. Conrad, Technical Note A new method of velocity calibration for erosion testing, 101 (1985) 69–76.
- [238] A.W. Ruff, L.K. Ives, Short Communication Measurement of solid particle velocity in erosive wear, *Wear.* 35 (1975) 195–199.

- [239] M.R. Ramesh, S. Prakash, S.K. Nath, P.K. Sapra, B. Venkataraman, Solid particle erosion of HVOF sprayed WC-CoNiCrFeSiB coatings, *Wear*. 269 (2010) 197–205.
- [240] H.. Hawthorne, B. Arsenault, J.. Immarigeon, J.. Legoux, V.. Parameswaran, Comparison of slurry and dry erosion behaviour of some HVOF thermal sprayed coatings, *Wear*. 225–229 (1999) 825–834.
- [241] J.K.N. Murthy, D.S. Rao, B. Venkataraman, Effect of grinding on the erosion behaviour of a WC – Co – Cr coating deposited by HVOF and detonation gun spray processes, 249 (2001) 592–600.
- [242] R.G. Rateick, K.R. Karasek, A.J. Cunningham, K.C. Goretta, J.L. Routbort, Solid-particle erosion of tungsten carbide/cobalt cermet and hardened 440C stainless steel-A comparison, *Wear*. 261 (2006) 773–778.
- [243] H. Teng, C. Hsu, S. Chiu, D. Wen, Erosion Behavior of CA-15 Tempered Martensitic Stainless Steel, 44 (2003) 1480–1487.
- [244] H.S. Sidhu, B.S. Sidhu, S. Prakash, Solid particle erosion of HVOF sprayed NiCr and Stellite-6 coatings, *Surf. Coat. Technol.* 202 (2007) 232–238.
- [245] Y.Y. Santana, P.O. Renault, M. Sebastiani, J.G. La Barbera, J. Lesage, E. Bemporad, E. Le Bourhis, E.S. Puchi-Cabrera, M.H. Staia, Characterization and residual stresses of WC-Co thermally sprayed coatings, *Surf. Coatings Technol.* 202 (2008) 4560–4565.
- [246] P. Kulu, I. Hussainova, R. Veinthal, Solid particle erosion of thermal sprayed coatings, *Wear*. 258 (2005).
- [247] P.S. Babu, B. Basu, G. Sundararajan, The influence of erodent hardness on the erosion behavior of detonation sprayed WC-12Co coatings, *Wear*. 270 (2011) 903–913.
- [248] P.S. Babu, B. Basu, G. Sundararajan, The influence of erodent hardness on the erosion behavior of detonation sprayed WC-12Co coatings, *Wear*. 270 (2011) 903–913.
- [249] R.J.K. Wood, J. Barber, B.G. Mellor, The development of sub-surface damage during high energy solid particle erosion of a thermally sprayed WC–Co–Cr coating, *Wear*. (2005).
- [250] Y. Liu, W. Liu, Y. Ma, S. Meng, C. Liu, L.S.T. Long, A comparative study on wear and corrosion behaviour of HVOF- and HVOF-sprayed WC–10Co–4Cr coatings, *Surf. Eng.* (2015) 1–9.
- [251] I. Hussainova, Some aspects of solid particle erosion of cermets, *Tribol. Int.* 34 (2001) 89–93.
- [252] L.M. Berger, S. Saaro, T. Naumann, M. Wiener, V. Weihnacht, S. Thiele, J. Suchánek, Microstructure and properties of HVOF-sprayed chromium alloyed WC-Co and WC-

- Ni coatings, *Surf. Coatings Technol.* 202 (2008) 4417–4421.
- [253] L. Thakur, N. Arora, Solid Particle Erosion Behavior of WC-CoCr Nanostructured Coating, *Tribol. Trans.* 56 (2013) 781–788.
- [254] P. Kulu, I. Hussainova, R. Veinthal, Solid particle erosion of thermal sprayed coatings, *Wear.* (2005).

APPENDICES

Appendix I

(Solid particle erosion experimental data of uncoated
CA6NM steel substrate)

(i) Cumulative volume loss at 30° impingement angle

Test duration (min)	35 m/s impingement velocity			70 m/s impingement velocity		
	Wt. loss* (mg)	Vol. loss (cm ³)	Cum. Vol. loss (cm ³)	Wt. loss* (mg)	Vol. loss (cm ³)	Cum. Vol. loss (cm ³)
2	0.9	0.0001169	1.17E-04	1.51	0.000196104	1.96E-04
4	0.77	0.0001	2.17E-04	1.32	0.000171429	3.68E-04
6	0.98	0.0001273	3.44E-04	1.61	0.000209091	5.77E-04
8	1.11	0.0001442	4.88E-04	1.89	0.000245455	8.22E-04
10	1.03	0.0001338	6.22E-04	1.75	0.000227273	1.05E-03
12	0.75	9.74E-05	7.19E-04	1.28	0.000166234	1.22E-03
14	0.81	0.0001052	8.25E-04	1.36	0.000176623	1.39E-03

(ii) Cumulative volume loss at 60° impingement angle

Test duration (min)	35 m/s impingement velocity			70 m/s impingement velocity		
	Wt. loss* (mg)	Vol. loss (cm ³)	Cum. Vol. loss (cm ³)	Wt. loss* (mg)	Vol. loss (cm ³)	Cum. Vol. loss (cm ³)
2	0.69	8.961E-05	8.96E-05	1.26	0.0001636	1.64E-04
4	0.89	0.0001156	2.05E-04	1.63	0.0002117	3.75E-04
6	0.69	8.961E-05	2.95E-04	1.41	0.0001831	5.58E-04
8	0.81	0.0001052	4.00E-04	1.21	0.0001571	7.16E-04
10	0.59	7.662E-05	4.77E-04	1.03	0.0001338	8.49E-04
12	0.74	9.61E-05	5.73E-04	1.33	0.0001727	1.02E-03
14	0.69	8.961E-05	6.62E-04	1.25	0.0001623	1.18E-03

*Average of two samples

(iii) Cumulative volume loss at 90° impingement angle

Test duration (min)	35 m/s impingement velocity			70 m/s impingement velocity		
	Wt. loss* (mg)	Vol. loss (cm ³)	Cum. Vol. loss (cm ³)	Wt. loss* (mg)	Vol. loss (cm ³)	Cum. Vol. loss (cm ³)
2	0.6	7.79221E-05	7.79E-05	1.12	0.0001455	1.45E-04
4	0.43	5.58442E-05	1.34E-04	0.93	0.0001208	2.66E-04
6	0.54	7.01299E-05	2.04E-04	1.08	0.0001403	4.06E-04
8	0.64	8.31169E-05	2.87E-04	1.31	0.0001701	5.77E-04
10	0.67	8.7013E-05	3.74E-04	1.17	0.0001519	7.29E-04
12	0.49	6.36364E-05	4.38E-04	0.86	0.0001117	8.40E-04
14	0.62	8.05195E-05	5.18E-04	0.97	0.000126	9.66E-04

*Average of two samples

Appendix II

(Solid particle erosion experimental data of HVOF coated CA6NM steel substrate)

(i) Cumulative volume loss at 30° impingement angle

Test duration (min)	35 m/s impingement velocity			70 m/s impingement velocity		
	Wt. loss* (mg)	Vol. loss (cm ³)	Cum. Vol. loss (cm ³)	Wt. loss* (mg)	Vol. loss (cm ³)	Cum. Vol. loss (cm ³)
2	0.39	3.37E-05	3.37E-05	0.72	6.23E-05	6.23E-05
4	0.46	3.98E-05	7.35E-05	0.78	6.75E-05	1.30E-04
6	0.35	3.03E-05	1.04E-04	0.6	5.19E-05	1.82E-04
8	0.49	4.24E-05	1.46E-04	0.85	7.35E-05	2.55E-04
10	0.34	2.94E-05	1.76E-04	0.58	5.02E-05	3.05E-04
12	0.36	3.11E-05	2.07E-04	0.63	5.45E-05	3.60E-04
14	0.3	2.59E-05	2.33E-04	0.54	4.67E-05	4.07E-04

(ii) Cumulative volume loss at 60° impingement angle

Test duration (min)	35 m/s impingement velocity			70 m/s impingement velocity		
	Wt. loss* (mg)	Vol. loss (cm ³)	Cum. Vol. loss (cm ³)	Wt. loss* (mg)	Vol. loss (cm ³)	Cum. Vol. loss (cm ³)
2	0.51	4.41E-05	4.41E-05	1.1	9.52E-05	9.52E-05
4	0.67	5.80E-05	1.02E-04	1.22	1.06E-04	2.01E-04
6	0.62	5.36E-05	1.56E-04	1.1	9.52E-05	2.96E-04
8	0.7	6.06E-05	2.16E-04	1.3	1.12E-04	4.08E-04
10	0.53	4.58E-05	2.62E-04	0.95	8.22E-05	4.90E-04
12	0.52	4.50E-05	3.07E-04	1.01	8.74E-05	5.78E-04
14	0.54	4.67E-05	3.54E-04	0.92	7.95E-05	6.57E-04

*Average of two samples

(iii) Cumulative volume loss at 90° impingement angle

Test duration (min)	35 m/s impingement velocity			70 m/s impingement velocity		
	Wt. loss* (mg)	Vol. loss (cm ³)	Cum. Vol. loss (cm ³)	Wt. loss* (mg)	Vol. loss (cm ³)	Cum. Vol. loss (cm ³)
2	0.48	4.15E-05	4.15E-05	0.98	8.48E-05	8.48E-05
4	0.51	4.41E-05	8.56E-05	0.95	8.22E-05	1.67E-04
6	0.62	5.36E-05	1.39E-04	0.98	8.48E-05	2.52E-04
8	0.52	4.50E-05	1.84E-04	1.11	9.60E-05	3.48E-04
10	0.5	4.33E-05	2.28E-04	1.03	8.91E-05	4.37E-04
12	0.34	2.94E-05	2.57E-04	0.87	7.53E-05	5.12E-04
14	0.3	2.59E-05	2.83E-04	0.8	6.92E-05	5.81E-04

*Average of two samples

Appendix III

(Solid particle erosion experimental data of HVOF coated CA6NM steel substrates)

(i) Cumulative volume loss at 30° impingement angle

Test duration (min)	35 m/s impingement velocity			70 m/s impingement velocity		
	Wt. loss* (mg)	Vol. loss (cm ³)	Cum. Vol. loss (cm ³)	Wt. loss* (mg)	Vol. loss (cm ³)	Cum. Vol. loss (cm ³)
2	0.23	1.67E-05	1.70E-05	0.48	3.54E-05	3.55E-05
4	0.19	1.41E-05	3.10E-05	0.41	3.03E-05	6.58E-05
6	0.22	1.62E-05	4.73E-05	0.47	3.47E-05	1.01E-04
8	0.28	2.06E-05	6.80E-05	0.37	2.73E-05	1.28E-04
10	0.19	1.4E-05	8.20E-05	0.44	3.25E-05	1.60E-04
12	0.26	1.92E-05	1.01E-04	0.52	3.84E-05	1.99E-04
14	0.4	2.95E-05	1.31E-04	0.46	3.39E-05	2.33E-04

(ii) Cumulative volume loss at 60° impingement angle

Test duration (min)	35 m/s impingement velocity			70 m/s impingement velocity		
	Wt. loss* (mg)	Vol. loss (cm ³)	Cum. Vol. loss (cm ³)	Wt. loss* (mg)	Vol. loss (cm ³)	Cum. Vol. loss (cm ³)
2	0.49	3.62E-05	3.62E-05	0.75	5.54E-05	5.54E-05
4	0.45	3.32E-05	6.95E-05	0.88	6.50E-05	1.20E-04
6	0.41	3.03E-05	9.98E-05	0.79	5.83E-05	1.79E-04
8	0.39	2.88E-05	1.29E-04	0.74	5.46E-05	2.34E-04
10	0.35	2.58E-05	1.54E-04	0.64	4.73E-05	2.81E-04
12	0.45	3.32E-05	1.88E-04	0.73	5.39E-05	3.35E-04
14	0.36	2.66E-05	2.14E-04	0.66	4.87E-05	3.84E-04

*Average of two samples

(iii) Cumulative volume loss at 90° impingement angle

Test duration (min)	35 m/s impingement velocity			70 m/s impingement velocity		
	Wt. loss* (mg)	Vol. loss (cm ³)	Cum. Vol. loss (cm ³)	Wt. loss* (mg)	Vol. loss (cm ³)	Cum. Vol. loss (cm ³)
2	0.34	2.51E-05	2.51E-05	0.67	4.95E-05	4.95E-05
4	0.31	2.29E-05	4.80E-05	0.58	4.28E-05	9.24E-05
6	0.45	3.32E-05	8.13E-05	0.6	4.43E-05	1.37E-04
8	0.33	2.43E-05	1.06E-04	0.69	5.09E-05	1.88E-04
10	0.29	2.14E-05	1.27E-04	0.55	4.06E-05	2.28E-04
12	0.39	2.88E-05	1.56E-04	0.62	4.58E-05	2.74E-04
14	0.31	2.29E-05	1.79E-04	0.59	4.36E-05	3.18E-04

*Average of two samples

List of Publications

International Journal Publications

1. **Anurag Hamilton, Ashok Sharma, Upender Pandel**, "Solid particle erosion resistance of HVOF sprayed WC-10Co-4Cr coating on CA6NM steel" *Surface Review and Letters*, Vol. 24, Suppl. (2017)

DOI: 10.1142/S0218625X18500117 (*SCI Indexed*)

2. **Anurag Hamilton, Ashok Sharma, Upender Pandel**, "Effect of Impingement Angle on Erosion Resistance of HVOF Sprayed WC-10Co-4Cr Coating on CA6NM Steel" *Key Engineering Materials* Vol. 751, pp 79-83

DOI:10.4028/www.scientific.net/KEM.751.79 (Proceeding of 9th International Conference on Materials Science and Technology, Bangkok) (*Scopus Indexed*)

Other publication

1. **Anurag Hamilton, Ashok Sharma, Upender Pandel**, "Effect of impingement velocity on solid particle erosion behaviour of CA6NM hydroturbine steel" AMPCO-2017, IIT Roorkee, 30 Nov- 2 Dec. 2017

2. **Anurag Hamilton, Ashok Sharma, Upender Pandel**, "Different methods to combat erosion in hydro turbine" presented in a National workshop on Mechanical Failures (MF-2015) at BRCM CET Bahal, Haryana, 11-12 September 2015.

Award

1. Winner of **Thai parkerizing Best student paper Runner-up award** and award price of 20000 Bhat at The 9th International Conference on Materials Science and Technology, Bangkok (14th-15th Dec. 2016) for the paper in Surface Engineering and Heat treatment session entitled "Effect of Impingement Angle on Erosion Resistance of HVOF Sprayed WC-10Co-4Cr Coating on CA6NM Steel."

Effect of Impingement Angle on Erosion Resistance of HVOF Sprayed WC-10Co-4Cr Coating on CA6NM Steel

Anurag Hamilton^{a*}, Ashok Sharma^b, Upender Pandel^c

Department of Metallurgical and Materials Engineering,
Malaviya National Institute of Technology Jaipur, Jaipur-302017, India

^aa.hamilton2107@gmail.com, ^bashok.mnit12@gmail.com, ^cupandel.meta@mnit.ac.in

Keywords: CA6NM steel, HVOF, Microstructure, Erosion resistance

Abstract. In the present investigation, WC–10Co–4Cr coating was deposited by high velocity oxy-fuel (HVOF) process on CA6NM hydro turbine steel to improve its erosion resistance. The coating was characterized in term of crosssectional microstructure, phase, microhardness and fracture toughness using a field emission scanning electron microscope (FESEM), X-ray diffractometer and microhardness tester respectively. Solid particle erosion resistance of the substrate and coating were evaluated by air jet erosion tester at two different impingement angles (30° and 90°). Coating microstructure has shown a homogeneous and well-bonded laminar morphology. The microhardness of the coating was observed more than three times higher than CA6NM substrate. This resulted in significant improvement in erosion resistance of coated CA6NM steel at both impingement angles.

Introduction

WC-Co based cermets are widely used in industry to mitigate the problem of erosion []. In WC-Co based cermets, hard WC particles provide the wear resistant property to the material, while the cobalt binder provides ductility and toughness. High-velocity oxygen-fuel (HVOF) thermal spray process is mainly used for depositing WC–Co powders. During HVOF thermal spraying, cermet powder is melted and accelerated towards the substrate. Upon impact they solidify and forms, splats [1].

HVOF sprayed WC-Co coatings are widely used in the hydropower industry for coating of the hydro turbine and its components. The high hardness of WC-Co coatings prevents the base material from attack of silt particle. Several attempts have been made by researchers to study the erosion performance of thermal sprayed hydro turbine steel. However, it has been observed that WC-Co based cermets are superior to other coating powders. It is mainly due to composite nature of the coating, which gives it hardness, toughness, and ductility at the same time. Bhandari et al. [2] deposited a WC-Co-Cr coating on CF8M steel by detonation gun (D-gun) thermal spraying process and studied their slurry erosion behavior. It was observed that WC-Co-Cr coated steel has lower erosion rate compared to bare steel, which is due to high hardness of coating which prevented base material from silt. Singh et al. [3] studied the slurry erosion behavior of (50%) WC-Co-Cr and (50%) Ni-Cr-B-Si plasma thermal spray coated CA6NM steel. It was observed that coated steel shows better erosion resistance than uncoated steel. Till now most of the research is focused on testing slurry erosion behavior of WC-Co coated hydro turbine steel. On the other hand, solid particle erosion tester is able to generate severe erosion condition in less time. Solid particle erosion behavior study of WC-Co-Cr coated CA6NM steel at different impingement angles is scarce in literature. In the present work, solid particle erosion behavior study of HVOF sprayed WC-Co-Cr coating on CA6NM steel at different impingement angle was carried out, in order to understand the erosion mechanism in a better way.

Experimental

Substrate and Coating deposition. A hydro turbine steel of CA6NM grade (ASTM 743) was used as a substrate material for the deposition of the coating. As - cast steel test block was machined, and

samples of (25mm x 25mm x 5mm) and (25mm x 20mm x 5mm) were prepared using wire-cut electric discharge machine (EDM). The WC-10Co-4Cr powder (-45 to +15 μ m) was deposited onto CA6NM hydro turbine steel using high velocity oxy-fuel process using Hypojet-HP2100 HVOF spray system (Make: Metallizing Export Company Jodhpur, India). The coating was deposited on 103 mm x 50 mm x 5 mm plates and samples of (25mm x 25mm x 5mm) and (25mm x 20mm x 5mm) were prepared using wire-cut electric discharge machine (EDM) for erosion testing. Before the coating deposition, the steel samples were grit blasted.

Coating characterization. X-ray diffraction (XRD) was conducted for the powder and as-sprayed coatings with X'Pert Powder PANalytical with Cu K α radiation. To characterize the microstructure of coating, cross-section of the as-sprayed coating was prepared by embedding samples in conducting resin, grinding and polishing to 1 μ m finish. These were examined in a NOVA Nano 450 FESEM operated at 20 kV. FESEM is also used for analyzing the surface morphology after erosion test for coated and uncoated steel. Porosity was determined using Image analysis of cross-sectional FESEM micrograph (10,000X). A total of ten micrographs were used to calculate the average porosity of coating. The density of the coating was calculated using volume fraction of the WC, binder (Co-Cr) and pores. The density of the WC ($\rho_{WC} = 15.7 \text{ g/cm}^3$) and binder ($\rho_{Co-Cr} = 8.6 \text{ g/cm}^3$) was taken to calculate the density of the coating. Vickers micro Hardness measurement was performed on the polished transverse section of the coatings with INNOVATEST (NEXUS 4000) hardness tester at 300 g load with 10 s dwell time. The fracture toughness of coating was determined by the indentation method. A Vickers indenter was used on metallographically prepared cross sections of coating with a 5 kg load with 10 s dwell time. The fracture toughness (K_{Ic}) of the coatings was determined by the indentation method using the Evans and Wilshaw equation as given below:

$$K_{Ic} = 0.079 \frac{P}{a^{3/2}} \log 4.5 \left(\frac{a}{c} \right). \quad (1)$$

Where 'P' applied indentation load (mN), and 'a' and 'c' correspond to the length of the indentation half-diagonal (μ m) and crack length from the center of the indent (μ m) crack length, respectively. The 'c/a' ratio for use in this equation is $0.6 \leq c/a < 4.5$. Average of ten readings along with standard deviation is reported.

Erosion test procedure. The erosion test was performed using air jet erosion tester (Model: TR, DUCOM Bangalore). Erosion test was performed as per ASTM G-76-13 test standard. Alumina particle (50 μ m) is used as erodent for erosion testing. To provide an initial standard surface condition before erosion test, all specimen were polished using 0/0, 1/0, 2/0, 3/0, and 4/0 grades of emery paper. Cloth wheel polishing was done to obtain a mirror finish using a diamond paste. Each sample was removed after every 2 min to determine the mass loss. The impingement angles used for the tests were 30° and 90°. These angles were selected to evaluate the behavior of these materials at low and high impingement angles. A particle velocity of 70 m/sec is used to replicate severe erosion condition encountered by hydro turbine component, and an abrasive flow rate of 2 g/min were used to conduct the tests. Particle velocity was measured using the double disc rotating method with an accuracy of ± 2 m/s. The abrasive flow rate was measured by collecting the abrasive in a container during 1 min. Before and after the tests, each specimen was weighed using a precision electronic weighing balance with an accuracy of 0.0001 g to observe the difference in weight loss for each test. The weight loss was converted into volume loss to obtain the precise data because the WC-10Co-4Cr coating and substrate possess different densities.

Results and Discussion

Phase constitution of powder and coatings. The X-ray diffraction patterns for the surface of the HVOF sprayed WC-10Co-4Cr coating, and the feedstock powder is shown in Fig. 1. In feedstock powder, Co and WC are main phases that are observed. In the case of coating, W_2C phase is also observed which is formed due to decarburization of WC during spraying. Traces of Co_3W_3C and Co phases was also noticed.

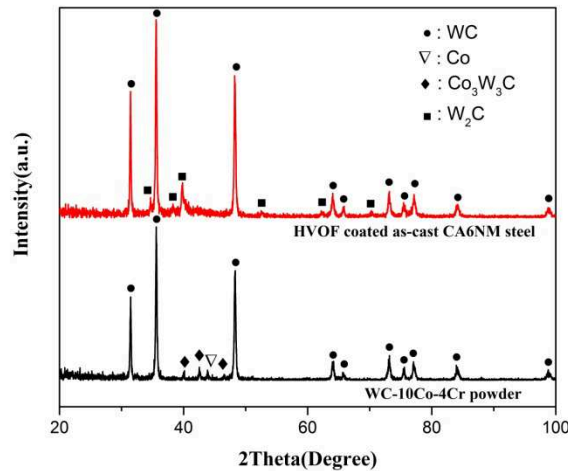


Fig. 1. XRD pattern of the WC-10Co-4Cr feedstock powder and HVOF coated CA6NM steel.

Microstructure and mechanical properties of coating. The cross-sectional FESEM micrograph of the HVOF sprayed WC-10Co-4Cr coating on the CA6NM steel has been shown in Fig. 2. At lower magnification coating-substrate interface, coating, and the substrate can be seen clearly. It is observed that coating has a homogeneous laminar structure which is well bonded to the substrate. At higher magnification pores and interlaminar oxidation can be seen. The average coating thickness of coating is found to be $305 \pm 7 \mu m$.

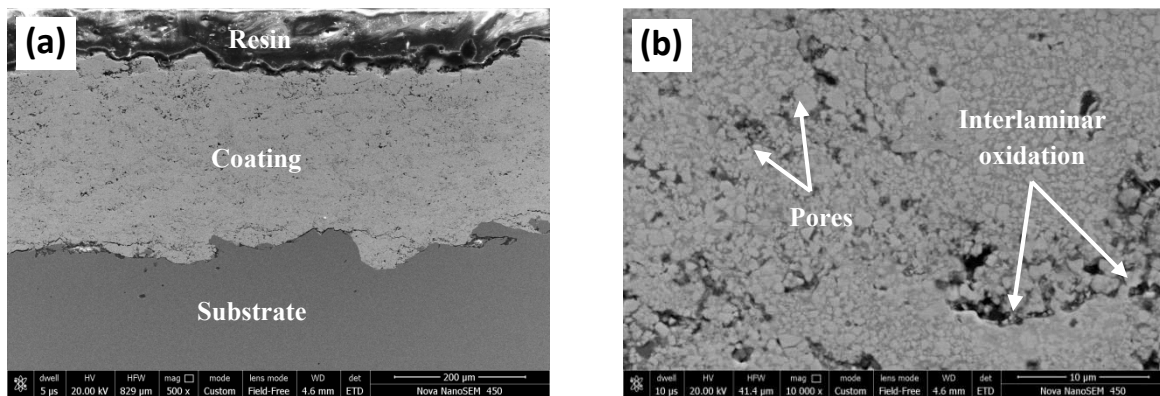


Fig. 2. Cross-sectional FESEM micrograph of WC-10Co-4Cr coating deposited on as - cast CA6NM steel sample: (a) at lower magnification; (b) at higher magnification.

The average and the standard deviation value of indentation fracture toughness and cross-sectional microhardness values of investigated samples are reported in Table 1. The fracture toughness and microhardness value of the coatings were also measured along the depth from the coating to the substrate.

Table 1. Indentation fracture toughness and cross-sectional microhardness of WC-10Co-4Cr coating and uncoated CA6NM steel.

	Indentation fracture toughness ($MPa m^{1/2}$)	Cross-sectional microhardness ($HV_{0.3}$)
WC-10Co-4Cr coating	2.31 ± 0.19	1107 ± 41
Uncoated CA6NM steel	-	338 ± 29

Erosion behavior of the uncoated and coated steel samples

Fig. 4 (a) and (b) shows the cumulative volume loss of the uncoated and WC-10Co-4Cr coating as a function erosion time at 30° and 90° impingement angle for 70 m/s impact velocity.

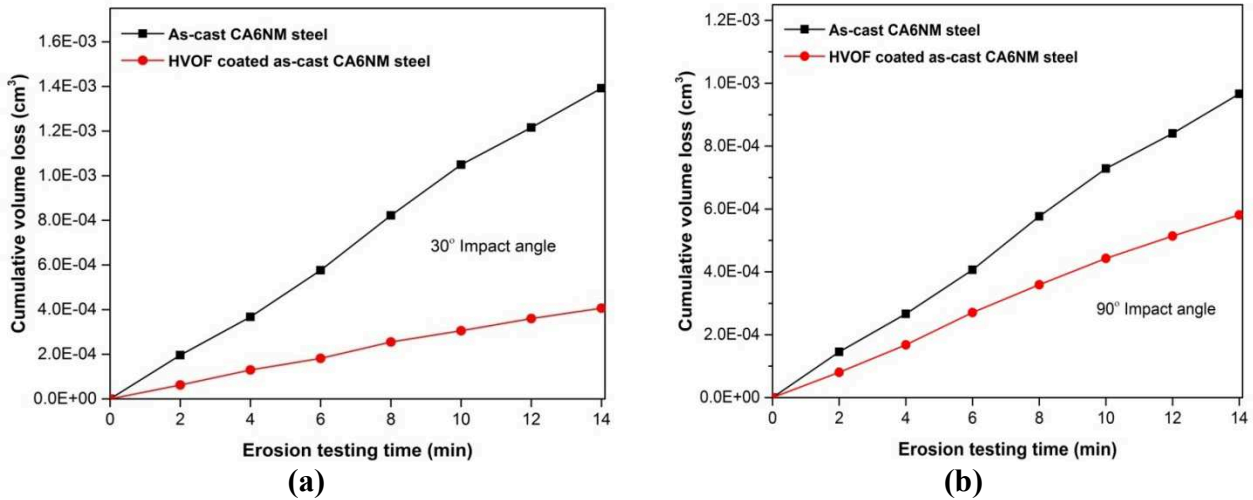


Fig. 4. Cumulative volume loss of uncoated and HVOF coated as-cast CA6NM steel as a function of time at 30° impingement angle (a) and 90° impingement angle (b).

It is observed that the cumulative volume loss of WC-10Co-4Cr coating ($4.07E-04 \text{ cm}^3$) is lower than uncoated CA6NM steel ($1.39E-03 \text{ cm}^3$) at 30° impingement angle. The FESEM micrographs of eroded surfaces of both uncoated and coated steel at 30° impingement angle are shown in Fig. 5 (a) and Fig. 6 (a). The formation of lips in uncoated and coated steel indicate that material is mainly removed by cutting and ploughing. In the case of 90° impingement angle, it is observed that the cumulative volume loss of WC-10Co-4Cr coating ($5.81E-04 \text{ cm}^3$) is also lower than uncoated CA6NM steel ($9.66E-04 \text{ cm}^3$). The FESEM micrographs of eroded surfaces of both uncoated and coated steel at 30° impingement angle are shown in Fig. 5 (b) and Fig. 6 (b).

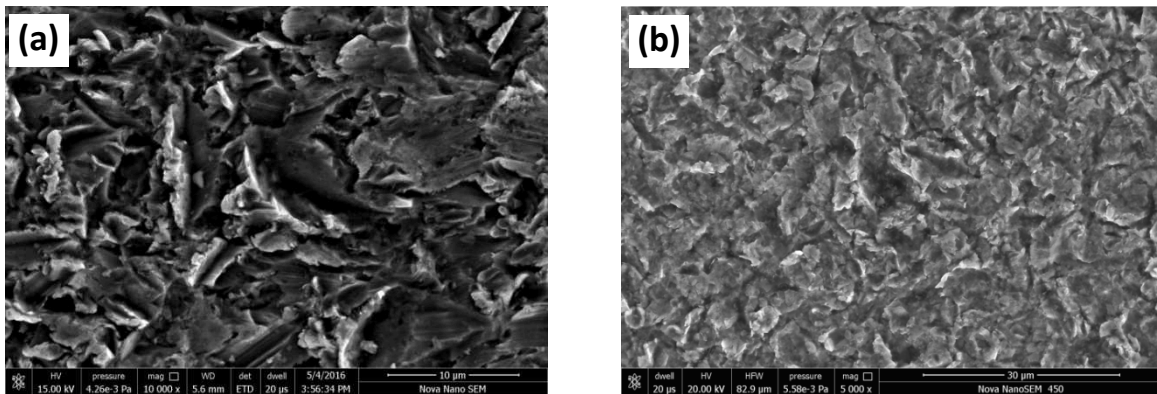


Fig.5. FESEM micrographs of the eroded surface of uncoated steel at 30° impingement angle (a) and 90° impingement angle (b).

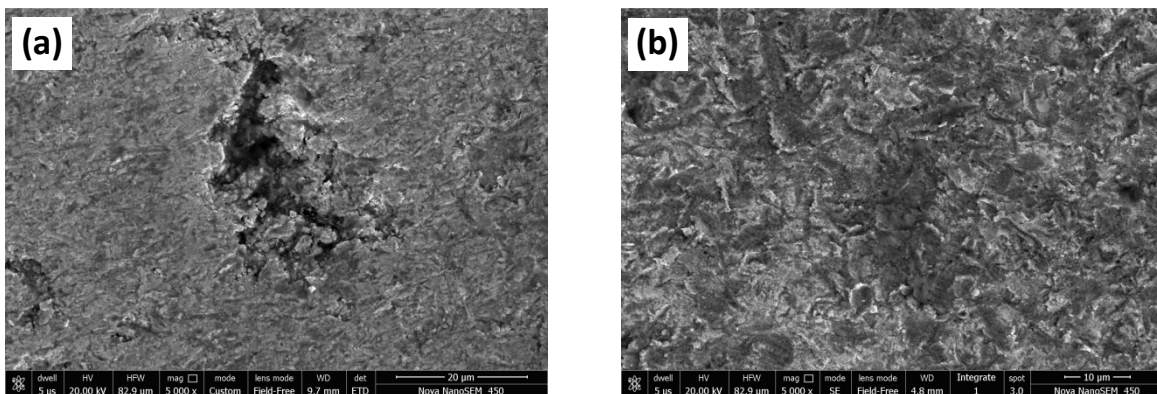


Fig. 6. FESEM micrographs of the eroded surface of coated steel at 30° impingement angle (a) and 90° impingement angle (b).

Conclusions

1. The polished cross-sectional microstructure of HVOF sprayed WC-10Co-4Cr coating showed a homogeneous, well-bonded laminar structure with low porosity.
2. The HVOF-sprayed WC-10Co-4Cr coating enhanced the erosion resistance of the CA6NM steel. This may be attributed to its higher hardness of coating as compared to the uncoated steel.

References

- [1] Wang Q, Zhang S, Cheng Y, Xiang J, Zhao X, Yang G. Wear and corrosion performance of WC-10Co4Cr coatings deposited by different HVOF and HVAF spraying processes. Surf Coatings Technol 2013.
- [2] Bhandari S, Singh H, Kumar H, Rastogi V. Slurry erosion performance study of detonation gun-sprayed WC-10Co-4Cr coatings on CF8M steel under hydro-accelerated conditions. J Therm Spray Technol 2012.
- [3] Singh H, Goyal K, Goyal DK. Slurry Erosion Behaviour of Plasma Thermal Sprayed (50 %) WC-Co-Cr and Ni-Cr-B-Si Coatings of Different Thickness on CA6NM Turbine Steel Material 2014.

SOLID PARTICLE EROSION RESISTANCE OF HVAF- SPRAYED WC-10Co-4Cr COATING ON CA6NM STEEL

ANURAG HAMILTON*, ASHOK SHARMA and UPENDER PANDEL
*Department of Metallurgical and Materials Engineering,
Malaviya National Institute of Technology Jaipur, Jaipur 302017, India*
**a.hamilton2107@gmail.com*

Received 27 September 2016

Revised 4 January 2017

Accepted 8 March 2017

Published 20 April 2017

In the present investigation, WC-10Co-4Cr coating was deposited by high velocity air-fuel (HVAF) process on CA6NM hydro turbine steel. A detailed microstructural and phase compositional study was carried out on the coating. Mechanical properties of the coating were also evaluated. WC-10Co-4Cr coating showed a homogeneous, well-bonded structure with low porosity, which is mainly attributed to less decarburization of WC. Erosion resistance of the coating was evaluated by air jet erosion tester at three different impingement angles (30°, 60° and 90°) for 35 and 70 m/s impact velocities. The FESEM micrographs were taken, before and after erosion tests, to determine the erosion mechanism. The test results revealed that the coating protects the substrate at 30°, 60° and 90° impingement angles. At 70 m/s impact velocity, uncoated and coated steel showed higher cumulative volume loss than in the case of 35 m/s impact velocity. It was observed that uncoated steel showed a ductile behavior during erosion and WC-10Co-4Cr coating showed mixed (ductile and brittle) mode of fracture during erosion.

Keywords: CA6NM steel; HVAF; erosion resistance.

1. Introduction

Hydropower plants play a vital role in fulfilling India's domestic energy requirements. Although hydropower is the most important and cheapest renewable source of energy, hydropower plants encounter problems like silt erosion, which reduces its operational capabilities.¹⁻³ In India, the problem of silt erosion is faced by hydropower plants located in Himalayan rivers, which is due to steep topography and geographically young mountains of the region.⁴ In particular, blades, guide vanes, bearing bodies and nozzles, etc. bear high risks of being damaged by silt particles. Silt erosion intensity depends on different parameters such as silt size, hardness, and concentration, the velocity of water and base material

properties.⁵⁻⁷ To counteract the problem of silt erosion, different researchers have suggested various solutions.⁸⁻¹⁰ However, it has been found that the erosion resistance of the turbine steel can be improved by the deposition of thermal spray coatings.^{11,12} Thermal spray techniques are versatile means of developing coating with low porosity, good adhesive strength, low oxide contents, and high inter-splat strength.^{13,14} Several different types of coating powders have been attempted by various researchers^{15,16} to improve erosion resistance of turbine blades. It has been observed that WC-Co-Cr-based coating gives excellent erosion performance in comparison to other type of powders,^{17,18} which is due to the presence of hard WC particle in a tough and ductile Co-Cr

*Corresponding author.

matrix.¹⁹ At present, HVOF process is widely used for developing erosion resistant coating on hydro turbine steel.^{20,21} However, this process leads to the considerable amount of decarburization which deteriorates the erosion resistance of the coating.^{22,23} Recently, high-velocity air fuel (HVOF) system is gaining attention among researchers.^{24–26} This process operates at a much lower combustion temperature using compressed air (not oxygen) for combustion.²⁷ Therefore, there is an urgent need to explore the possibility of application of HVOF coating for erosion resistance application of hydro turbine. There are several methods to evaluate different types of erosion. Generally, slurry and slurry jet erosion are most widely used for evaluating erosion resistance of hydro turbine steel in lab scale.^{8,15} However, it is not possible to generate severe erosion condition in them as water acts as a cushioning agent and reduces the kinetic energy of impinging particles.^{28,29} On the other hand, air jet erosion tester is able to generate severe erosion condition in lab scale. Thakur *et al.*²⁸ studied the slurry and air jet erosion behavior of HVOF sprayed WC-Co-Cr cermet coatings. It was observed that air jet erosion tester resulted in higher damage to the substrate in comparison to slurry erosion, which is mainly attributed to the higher velocity of erodent particle in the case of air jet erosion tester. Hawthorne *et al.*²⁹ studied the performance of different HVOF sprayed coatings under slurry jet erosion and air jet erosion tester. It was observed that slurry jet erosion tester shows lower erosion rates in comparison to air jet erosion tester. Lower erosion rates in slurry jet erosion test are due to the difference in real erodent target velocity, which is mitigated by water. Chauhan *et al.*³⁰ and Kumar *et al.*¹² have also used the solid particle erosion testing method to evaluate the erosion performance of hydro turbine steel and reported encouraging results in shorter erosion time. Therefore, solid particle erosion test is used for evaluating erosion resistance of steel.

In the literature, solid particle erosion resistance study of HVOF sprayed WC-10Co-4Cr-based coating deposited on CA6NM steel is very few. Hence, the

present study was carried out with an objective to gain knowledge on solid particle erosion resistance of HVOF-sprayed WC-10Co-4Cr-based coating on CA6NM steel. The study shall provide useful information regarding the microstructure-property correlation of HVOF-sprayed WC-10Co-4Cr coating on CA6NM steel. At the same time, the study will also try to address the issue of silt erosion in the hydro turbine.

2. Experimental Procedure

2.1. Substrate

A hydro turbine steel of CA6NM grade (ASTM 743) was used as a substrate material for the deposition of the coating. As-cast steel test block was machined, and samples of $25 \times 25 \times 5$ mm and $25 \times 20 \times 5$ mm were prepared using wire-cut electric discharge machine (EDM) for erosion testing. Plates of $103 \times 50 \times 5$ mm were also cut from the same test block for coating deposition. The chemical composition of the material is given in Table 1.

2.2. Coating deposition

The WC-10Co-4Cr powder (H.C. Starck Amperit 556.059) was deposited onto CA6NM steel using high velocity air-fuel process at PTC-Innovation AB, Sweden. Spraying was done with a Uniquecoat M3 torch with the 4L2 secondary nozzle. The coating was deposited on $103 \times 50 \times 5$ mm plates and samples of $25 \times 25 \times 5$ mm and $25 \times 20 \times 5$ mm were prepared from the same plate using wire-cut EDM for erosion testing. Before the coating deposition, the steel samples were grit blasted. The spraying parameters are given in Table 2.

Figure 1 shows the morphology of the feedstock powder. Feedstock powder particles exhibit spherical morphology, which provides excellent fluidity and stability during spraying.

Table 1. Chemical composition of cast CA6NM steel (wt.%).

Element	C	Cr	Ni	Mn	Si	Mo	S	P	Fe
Composition/wt.%	0.06	11.88	3.65	0.61	0.45	0.61	0.002	0.028	Bal.

Table 2. Parameters used in HVOF-spraying.

Standoff distance	300 mm
Feed rate	200 g/min
Deposition rate	20 $\mu\text{m}/\text{pass}$
Number of passes	17

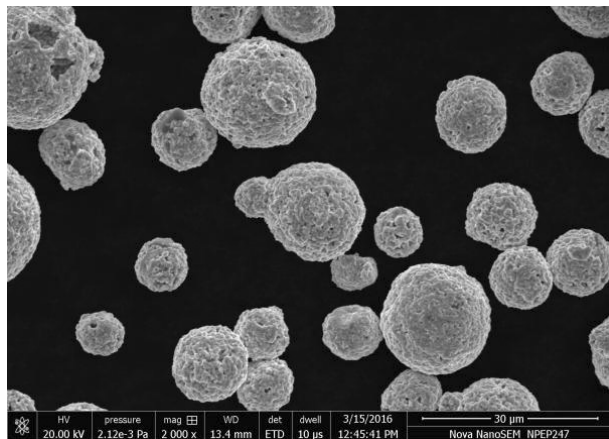


Fig. 1. FESEM micrograph of WC-10Co-4Cr feedstock powder.

2.3. Coating characterization

To identify the phase composition, the XRD patterns of the feedstock powder and as-sprayed coatings were recorded with X'Pert Powder PANalytical with Cu $K\alpha$ radiation. To characterize the microstructure of coating, cross-section of the as-sprayed coating was prepared by mounting samples in conducting resin, grinding and polishing to 1 μm finish. These were examined in a NOVA Nano 450 field emission scanning electron microscope (FESEM) operated at 20 kV. FESEM is also used for analyzing the surface morphology after erosion test for coated and uncoated steel. The surface roughness of the uncoated and sprayed samples after polishing was measured using a surface roughness tester (Surftest SJ 301, Mitutoyo). Image analysis was done on cross-sectional FESEM micrograph (10,000X) of the coating to evaluate volume fraction of the WC, binder (Co-Cr) and porosity. The density of the coating was calculated by subtracting volume fraction of porosity from that of the WC and binder (Co-Cr).¹² The density of the WC ($\rho_{\text{WC}} = 15.7 \text{ g/cm}^3$) and binder ($\rho_{\text{Co-Cr}} = 8.6 \text{ g/cm}^3$) was taken to calculate the density of the coating. Vickers microhardness measurements were performed

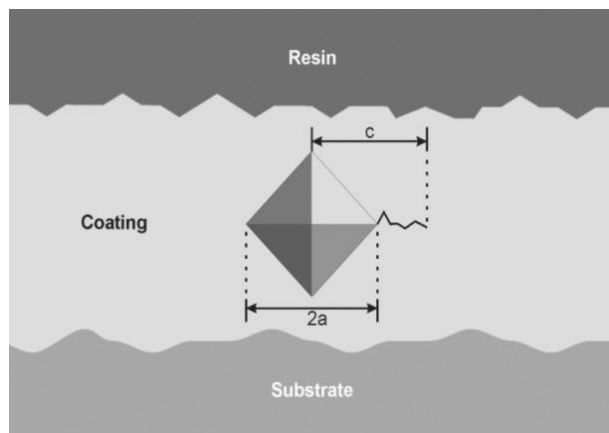


Fig. 2. Schematic depiction of the Vickers indentation and crack geometry.

on the polished transverse section of the coatings with INNOVATEST (NEXUS 4000) hardness tester at 300 g load with 10 s dwell time. The fracture toughness of coating was determined by the indentation method. A Vickers indenter was used on metallographically prepared cross-sections of coating with a 5 kg load with 10 s dwell time. The indenter was loaded such that the two indent diagonals were parallel and perpendicular to the substrate/coating interface, respectively. The length of the cracks, both parallel and normal to the substrate-coating interface, produced by the indentation technique was measured using FESEM micrograph.

The fracture toughness (K_{IC}) of the coatings was determined by the indentation method using the Evans and Wilshaw³¹ equation as given below:

$$K_{\text{IC}} = 0.079 \frac{P}{a^{3/2}} \log 4.5 \left(\frac{a}{c} \right). \quad (1)$$

Where ' P ' is the applied indentation load (mN), and ' a ' and ' c ' correspond to the length of the indentation half-diagonal (μm) and crack length from the center of the indent (μm), respectively as shown in Fig. 2.

The ' c/a ' ratio for use in this equation is $0.6 \leq c/a < 4.5$. Average of ten readings along with standard deviation is reported.

2.4. Erosion test procedure

The erosion behavior of cast and coated CA6NM steel was evaluated using air jet erosion tester (Model: TR-471-400 DUCOM Bangalore). Erosion test was

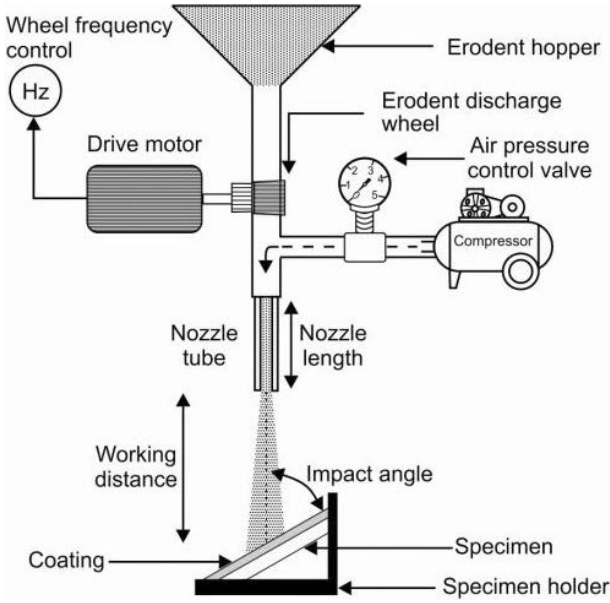


Fig. 3. Schematic view of air jet erosion tester used for solid particle erosion testing.¹²

performed as per ASTM G-76-13 test standard.³² Schematic diagram of the air jet erosion tester¹² used for these experiments is shown in Fig. 3. The erosion test parameters utilized in the present study are provided in Table 3.

In this erosion tester, the abrasive particles were accelerated from a nozzle by using a compressed air stream that caused them to impact on the surface of the material. Figure 4 shows the FESEM micrograph of alumina particle (50 μm) used for erosion testing; it was observed that the particles are flaky and angular in shape. To provide an initial standard surface

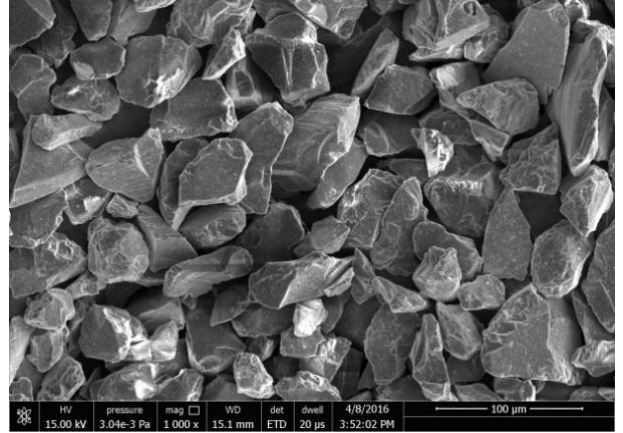


Fig. 4. Morphology of alumina particles.

condition before the erosion test, all specimens were abraded using 0/0, 1/0, 2/0, 3/0, and 4/0 grades of emery paper. Cloth wheel polishing was done to obtain a mirror finish using a diamond paste. Each sample was removed after every 2 min to determine the mass loss. The impingement angles used for the tests were 30°, 60° and 90°. These angles were selected to evaluate the behavior of these materials at low, intermediate and high impingement angles. A particle velocity of 35 and 70 m/s was used to replicate severe erosion condition, and an abrasive flow rate of 2 g/min was used to conduct the tests. Particle velocity was measured with an accuracy of ± 2 m/s, using the double disc rotating method as shown in Fig. 5. In this apparatus, two disks are attached to a common rotating shaft. A radial slot is cut on top disk and the lower disk is coated with a thin layer of paint. Stream of erodent is allowed to strike on the top disk for 10 min and elliptical shape scar is formed on the bottom disk, which is measured using a protractor. Velocity is measured using the formula as given below

$$V = [H \times N] \times [360/A], \quad (2)$$

where H is the Distance between disks in m (0.03);

N is the Revolution per second of double disk system(5000/60);

A is the Angle of Incidence.³³

The abrasive flow rate was measured by collecting the abrasive in a container during 1 min. Before and after the tests, each specimen was weighed using a digital balance with an accuracy of 0.0001 g to observe the difference in weight loss for each test. The weight loss was converted into volume loss to obtain

Table 3. Parameters used in solid particle erosion testing.

Erodent particle	Alumina
Average erodent particle size	50 μm
Impact velocity	35 and 70 m/s
Erodent discharge	2 gm/min
Test gas	compressed air
Standoff distance	10 mm
Nozzle diameter	1.5 mm
Impact angle	30°, 60° and 90°
Test duration	Cycles of 2 min
Test temperature	Room temperature
Sample size	(25 \times 25 \times 5) mm and (25 \times 20 \times 5) mm

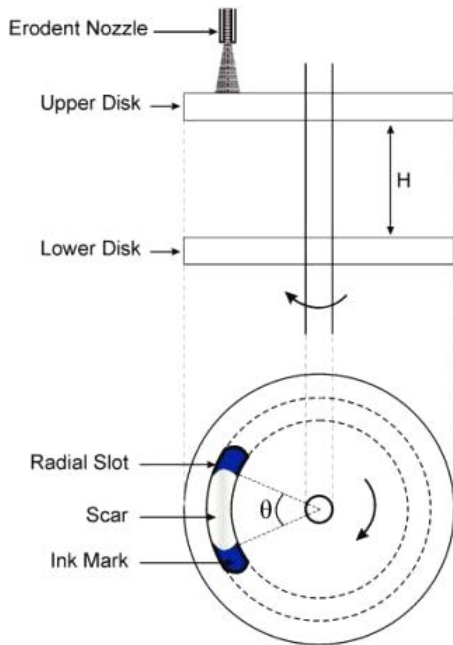


Fig. 5. Schematic diagram of the double disk apparatus.

the precise data because the WC-10Co-4Cr coating and substrate possess different densities. Micrographs of the eroded surfaces were obtained using an FESEM to analyze the specimens and to identify the possible erosion mechanisms.

3. Results and Discussion

3.1. Substrate microstructure and properties

The optical and field emission scanning electron microstructure of as-cast CA6NM steel is illustrated in

Figs. 6(a) and 6(b). The microstructure of as-cast CA6NM steel consists of packets of lath martensitic needles. Apart from these packets, the structure also exhibits the presence of delta ferrite.³⁴ Table 4 shows the mechanical properties of the as-cast CA6NM steel, average of three readings is shown.

3.2. Phase constitution of powder and coatings

The X-ray diffraction patterns for the surface of the HVOF-sprayed WC-10Co-4Cr coating and the feedstock powder are shown in Fig. 7. There is no significant difference observed between the diffraction pattern of the feedstock powder and that of the coating,³⁵ where both the powder and coating contained WC as the primary phase. Traces of $\text{Co}_3\text{W}_3\text{C}$ and Co phases were also noticed. Traces of W_2C phase are also observed in HVOF-sprayed coating, which indicates that there is very little or negligible decarburization in the coating. In HVOF coating, higher particle velocity and lower particle temperature during spraying are the main factors, which result in a lower degree of decarburization.

3.3. Microstructure, porosity and density of coating

The cross-sectional FESEM micrograph of the HVOF-sprayed WC-10Co-4Cr coating on the CA6NM steel has been shown in Fig. 8. Even at lower magnification (Fig. 8(a)), coating–substrate interface, coating, and the substrate can be seen clearly. It is observed that coating has a homogeneous structure, which is dense

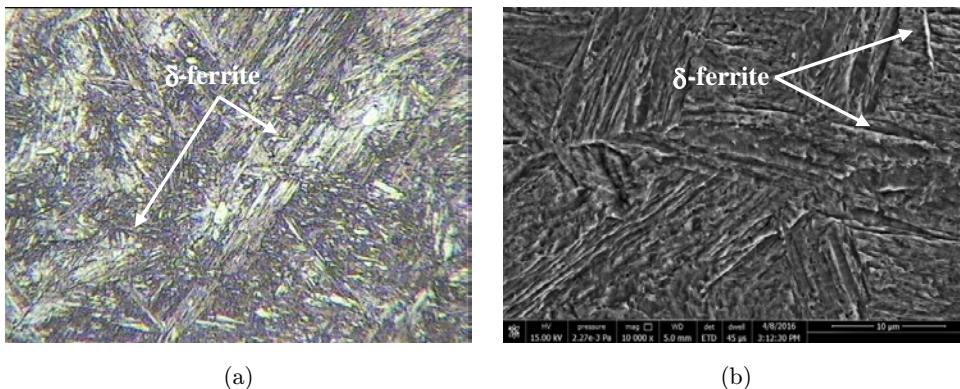


Fig. 6. (a) Optical and (b) FESEM micrograph of cast CA6NM steel.

Table 4. Mechanical properties of the as-cast CA6NM alloy steel.

Properties material	YS (MPa)	UTS (MPa)	Ductility (% elongation)	Impact strength (Joules)
CA6NM steel	652 ± 48	892 ± 66	13 ± 4	42 ± 8

and well bonded to the substrate. At higher magnification, secondary electron mode micrograph (Fig. 8(b)) porosity present in the coating can be observed. At higher magnification backscatter mode micrograph (Fig. 8(c)) islands of bright regions are observed in between the dark region, in which bright region corresponds to WC rich phase (“Point 1”) and the latter corresponds to Co-Cr rich phase (“Point 2”). EDS analysis of points is shown in Table 5. It is also observed that WC grains appear blocky in shape without any deformation and dissolution. Therefore, it can be inferred that the Co-Cr metallic binder was wholly or partially melted, while the WC-particles mostly remained in the solid state during spraying. This clearly indicates that very little decomposition of WC has taken place during spraying. Unlike HVOF-sprayed WC-10Co-4Cr coating,³⁶ no laminar morphology is observed in HVOF-sprayed coating, which indicates that less decarburization of WC has taken place. The average coating thickness as measured from cross-sectional FESEM micrograph is about $341 \pm 6 \mu\text{m}$. Although minute pores are visible in

the coating, it is less porous than HVOF-sprayed WC-10Co-4Cr coatings.³⁷ The reason for this is shorter particle residence time in the HVOF jet, which lowers the oxidation of particles. The porosity percentage in terms of the area fraction of pores was observed to be $0.98 \pm 0.25\%$. The average density of the coating was observed to be 13.53 g/cm^3 .

3.4. Indentation fracture toughness, cross-sectional microhardness and surface roughness of coating

The average and the standard deviation value of indentation fracture toughness, cross-sectional microhardness, and surface roughness Ra values of investigated samples are reported in Table 6. The fracture toughness value was calculated at the polished cross-section of the coating. It was observed that cracks are generated parallel to the coating–substrate interface, as shown in Fig. 9. Cracks were not observed in the perpendicular direction which attributed to the anisotropic behavior of coating. The microhardness of the coating was also measured along the depth from the coating to the substrate. The microhardness values of coating were found to be in the range of 1285–1352 Hv. It was observed that microhardness value oscillates in a narrow range (1285–1352), which is mainly due to low porosity and uniform microstructure of the coating. Surface roughness for coated and uncoated steel after polishing is measured before starting the erosion test, to provide a uniform initial condition for erosion.

3.5. Effect of impingement angle on erosion

Figure 10 shows the actual picture of the erosion scar formed at 30°, 60° and 90° impingement angles and their respective sample holders. The smaller size of 30° impingement angle sample is attributed to sample holder geometry, which helps in maintaining

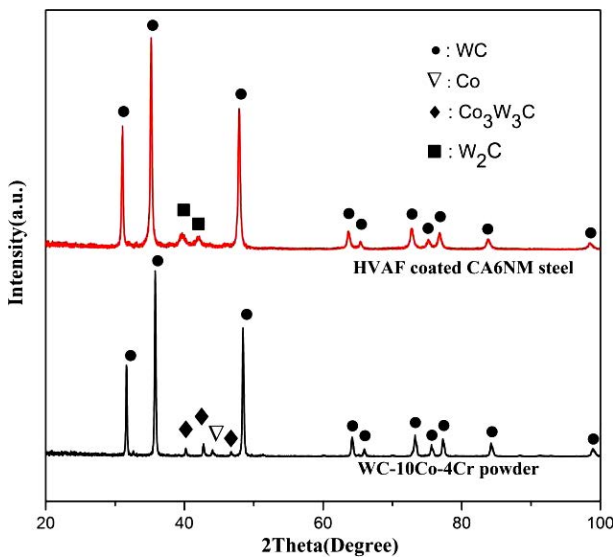


Fig. 7. XRD pattern of the WC-10Co-4Cr feedstock powder and HVOF coated CA6NM steel.

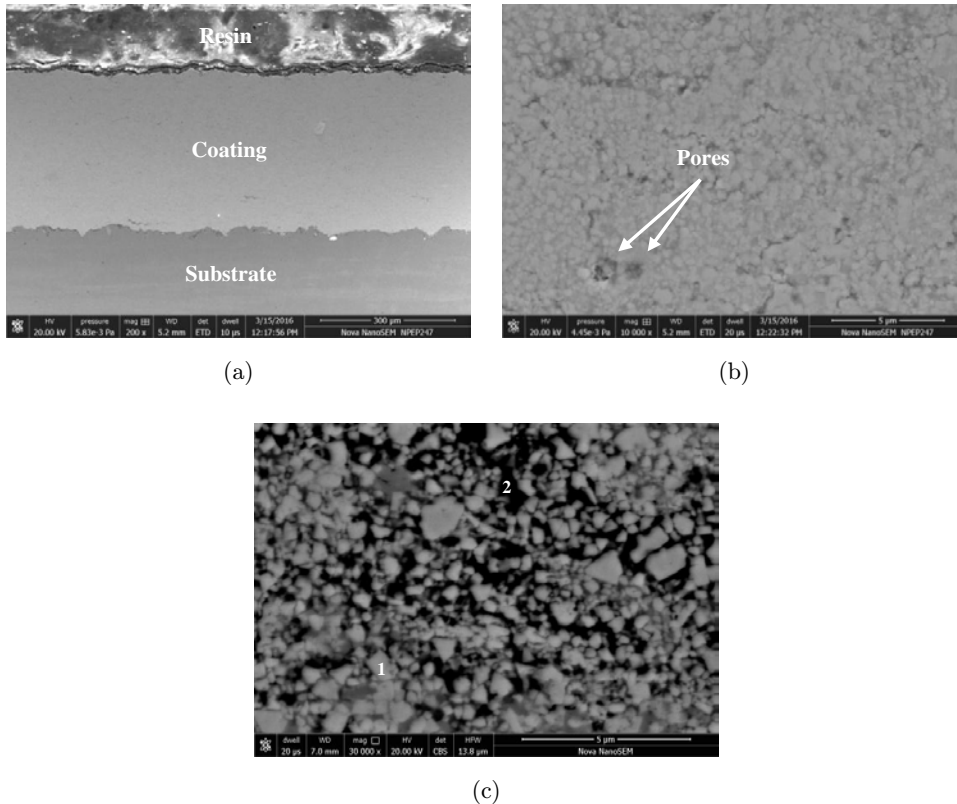


Fig. 8. Cross-sectional FESEM micrograph of WC-10Co-4Cr coating deposited on as-cast CA6NM steel substrate: (a) at lower magnification (Secondary electron mode); (b) at higher magnification (secondary electron mode) and (c) at back scatter mode.

constant distance (10 mm) between nozzle and the sample for all the impingement angles. The center region of the eroded scar (Region “1”) shows the

region of erosion and on its periphery, it is surrounded by a region of elastically loaded material (Region “2”).³⁸ At 30° impingement angle, contact area of erodent with substrate is high and erosion scar of ellipsoid shape covering the entire length of the sample is observed. At 60° impingement angle, the material is eroded forming a perfect ellipsoid shape depression, which is because of the contact area being lower than 30°. While at 90° impingement angle, the material is eroded creating a perfect circular shape depression. The difference observed in the erosion profile is due to the difference in the angle of impingement.

Table 5. EDS analysis of points as marked in Fig. 8(c).

Point	Chemical composition (wt.%)			
	W	Co	Cr	C
1	84.00	7.49	3.57	4.94
2	62.77	15.02	17.57	4.53

Table 6. Indentation fracture toughness, cross-sectional microhardness and surface roughness of uncoated CA6NM steel and WC-10Co-4Cr coating.

	Indentation fracture toughness (MPa m ^{1/2})	Cross-sectional microhardness (HV _{0.3})	Surface roughness (Ra)
WC-10Co-4Cr coating	6.60 ± 0.21	1327 ± 26	0.31
Uncoated CA6NM steel	—	338 ± 29	0.27

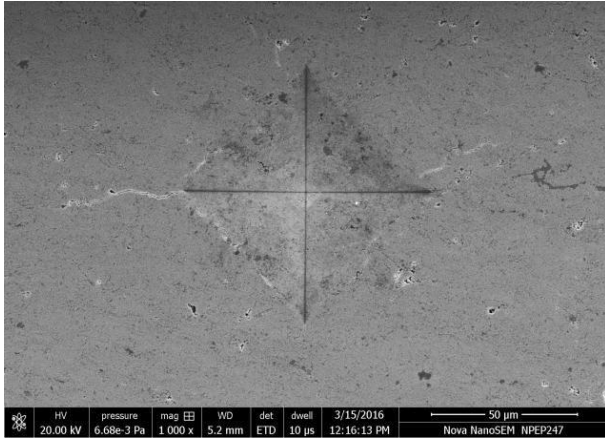


Fig. 9. FESEM micrograph of Vickers indentation on the polished cross-section of coated steel.

3.6. Erosion behavior of the uncoated and coated steel

Figure 11 shows the cumulative volume loss of the uncoated and WC-10Co-4Cr coating as a function of erosion time (14 min) at 30° impingement angle for 35 and 70 m/s impact velocity.

It is observed that the cumulative volume loss of WC-10Co-4Cr coating at 35 m/s ($1.31 \times 10^{-4} \text{ cm}^3$) and 70 m/s ($2.33 \times 10^{-4} \text{ cm}^3$) is lower than the uncoated CA6NM steel for 35 m/s ($8.25 \times 10^{-4} \text{ cm}^3$) and 70 m/s ($1.39 \times 10^{-3} \text{ cm}^3$) impact velocity. At low impact angle (30°), the horizontal component (shear force) of the kinetic energy of the impinging particles is higher than the vertical component (normal force), as shown in Fig. 13. Thus, the force to slide on the surface is

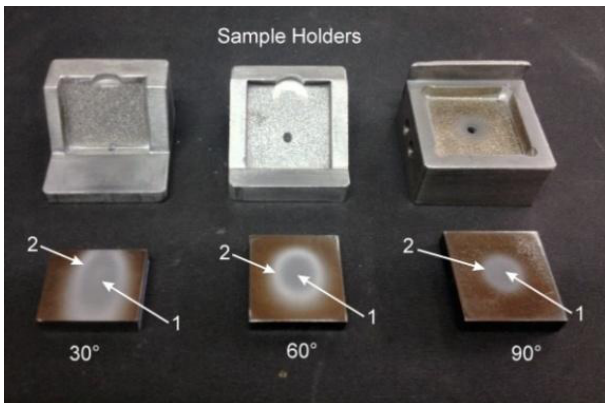


Fig. 10. Actual picture of the erosion scar formed on eroded samples at 30°, 60° and 90° impingement angles and their respective sample holder.

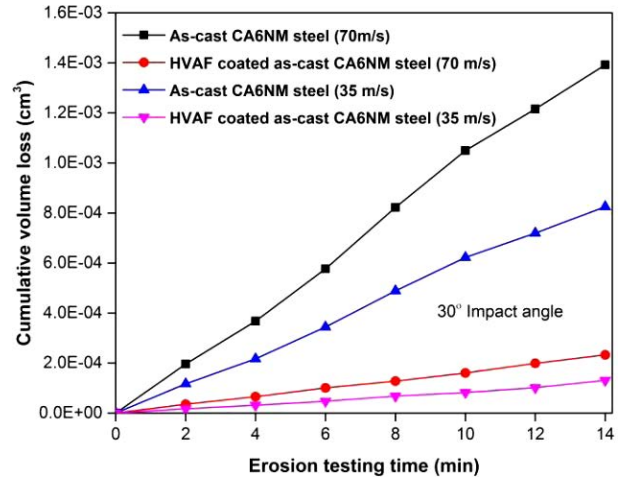


Fig. 11. Cumulative volume loss of uncoated and HVAF coated as-cast CA6NM steel as a function of erosion time (14 min) at 30° impingement angle for 35 and 70 m/s impact velocity.

higher than the force to penetrate the surface, and it results in the formation of plough and lips in uncoated and coated steel. These lips are fractured or removed from the grooves with further impingement of particles. The FESEM micrographs of eroded surfaces of

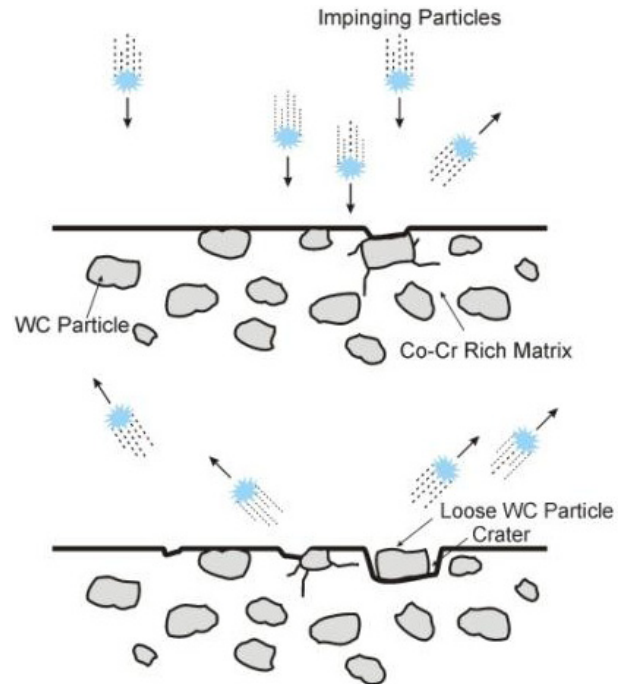


Fig. 12. Mechanism of material removal at 90° impingement angle.

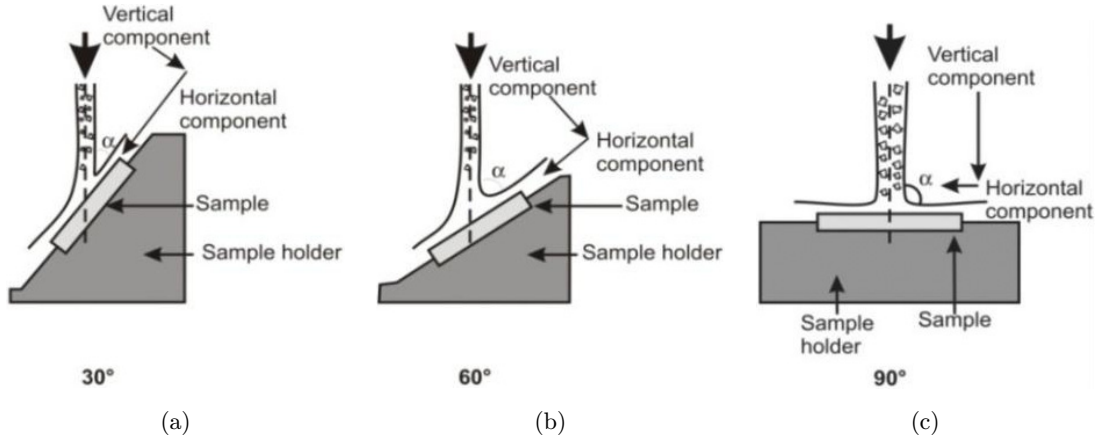


Fig. 13. Schematic depiction of the erosion mechanism at (a) 30°, (b) 60° and (c) 90°.

both uncoated and coated steel at 30° impingement angle are shown in Figs. 14(b), 14(c), 15(b) and 15(c). The formation of lips and grooves in uncoated and coated steel indicate that the material is mainly removed by cutting and ploughing. FESEM micrograph of uneroded surfaces of as-cast and coated steel

is shown in Figs. 14(a) and 15(a). Cumulative volume loss of uncoated and WC-10Co-4Cr coating as a function of erosion time (14 min) at 60° impingement angle is shown in Fig. 16. It is observed that WC-10Co-4Cr coating at 35 m/s ($2.14 \times 10^{-4} \text{ cm}^3$) and 70 m/s ($3.84 \times 10^{-4} \text{ cm}^3$) also shows lower cumulative

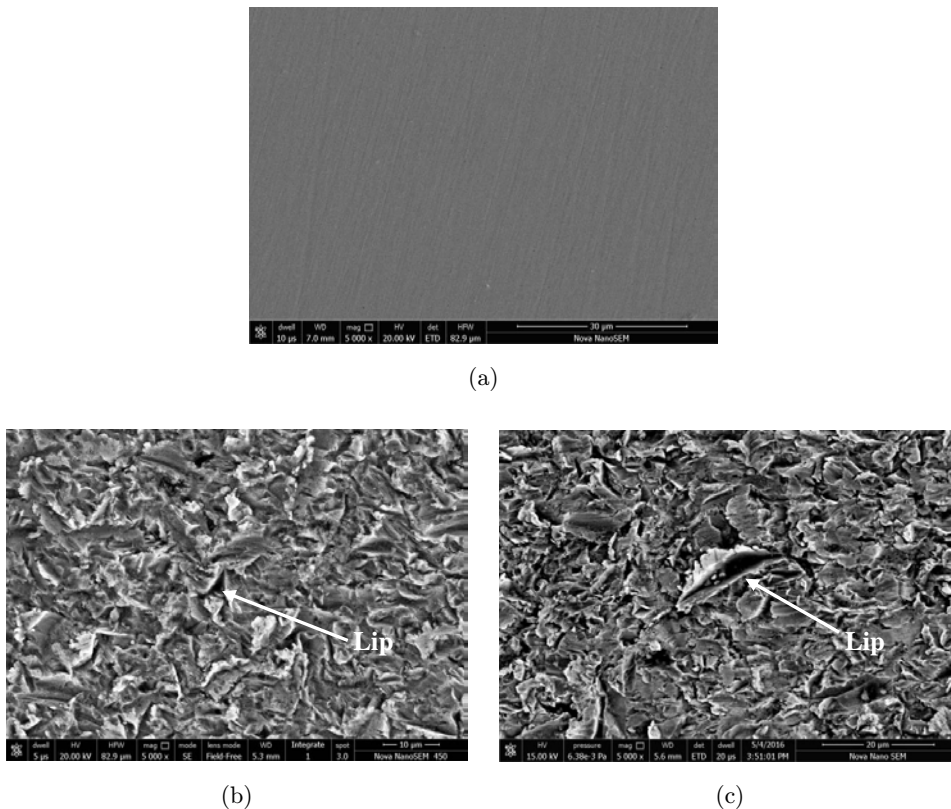


Fig. 14. FESEM micrographs of the uneroded uncoated steel (a) and eroded steel (14 min) at 30° impingement angle (b, c), 60° impingement angle (d, e), 90° impingement angle (f, g) (b, d, f is for 35 m/s and c, e, g is for 70 m/s impact velocity).

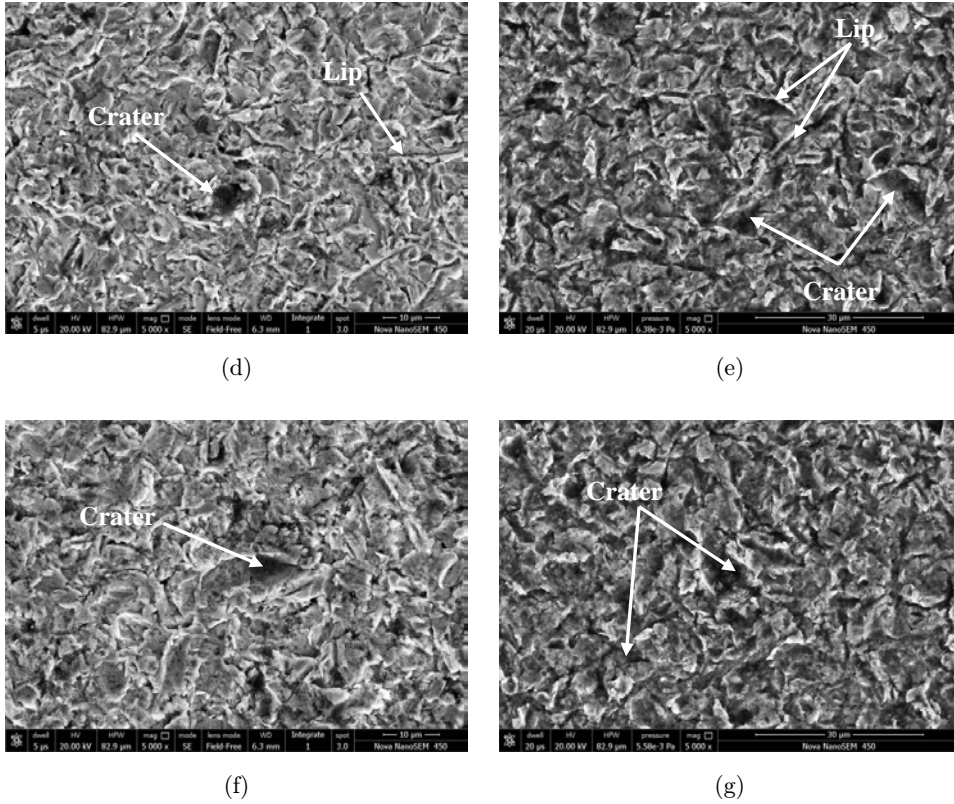
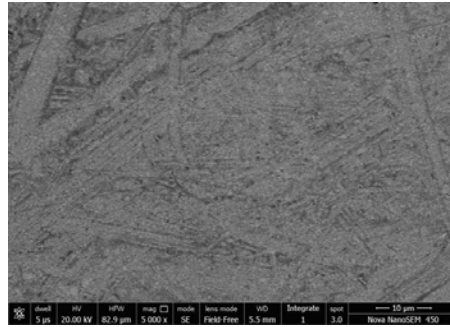


Fig. 14. (Continued)

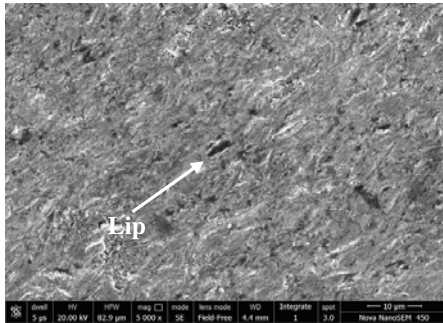
volume loss in comparison to uncoated CA6NM steel at 35 m/s ($6.62 \times 10^{-4} \text{ cm}^3$) and 70 m/s ($1.18 \times 10^{-3} \text{ cm}^3$). For medium incident angle (60°), the horizontal component (shear force) of the kinetic energy of the impinging particles and the vertical component (normal force) are close to equal, as shown in Fig. 13. The material removal mainly takes place due to combined action of cutting and plastic deformation, which results in the formation of grooves and craters. Figures 14(d) and 14(e) and 15(d) and 15(e) show the FESEM micrographs of the eroded surfaces of both coated and uncoated steel at 60° impingement angle. Eroded surfaces of uncoated and coated steel revealed the presence of lips and craters at the different locations. Figure 17 shows the cumulative volume loss of the uncoated and WC-10Co-4Cr coating as a function of erosion time (14 min) at 90° impingement angle. It is observed that in this condition also the cumulative volume loss of WC-10Co-4Cr coating at 35 m/s ($1.79 \times 10^{-4} \text{ cm}^3$) and 70 m/s ($3.18 \times 10^{-4} \text{ cm}^3$) is lower than uncoated CA6NM steel at 35 m/s ($5.18 \times 10^{-4} \text{ cm}^3$) and 70 m/s ($9.66 \times 10^{-4} \text{ cm}^3$). For the high

impingement angle (90°), the vertical component (normal force) of the kinetic energy is higher than the horizontal component (shear force), as shown in Fig. 13. This provides bigger indented force and the erodent penetrates into the surface resulting in the formation of craters. Figures 14(f) and 14(g) and 15(f) and 15(g) show the FESEM micrographs of the eroded surfaces of both coated and uncoated steel at 90° impingement angle, the eroded surfaces of uncoated and coated steel are free from ploughs. Deep craters are instead observed which are formed due to dislodging of material by erodent particles.

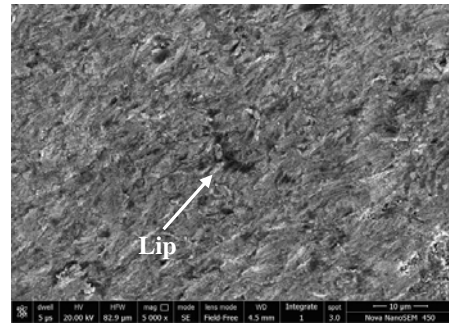
It is, therefore, reasonable to summarize that, in general, the erosion in uncoated steel at low impingement angles took place by micro ploughing and micro cutting, which resulted in the formation of long and narrow grooves. In the case of high impact angle, material removal took place due to plastic deformation and formation of deep crater whereas in the case of intermediate angle, erosion took place by the combined action of cutting and plastic deformation, which resulted in the formation of cutting grooves



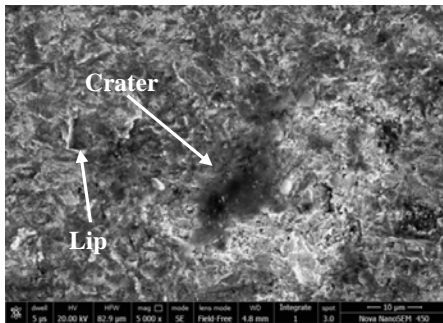
(a)



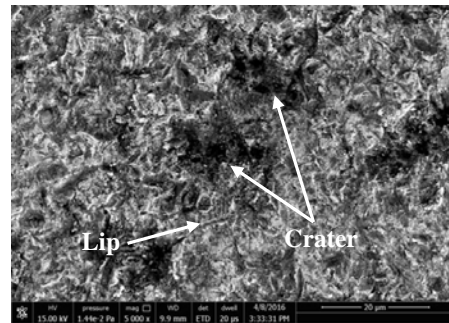
(b)



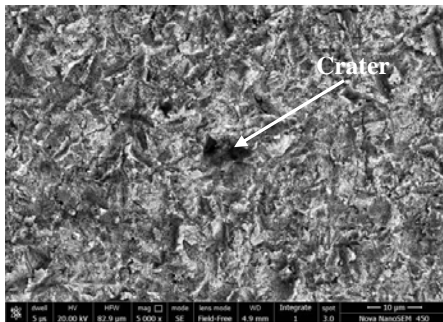
(c)



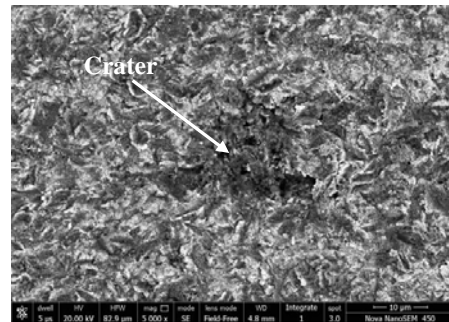
(d)



(e)



(f)



(g)

Fig. 15. FESEM micrographs of the uneroded coated steel (a) and eroded coated steel (14 min) at 30° impingement angle (b, c), 60° impingement angle (d, e), 90° impingement angle (f, g) (b, d, f is for 35 m/s and c, e, g is for 70 m/s impact velocity).

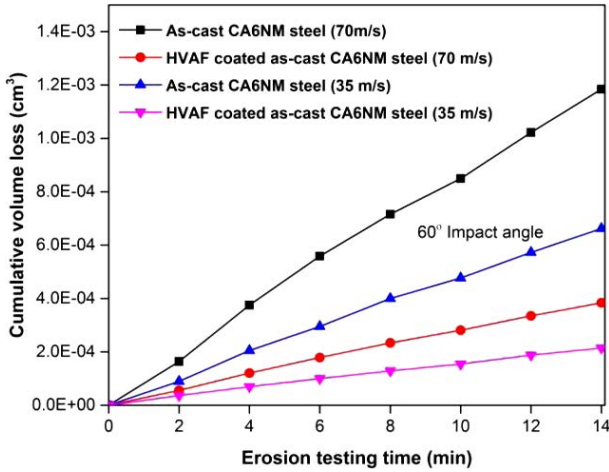


Fig. 16. Cumulative volume loss of uncoated and HVAF coated as-cast CA6NM steel as a function of erosion time (14 min) at 60° impingement angle for 35 and 70 m/s impact velocity.

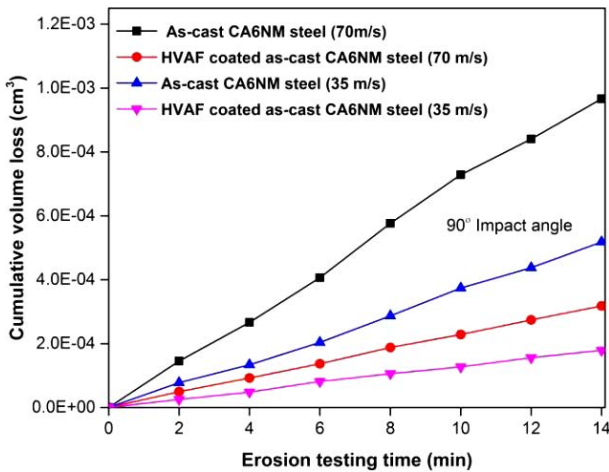


Fig. 17. Cumulative volume loss of uncoated and HVAF coated as-cast CA6NM steel as a function of erosion time (14 min) at 90° impingement angle for 35 and 70 m/s impact velocity.

and extrusion craters.³⁹ In the case of WC-10Co-4Cr coating, localized erosion has taken place, material removal mechanism at low impact angle was due to micro cutting and microploughing,⁴⁰ the same is observed by Kulu *et al.*⁴¹ and Feng *et al.*⁴² Removal of splats is also noticed, which is mainly due to large tangential forces acting on the splats due to the impinging particle striking at a low impact angle, which resulted in the detachment of the splats. At high impact angle, material removal took place by removal of a single grain of WC, the mechanism is illustrated in Fig. 12. Impinging erodent particle removes the binder phase from the surface and it results into the accumulation of plastic strain in WC particles and eventually cracks are generated in-between WC grains, which results in the removal of single WC particle.⁴³ In the case of intermediate angle, material removal takes place due to the mixed mode of micro cutting and removal of a single grain of WC.³⁹ The erosion mechanisms responsible for material removal are summarized in Table 7. Figure 18 shows the effect of 30°, 60° and 90° impingement angles on cumulative volume loss for uncoated CA6NM steel and WC-10Co-4Cr coating.

The maximum cumulative volume loss for uncoated CA6NM steel was observed at 30° impingement angle, followed by 60° and 90°. However, in the case of WC-10Co-4Cr coating, it is worth noticing that, the maximum cumulative volume loss was observed at 60° impingement angle, followed by 90° and 30°. The shifting of maximum cumulative volume loss from low to intermediate impingement angle in the case of coating shows that coating exhibits a mixed mode of failure during erosion. The WC-10Co-4Cr coating contains brittle WC particle in ductile Co-Cr matrix, which imparts a dual (ductile and brittle) behavior in coating, and the same has been observed by Murthy *et al.*⁴⁴ and Kulu *et al.*,⁴¹ with increase in

Table 7. Erosion mechanisms in case of 30°, 60° and 90° impingement angles for uncoated and coated samples.

Sample	Impingement angles		
	30°	60°	90°
Uncoated steel	Cutting and ploughing	Cutting and plastic deformation	Plastic deformation
WC-10Co-4Cr coating	Cutting and removal of Splat	Cutting and removal of a single grain of WC	Removal of a single grain of WC

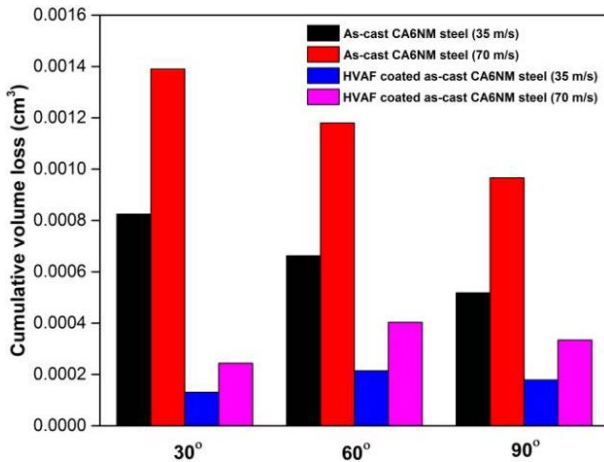


Fig. 18. Comparison of cumulative volume loss of uncoated and HVAF coated as-cast CA6NM steel at 30°, 60° and 90° impingement angles for 35 and 70 m/s impact velocity.

the brittle content in the coating, the maximum cumulative volume loss tends to shift from low to high impingement angles. At 70 m/s impact velocity, high cumulative volume loss is observed in comparison to that of 35 m/s, which is attributed to the higher kinetic energy of impacting particle. The coated steel shows nearly four times better erosion resistance than the uncoated steel at 30°, 60° and 90° impingement angles. This indicates that HVAF-sprayed WC-10Co-4Cr coating can improve the erosion resistance of hydro turbine component under low, medium and high impingement angles.

4. Conclusion

The HVAF thermal spraying technique was used successfully to deposit WC-10Co-4Cr coating on CA6NM steel substrate. The uncoated and coated steels were subjected to solid particle erosion testing at three different impingement angles (30°, 60° and 90°) for 35 and 70 m/s impact velocity. From the experimental results and examination of the micrographs of the coated and uncoated steel before and after the erosion test, the following conclusions are drawn:

(1) The polished cross-sectional microstructure of HVAF-sprayed WC-10Co-4Cr coating shows a homogeneous, well-bonded structure with low porosity.

- (2) The HVAF-sprayed WC-10Co-4Cr coating enhanced the erosion resistance of the CA6NM steel. This may be attributed to its higher hardness of coating as compared to the uncoated steel.
- (3) Higher cumulative volume loss is observed at 70 m/s impact velocity in comparison to 35 m/s impact velocity for coated and uncoated steel. This is attributed to the higher kinetic energy of erodent in the case of 70 m/s impact velocity.
- (4) Uncoated steel showed a ductile behavior during erosion. However, WC-10Co-4Cr coating showed mixed (ductile and brittle) mode of failure during erosion.

References

- U. Dorji and R. Ghomashchi, *Eng. Fail. Anal.* **44** (2014) 136–147.
- R. Singh, S. K. Tiwari and S. K. Mishra, *J. Mater. Eng. Perform.* **21** (2012) 1539–1551.
- B. S. Thapa, O. G. Dahlhaug and B. Thapa, *Renew. Sustain. Energy Rev.* **49** (2015) 1100–1113.
- A. Kumar, G. Tripathi, A. Hamilton and A. Sharma, *SOJ Mater. Sci. Eng.* **4**(1) (2016) 1–5.
- M. K. Padhy and R. P. Saini, *Energy* **34** (2009) 1477–1483.
- A. Kumar, A. Sharma and S. Goel, *Mater. Sci. Eng. A.* **637** (2015) 56–62.
- G. F. Truscott, *Wear* **20** (1972) 29–50.
- T. Manisekaran, M. Kamaraj, S. M. Shariff and S. V. Joshi, *J. Mater. Eng. Perform.* **16** (2007) 567–572.
- S. A. Romo, J. F. Santa, J. E. Giraldo and A. Toro, *Tribol. Int.* **47** (2012) 16–24.
- S. S. Basha, V. M. Periasamy, M. Kamaraj and S. M. Shariff, *J. Mater. Eng. Perform.* **22** (2013) 3689–3698.
- J. F. Santa, J. C. Baena and A. Toro, *Wear* **263** (2007) 258–264.
- A. Kumar, A. Sharma and S. K. Goel, *Appl. Surf. Sci.* **370** (2016) 418–426.
- C. Verdon, A. Karimi and J. Martin, *Mater. Sci. Eng. A.* **246** (1998) 11–24.
- K. Kumari, K. Anand, M. Bellacci and M. Giannozzi, *Wear* **268** (2010) 1309–1319.
- D. K. Goyal, H. Singh, H. Kumar and V. Sahni, *J. Tribol.* **136** (2014) 1–11.
- S. Bhandari, H. Singh, H. K. Kansal and V. Rastogi, *Tribol. Lett.* **45** (2012) 319–331.
- J. F. Santa, L. A. Espitia, J. A. Blanco, S. A. Romo and A. Toro, *Wear* **267** (2009) 160–167.
- D. W. Wheeler and R. J. K. Wood, *Wear* **258** (2005) 526–536.
- T. Peat, A. Galloway, A. Toumpis and D. Harvey, *Surf. Coatings Technol.* **299** (2016) 37–48.
- D. K. Goyal, H. Singh, H. Kumar and V. Sahni, *J. Therm. Spray Technol.* **21** (2012) 838–851.

21. M. Sharma, D. K. Goyal, N. Kumar and R. Sharma, *Int. J. Emerg. Technol.* **3** (2012) 118–122.
22. D. Fu, H. Xiong and Q. Wang, *J. Mater. Eng. Perform.* **25** (2016) 4352–4358.
23. B. H. Kear, G. Skandan and R. K. Sadangi, *Scripta mater.* **44** (2001) 1703–1707.
24. C. Lyphout and K. Sato, *Surf. Coat. Technol.* **258** (2014) 447–457.
25. I. Hulka, D. Utu, V. A. Serban, M. L. Dan, V. Matikainen and P. Vuoristo, *Chem. Bull. "POLITEHNICA" Univ. (Timisoara)*. **61**(75) (2016) 1–5.
26. H. Myalska, G. Moskal and K. Szymaski, *Surf. Coatings Technol.* **260** (2014) 303–309.
27. H. Myalska, K. Szymański and G. Moskal, *Arch. Metall. Mater.* **60** (2015) 759–766.
28. L. Thakur and N. Arora, *Wear* **303** (2013) 405–411.
29. H. M. Hawthorne, B. Arsenault, J. P. Immarigeon, J. G. Legoux and V. R. Parameswaran, *Wear* **225** (1999) 825–834.
30. A. K. Chauhan, D. B. Goel and S. Prakash, *Bull. Mater. Sci.* **33** (2010) 483–489.
31. A. G. Evans and T. R. Wilshaw, *Acta Metall.* **24** (1976) 939–956.
32. ASTM G76-13, Standard Test Method for Conducting Erosion Tests by Solid Particle Impingement Using Gas Jets (2013), pp. 1–6.
33. S. K. Horis, K. Anand, H. Conrad and R. O. Scattergood, *Wear* **101** (1985) 69–76.
34. D. B. Goel, *Proc. 3rd Int. Conf. Silting Problems in Hydropower Projects* (2008), pp. 1–10.
35. Q. Wang, Z. Tang and L. Cha, *J. Mater. Eng. Perform.* **24** (2015) 2435–2443.
36. Q. Wang, S. Zhang, Y. Cheng, J. Xiang, X. Zhao and G. Yang, *Surf. Coatings Technol.* **218** (2013) 127–136.
37. D. K. Goyal, H. Singh, H. Kumar and V. Sahni, *Wear* **289** (2012) 46–57.
38. M. R. Ramesh, S. Prakash, S. K. Nath, P. K. Sapra and B. Venkataraman, *Wear* **269** (2010) 197–205.
39. P. S. Babu, B. Basu and G. Sundararajan, *Wear* **270** (2011) 903–913.
40. T. Peat, A. Galloway, A. Toumpis, D. Harvey and W.-H. Yang, *Surf. Coatings Technol.* **300** (2016) 118–127.
41. P. Kulu, I. Hussainova and R. Veinthal, *Wear* **258** (2005) 488–496.
42. Z. Feng and A. Ball, *Wear* **233–235** (1999) 674–684.
43. B. G. Mellor and R. J. K. Wood, *Wear* **259** (2005) 125–134.
44. J. K. N. Murthy, D. S. Rao and B. Venkataraman, *Wear* **249** (2001) 592–600.

of silt in river increases to alarmingly high level during monsoon season. Silt erosion depends upon different parameters such as silt size, hardness and concentration, velocity of water and base material properties. In most cases, this can be minimized by controlling the above mentioned parameters, but during the monsoon season, it becomes impossible to control these parameters which cause erosion. Silt erosion has impact on reliability of a turbine runner. The change of runner profile alters the flow pattern causing loss of efficiency. Extensive research work has been carried out in last decade to mitigate problem of silt erosion. Deposition of the hard surface coating materials are attempted by many investigators. Thermal spray processes such as flame spray, plasma spray, detonation gun and High velocity oxy fuel (HVOF) process are widely used to improve surface protection against corrosion and wear, in power generation plants. In this review paper, research undertaken in this field by several investigators have been discussed. Based on literature survey various aspects related to silt erosion in hydro turbine materials and suitable remedial measures suggested by various investigators have been discussed.

HOT TEARING IN ALUMINIUM CAST ALLOYS

Sachin Kumar Rathi^{*1}, Ashok Sharma¹, Marisa Di Sabatino²

¹Department of Metallurgical and Materials Engineering, Malaviya National Institute of Technology Jaipur, Jaipur-302017, India

²Department of Materials Science and Engineering, Norwegian University Science and Technology 7491 Trondheim, Norway.

Email: sachin.baryons@gmail.com (Sachin Rathi), ashok.mnit12@gmail.com (Ashok Sharma), marisa.di.sabatino@material.ntnu.no (Marisa Di Sabatino)

Hot tearing is a common and serious problem in casting of aluminium alloys. When a molten metal is poured through a permanent mold casting (PMC), a crack is appeared the junction of casting near the sprue bar. Hot tear is a phenomenon of liquid feeding during the last stage of solidification. If feeding is not sufficient then a tensile load is developed in the mushy zone; resulting a crack is present on the surface of the casting. These cracks may be of micro and macro types. When the mold temperature is increased and grain refiner is added to the melt, the feeding of the material in the last stage of solidification is increased so no crack formed. It was accomplished that a fine equiaxed, dendritic grain morphology was optimum to reduce hot tearing. In order to achieve better hot tearing resistance, the ranges of pouring and mold temperatures are suggested to be 700- 720 ° C and more than 250 ° C for Al- alloy.

Keywords: Casting, solidification, mushy zone.

STUDY OF FRICTION AND WEAR BEHAVIOR OF AZ91 ALLOY

Vatsala Chaturvedi¹, Ashok Sharma², Upender Pandel²

¹Research Scholar, ²Professor, Dept. of Metallurgical and Materials Engg. MNIT Jaipur

AZ91 alloy having applications in automobiles, aerospace industries etc. During service this AZ91 alloy come across wear and friction. This causes a damage of the component over a period of time. Therefore, mechanical properties of AZ91 alloy should be improved to resist war and friction. Grain refinement is widely used to improve the mechanical properties of the alloy. Grain refinement is achieved by inoculation, rapid cooling, and ultrasonic, electromagnetic and mechanical vibrations. In the present case, mechanical vibrations have been imposed on cast alloy during solidification. It has been observed that the alloy cast at 15 Hz showed best grain refinement. The alloys cast were studied on pin-on- disc machine to measure the wear resistance. Fine grain sized alloy showed better wear and friction resistance in comparison to casting having coarser grains.

Keywords: AZ91 alloy, mechanical vibrations, wear and friction.

National Workshop Metallurgical Failures

September 11-12, 2015

MF 2015



BRCM College of Engineering & Technology
Bahal 127028, Bhiwani (Haryana)

Organized by: **Mechanical Engineering Society**, Department of Mechanical Engineering

Venue:

Seminar Hall Mechanical Block

PROGRAM

DATE	TIME hrs	EVENT
September 11, 2015	9.30 – 10.15	Inaugural Function
	10.15 – 10.30	Tea
	10.30 – 13.15	Technical Session I <ul style="list-style-type: none"> • Dr D B Goel, BRCM CET Bahal Cracking – The cause Of Metal Failures • Dr R P Mishra, BITS Pilani Modeling and Simulation of cutting tool wear
	13.15 – 14.15	LUNCH in Annapurna Mess
	14.15 – 16.15	Technical Session II <ul style="list-style-type: none"> • Vatsala Chaturvedi, MNIT Jaipur Study of friction and wear behaviour of AZ91 Alloy • Sachin Kumar Rathi, MNIT Jaipur Hot tearing in Aluminium Cast Alloys • Anurag Hemilton, MNIT Jaipur Different methods to combat erosion in hydro turbine
	16.30 – 19.00	Visit to Pahadi Mata Mabdir
September 12, 2015	9.30 – 12.00	Technical Session III <ul style="list-style-type: none"> • Shri K P Singh, BHEL Failure Analysis of a steel casting • Dr Sanjay Panwar, MMU Mullana Failure in Engineering Materials
	12.00 – 13.00	Valedictory Function

ABSTRACTS

CRACKING - THE CAUSE OF METAL FAILURES

Dr D B Goel, Emeritus Professor, BRCM CET, Bahal
E-mail: dbgoel@brcm.edu.in

Almost all metallurgical failures occur by nucleation and growth of cracks. In brittle materials, cracks propagate at catastrophic speeds, whereas in ductile materials nucleation and propagation of cracks is rather a slow process. Possibility of cracking in metals exists in various processes, viz. metal working like rolling, forging, extrusion etc, solidification, heat treatment, phase transformations and welding. Stresses generated during service also lead to a large variety of cracking and failures in metals. If mechanical working operations like rolling, forging, extrusion etc are carried out with heavy reductions in various passes, stresses may develop beyond the UTS and formation of cracks may begin leading to failures. During solidification, contraction stresses developed are the main cause of cracking and failures. Dissolved hydrogen in steels is also many times responsible for development of cracks, which is referred to as hydrogen cracking. In various heat treatments failures are accompanied by phase transformations like martensite transformation in steels and formation of brittle constituents in ferrous and nonferrous materials. In welding poor weld design leads to contraction stresses which become responsible for weld failures. Service conditions also are a major source of cracking and failures. Components undergoing fatigue and creep are liable to develop an internal defect structure which makes conditions suitable for nucleation and growth of cracks leading to failures.

The presentation will focus on the critical analysis of the causes and relevant remedial measures to be taken to minimize cracking and increasing the life of metal components.

FAILURE ANALYSIS OF A STEEL CASTING

KP Singh, Consultant, Former General Manager BHEL, Hardwar
E-mail: kpsinghmadhu@gmail.com

Coulisseau is a low alloy steel casting with a single piece wt. of 17.5 t. It is nearly 3 m long and 1.5 m wide. A very heavy section approx. 0.9 m is joined with comparatively thin section. The casting is a component of Press used for processing of metal scrap.

Casting was made in resin bonded sand and melting done in Induction Furnace. The metal was routed through Ladle Metallurgy process. The casting was hardened and tempered. The casting was subjected to MP, UT and DP testing as per specification. Mechanical testing was done to conform to desired values. During final machining at customer end cracks were observed. Initially the defects were found up to 20-40 mm but on further processing defects progressed up to 80 mm. The casting was ultimately rejected. Investigations were carried out. All data during manufacturing viz Moulding, Melting, Heat Treatment, Upgradation was collected. Site visited. Visual inspection, UT & DP testing, Hardness measurements done around defective area/s. Brain storming was done and Cause Effect diagram drawn. Process parameters were re-worked Method modified and In Process Control strengthened. With all these, new casting was made and supplied. The casting has been accepted and working satisfactorily.

MODELING AND SIMULATION OF CUTTING TOOL WEAR

Dr R P Mishra, Asstt professor, Dept of Mech Engg, BITS Pilani
E-mail: rpm@pilani.bits-pilani.ac.in

The main goal of this work is to develop a methodology for studying and quantifying the wear phenomenon in cutting tools. Cutting tool life is an important factor in various metal cutting and machining processes. A

short tool life is uneconomical as tool repair and replacement is expensive. A tool that cannot perform its desired function can be declared as failed. The tool life is defined as the length of time the tool can be used. As a result factors affecting tool life should be monitored to reduce their consequences. Tool wear is the gradual failure of a cutting tool due to its regular and continuous use. Some of the effects of tool wear are poor surface finish, lack of dimensional accuracy and increase in cutting temperatures. During machining most of the input power is converted into heat, resulting in high cutting temperatures. Increased temperature results in thermal damage of tool as well as machined and finished surface. In this workshop we will try to present the analysis of factors which affect tool wear like cutting speed, depth of cut and feed. We also try to study the effect of cutting parameters on surface roughness. We also try to understand the variation of tool wear with time as the parameters like cutting speed and feed rate are changed. Increase in cutting speed generally improves the surface finish quality but it can also result in higher tool wear. The depth of the cut generally does not significantly affect the tool wear and surface roughness.

Keywords: Tool life, Tool wear, cutting parameters, surface roughness.

FAILURES IN ENGINEERING MATERIALS

Dr Sanjay Panwar, Associate Professor

Department of Physics, Maharishi Markandeshwar University, Mullana (Ambala) – 133 207
E-mail: dr.spanwar@gmail.com

The failure of engineering materials, while in service, has always been an undesirable phenomenon. The failure occurs for several reasons and includes losses of human lives, economic losses and interference with the availability of products and services. When capital expenditures are made for plant equipment, it is routine to ensure that the equipment will satisfy the performance and reliability requirements. The unanticipated failures can occur for a variety of reasons, and result in economic losses, disruption in plant operation and safety implications. The usual causes of failures include improper material selection, processing and inadequate design of the components. In order to minimize the frequency and severity of such failures, it is necessary to understand the failures and to confront their causes. The common expectation for the operation of plant equipment, when commitments are made for major capital outlays, is that the plant equipment will operate in accordance with the applicable performance specifications and acceptable reliability. Trouble free operation of such plant equipment over a period of time is an almost universal goal of the operators; however, it is not always possible to achieve this objective.

To prevent failures and to minimize the severity and consequences, it is necessary to identify and understand the causes of failure and contributing factors. Metallurgical failure analysis is perhaps the most widely used approach. Metallurgical failure analysis includes scientific laboratory examinations of metallurgical evidence and exploration of background information of plant equipment failure. Laboratory procedures emphasize on the failed component itself and generally comprise of the detailed metallographic examinations, elemental analysis, presence of extraneous or second phase particles, mechanical property measurements and fractographic examinations etc

DIFFERENT METHODS TO COMBAT EROSION IN HYDRO TURBINE

Anurag Hamilton, Ashok Sharma, Upender Pandel
Department of Metallurgical and Materials Engineering, Malaviya National Institute of Technology Jaipur,
Jaipur-302017, India
E-mail: sunnyy8@gmail.com (Anurag Hamilton), ashok.mnit12@gmail.com (Ashok Sharma)

The Himalyan rivers provide a great potential for hydropower generation due to its steep gradient, steep topography and fragile geography. However, due to geographically young mountains of the region amount